

國立交通大學

機械工程學系

碩士論文

R-134a 冷媒在狹窄雙套管中

蒸發熱傳之實驗研究

Experimental Study of Evaporation Heat Transfer of

R-134a in a Narrow Annular Duct



研究生：李浚圩

指導老師：林清發教授

中華民國九十七年六月

R-134a 冷媒在狹窄雙套管中

蒸發熱傳之實驗研究

Experimental Study of Evaporation Heat Transfer of  
R-134a in a Narrow Annular Duct

研 究 生：李浚圩

Student: Chun-Yu Lee

指 導 老 師：林清發

Advisor: Tsing-Fa Lin

國 立 交 通 大 學

機械工程研究所



Submitted to Institute of Mechanical Engineering

College of Engineering

National Chiao Tung University

In partial Fulfillment of the Requirements

For the Degree of

Master of Science

In Mechanical Engineering

June 2008

Hsinchu, Taiwan, Republic of China

中華民國 九十七 年 六 月

# 國立交通大學

## 論文口試委員會審定書

本校 機械工程 學系碩士班 李浚圩 君

所提論文(中文) R-134a 冷媒在狹窄雙套管中蒸發熱傳  
之實驗研究

(英文) Experimental Study of Evaporation Heat Transfer  
of R-134a in a Narrow Annular Duct

合於碩士資格水準、業經本委員會評審認可。

口試委員：

李聖雄

何清廷

潘欽

指導教授：

林清發

系主任：

廖海

教授

中華民國 97 年 06 月 13 日

## 誌謝

兩年的研究生生活很快的在今年年中劃下句點。想當初隻身進入交大，對於一切如此的陌生，但在這充滿學術氣息的環境下，讓我在知識上成長許多。然而一開始對於雙向流是非常的陌生，直到現在本論文的完成，要感謝很多人，首先要感謝指導教授林清發博士嚴謹及殷切的指導，使學生能培養出獨立思考、釐清並自行解決問題的能力，在每次實驗細節討論與論文指導潤筆中，所獲得的不僅是實驗結果物理意義深邃的闡釋，更是治學一絲不苟的呈現，這些都令我受益匪淺，在此獻上最高謝意。在研究所期間，要感謝博士班陳尚緯、謝汎鈞、張文瑞、陳建安等博士班學長以及李凱文、廖峻樟學長的指導與建議，使我受益匪淺。

求學中的同學長志、永龍及壹龍不管在修課或做實驗過程中都是亦師亦友，使我在研究所緊湊忙碌又充滿歡樂的氣氛中度過，令我永生難忘。其次要感謝譚徵、書磊、文慶學弟等，這些努力的學弟幫忙及合作，希望你們能夠繼續保持實驗室優良傳統，並帶著實驗室的進步。

感謝清華大學潘欽主任、成功大學何清政教授以及核能研究所的李堅雄博士在口試中提出各項建設性的建議，使得本論文更趨完備。

最後要感謝奶奶、父母親以及姊姊在這段日子裏無怨無悔的付出以及支持，使我能無後顧之憂專注於研究。並且要特別感謝女友佩琪的陪伴，在這段精彩的研究生生活是你陪伴我渡過，你的關心與支持使我有勇氣面對一切困難的挑戰，使我無後顧之憂的獲得碩士學位。

最後，僅以本文獻給我所關心的人和所有關心我的人。

今日我以交大為榮 願他日交大以我為榮

浚圩 謹致

2008, 6 於新竹交大



# R-134a 冷媒在狹窄雙套管中蒸發熱傳之實驗研究

研究生：李浚圩

指導教授：林清發

國立交通大學機械工程學系

## 摘要

本論文是針對 R-134a 冷媒在狹窄雙套管中的蒸發熱傳和可看見的蒸發流動特性之實驗研究。管子的間隙固定在 1.0、2.0 和 5.0mm。在實驗中，探討了管徑尺寸、冷媒質通量、飽和溫度、熱通量以及蒸氣乾度對熱傳遞係數及蒸發流動特性之影響。在實驗參數的範圍上，在間隙 5.0mm 中，冷媒質量通量  $G$  從 100 到 300 kg/m<sup>2</sup>s，熱通量  $q$  從 5 到 15 kW/m<sup>2</sup>，蒸氣乾度由 0.05 到 0.95 以及冷媒飽和溫度  $T_{\text{sat}}$  從 5 到 15°C。對於間隙 2.0 和 1.0mm，在系統迴路的穩定性考量上，我們設定  $G$  的變化分別為 300 到 500 以及 500 到 700 kg/m<sup>2</sup>s，其他實驗參數範圍相同於間隙 5.0mm。

首先是間隙 1.0 和 2.0mm 可以很清楚的看到蒸發熱傳遞係數上升隨著冷媒蒸氣乾度的上升呈現近似線性的關係以及在高  $G$  中上升較明顯。此外，蒸發熱傳遞係數上升明顯的在增加的  $q$  中。並且，蒸發熱傳遞係數顯著上升對於上升的飽和溫度，但是在較窄的管中低熱通量和高質量通量上影響較不明顯。再者，除了在低蒸氣乾度下熱傳遞係數上升明顯隨著上升的冷媒質量通量。在較小的間隙中造成很明顯熱傳遞係數的上升。在較寬間隙 5.0mm 中與小間隙中有相似的趨勢除了在加熱表面上液膜的乾化。當液膜的乾化現象產生隨著蒸氣乾度的上升蒸發熱傳遞係數則會降低。

除了前述熱傳的數據以外，R-134a 蒸發流動的相片由全管的側面以及在管中間小區域所拍攝都在此可以看到。在間隙 1.0 和 2.0mm，低蒸氣乾度下加熱表面氣泡成核很重要。此外，在間隙 1.0mm 低蒸氣乾度下小氣泡合併成大氣泡再由大氣泡合併成彈狀氣泡較為明顯以及氣泡被驅散在大的液袋區

裡。中乾度下，氣泡的成核在加熱表面上仍然可以看見以及在管中主要為蒸氣流過內管的液膜所帶走熱所主導流譜為環形雙向流，在液氣介面上有不規則的波動存在。更高的蒸氣乾度下以環形雙向流主導，環形雙向流主導普遍在高熱通量、低冷媒質量通量和高飽和溫度。在間隙 5.0mm 中重力的影響變得非常大，蒸氣流在管中上半部，液體流在管子下半部因此以分層雙向流所主導。此外，在低冷媒質量通量和高蒸氣乾度加熱表面上液膜乾化的發生在管中下游的區域，並且在高蒸氣乾度、高熱通量以及低冷媒飽和溫度下會使得乾化往上游移動。

最後，我們將 R-134a 蒸發熱傳遞係數在所有間隙中的實驗資料做分析，並求出經驗公式。



# Experimental Study of Evaporation Heat Transfer of R-134a in a Narrow Annular Duct

**Student: Chun-Yu Li**

**Advisor: Prof. Tsing-Fa Lin**

**Institute of Mechanical Engineering**

**National Chiao Tung University**

## ABSTRACT

An experiment is carried out in the present study to investigate the evaporation heat transfer and associated evaporating flow characteristics for refrigerant R-134a flowing in a horizontal narrow annular duct. The gap of the duct is fixed at 1.0, 2.0 and 5.0 mm. In the experiment, the effects of the duct gap, refrigerant mass flux and saturation temperature, imposed heat flux and vapor quality of the refrigerant on the measured evaporation heat transfer coefficient  $h_e$  and the evaporating flow characteristics will be examined in detail. For the duct gap of 5.0 mm, the refrigerant mass flux  $G$  is varied from 100 to 300 kg/m<sup>2</sup>s, imposed heat flux  $q$  from 5 to 15 kW/m<sup>2</sup>, vapor quality  $x_m$  from 0.05 to 0.95 and refrigerant saturation temperature  $T_{sat}$  from 5 to 15°C. While for the gap of 2.0 and 1.0 mm,  $G$  is respectively varied from 300 to 500 and from 500 to 700 kg/m<sup>2</sup>s with the other parameters varied in the same ranges as those for  $\delta=5.0$  mm.

The experimental data for  $\delta=1.0$  and 2.0 mm clearly show that evaporation heat transfer coefficient increases almost linearly with the vapor quality of the refrigerant and the increase is more significant at a higher  $G$ . Besides, the evaporation heat transfer coefficients also rise substantially at increasing  $q$ . Moreover, a significant increase in the evaporation heat transfer coefficients results for a rise in  $T_{sat}$ , but effects are less pronounced in the narrower duct at a low imposed heat flux and a high refrigerant mass flux. Furthermore, the evaporation heat

transfer coefficients increase substantially with the refrigerant mass flux except at low vapor quality. We also note that reducing the duct gap causes a significant increase in  $h_r$ . For the duct with the wider gap of 5.0 mm the effects of the experimental parameters on  $h_r$  resemble that in the small duct gap except the liquid film covering the heating surface becomes dryout at some downstream locations at low mass flux and high vapor quality. This liquid film dryout results in a reduction of  $h_r$  with  $x_m$ .

In addition to the heat transfer data presented above, the photos of R-134a evaporating flow are taken from the duct side over the entire duct and over a small region around the middle axial location. In the flow visualization for the small ducts with  $\delta=1.0$  and 2.0 mm the bubble nucleation on the heating surface is found to be important at low vapor quality. Besides, at low vapor quality merging of small bubbles to form big bubbles and merging of big bubbles into bubble slugs take place, which is more pronounced at the smaller duct gap for  $\delta=1.0$  mm. Moreover, bubbles dispersed in a large liquid slug appear in the duct. At the intermediate vapor quality some bubble nucleation on the heating surface still exists and the flow in the duct is dominated by the vapor flow over thin liquid film around the inner pipe, an annular two-phase flow pattern. Irregular waves appear at the vapor-liquid interface. At the very high vapor quality bubble nucleation can still be seen at high imposed heat flux although the liquid film covering the heating surface is relatively thin. At this high quality the duct is also dominated by the annular two-phase flow. The annular two-phase flow prevails in a larger portion of the duct at higher imposed flux, lower refrigerant mass flux, and higher refrigerant saturated temperature. In the duct with the wider gap of 5.0 mm the effects of the gravity on the evaporating flow are larger, resulting a stratified two-phase flow with the vapor and liquid flows respectively dominated in the upper and lower parts of the duct. Besides, at low refrigerant mass flux and high vapor quality dryout of the liquid film on the heating surface occurs at some downstream locations. These dryout locations move upstream at



higher vapor quality, higher imposed heat flux and lower refrigerant saturated temperature.

Finally, the empirical correlations for the present measured heat transfer coefficient for the R-134a evaporation in the annular ducts were provided.



# CONTENTS

<b>ABSTRACT</b>	<b>i</b>
<b>CONTENTS</b>	<b>iv</b>
<b>LIST OF TABLES</b>	<b>vi</b>
<b>LIST OF FIGURES</b>	<b>vii</b>
<b>NOMENCLATURE</b>	<b>xv</b>
<b>CHAPTER 1 INTRODUCTION</b>	<b>1</b>
1.1 Motivation of the Present Study	1
1.2 Literature Review	2
1.2.1 Single-Phase Heat Transfer in Small Channels	2
1.2.2 Evaporation Heat Transfer in Conventional Channels	3
1.2.3 Evaporation Heat Transfer in Small Channels	6
1.3 Objective of the Present Study	7
<b>CHAPTER 2 EXPERIMENTAL APPARATUS AND PROCEDURES</b>	<b>9</b>
2.1 Refrigerant Flow Loop	9
2.2 Test Section	10
2.3 Hot-Water Loop for Preheater	11
2.4 Water-Glycol Loop	12
2.5 Programmable DC Power Supply	12
2.6 Photographic System	12
2.7 Data Acquisition	13
2.8 Experimental Procedures	14
2.9 Experimental Parameters	14

<b>CHAPTER 3 DATA REDUCTION</b>	<b>23</b>
3.1 Single Phase Heat Transfer	23
3.2 Two Phase Heat Transfer	25
3.3 Uncertainty Analysis	27
<b>CHAPTER 4 RESULTS AND DISCUSSION</b>	<b>29</b>
4.1 Single-Phase Heat Transfer	30
4.2 Evaporation Heat Transfer in Narrow Annular Duct with $\delta=2.0$ mm	31
4.3 Evaporation Heat Transfer in Narrower Annular Duct ( $\delta=1.0$ mm)	33
4.4 Characteristics of R-134a Evaporating Flow in Narrow Annular Duct	35
4.5 Evaporation Heat Transfer and Flow Characteristics in Wider Annular Duct with $\delta=5.0$ mm	38
4.6 Correlation Equation for Evaporation Heat Transfer Coefficients	40
<b>CHAPTER 5 CONCLUDING REMARKS</b>	<b>121</b>
<b>REFERENCES</b>	<b>123</b>

## LIST OF TABLES

Table 1.1	Comparison of some properties of three HFCs refrigerants for air conditioning and refrigeration applications	8
Table 2.1	List of conditions of the experimental parameters for R-134a	16
Table 2.2	Thermophysical properties of R-134a refrigerant	17
Table 3.1	Summary of the uncertainty analysis	28
Table 4.1	Relation between the mean vapor quality, void fraction and liquid film thickness estimated from the separated two-phase flow model	42





## LIST OF FIGURES

Fig. 2.1	Schematic of experimental system for the annular duct	18
Fig. 2.2	The detailed arrangement of the test section for the annular duct	19
Fig. 2.3	The cross-sectional view of the annular duct showing the heater and locations of the thermocouples.	20
Fig. 2.4	Schematic of heat flux control loop	21
Fig. 4.1	Comparison of the present single-phase liquid convection heat transfer data $h_l(a)$ and $Nu_l(b)$ with the correlations of Gnielinski and Dittus-Boelter.	43
Fig. 4.2	Comparison of the present single-phase liquid convection heat transfer data $h_l(a)$ and $Nu_l(b)$ with the correlations of Gnielinski and Dittus-Boelter.	44
Fig. 4.3	Variations of R-134a evaporation heat transfer coefficient with vapor quality in $\delta = 2.0$ mm narrow duct at $T_{sat}=5^\circ\text{C}$ for various $G$ for (a) $q = 5 \text{ kW/m}^2$ , (b) $q = 10 \text{ kW/m}^2$ and (c) $q = 15 \text{ kW/m}^2$ .	45
Fig. 4.4	Variations of R-134a evaporation heat transfer coefficient with vapor quality in $\delta = 2.0$ mm narrow duct at $T_{sat}=10^\circ\text{C}$ for various $G$ for (a) $q = 5 \text{ kW/m}^2$ , (b) $q = 10 \text{ kW/m}^2$ and (c) $q = 15 \text{ kW/m}^2$ .	46
Fig. 4.5	Variations of R-134a evaporation heat transfer coefficient with vapor quality in $\delta = 2.0$ mm narrow duct at $T_{sat}=15^\circ\text{C}$ for various $G$ for (a) $q = 5 \text{ kW/m}^2$ , (b) $q = 10 \text{ kW/m}^2$ and (c) $q = 15 \text{ kW/m}^2$ .	47
Fig. 4.6	Variations of R-134a evaporation heat transfer coefficient with vapor quality in $\delta = 2.0$ mm narrow duct at $G=300 \text{ kg/m}^2\text{s}$ for various $T_{sat}$ for (a) $q = 5 \text{ kW/m}^2$ , (b) $q = 10 \text{ kW/m}^2$ and (c) $q = 15 \text{ kW/m}^2$ .	48
Fig. 4.7	Variations of R-134a evaporation heat transfer coefficient with vapor quality in $\delta = 2.0$ mm narrow duct at $G=400 \text{ kg/m}^2\text{s}$ for various $T_{sat}$ for (a) $q = 5 \text{ kW/m}^2$ , (b) $q = 10 \text{ kW/m}^2$ and (c) $q = 15 \text{ kW/m}^2$ .	49
Fig. 4.8	Variations of R-134a evaporation heat transfer coefficient with vapor quality in $\delta = 2.0$ mm narrow duct at $G=500 \text{ kg/m}^2\text{s}$ for various $T_{sat}$ for (a) $q = 5 \text{ kW/m}^2$ , (b) $q = 10 \text{ kW/m}^2$ and (c) $q = 15 \text{ kW/m}^2$ .	50

- Fig. 4.9 Variations of R-134a evaporation heat transfer coefficient with vapor quality in  $\delta = 2.0$  mm narrow duct at  $G=300$  kg/m<sup>2</sup>s for various  $q$  for (a)  $T_{\text{sat}}=5^{\circ}\text{C}$ , (b)  $T_{\text{sat}}=10^{\circ}\text{C}$  and (c)  $T_{\text{sat}}=15^{\circ}\text{C}$ . 51
- Fig. 4.10 Variations of R-134a evaporation heat transfer coefficient with vapor quality in  $\delta = 2.0$  mm narrow duct at  $G=400$  kg/m<sup>2</sup>s for various  $q$  for (a)  $T_{\text{sat}}=5^{\circ}\text{C}$ , (b)  $T_{\text{sat}}=10^{\circ}\text{C}$  and (c)  $T_{\text{sat}}=15^{\circ}\text{C}$ . 52
- Fig. 4.11 Variations of R-134a evaporation heat transfer coefficient with vapor quality in  $\delta = 2.0$  mm narrow duct at  $G=500$  kg/m<sup>2</sup>s for various  $q$  for (a)  $T_{\text{sat}}=5^{\circ}\text{C}$ , (b)  $T_{\text{sat}}=10^{\circ}\text{C}$  and (c)  $T_{\text{sat}}=15^{\circ}\text{C}$ . 53
- Fig. 4.12 Variations of R-134a evaporation heat transfer coefficient with vapor quality in  $\delta = 1.0$  mm narrow duct at  $T_{\text{sat}}=5^{\circ}\text{C}$  for various  $G$  for (a)  $q = 5$  kW/m<sup>2</sup>, (b)  $q = 10$  kW/m<sup>2</sup> and (c)  $q = 15$  kW/m<sup>2</sup>. 54
- Fig. 4.13 Variations of R-134a evaporation heat transfer coefficient with vapor quality in  $\delta = 1.0$  mm narrow duct at  $T_{\text{sat}}=10^{\circ}\text{C}$  for various  $G$  for (a)  $q = 5$  kW/m<sup>2</sup>, (b)  $q = 10$  kW/m<sup>2</sup> and (c)  $q = 15$  kW/m<sup>2</sup>. 55
- Fig. 4.14 Variations of R-134a evaporation heat transfer coefficient with vapor quality in  $\delta = 1.0$  mm narrow duct at  $T_{\text{sat}}=15^{\circ}\text{C}$  for various  $G$  for (a)  $q = 5$  kW/m<sup>2</sup>, (b)  $q = 10$  kW/m<sup>2</sup> and (c)  $q = 15$  kW/m<sup>2</sup>. 56
- Fig. 4.15 Variations of R-134a evaporation heat transfer coefficient with vapor quality in  $\delta = 1.0$  mm narrow duct at  $G=500$  kg/m<sup>2</sup>s for various  $T_{\text{sat}}$  for (a)  $q = 5$  kW/m<sup>2</sup>, (b)  $q = 10$  kW/m<sup>2</sup> and (c)  $q = 15$  kW/m<sup>2</sup>. 57
- Fig. 4.16 Variations of R-134a evaporation heat transfer coefficient with vapor quality in  $\delta = 1.0$  mm narrow duct at  $G=600$  kg/m<sup>2</sup>s for various  $T_{\text{sat}}$  for (a)  $q = 5$  kW/m<sup>2</sup>, (b)  $q = 10$  kW/m<sup>2</sup> and (c)  $q = 15$  kW/m<sup>2</sup>. 58
- Fig. 4.17 Variations of R-134a evaporation heat transfer coefficient with vapor quality in  $\delta = 1.0$  mm narrow duct at  $G=700$  kg/m<sup>2</sup>s for various  $T_{\text{sat}}$  for (a)  $q = 5$  kW/m<sup>2</sup>, (b)  $q = 10$  kW/m<sup>2</sup> and (c)  $q = 15$  kW/m<sup>2</sup>. 59
- Fig. 4.18 Variations of R-134a evaporation heat transfer coefficient with vapor quality in  $\delta = 1.0$  mm narrow duct at  $G=500$  kg/m<sup>2</sup>s for various  $q$  for (a)  $T_{\text{sat}}=5^{\circ}\text{C}$ , (b)  $T_{\text{sat}}=10^{\circ}\text{C}$  and (c)  $T_{\text{sat}}=15^{\circ}\text{C}$ . 60
- Fig. 4.19 Variations of R-134a evaporation heat transfer coefficient with vapor quality

in  $\delta = 1.0$  mm narrow duct at  $G=600$  kg/m<sup>2</sup>s for various  $q$  for (a)  $T_{\text{sat}}=5^{\circ}\text{C}$ , (b)  $T_{\text{sat}}=10^{\circ}\text{C}$  and (c)  $T_{\text{sat}}=15^{\circ}\text{C}$ .

61

Fig. 4.20 Variations of R-134a evaporation heat transfer coefficient with vapor quality in  $\delta = 1.0$  mm narrow duct at  $G=700$  kg/m<sup>2</sup>s for various  $q$  for (a)  $T_{\text{sat}}=5^{\circ}\text{C}$ , (b)  $T_{\text{sat}}=10^{\circ}\text{C}$  and (c)  $T_{\text{sat}}=15^{\circ}\text{C}$ .

62

Fig. 4.21 Variations of R-134a evaporation heat transfer coefficient with vapor quality at  $q = 5$  kW/m<sup>2</sup> and  $G=500$  kg/m<sup>2</sup>s for various  $\delta$  for (a)  $T_{\text{sat}}=5^{\circ}\text{C}$ , (b)  $T_{\text{sat}}=10^{\circ}\text{C}$  and (c)  $T_{\text{sat}}=15^{\circ}\text{C}$ .

63

Fig. 4.22 Variations of R-134a evaporation heat transfer coefficient with vapor quality at  $q = 10$  kW/m<sup>2</sup> and  $G=500$  kg/m<sup>2</sup>s for various  $\delta$  for (a)  $T_{\text{sat}}=5^{\circ}\text{C}$ , (b)  $T_{\text{sat}}=10^{\circ}\text{C}$  and (c)  $T_{\text{sat}}=15^{\circ}\text{C}$ .

64

Fig. 4.23 Variations of R-134a evaporation heat transfer coefficient with vapor quality at  $q = 15$  kW/m<sup>2</sup> and  $G=500$  kg/m<sup>2</sup>s for various  $\delta$  for (a)  $T_{\text{sat}}=5^{\circ}\text{C}$ , (b)  $T_{\text{sat}}=10^{\circ}\text{C}$  and (c)  $T_{\text{sat}}=15^{\circ}\text{C}$ .

65

Fig. 4.24 Variations of R-134a evaporation heat transfer coefficient with vapor quality at  $q = 5$  kW/m<sup>2</sup>,  $\delta = 1.0$  mm and  $\delta = 2.0$  mm for various  $G$  for (a)  $T_{\text{sat}}=5^{\circ}\text{C}$  and (b)  $T_{\text{sat}}=15^{\circ}\text{C}$ .

66

Fig. 4.25 Variations of R-134a evaporation heat transfer coefficient with vapor quality at  $G=500$  kg/m<sup>2</sup>s,  $\delta = 1.0$  mm and  $\delta = 2.0$  mm for various  $T_{\text{sat}}$  for (a)  $q = 5$  kW/m<sup>2</sup> and (b)  $q = 10$  kW/m<sup>2</sup>.

67

Fig. 4.26 Variations of R-134a evaporation heat transfer coefficient with vapor quality at  $G=500$  kg/m<sup>2</sup>s,  $\delta = 1.0$  mm and  $\delta = 2.0$  mm for various  $q$  for (a)  $T_{\text{sat}}=5^{\circ}\text{C}$ , (b)  $T_{\text{sat}}=10^{\circ}\text{C}$  and (c)  $T_{\text{sat}}=15^{\circ}\text{C}$ .

68

Fig. 4.27 Photos of flow in the evaporation of R-134a in the entire duct and a small region around middle axial location at  $G=300$  kg/m<sup>2</sup>s,  $T_{\text{sat}} = 15^{\circ}\text{C}$ ,  $\delta = 2.0$  mm,  $q = 5$  kW/ m<sup>2</sup> for (a)  $x_m = 0.05$ , (b)  $x_m = 0.54$  and (c)  $x_m = 0.94$ .

70

Fig. 4.28 Photos of flow in the evaporation of R-134a in the entire duct and a small region around middle axial location at  $G=300$  kg/m<sup>2</sup>s,  $T_{\text{sat}} = 15^{\circ}\text{C}$ ,  $\delta = 2.0$  mm,  $q = 15$  kW/ m<sup>2</sup> for (a)  $x_m = 0.05$ , (b)  $x_m = 0.54$  and (c)  $x_m = 0.95$ .

71

Fig. 4.29 Photos of flow in the evaporation of R-134a in the entire duct and a small region around middle axial location at  $G=300$  kg/m<sup>2</sup>s,  $T_{\text{sat}} = 5^{\circ}\text{C}$ ,  $\delta = 2.0$  mm,

$q = 15 \text{ kW/ m}^2$  for (a)  $x_m = 0.06$ , (b)  $x_m = 0.50$  and (c)  $x_m = 0.95$ . 72

Fig. 4.30 Photos of flow in the evaporation of R-134a in the entire duct and a small region around middle axial location at  $G=400 \text{ kg/m}^2\text{s}$ ,  $T_{\text{sat}} = 15^\circ\text{C}$ ,  $\delta = 2.0 \text{ mm}$ ,  $q = 5 \text{ kW/ m}^2$  for (a)  $x_m = 0.07$ , (b)  $x_m = 0.49$  and (c)  $x_m = 0.93$ . 73

Fig. 4.31 Photos of flow in the evaporation of R-134a in the entire duct and a small region around middle axial location at  $G=400 \text{ kg/m}^2\text{s}$ ,  $T_{\text{sat}} = 15^\circ\text{C}$ ,  $\delta = 2.0 \text{ mm}$ ,  $q = 15 \text{ kW/ m}^2$  for (a)  $x_m = 0.05$ , (b)  $x_m = 0.52$  and (c)  $x_m = 0.93$ . 74

Fig. 4.32 Photos of flow in the evaporation of R-134a in the entire duct and a small region around middle axial location at  $G=400 \text{ kg/m}^2\text{s}$ ,  $T_{\text{sat}} = 5^\circ\text{C}$ ,  $\delta = 2.0 \text{ mm}$ ,  $q = 15 \text{ kW/ m}^2$  for (a)  $x_m = 0.07$ , (b)  $x_m = 0.49$  and (c)  $x_m = 0.95$ . 75

Fig. 4.33 Photos of flow in the evaporation of R-134a in the entire duct and a small region around middle axial location at  $G=500 \text{ kg/m}^2\text{s}$ ,  $T_{\text{sat}} = 15^\circ\text{C}$ ,  $\delta = 2.0 \text{ mm}$ ,  $q = 5 \text{ kW/ m}^2$  for (a)  $x_m = 0.06$ , (b)  $x_m = 0.50$  and (c)  $x_m = 0.93$ . 76

Fig. 4.34 Photos of flow in the evaporation of R-134a in the entire duct and a small region around middle axial location at  $G=500 \text{ kg/m}^2\text{s}$ ,  $T_{\text{sat}} = 15^\circ\text{C}$ ,  $\delta = 2.0 \text{ mm}$ ,  $q = 15 \text{ kW/ m}^2$  for (a)  $x_m = 0.07$ , (b)  $x_m = 0.52$  and (c)  $x_m = 0.93$ . 77

Fig. 4.35 Photos of flow in the evaporation of R-134a in the entire duct and a small region around middle axial location at  $G=500 \text{ kg/m}^2\text{s}$ ,  $T_{\text{sat}} = 5^\circ\text{C}$ ,  $\delta = 2.0 \text{ mm}$ ,  $q = 15 \text{ kW/ m}^2$  for (a)  $x_m = 0.06$ , (b)  $x_m = 0.53$  and (c)  $x_m = 0.95$ . 78

Fig. 4.36 Photos of flow in the evaporation of R-134a in a small region around middle axial location at  $\delta = 2 \text{ mm}$  and  $G=300 \text{ kg/m}^2\text{s}$  for various imposed heat fluxes, saturated temperatures and vapor quality. 79

Fig. 4.37 Photos of flow in the evaporation of R-134a in a small region around middle axial location at  $\delta = 2 \text{ mm}$  and  $G=400 \text{ kg/m}^2\text{s}$  for various imposed heat fluxes, saturated temperatures and vapor quality. 80

Fig. 4.38 Photos of flow in the evaporation of R-134a in a small region around middle axial location at  $\delta = 2 \text{ mm}$  and  $G=500 \text{ kg/m}^2\text{s}$  for various imposed heat fluxes, saturated temperatures and vapor quality. 81

Fig. 4.39 Photos of flow in the evaporation of R-134a in the entire duct and a small region around middle axial location at  $G=500 \text{ kg/m}^2\text{s}$ ,  $T_{\text{sat}} = 15^\circ\text{C}$ ,  $\delta = 1.0 \text{ mm}$ ,  $q = 5 \text{ kW/ m}^2$  for (a)  $x_m = 0.06$ , (b)  $x_m = 0.50$  and (c)  $x_m = 0.94$ . 82



- Fig. 4.40 Photos of flow in the evaporation of R-134a in the entire duct and a small region around middle axial location at  $G=500 \text{ kg/m}^2\text{s}$ ,  $T_{\text{sat}} = 15^\circ\text{C}$ ,  $\delta = 1.0 \text{ mm}$ ,  $q = 15 \text{ kW/m}^2$  for (a)  $x_m = 0.06$ , (b)  $x_m = 0.49$  and (c)  $x_m = 0.95$ . 83
- Fig. 4.41 Photos of flow in the evaporation of R-134a in the entire duct and a small region around middle axial location at  $G=500 \text{ kg/m}^2\text{s}$ ,  $T_{\text{sat}} = 5^\circ\text{C}$ ,  $\delta = 1.0 \text{ mm}$ ,  $q = 15 \text{ kW/m}^2$  for (a)  $x_m = 0.05$ , (b)  $x_m = 0.52$  and (c)  $x_m = 0.94$ . 84
- Fig. 4.42 Photos of flow in the evaporation of R-134a in the entire duct and a small region around middle axial location at  $G=600 \text{ kg/m}^2\text{s}$ ,  $T_{\text{sat}} = 15^\circ\text{C}$ ,  $\delta = 1.0 \text{ mm}$ ,  $q = 5 \text{ kW/m}^2$  for (a)  $x_m = 0.06$ , (b)  $x_m = 0.51$  and (c)  $x_m = 0.95$ . 85
- Fig. 4.43 Photos of flow in the evaporation of R-134a in the entire duct and a small region around middle axial location at  $G=600 \text{ kg/m}^2\text{s}$ ,  $T_{\text{sat}} = 15^\circ\text{C}$ ,  $\delta = 1.0 \text{ mm}$ ,  $q = 15 \text{ kW/m}^2$  for (a)  $x_m = 0.06$ , (b)  $x_m = 0.51$  and (c)  $x_m = 0.95$ . 86
- Fig. 4.44 Photos of flow in the evaporation of R-134a in the entire duct and a small region around middle axial location at  $G=600 \text{ kg/m}^2\text{s}$ ,  $T_{\text{sat}} = 5^\circ\text{C}$ ,  $\delta = 1.0 \text{ mm}$ ,  $q = 15 \text{ kW/m}^2$  for (a)  $x_m = 0.06$ , (b)  $x_m = 0.49$  and (c)  $x_m = 0.94$ . 87
- Fig. 4.45 Photos of flow in the evaporation of R-134a in the entire duct and a small region around middle axial location at  $G=700 \text{ kg/m}^2\text{s}$ ,  $T_{\text{sat}} = 15^\circ\text{C}$ ,  $\delta = 1.0 \text{ mm}$ ,  $q = 5 \text{ kW/m}^2$  for (a)  $x_m = 0.05$ , (b)  $x_m = 0.50$  and (c)  $x_m = 0.93$ . 88
- Fig. 4.46 Photos of flow in the evaporation of R-134a in the entire duct and a small region around middle axial location at  $G=700 \text{ kg/m}^2\text{s}$ ,  $T_{\text{sat}} = 15^\circ\text{C}$ ,  $\delta = 1.0 \text{ mm}$ ,  $q = 15 \text{ kW/m}^2$  for (a)  $x_m = 0.06$ , (b)  $x_m = 0.50$  and (c)  $x_m = 0.94$ . 89
- Fig. 4.47 Photos of flow in the evaporation of R-134a in the entire duct and a small region around middle axial location at  $G=700 \text{ kg/m}^2\text{s}$ ,  $T_{\text{sat}} = 5^\circ\text{C}$ ,  $\delta = 1.0 \text{ mm}$ ,  $q = 15 \text{ kW/m}^2$  for (a)  $x_m = 0.05$ , (b)  $x_m = 0.49$  and (c)  $x_m = 0.93$ . 90
- Fig. 4.48 Photos of flow in the evaporation of R-134a in a small region around middle axial location at  $\delta = 1 \text{ mm}$  and  $G=500 \text{ kg/m}^2\text{s}$  for various imposed heat fluxes, saturated temperatures and vapor quality. 91
- Fig. 4.49 Photos of flow in the evaporation of R-134a in a small region around middle axial location at  $\delta = 1 \text{ mm}$  and  $G=600 \text{ kg/m}^2\text{s}$  for various imposed heat fluxes, saturated temperatures and vapor quality. 92
- Fig. 4.50 Photos of flow in the evaporation of R-134a in a small region around middle

axial location at  $\delta = 1$  mm and  $G=700$  kg/m<sup>2</sup>s for various imposed heat fluxes, saturated temperatures and vapor quality. 93

Fig. 4.51 Variations of R-134a evaporation heat transfer coefficient with vapor quality in  $\delta = 5.0$  mm narrow duct at  $T_{\text{sat}}=5^{\circ}\text{C}$  for various  $G$  for (a)  $q = 5$  kW/m<sup>2</sup>, (b)  $q = 10$  kW/m<sup>2</sup> and (c)  $q = 15$  kW/m<sup>2</sup>. 94

Fig. 4.52 Variations of R-134a evaporation heat transfer coefficient with vapor quality in  $\delta = 5.0$  mm narrow duct at  $T_{\text{sat}}=10^{\circ}\text{C}$  for various  $G$  for (a)  $q = 5$  kW/m<sup>2</sup>, (b)  $q = 10$  kW/m<sup>2</sup> and (c)  $q = 15$  kW/m<sup>2</sup>. 95

Fig. 4.53 Variations of R-134a evaporation heat transfer coefficient with vapor quality in  $\delta = 5.0$  mm narrow duct at  $T_{\text{sat}}=15^{\circ}\text{C}$  for various  $G$  for (a)  $q = 5$  kW/m<sup>2</sup>, (b)  $q = 10$  kW/m<sup>2</sup> and (c)  $q = 15$  kW/m<sup>2</sup>. 96

Fig. 4.54 Variations of R-134a evaporation heat transfer coefficient with vapor quality in  $\delta = 5.0$  mm narrow duct at  $G=100$  kg/m<sup>2</sup>s for various  $T_{\text{sat}}$  for (a)  $q = 5$  kW/m<sup>2</sup>, (b)  $q = 10$  kW/m<sup>2</sup> and (c)  $q = 15$  kW/m<sup>2</sup>. 97

Fig. 4.55 Variations of R-134a evaporation heat transfer coefficient with vapor quality in  $\delta = 5.0$  mm narrow duct at  $G=200$  kg/m<sup>2</sup>s for various  $T_{\text{sat}}$  for (a)  $q = 5$  kW/m<sup>2</sup>, (b)  $q = 10$  kW/m<sup>2</sup> and (c)  $q = 15$  kW/m<sup>2</sup>. 98

Fig. 4.56 Variations of R-134a evaporation heat transfer coefficient with vapor quality in  $\delta = 5.0$  mm narrow duct at  $G=300$  kg/m<sup>2</sup>s for various  $T_{\text{sat}}$  for (a)  $q = 5$  kW/m<sup>2</sup>, (b)  $q = 10$  kW/m<sup>2</sup> and (c)  $q = 15$  kW/m<sup>2</sup>. 99

Fig. 4.57 Variations of R-134a evaporation heat transfer coefficient with vapor quality in  $\delta = 5.0$  mm narrow duct at  $G=100$  kg/m<sup>2</sup>s for various  $q$  for (a)  $T_{\text{sat}}=5^{\circ}\text{C}$ , (b)  $T_{\text{sat}}=10^{\circ}\text{C}$  and (c)  $T_{\text{sat}}=15^{\circ}\text{C}$ . 100

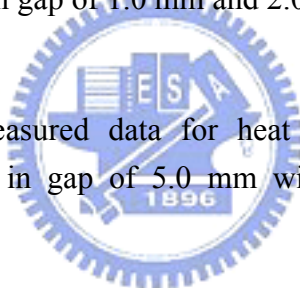
Fig. 4.58 Variations of R-134a evaporation heat transfer coefficient with vapor quality in  $\delta = 5.0$  mm narrow duct at  $G=200$  kg/m<sup>2</sup>s for various  $q$  for (a)  $T_{\text{sat}}=5^{\circ}\text{C}$ , (b)  $T_{\text{sat}}=10^{\circ}\text{C}$  and (c)  $T_{\text{sat}}=15^{\circ}\text{C}$ . 101

Fig. 4.59 Variations of R-134a evaporation heat transfer coefficient with vapor quality in  $\delta = 5.0$  mm narrow duct at  $G=300$  kg/m<sup>2</sup>s for various  $q$  for (a)  $T_{\text{sat}}=5^{\circ}\text{C}$ , (b)  $T_{\text{sat}}=10^{\circ}\text{C}$  and (c)  $T_{\text{sat}}=15^{\circ}\text{C}$ . 102

Fig. 4.60 Variations of R-134a evaporation heat transfer coefficient with vapor quality at  $q = 5$  kW/m<sup>2</sup> and  $G=300$  kg/m<sup>2</sup>s for various  $\delta$  for (a)  $T_{\text{sat}}=5^{\circ}\text{C}$ , (b)  $T_{\text{sat}}=10$

°C and (c) $T_{\text{sat}}=15^{\circ}\text{C}$ .	103
Fig. 4.61 Variations of R-134a evaporation heat transfer coefficient with vapor quality at $q = 10 \text{ kW/m}^2$ and $G=300 \text{ kg/m}^2\text{s}$ for various $\delta$ for (a) $T_{\text{sat}}=5^{\circ}\text{C}$ , (b) $T_{\text{sat}}=10^{\circ}\text{C}$ and (c) $T_{\text{sat}}=15^{\circ}\text{C}$ .	104
Fig. 4.62 Variations of R-134a evaporation heat transfer coefficient with vapor quality at $q = 15 \text{ kW/m}^2$ and $G=300 \text{ kg/m}^2\text{s}$ for various $\delta$ for (a) $T_{\text{sat}}=5^{\circ}\text{C}$ , (b) $T_{\text{sat}}=10^{\circ}\text{C}$ and (c) $T_{\text{sat}}=15^{\circ}\text{C}$ .	105
Fig. 4.63 Photos of flow in the evaporation of R-134a in the entire duct at $G=100 \text{ kg/m}^2\text{s}$ , $T_{\text{sat}} = 15^{\circ}\text{C}$ , $\delta = 5.0 \text{ mm}$ , $q = 5 \text{ kW/ m}^2$ for (a) $x_m = 0.05$ , (b) $x_m = 0.49$ and (c) $x_m = 0.95$ .	106
Fig. 4.64 Photos of flow in the evaporation of R-134a in the entire duct at $G=100 \text{ kg/m}^2\text{s}$ , $T_{\text{sat}} = 15^{\circ}\text{C}$ , $\delta = 5.0 \text{ mm}$ , $q = 15 \text{ kW/ m}^2$ for (a) $x_m = 0.05$ , (b) $x_m = 0.50$ and (c) $x_m = 0.94$ .	107
Fig. 4.65 Photos of flow in the evaporation of R-134a in the entire duct at $G=100 \text{ kg/m}^2\text{s}$ , $T_{\text{sat}} = 5^{\circ}\text{C}$ , $\delta = 5.0 \text{ mm}$ , $q = 15 \text{ kW/ m}^2$ for (a) $x_m = 0.05$ , (b) $x_m = 0.50$ and (c) $x_m = 0.94$ .	108
Fig. 4.66 Photos of flow in the evaporation of R-134a in the entire duct at $G=200 \text{ kg/m}^2\text{s}$ , $T_{\text{sat}} = 15^{\circ}\text{C}$ , $\delta = 5.0 \text{ mm}$ , $q = 5 \text{ kW/ m}^2$ for (a) $x_m = 0.05$ , (b) $x_m = 0.51$ and (c) $x_m = 0.94$ .	109
Fig. 4.67 Photos of flow in the evaporation of R-134a in the entire duct at $G=200 \text{ kg/m}^2\text{s}$ , $T_{\text{sat}} = 15^{\circ}\text{C}$ , $\delta = 5.0 \text{ mm}$ , $q = 15 \text{ kW/ m}^2$ for (a) $x_m = 0.05$ , (b) $x_m = 0.53$ and (c) $x_m = 0.95$ .	110
Fig. 4.68 Photos of flow in the evaporation of R-134a in the entire duct at $G=200 \text{ kg/m}^2\text{s}$ , $T_{\text{sat}} = 5^{\circ}\text{C}$ , $\delta = 5.0 \text{ mm}$ , $q = 15 \text{ kW/ m}^2$ for (a) $x_m = 0.05$ , (b) $x_m = 0.53$ and (c) $x_m = 0.94$ .	111
Fig. 4.69 Photos of flow in the evaporation of R-134a in the entire duct at $G=300 \text{ kg/m}^2\text{s}$ , $T_{\text{sat}} = 15^{\circ}\text{C}$ , $\delta = 5.0 \text{ mm}$ , $q = 5 \text{ kW/ m}^2$ for (a) $x_m = 0.05$ , (b) $x_m = 0.50$ and (c) $x_m = 0.95$ .	112
Fig. 4.70 Photos of flow in the evaporation of R-134a in the entire duct at $G=300 \text{ kg/m}^2\text{s}$ , $T_{\text{sat}} = 15^{\circ}\text{C}$ , $\delta = 5.0 \text{ mm}$ , $q = 15 \text{ kW/ m}^2$ for (a) $x_m = 0.05$ , (b) $x_m = 0.51$ and (c) $x_m = 0.94$ .	113

- Fig. 4.71 Photos of flow in the evaporation of R-134a in the entire duct at  $G=300$   $\text{kg/m}^2\text{s}$ ,  $T_{\text{sat}} = 5^\circ\text{C}$ ,  $\delta = 5.0$  mm,  $q = 15$   $\text{kW/m}^2$  for (a)  $x_m = 0.05$ , (b)  $x_m = 0.50$  and (c)  $x_m = 0.95$ . 114
- Fig. 4.72 Photos of flow in the evaporation of R-134a in a small region around middle axial location at  $\delta = 5.0$  mm and  $G=100$   $\text{kg/m}^2\text{s}$  for various imposed heat fluxes, saturated temperatures and vapor quality. 115
- Fig. 4.73 Photos of flow in the evaporation of R-134a in a small region around middle axial location at  $\delta = 5.0$  mm and  $G=200$   $\text{kg/m}^2\text{s}$  for various imposed heat fluxes, saturated temperatures and vapor quality. 116
- Fig. 4.74 Photos of flow in the evaporation of R-134a in a small region around middle axial location at  $\delta = 5.0$  mm and  $G=300$   $\text{kg/m}^2\text{s}$  for various imposed heat fluxes, saturated temperatures and vapor quality. 117
- Fig. 4.75 Comparison of the measured data for heat transfer coefficient for the evaporation of R-134a in gap of 1.0 mm and 2.0 mm narrower ducts with the proposed correlation. 118
- Fig. 4.76 Comparison of the measured data for heat transfer coefficient for the evaporation of R-134a in gap of 5.0 mm wider duct with the proposed correlation. 119





## NOMENCLATURE

A	heat transfer area of the annular duct, m <sup>2</sup>
Bo	Boiling number, $Bo = \frac{q}{G \cdot i_{fg}}$ , dimensionless
c <sub>p</sub>	specific heat, J/kg°C
D	diameter of duct, m
D <sub>h</sub>	hydraulic diameter, m, $D_h = 4A_c/P = (D_o - D_i)$
f <sub>f</sub>	friction factor
g	acceleration due to gravity, m/s <sup>2</sup>
G	mass flux, kg/m <sup>2</sup> s
h	heat transfer coefficient, W/m <sup>2</sup> °C
i <sub>fg</sub>	enthalpy of vaporization, J/kg
I	measured current from DC power supply, A
k	thermal conductivity, W/m°C
t <sub>lf</sub>	liquid film thickness, μm
N <sub>conf</sub>	Confinement number, $N_{conf} = \frac{(\sigma/(g\Delta\rho))^{0.5}}{D_h}$ , dimensionless
Nu	Nusselt number, $Nu = \frac{hD_h}{k}$ , dimensionless



P	system pressure, kpa
Pr	Prandtl number, $Pr = \frac{\mu \cdot C_p}{k}$ , dimensionless
q	average imposed heat flux, $W/m^2$
Q	heat transfer rate, W
R	radius of duct, m
Ra	Rayleigh number, $g\beta\Delta TH^3/\alpha\nu$
Re	Reynolds number, $Re = \frac{G \cdot D_h}{\mu}$ , dimensionless
T	temperature, °C
T <sub>sat</sub>	saturated temperature of the refrigerant R-134a, °C
V	measured voltage from DC power supply, V
W	mass flow rate
<i>x</i>	vapor quality
X <sub>tt</sub>	Martnelli parameter
z	coordinate (downstream coordinate for annular duct flow), mm

### Greek Symbols

$\Delta T$	temperature difference, °C
$\delta$	gap size, mm

$\mu$	viscosity, $\text{N} \cdot \text{s} / \text{m}^2$
$\rho$	density, $\text{kg} / \text{m}^3$
$\Delta \rho$	density difference, $\Delta \rho = \rho_l - \rho_g$ , $\text{kg} / \text{m}^3$
$\sigma$	surface tension, $\text{N} / \text{m}$
$\alpha$	void fraction, dimensionless

### Subscripts

ave	average
exp	experimental value
fg	difference between liquid phase and vapor phase
g	vapor
i, o	inside and outside diameter of the smooth pipe
l	all-liquid nonboiling heat transfer
m	average value for the two phase mixture or between the inlet and exit
n	net power input to the refrigerant R-134a
p	preheater
r	refrigerant side
s	heater surface
sat	saturated flow boiling



sub        subcooled flow boiling

w        duct wall



# CHAPTER 1

## INTRODUCTION

### 1.1 Motivation of the Present Study

In air conditioning system design, the refrigerant chosen to be used in the refrigeration loop is known to play an important role. The hydrochlorofluorocarbons refrigerants (HCFCs) such as refrigerant R-22 and the chlorofluorocarbons refrigerants (CFCs) such as refrigerants CFC-11, CFC-12, CFC-113, CFC-114 and CFC-115 have been employed for many years. However, the chlorine ions contained in these refrigerants have resulted in the destruction of the ozone layer in the arctic area and the global warming. Thus the Montreal Protocol signed in 1987 only allowed the use of the CFCs up to 1996 and the HCFCs are going to be phased out in 2020. Consequently, the search for the replacement of CFCs and HCFCs becomes very urgent. Various non-chlorine alternative refrigerants such as R-134a, R-290, R-401A, R-407C and R-410A have been considered to be suitable and some are currently in use.

It is well known that R-134a is a single-component HFC refrigerant and has similar thermophysical properties to R-12. Hence refrigerant R-134a has been extensively used currently in many refrigeration and air-conditioning systems to replace R-12 and R-22. The operating conditions of refrigerants R-134a, R-407C and R-410A are compared in Table 1.1 based on the information from Cavallini (1996) [1] & Devotta et al. (2001) [2].

In many refrigeration and air-conditioning systems, using small channels is a good choice because of its low thermal resistance, very high ratio of surface area to volume, low inventory, small volumes and lower total mass of working fluids. Thus the use of compact heat exchangers to promote the thermal performance of these systems is beneficial. The

understanding of the evaporation heat transfer characteristics of R-134a in small channels is therefore needed.

## 1.2 Literature Review

The size of the channels in a compact heat exchanger can significantly affect the performance of the exchanger, suggesting that the channel confinement effects on the two-phase flow in the loop are important. In classifying the channel size Kandlikar [3,4] proposed : (1)  $D_h > 3\text{mm}$  for the conventional channels, (2)  $200\mu\text{m} < D_h < 3\text{mm}$  for the mini-channels, (3)  $10\mu\text{m} < D_h < 200\mu\text{m}$  for the micro-channels, (4)  $1\mu\text{m} < D_h < 10\mu\text{m}$  for the transitional micro-channels, (5)  $0.1\mu\text{m} < D_h < 1\mu\text{m}$  for the transitional nano-channels, and (6)  $D_h \leq 0.1\mu\text{m}$  for the molecular nano-channels. Cornwell and Kew [5] investigated refrigerant R-141b boiling in a horizontal tube with its inner diameter ranging from 1.39 to 3.69 mm. In this study, they introduced a new dimensionless group named as the confinement

number,  $N_{\text{conf}} \equiv \frac{\left[ \sigma / \left( g \left( \rho_l - \rho_g \right) \right) \right]^{1/2}}{D_h}$ , which represented the importance of the restriction of

the flow by the small size of the channel. They showed that the confined boiling occurred when  $N_{\text{conf}} > 0.5$ . Accordingly, the effects of the tube confinement can be significant for two-phase flow in micro and mini channels.

### 1.2.1 Single-Phase Heat Transfer in Small Channels

In 1995, Peng and Wang [6] studied single-phase heat transfer for liquid methanol in a small rectangular channels with  $D_h = 0.31, 0.51$  and  $0.646$  mm. Their experimental data showed that liquid velocity, liquid properties, and geometry of the channels all exhibited significant effects on the heat transfer performance. Specifically, increasing the liquid velocity

and channel number caused enhancement in heat transfer. In a continuing investigation for water [7] they also found that the geometric configuration of channels had a significant effect on the single-phase convective heat transfer and flow characteristics. Besides, the turbulent heat transfer was noted to depend on a new dimensionless variable,  $Z$  defined as  $\frac{\min(H, W)}{\max(H, W)}$ ,  $H$  and  $W$  are the height and width of the channel, respectively.

Recently in an experiment for R-134a liquid flow in mini-channels for a vertical liquid up-flow, Agostini et al. [8] compared their heat transfer data with some existing correlations. They concluded that the correlation of Gnielinsky correlation [9] was good for  $2300 < Re < 10^6$  and  $0.6 < Pr < 10^5$ , and the Dittus-Boelter correlation [10] was good for  $Re > 10^5$  and  $0.7 < Pr < 16700$ .

### 1.2.2 Evaporation Heat Transfer in Conventional Channels

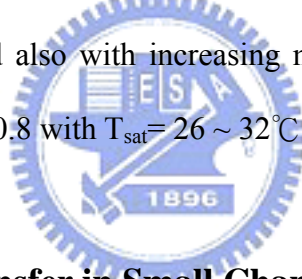
In the following the relevant literature on the evaporation heat transfer of Refrigerants in conventional and other enhanced tubes is reviewed.

Lazarek and Black [11] studied evaporative heat transfer, pressure drop and critical heat flux in a vertical tube with R-113 ( $D_h=31$  mm). They showed that the R-113 evaporative heat transfer coefficient increased with the heat flux for the vapor quality up to about 60%. Experimental data was taken for the two-phase heat transfer characteristics of R-22/R-407C in a smooth tube ( $D_h=6.5$  mm) by Wang and Chiang [12] for the vapor quality varied from 0.1 to 0.9 with the refrigerant saturated temperature  $T_{sat}= 2^\circ\text{C}$ . The R-22 evaporation heat transfer coefficient was found to increase with increasing mass flux and vapor quality. However, the R-407C evaporation heat transfer coefficient increased with increasing mass flux but decreased with increasing vapor quality. The evaporative heat transfer of refrigerant R-134a



under forced flow conditions in a horizontal tube ( $D_h=7.2$  mm) was examined by Hartnett and Minkowycz [13]. Their results indicated that the evaporation heat transfer coefficients of R-1314a increased with increasing vapor quality for the vapor quality varied from 0.1 to 0.8 with the refrigerant saturated temperature  $T_{sat}= 4^\circ\text{C}$  and  $25^\circ\text{C}$ . At low refrigerant vapor quality for  $x < 0.35$  and low saturation temperature, the refrigerant mass flux was found to have almost no effect on the evaporation heat transfer coefficient. For the vapor quality ranging from 0.35 to 0.6, the evaporation heat transfer coefficient increased slightly at increasing mass flux. When the vapor quality was much higher than 0.6, the evaporation heat transfer coefficient increased evidently with the refrigerant mass flux. Choi et al. [14] investigated the evaporation heat transfer of R-32, R-134a, R-32/134a, and R-32/125/134a inside a horizontal smooth tube ( $D_h=7.75$  mm) for the vapor quality ranging from 0.05 to 0.95 with the refrigerant saturated temperature varied from  $-12^\circ\text{C}$  to  $17^\circ\text{C}$ . They found that the evaporation heat transfer coefficient increased also with increasing mass flux and vapor quality. Besides, at low vapor quality the evaporation heat transfer coefficient increased strongly with heat flux. But at high vapor quality, the heat flux, however, does not exhibit noticeable effect on the evaporation heat transfer coefficient. Yu et al. [15] studied the heat transfer and flow pattern in flow boiling of R-134a in horizontal smooth and microfin tubes ( $D_h=10.7$  mm). Their results also indicated that the evaporation heat transfer coefficient increased with increasing mass flux and vapor quality for the vapor quality up to 0.7 with  $T_{sat}= 6^\circ\text{C}$ . Characteristics of condensing and evaporating heat transfer using hydrocarbon refrigerants were investigated by Lee et al. [16] for R-290, R-600a, R-1270 and R-22 ( $D_h=12.7$  mm) covering the vapor quality from 0.1 to 0.99 with  $T_{sat}= 14^\circ\text{C}$ . They reported that the evaporation heat transfer coefficient increased with the vapor quality. Besides, the evaporation heat transfer coefficient is highest for R-1270 and lowest for R-22. Moreover, R-290 has higher evaporation heat transfer coefficient than R-600a. Wongwises and

Polsongkram [17] investigated the evaporation heat transfer and pressure drop of HFC-134a in a helically coiled concentric tube-in-tube heat exchanger ( $D_h=7.2$  mm). Their results show that the evaporation heat transfer coefficient increases with increasing vapor quality, mass flux, heat flux and saturation temperature for the vapor quality ranging from 0.1 to 0.9 with  $T_{sat}= 10^\circ\text{C}$  to  $20^\circ\text{C}$ . Park and Hrnjak [18] studied the  $\text{CO}_2$  and R-410A flow boiling heat transfer, pressure drop, and flow pattern at low temperatures in a horizontal smooth tube ( $D_h=6.1$  mm). They found that the evaporation heat transfer coefficient of R-410A increased with the mass flux and vapor quality. Besides, the evaporation heat transfer coefficient of  $\text{CO}_2$  is higher than R-410A for the vapor quality varied from 0.1 to 0.8 with  $T_{sat}= -15^\circ\text{C}$  and  $-30^\circ\text{C}$ . Condensation heat transfer of R-134a inside a microfin tube with different tube inclinations ( $D_h=8.92$  mm) examined by Akhavan-Behabadi et al. [19] indicated that the condensation heat transfer coefficient increased also with increasing mass flux and vapor quality for the vapor quality ranging from 0.2 to 0.8 with  $T_{sat}= 26 \sim 32^\circ\text{C}$ .



### 1.2.3 Evaporation Heat Transfer in Small Channels

A comprehensive review of saturated flow boiling in small passages of compact heat-exchangers conducted by Watel [20] suggests that the heat transfer mechanism in the evaporation of refrigerants in small channels is dominated by conduction and convection through the liquid film and the interfacial vaporization. The evaporation heat transfer coefficient depends mainly on the refrigerant mass flux and vapor quality.

Evaporation heat transfer and pressure drop of refrigerant R-134a in a bank of 28 small pipes ( $D_h=2.0$  mm) were experimentally investigated by Yan and Lin [21,22] for the vapor quality ranging from 0.1 to 0.95 with the refrigerant saturated temperature  $T_{sat}= 5^\circ\text{C}$  to  $31^\circ\text{C}$ . They found that the evaporation heat transfer coefficient increased with increasing heat flux at

low vapor quality. But the evaporation heat transfer coefficient decreased with increasing heat flux at high quality. Besides, an increase in the refrigerant saturated temperature results in an increase in the evaporation heat transfer coefficient. Yun et al. [23] studied the convective boiling heat transfer characteristics of CO<sub>2</sub> in small channels ( $D_h=1.08$  and  $1.54$  mm) covering the vapor quality from 0.15 to 0.9 for  $T_{sat}= 0^{\circ}\text{C}$  to  $10^{\circ}\text{C}$ . Their results indicated that before the liquid film dryout the evaporation heat transfer coefficient increased with heat flux. Besides, the evaporation heat transfer coefficient increased with increasing refrigerant saturated temperature and decreasing channel hydraulic diameter. Moreover, the CO<sub>2</sub> evaporation heat transfer coefficient was higher than R-134a by 53%. An experimental study was carried out by Lie et al. [24] to examine the evaporation heat transfer characteristics of refrigerants R-134a and R-407C in horizontal bank of small tubes ( $D_h=0.83$  and  $2.0$  mm) for the vapor quality ranging from 0.2 to 0.8 at the refrigerant saturated temperature  $T_{sat}= 5^{\circ}\text{C}$  to  $15^{\circ}\text{C}$ . They showed that the evaporation heat transfer coefficient increased at increasing heat flux, saturated temperature and mass flux. Besides, the evaporation heat transfer coefficient increases almost linearly with the vapor quality. Moreover, the evaporation heat transfer coefficient of R-407C was higher than R-134a. Evaporative heat transfer and pressure drop of R-410A in small channels ( $D_h=1.33$  and  $1.44$  mm) were investigated by Yun et al. [25] for the vapor quality varied from 0.05 to 0.9 at the saturated temperature  $T_{sat}= 0^{\circ}\text{C}$  to  $10^{\circ}\text{C}$ . Their results indicated that before the dryout, the evaporation heat transfer coefficient was independent of the refrigerant saturated temperature, heat flux and mass flux. But after the dryout the evaporation heat transfer coefficient increased at increasing refrigerant saturated temperature, heat flux and mass flux. Choi et al. [26] studied the flow boiling heat transfer of R-22, R-134a, and CO<sub>2</sub> in horizontal minichannels ( $D_h=1.5$  and  $3.0\text{mm}$ ) covering the vapor quality from 0.05 to 0.95 at the refrigerant saturated temperature  $T_{sat}= 10^{\circ}\text{C}$ . They reported

that the heat transfer coefficient increased with the heat flux. Besides, they found that the dryout quality became lower for a higher heat flux.

### **1.3 Objective of the Present Study**

In recent years, environmental concerns over the use of CFCs as working fluids in refrigeration and air-conditioning systems have led to the development of alternative refrigerants. Among these alternatives, refrigerants R-134a, R-407C and R-410A are often used as substitutes for refrigerant HCFC-22. Besides, the use of compact heat exchangers in these systems is beneficial in improving their efficiencies. The above literature review, however, indicates that the experimental data for the evaporation heat transfer of HFC refrigerants in small tubes are still rare. In this investigation we intend to measure the evaporation heat transfer coefficient and visualize the associated evaporating flow characteristics of refrigerants R-134a in horizontal narrow annular ducts. The effects of the refrigerant vapor quality, saturated temperature, mass flux and the imposed heat flux on the evaporation heat transfer and evaporating flow characteristics in the narrow annular ducts will be examined in detail.

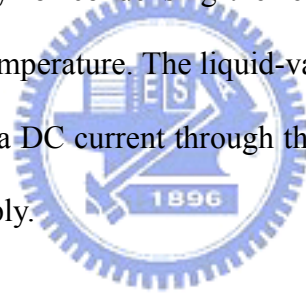
**Table 1.1 Comparison of some properties of three HFCs refrigerants for air conditioning and refrigeration applications**

Refrigerant	R-134a	R-407C	R-410A
Component	HFC-134a	HFC-32/125/134a	HFC-32/125
Wt %	100 %	23/25/52%	50/50%
Comparison with R-22	1. lower working pressure. 2. friction pressure drop is larger in the same capability of freezing.	1. zeotropic refrigerant, and the components charge easy. 2. working pressure is same with R-22.	1. near-azeotropic refrigerant. 2. working pressure is five times higher than R-22. 3. friction pressure drop is smaller.
The energy efficiency ratio relative to R-22	72~90	90~97	94~100
Molecule quality	102.3	85.62	72.6
Remark	1. the volume of operating system becomes larger. 2. the air-out volume of compress is larger.	1. the solutions of variation of R-407C components.	1. the design of system must to consider the strong and optimum elements.
Green-house effect (100 years)	1300	1526	1725
Toxicity limit (kg/m <sup>3</sup> )	0.25	0.31	0.44
Boiling point (°C)	-26.2	-43.6 R32 (-51.8°C) / R125 (-48.5°C) / R134a (-26.2°C)	-52.7 R32 (-51.8°C) / R125 (-48.5°C)
Temperature glides	—	10 °F	< 1 °F

## CHAPTER 2

### EXPERIMENTAL APPARATUS AND PROCEDURES

The experimental apparatus used in the present study to investigate the evaporation heat transfer of refrigerant R-134a in a horizontal narrow annular duct is schematically shown in Fig. 2.1. The apparatus consists of three main loops, namely, a refrigerant loop, a water-glycol loop and a hot-water loop for preheater, along with a data acquisition system and a 100V-50A programmable DC power supply (model 62012P-100-50). Refrigerant R-134a is circulated in the refrigerant loop. We need to control the temperature and flow rate in the water-glycol loop to obtain enough cooling capacity for condensing the refrigerant vapor and for maintaining the refrigerant liquid at a preset temperature. The liquid-vapor mixture of the refrigerant in the narrow duct is heated by passing a DC current through the inner pipe in the test section from the programmable DC power supply.



#### 2.1 Refrigerant Loop

The main components in the refrigerant loop include an oil-free variable-speed refrigerant pump, an accumulator, a mass flow meter, a test section, a condenser, a sub-cooler, a receiver, a filter/dryer, and four sight glasses. An AC motor is used to control the refrigerant mass flow rate through the change of the inverter frequency. The flow rate can also be adjusted by regulating a by-pass valve installed in the by-pass flow path. The refrigerant at the outlet of the refrigerant pump is kept subcooled to avoid any vapor flow through the mass flow meter. The flow meter (Micro motion RFT9739) has an accuracy of  $\pm 1\%$ . The preheater is used to heat the subcooled refrigerant R-134a to a specified vapor quality at the test section inlet by receiving heat from the hot water in the hot-water loop. The vapor generated in the

test section is relieved in an oversized condenser/subcooler in the cold water-glycol loop. Leaving the subcooler, the liquid refrigerant flows back to the receiver at the bottom of the system. An accumulator is connected to a high-pressure nitrogen tank to dampen the fluctuations of the flow rate and pressure. The filter/dryer is used to filter the impurities and noncondensable gas possibly existing in the loop. Varying the temperature and flow rate of the water-glycol mixture flowing through the condenser and subcooler allows us to control the pressure of the refrigerant loop. Two absolute pressure transducers are respectively installed at the inlet and exit of the test section with a resolution up to  $\pm 2\text{kPa}$ . All the refrigerant and water temperatures are measured by copper-constantan thermocouples (T-type) with a calibrated accuracy of  $\pm 0.2^\circ\text{C}$ . The test section is thermally insulated with a polyethylene insulation layer of 19.5 mm thick so that heat loss from it can be reduced significantly.

## 2.2 Test Section

The evaporation of the refrigerant R-134a flow in an annular duct with a small clearance between the inner and outer pipes is explored. As schematically shown in Fig. 2.2, the test section of the experimental apparatus is a horizontal annular duct with the outer pipe made of Pyrex glass to permit the visualization of evaporation processes in the refrigerant flow. The outer Pyrex glass pipe is 160-mm long and 4-mm thick with inside diameter of 20 mm. Both ends of the pipe are connected with a copper tube of the same size by means of flanges and are sealed by O-rings. The inner smooth pipe has 10.0, 16.0 or 18.0 mm nominal outside diameter (the pipe wall thickness is 1.75 or 2.75 mm) and is 0.41 m long, so that the hydraulic diameter of the annular duct  $D_h$  is 10.0, 4.0 or 2.0 mm (corresponding to the gap size of 5.0, 2.0 or 1.0 mm for the duct). In order to insure the gap between the ducts being uniform, we first measure the average outside diameter of the inner pipe and the mean inside diameter of the Pyrex glass pipe by digital calipers having a resolution of 0.001mm. The absolute



accuracy of the measurement is in the range of 0.01 mm. Then we photo the top and side view pictures of the annular ducts and measure the average distance between the inside surface of the Pyrex glass pipe and the outside surface of the inner tube, with an absolute accuracy also in the range of 0.01mm. From the above procedures the duct gap is ascertained and its absolute uncertainty is estimated to be 0.019 mm. An electric cartridge heater of 160 mm in length and 12.5 mm in diameter with a maximum power output of 800W is inserted into the inner pipe. Furthermore, the pipe has an inactive heating zone of 10-mm long at each end and is insulated with Teflon blocks and thermally nonconducting epoxy to minimize heat loss from it. Thermal contact between the heater and the inner pipe is improved by coating a thin layer of heat-sink compound on the heater surface before installing the heater. Then, 8 T-type calibrated thermocouples are electrically insulated by covering their beads with the electrically nonconducting thermal bond before they are fixed on the inside surface of the inner pipe so that the voltage signals from the thermocouples are not interfered by the DC current passing through the cartridge heater. The thermocouples are positioned at three axial stations along the smooth pipe. At each axial station, two to four thermocouples are placed at top, bottom, or two sides of the pipe circumference with 180° or 90° apart. The outside surface temperature  $T_w$  of the inner pipe is then derived from the measured inside surface temperature by taking the radial heat conduction through the pipe wall into account. Figure 2.3 shows the detailed thermocouple locations at each axial station and the arrangement of the cartridge heater.

## 2.3 Hot-Water Loop for Preheater

In order to maintain the preset refrigerant temperature and vapor quality at the test section inlet, a water loop is used to preheat the refrigerant before it arrives at the inlet. The water loop for the preheater system includes a double-tube heat exchanger, having a heat

transfer area of  $0.12 \text{ m}^2$ , a 125-liter hot water container with three 2.0-kW heaters in it, and a 0.5-hp water pump which can deliver the hot water at specified temperature and flow rate to the preheater. In the preheater the hot water passes through the outer pipe while the liquid refrigerant flows in the inner pipe. The water flow rate is controlled by an AC motor through the change of the inverter frequency and by the by-pass valve. The connecting pipe between the preheater and test section is thermally insulated with a 5-cm thick polyethylene layer to reduce the heat loss from the pipe.

## **2.4 Water-Glycol Loop**

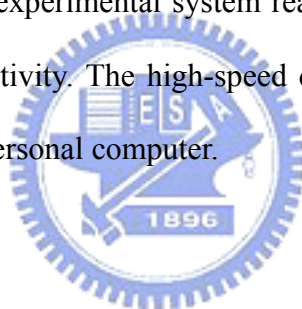
The water-glycol loop is designed for condensing the refrigerant vapor and for subcooling the liquid refrigerant. The water-glycol loop is cooled by a water cooled R-22 refrigeration system. The cooling capacity is 3.5-kW for the water-glycol mixture at  $-20^\circ\text{C}$ . The cold water-glycol mixture at a specified flow rate is driven by a 0.5-hp pump to the condenser as well as to the subcooler. A by-pass loop is provided to adjust the flow rate. By adjusting the mixture temperature and flow rate, the bulk temperature of the refrigerant in the subcooler can be controlled at a preset level.

## **2.5 Programmable DC Power Supply**

As described above, the inner pipe in the test section is heated by a 800-W cartridge heater. A 100V-50A programmable DC power supply (model 62012P-100-50) delivers the required electric current to the cartridge heater. A Yokogawa (WT210) digital power meter is used to measure the DC current through the cartridge heater and the voltage drop across the heater with an accuracy of  $\pm 1\%$ . Thus the power input to the heater can be calculated. Figure 2.4 schematically shows the detailed heat flux control loop.

## **2.6 Photographic System**

The photographic apparatus established in the present study to picture the qualitative characteristics of the evaporating flow in the annular duct consists of an IDT (X-Stream<sup>TM</sup> VISION XS-4) high speed CMOS digital camera, a Mitutoyo micro lens set, a 3-D positioning mechanism, a personal computer, and a Nikon digital camera. The high-speed digital camera can take photographs up to 143,307 frames/s with an image resolution of 512×16. Here, a recording rate of 10,000 frames/s with the highest image resolution of 512×256 is adopted to obtain the images of the evaporating flow. The digital camera shutter speed can be as short as 1/4000 second in taking the overview of the flow. In particular, the flow characteristics of the refrigerant in a small region around the middle axial location ( $z = 80$  mm) are visualized. Note that the symbol  $z$  denotes the axial coordinate measuring from the inlet of the heated test section. After the experimental system reaches a statistically steady state, we start recording the evaporation activity. The high-speed digital camera can store the images which are later downloaded to a personal computer.



## 2.7 Data Acquisition

The data acquisition unit includes a recorder (Yokogawa MX-100), a 24V-3A power supply, and a controller. The water flowmeter and differential pressure transducer need the power supply as a driver to output an electric current of 4 to 20 mA. The data signals are collected and converted by a hybrid recorder (Micro Motion RFT9739). The converted signals are then transmitted to a host computer through a GPIB interface for further calculation.

The unit automatically monitors all the T-Type thermocouples, pressure transducers, differential pressure transducer and mass flowmeters. The thermodynamic and transport properties of the refrigerants are obtained by a manual from AlliedSignal Co. Ltd. and by the ASHRAE handbook [27].

## 2.8 Experimental Procedures

Before a test is started, the temperature of refrigerant R-134a in the test section is compared with its saturation temperature corresponding to the measured saturation pressure and the allowable difference is kept in the range of 0.2-0.3K. Otherwise, the experimental system is re-evacuated and then re-charged to remove noncondensable gases existing in the refrigerant loop. A vacuum pump is used to evacuate noncondensable gases in the system to a low pressure of 0.010 pa in the loop. In the test the liquid refrigerant at the inlet of the test section is first maintained at a specified temperature by adjusting the water-glycol temperature and flow rate. In addition, we adjust the thermostat temperature in the hot-water loop to stabilize the refrigerant temperature at the test section inlet. Next, the temperature and flow rate of the hot-water loop for the preheater are adjusted to keep the vapor quality of R-134a at the test section inlet at the desired value. Then, we regulate the refrigerant pressure at the test section inlet by adjusting the opening of the gate valve locating right after the exit of the test section. Meanwhile, by changing the current of the DC motor connecting to the refrigerant pump, the refrigerant flow rate can be varied. The imposed heat flux from the heater to the refrigerant is adjusted by varying the electric current delivered from the programmable DC power supply. By measuring the current delivered to and voltage drop across the heater, we can calculate the heat transfer rate to the refrigerant. All tests are run at statistically steady-state conditions. The whole system is considered to be at a statistically steady state when the time variations of the system pressure and imposed heat flux are respectively within  $\pm 1\%$  and  $\pm 4\%$  of their mean levels, and the time variations of the heated wall temperature are less than  $\pm 0.2^\circ\text{C}$  for a period of 100 minutes. Then all the data channels are scanned every 0.05 second for a period of 20 seconds.

## 2.9 Experimental Parameters

The ranges of the experimental parameters and the corresponding dimensionless groups to be covered in the present study are listed in Table 2.1. It should be mentioned here that the range of the refrigerant mass flux is chosen to be different for different duct gap. This is due to the fact that the evaporating flow becomes relatively unstable outside the range of the refrigerant mass flux chosen in the present study. The unstable range of the refrigerant flow varies with the duct size. Moreover, some thermophysical properties of refrigerant R-134a is given in Table 2.2.



**Table 2.1 List of conditions of the experimental parameters for R-134a**

refrigerant	$\delta$	G	q	Tsat	Re	$N_{\text{conf}}$	$x_m$	$\alpha_m$	$\Delta x$
	(mm)	(kg/m <sup>2</sup> s)	(kW/m <sup>2</sup> )	(°C)					
R-134a	5	100 、 200 、 300	5 、 10 、 15	5 、 10 、 15	3,931~13,375	0.089~0.094	0.05~0.95	0.66~0.99	0.0006~0.0027
	2	300 、 400 、 500	5 、 10 、 15	5 、 10 、 15	4,717~8,917	0.22~0.23			0.0007~0.0085
	1	500 、 600 、 700	5 、 10 、 15	5 、 10 、 15	3,930~6,242	0.44~0.47			0.0018~0.0164

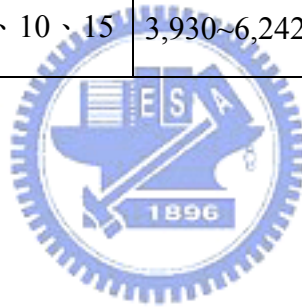


**Table 2.2 Thermophysical properties of refrigerant R-134a**

Thermophysical properties		R-134a		
Temperature (°C) (Saturated Pressure)		5 (349.8 kPa)	10 (414.6 kPa)	15 (488.6 kPa)
Viscosity $\mu$ ( $\mu\text{N}\cdot\text{s}/\text{m}^2$ )	Liquid $\mu_l$	254.4	238.8	224.3
	$\Delta\mu = \mu_l - \mu_g$	243.46	227.65	212.94
	Vapor $\mu_g$	10.94	11.15	11.36
Density $\rho$ ( $\text{kg}/\text{m}^3$ )	Liquid $\rho_l$	1278	1261	1243.5
	$\Delta\rho = \rho_l - \rho_g$	1260.86	1240.77	1219.735
	Vapor $\rho_g$	17.14	20.23	23.765
Enthalpy $i$ ( $\text{kJ}/\text{kg}$ )	Liquid $i_f$	206.75	213.6	220.5
	$\Delta i = i_g - i_f$	194.75	190.7	186.55
	Vapor $i_g$	401.5	404.3	407.05
Conductivity $k$ ( $\text{W}/\text{m}\cdot\text{K}$ )	Liquid $k_l$	0.0898	0.0876	0.08545
	Vapor $k_g$	0.01195	0.0124	0.01286
Surface Tension $\sigma(\text{N}/\text{m})$	Liquid	0.01075	0.01014	0.00944



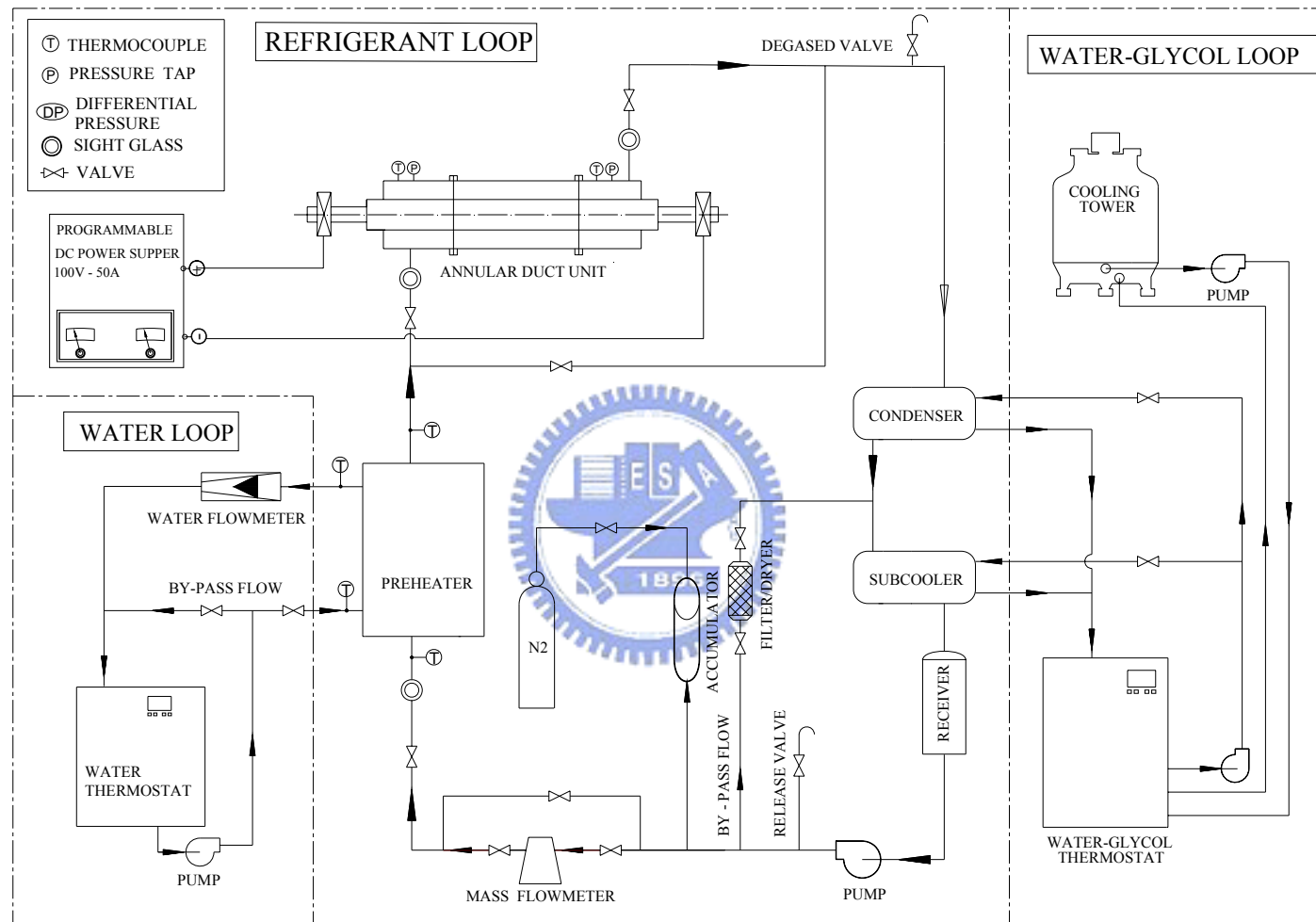


Fig. 2.1 Schematic of experimental system for the annular duct

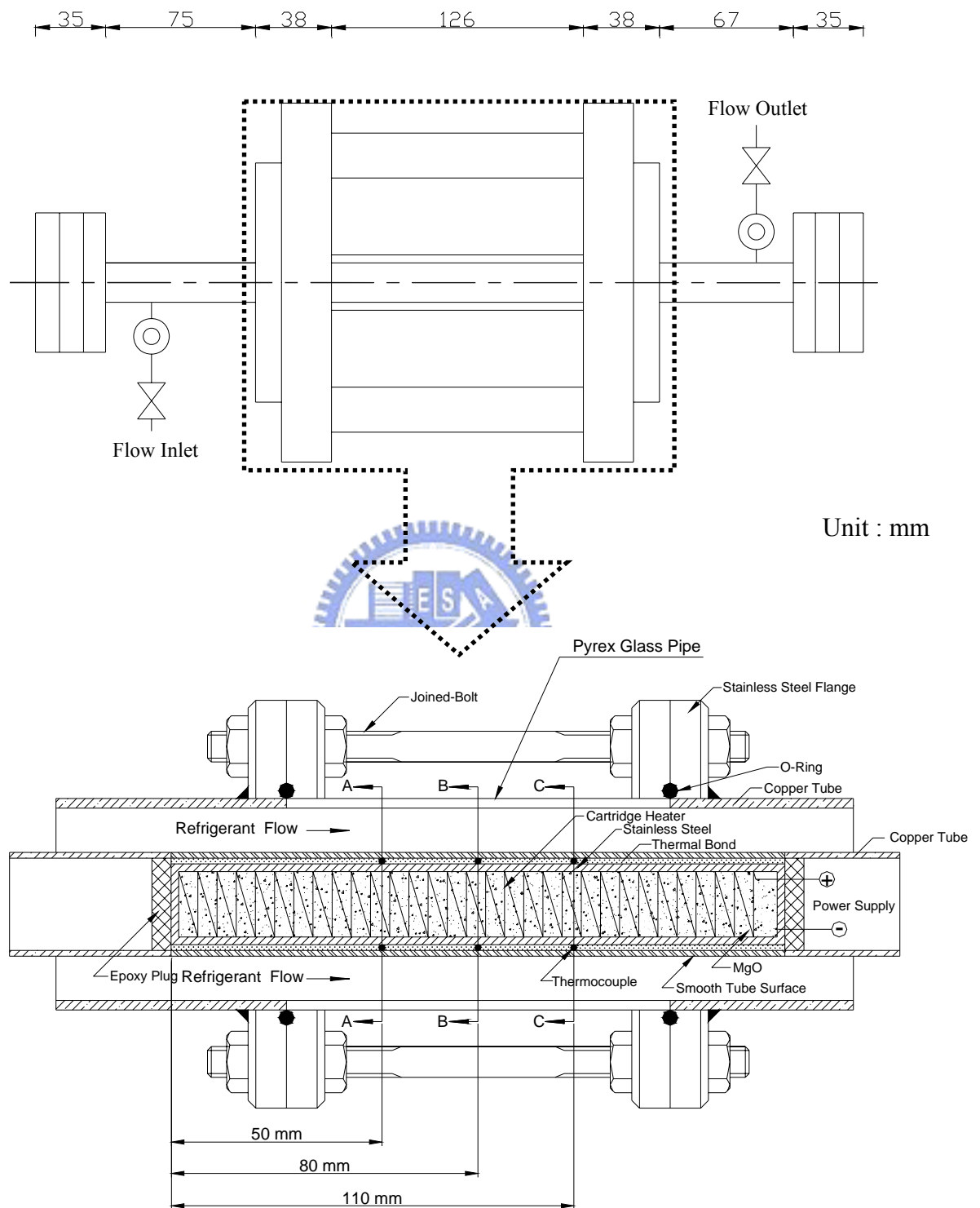
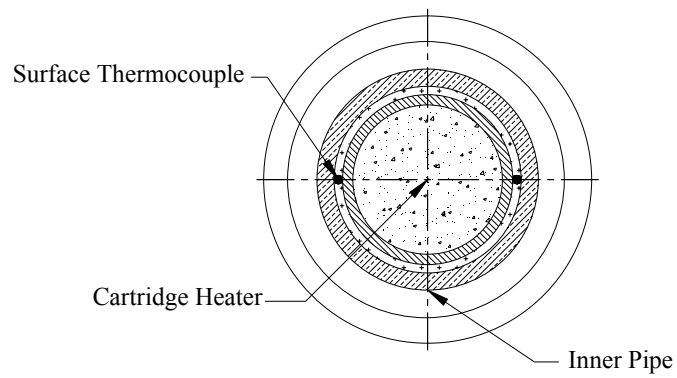
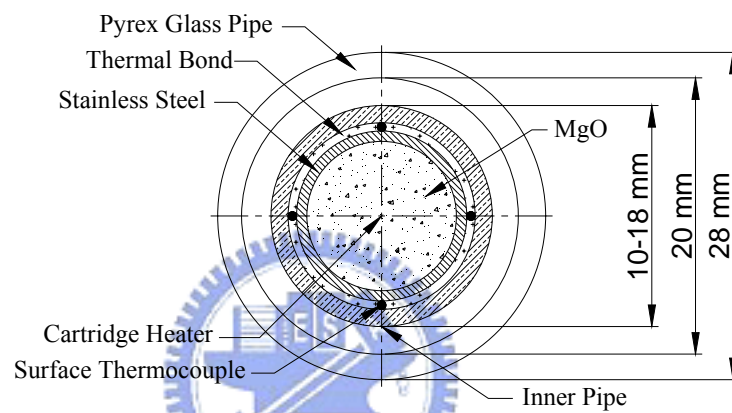


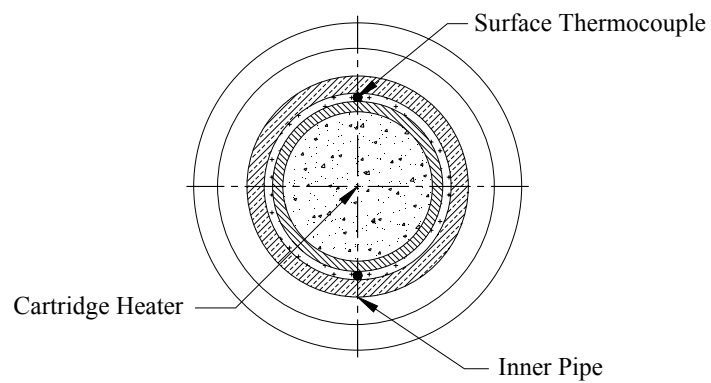
Fig. 2.2 The detailed arrangement of the test section for the annular duct



SECTION VIEW A-A



SECTION VIEW B-B



SECTION VIEW C-C

Fig. 2.3 The cross-sectional view of the annular duct showing the heater and locations of the thermocouples.

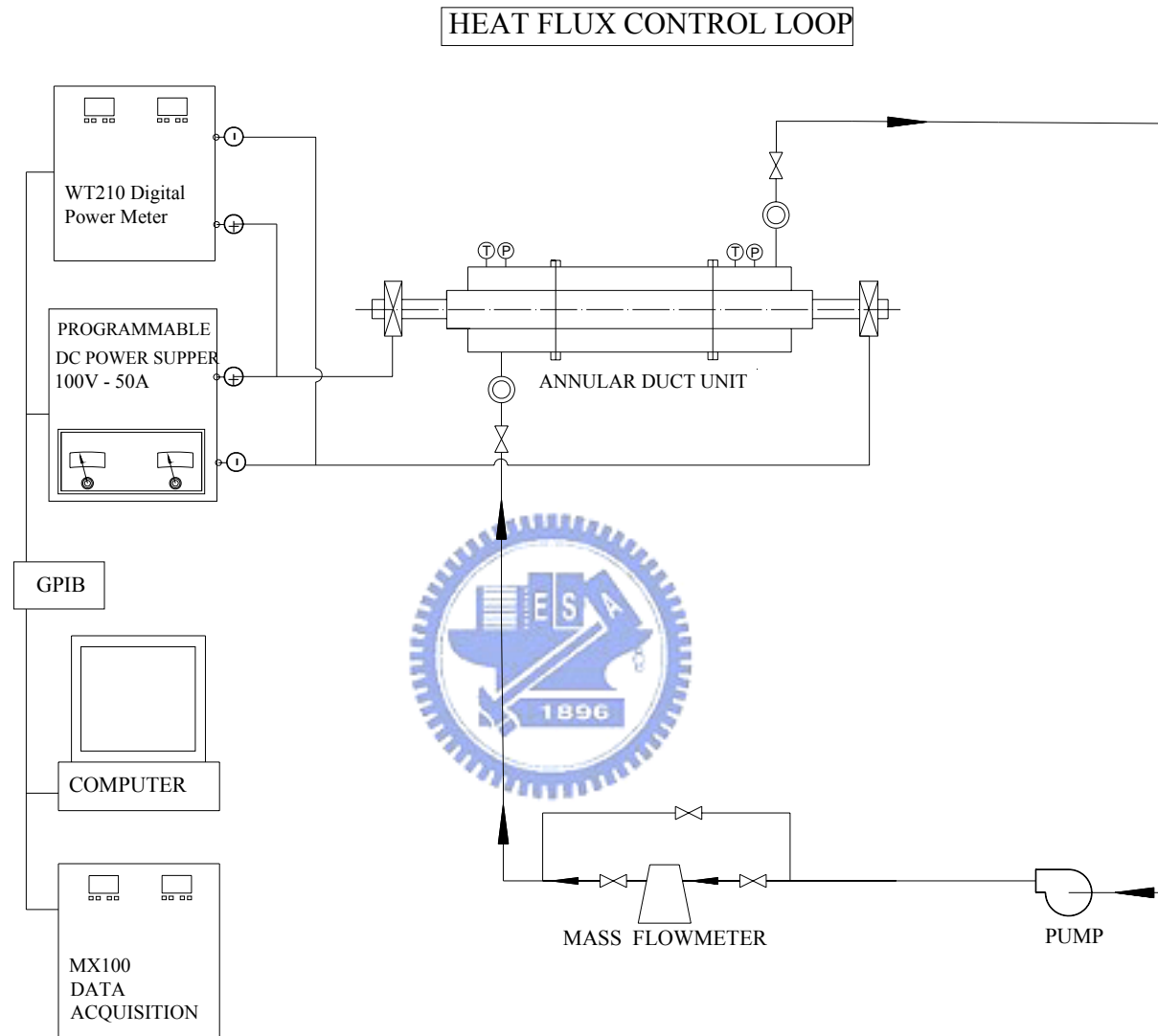


Fig. 2.4 Schematic of heat flux control loop



## CHAPTER 3

### DATA REDUCTION

In the present study of the evaporation heat transfer of R-134a in a narrow annular duct, the gap between the inner and outer circular pipes is fixed at 1.0, 2.0 and 5.0 mm with the refrigerant saturated temperature set at 5°C, 10°C and 15°C. The refrigerant mass flux ranges from 100 kg/m<sup>2</sup>s to 700 kg/m<sup>2</sup>s, the imposed heat flux is chosen at 5, 10 and 15KW/m<sup>2</sup>, and the mean refrigerant vapor quality is varied from 0.05 to 0.95. A data reduction analysis is needed to calculate the evaporation heat transfer coefficient from the raw data measured in the horizontal annular duct. The data reduction process is described in the following.

#### 3.1 Single-Phase Heat Transfer

The imposed heat flux to the refrigerant flow in the annular duct is calculated on the basis of the total power input  $Q_t$  and the total outside heat transfer area of the inner pipe of the annular duct  $A_s$ . The total power input is computed from the product of the measured voltage drop across the cartridge heater and the electric current passing through it. Hence the net power input to the test section  $Q_n$  is equal to  $(Q_t - Q_{loss})$ . The imposed heat flux at the outside surface of the inner pipe is then evaluated from the relation

$$q = Q_n / A_s \quad (3.1)$$

where  $V$  and  $I$  respectively represent the measured voltage drop and current. The total heat loss from the test section  $Q_{loss}$  is evaluated from the correlation for natural convection around a circular cylinder proposed by Churchill and Chu [28]. Their correlation is

$$\text{Nu}_a = \left\{ 0.6 + \frac{0.387 \text{Ra}_D^{1/6}}{\left[ 1 + (0.559/\text{Pr})^{9/16} \right]^{8/27}} \right\}^2 \quad (3.2)$$

where

$$\text{Ra}_D = g\beta(\overline{T}_{\text{ins}} - T_a) D_{\text{os}}^3 / \alpha \nu \quad (3.3)$$

To reduce the heat loss from the test section, we cover the test section with a 2.5-cm thick polyethylene insulation layer. We measured the mean temperature of the outside surface of the insulation layer  $\overline{T}_{\text{ins}}$  and ambient temperature  $T_a$ . Hence  $Q_{\text{loss}} = h_N (\overline{T}_{\text{ins}} - T_a) \cdot A_{\text{os}}$ ,

where  $A_{\text{os}}$  is the outside surface area of the insulation layer and  $h_N = \text{Nu}_a \cdot k_a / D_{\text{os}}$ . Note that

$D_{\text{os}}$  is the outer diameter of the cylindrical insulation layer. The results from this heat loss test indicate that the heat loss from the test section is generally less than 1% of the total power input no matter when single-phase flow or two-phase evaporating flow is in the duct.

The average single-phase convection heat transfer coefficient for the refrigerant flow over the entire heated surface in the annular duct is defined as

$$h_l = \frac{Q_n}{A_s \cdot (\overline{T}_w - T_{r,\text{ave}})} \quad (3.4)$$

and

$$T_{r,\text{ave}} = \frac{T_{r,i} + T_{r,o}}{2} \quad (3.5)$$

where  $Q_n$  is the net power input to the liquid refrigerant in the annular duct and  $T_{r,\text{ave}}$  is the average of the measured inlet and outlet temperatures of the refrigerant flow through the test



section, which is taken as the average bulk liquid refrigerant temperature. Note that  $\overline{T_w}$  denotes the average outside surface temperature of the inner pipe measured at the selected thermocouple locations. The outside surface temperature at each thermocouple location is deduced from the measured inside surface temperature of the inner pipe by subtracting the radial temperature drop due to the radial heat conduction in the pipe wall. Thus we have

$$T_w = T_{w,i} - Q_n \frac{\ln(D_o/D_i)}{2\pi k_w L} \quad (3.6)$$

### 3.2 Two-Phase Heat Transfer

In the two-phase test, we also estimate the heat loss from the test section by measuring the outside surface temperatures of the polyethylene insulation layer and the ambient temperature. The estimated heat loss from the test section by the procedures outlined above in section 3.1 is less than 0.5% for all cases and hence can be neglected.

The vapor quality of R-134a entering the test section inlet is evaluated from the energy balance for the preheater. Based on the temperature drop on the water side, the heat transfer in the preheater is calculated from the relation,

$$Q_{w,p} = W_{w,p} c_{p,w} (T_{w,p,i} - T_{w,p,o}) \quad (3.7)$$

While the heat transfer to the refrigerant in the preheater is the summation of the sensible heat transfer (for the temperature rise of the refrigerant to the saturated value) and latent heat transfer (for the evaporation of the refrigerant),

$$Q_{w,p} = Q_{sens} + Q_{lat} \quad (3.8)$$

here

$$\begin{aligned} Q_{\text{sens}} &= W_r c_{p,r} (T_{r,\text{sat}} - T_{r,p,i}) \\ Q_{\text{lat}} &= W_r i_{\text{fg}} x_{p,o} \end{aligned} \quad (3.9)$$

The above equations can be combined to evaluate the refrigerant quality at the exit of the preheater that is considered to be the same as the vapor quality of the refrigerant entering the test section. Specifically,

$$x_{\text{in}} = x_{p,o} = \frac{1}{i_{\text{fg}}} \left[ \frac{Q_{w,p}}{W_r} - c_{p,r} (T_{r,\text{sat}} - T_{r,p,i}) \right] \quad (3.10)$$

The total change of the refrigerant vapor quality in the test section is then deduced from the net heat transfer rate from the electric heater to the refrigerant in the test section, thus

$$\Delta x = \frac{Q_n}{W_r i_{\text{fg}}} \quad (3.11)$$

The mean vapor quality for the evaporation of R-134a in the test section at the middle axial location  $z=80$  mm is

$$x_m = x_{\text{in}} + \frac{\Delta x}{2} \quad (3.12)$$

Finally, the circumferential by average heat transfer coefficient for the evaporation of R-134a at the middle axial location in the test section is determined from the definition

$$h_r \equiv \frac{Q_n / A_s}{(\overline{T_{\text{wall}}} - T_{r,\text{sat}})} \quad (3.13)$$

Here  $\overline{T_{\text{wall}}}$  is the circumferential average outside surface temperature of the inner pipe at the middle axial location.

### 3.3 Uncertainty Analysis

Uncertainties of the heat transfer coefficients are estimated according to the procedures proposed by Kline and McClintock for the propagation of errors in physical measurement [29]. The results from this uncertainty analysis are summarized in Table 3.1.



**Table 3.1 Summary of the uncertainty analysis**

Parameter	Uncertainty
<b>Annular duct geometry</b>	
Length, width and thickness (%)	$\pm 1.0\%$
Gap size (%)	$\pm 5.0\%$
Area (%)	$\pm 2.0\%$
<b>Parameter measurement</b>	
Temperature, $T$ ( $^{\circ}\text{C}$ )	$\pm 0.2$
Temperature difference, $\Delta T$ ( $^{\circ}\text{C}$ )	$\pm 0.28$
System pressure, $P$ (MPa)	$\pm 0.002$
Mass flux of refrigerant, $G$ (%)	$\pm 2$
<b>Single-phase heat transfer</b>	
Imposed heat flux, $q$ (%)	$\pm 4.5$
Heat transfer coefficient, $h_{r,l}$ (%)	$\pm 12.5$
<b>Evaporation heat transfer</b>	
Imposed heat flux, $q$ (%)	$\pm 4.5$
Mean vapor quality, $x_m$ (%)	$\pm 9.5$
Heat transfer coefficient, $h_r$ (%)	$\pm 14$

## CHAPTER 4

### RESULTS AND DISCUSSION

Results from the present measured heat transfer data for the evaporation of R-134a in the narrow annular duct affected by the five experimental parameters, namely, the refrigerant mass flux, vapor quality, imposed heat flux, system pressure and duct size are illustrated here. The experiments are performed for the refrigerant mass flux  $G$  varying from 100 to 700 kg/m<sup>2</sup>s, imposed heat flux  $q$  fixed at 5, 10, 15 kW/m<sup>2</sup> and the system pressure  $p$  set at 349.8 kPa, 414.6 kPa and 488.6 kPa (corresponding respectively to the R-134a saturation temperature  $T_{\text{sat}} = 5^\circ\text{C}$ ,  $10^\circ\text{C}$  and  $15^\circ\text{C}$ ), and the vapor quality at the middle axial location of the duct  $x_m$  ranging from 0.05 to 0.95 for the annular gap of the duct  $\delta = 1.0, 2.0$  and 5.0 mm.

The mean void fraction  $\alpha_m$  and liquid film thickness  $t_{\text{lf}}$  at the middle axial location are estimated from the separated two-phase flow model proposed by Lockhart and Martinelli [30] as

$$\alpha_m = 1 - \frac{X_{\text{tt}}}{\sqrt{1 + 20X_{\text{tt}} + X_{\text{tt}}^2}} \quad (4.1)$$

And

$$t_{\text{lf}} = 0.5(1 - \alpha_m)R_o \left( \frac{R_o}{R_i} - \frac{R_i}{R_o} \right) \quad (4.2)$$

where

$$X_{tt}^2 = \left( \frac{1-x_m}{x_m} \right)^{1.8} \left( \frac{\rho_g}{\rho_l} \right) \left( \frac{\mu_l}{\mu_g} \right)^{0.2} \quad (4.3)$$

The results from this estimation are listed in Table 4.1. Note that the above results are only applicable to annular two-phase flow. The measured evaporation heat transfer data are expressed in terms of the evaporation heat transfer coefficient.

In what follows the effects of the experimental parameters on the R-134a circumferentially average evaporation heat transfer coefficient at the middle axial location are examined in detail. Besides, the results from visualizing the evaporation of the R-134a flow in the annular duct will be presented.

#### 4.1 Single-Phase Heat Transfer

Before beginning the evaporation experiments, the single-phase convective heat transfer tests are conducted for liquid R-134a flow in the annular duct. The measured single-phase convection heat transfer coefficients are compared with the correlations proposed by Gnielinski [9] and Dittus-Boelter [10]. In the single-phase heat transfer tests the refrigerant mass flux is varied from 75 to 1,200 kg/m<sup>2</sup>s for the annular gap of the duct  $\delta=1.0$  mm,  $\delta=2.0$  mm and  $\delta=5.0$  mm (corresponding to the Reynolds number of the refrigerant flow from 2,675 to 15,412) for the refrigerant saturated temperature  $T_{sat}=15^\circ\text{C}$  and inlet liquid subcooling  $\Delta T_{sub}=4^\circ\text{C}$ . Selected results from these tests are plotted in Figs. 4.1 and 4.2.

The Gnielinski correlation is

$$Nu_l = \frac{(f_f/8)(Re-1000)Pr}{1+12.7\sqrt{f_f/8}(Pr^{2/3}-1)} \quad \text{for } 2,300 < Re < 10^6 \quad (4.4)$$

$$\text{where } f_f = (1.82 \times \log_{10} \text{Re} - 1.64)^{-2} \quad (4.5)$$

The Dittus-Boelter correlation is

$$\text{Nu}_l = 0.023 \cdot \text{Re}^{0.8} \cdot \text{Pr}^{0.4} \quad \text{for } \text{Re} > 10^4 \quad (4.6)$$

The results in Figs. 4.1 and 4.2 manifest that the present data for  $h_l$  can be well correlated by the Gnielinski correlations with a mean absolute error of 6.3%.

## 4.2 Evaporation Heat Transfer in Narrow Annular Duct with $\delta=2.0$ mm

At first, the measured heat transfer data for the R-134a evaporation for the duct gap of 2.0 mm are presented in Figs 4.3 to 4.11 to illustrate the variations of the evaporation heat transfer coefficient at the middle axial location in the duct with the local vapor quality for various refrigerant mass flux  $G$ , imposed heat flux  $q$  and refrigerant saturated temperature  $T_{\text{sat}}$ . These results indicate that for given  $q$ ,  $T_{\text{sat}}$  and  $G$  the evaporation heat transfer coefficients increase almost linearly with the vapor quality, which is more prominent at a higher mass flux. The increase of the evaporation heat transfer coefficients with the vapor quality is considered to result from the fact that at a higher vapor quality the liquid film of the refrigerant on the heating surface becomes thinner. Hence the thermal resistance of the liquid film is reduced and heat transfer across the film is improved. Besides, at a higher vapor quality the mass flux of the vapor is larger and the vapor flow moves faster. This also improves the liquid-vapor interfacial heat transfer. To be more quantitative, the data in Fig. 4.5(a) show that at  $q=5 \text{ kW/m}^2$ ,  $G=500 \text{ kg/m}^2\text{s}$  and  $T_{\text{sat}}=15^\circ\text{C}$ , the R-134a evaporation heat transfer coefficients at  $x_m=0.07$  and  $0.92$  are respectively  $1,822$  and  $2,837 \text{ W/m}^2\text{C}$ . Hence an increase of 55.7% in  $h_r$  occurs for  $x_m$  raised from  $0.07$  to  $0.92$  for this case.

Then, the effects of the refrigerant mass flux on the R-134a evaporation heat transfer

for  $\delta=2.0$  mm shown in Figs. 4.3 to 4.5 indicate that the increase of  $h_r$  with the R-134a mass flux is rather significant except at low vapor quality. More specifically, larger increase in  $h_r$  with  $G$  is noted at a higher vapor quality. The increase in the evaporation heat transfer coefficients with the refrigerant mass flux is due to the higher liquid and vapor velocities for a higher mass flux. Besides, the higher liquid and vapor speeds respectively in the liquid film and vapor core can promote the turbulence level in the refrigerant flow and we have stronger interfacial evaporation and better convection of the vapor flow over the liquid film. Thus a higher evaporation heat transfer coefficient results for a higher mass flux. Quantitatively, according to the data in Fig. 4.5(a) for  $T_{\text{sat}}=15^\circ\text{C}$  and  $q=5$  kW/m<sup>2</sup> the quality-averaged evaporation heat transfer coefficients for  $G=400$  and  $500$  kg/m<sup>2</sup>s are 2,016 W/m<sup>2</sup>°C and 2,345 W/m<sup>2</sup>°C, respectively. Thus,  $\bar{h}_r$  is increased by 16.3% for the mass flux raised from 400 to 500 kg/m<sup>2</sup>s.

Next, the effects of the refrigerant saturated temperature on the R-134a evaporation heat transfer in the duct with  $\delta = 2.0$  mm are presented in Figs. 4.6 to 4.8 by showing the variations of the evaporation heat transfer coefficients with the vapor quality at  $T_{\text{sat}}=5, 10$  and  $15^\circ\text{C}$  for the mass flux  $G=300$  to  $500$  kg/m<sup>2</sup> at different imposed heat fluxes. The results indicate that the R-134a evaporation heat transfer coefficients rise with the saturated temperature of the refrigerant and the degree of this increase depends on the refrigerant mass flux, vapor quality and imposed heat flux. This trend in the variation of the evaporation heat transfer coefficient with the R-134a saturated temperature is ascribed to the fact that at a higher saturated temperature the latent heat of vaporization  $h_{fg}$  is lower, which in turn results in a higher evaporation rate of the liquid R-134a. Hence, the R-134a vapor in the duct flows at a higher speed, producing a higher convection effect and therefore a higher  $h_r$ . To quantitatively illustrate the effects of the saturated temperature on the R-134a



evaporation heat transfer coefficient, the quality-averaged evaporation heat transfer coefficients  $\bar{h}_r$  at  $G=500 \text{ kg/m}^2\text{s}$  and  $q=15 \text{ kW/m}^2$  are calculated from the data in Fig. 4.8(c). The results show that at  $T_{\text{sat}}= 5$  and  $15^\circ\text{C}$ ,  $\bar{h}_r$  are about  $3,079 \text{ W/m}^2\text{C}$  and  $3,797 \text{ W/m}^2\text{C}$ , respectively. Thus for  $T_{\text{sat}}$  raised from  $5^\circ\text{C}$  to  $15^\circ\text{C}$ ,  $\bar{h}_r$  is increased by 23.3%.

Finally, based on the data shown in Figs. 4.9 to 4.11 for  $\delta=2.0 \text{ mm}$  the R-134a evaporation heat transfer coefficient increases rather significantly with the imposed heat flux for various  $T_{\text{sat}}$  and  $G$  especially at low vapor quality. This significant increase of  $h_r$  with  $q$  reflects that the R-134a evaporation at the liquid-vapor interface in the refrigerant flow is substantially augmented by the increase in the imposed heat flux. Besides, at low vapor quality bubble nucleation on the heated surface is more important in the refrigerant flow. Thus raising the imposed heat flux can increase the bubble nucleation density, bubble generation frequency, and bubble growth, causing the evaporation heat transfer coefficient to increase more significantly with the imposed heat flux at low vapor quality. According to the data in Fig. 4.11(b) for  $T_{\text{sat}}=10^\circ\text{C}$  and  $G=500 \text{ kg/m}^2\text{s}$ , the quality-averaged evaporation heat transfer coefficients for  $q=5 \text{ kW/m}^2$  and  $15 \text{ kW/m}^2$  are  $2,277$  and  $3,424 \text{ W/m}^2\text{C}$ , individually. Thus for  $q$  raised from  $5$  to  $15 \text{ kW/m}^2$   $\bar{h}_r$  is increased by 50.4%.

### 4.3 Evaporation Heat Transfer in Narrower Annular Duct ( $\delta=1.0 \text{ mm}$ )

Attention is then turned to examining the heat transfer data for the R-134a evaporation for the smaller duct gap of  $1.0 \text{ mm}$ . The data for  $\delta=1.0 \text{ mm}$  measured here are presented in Figs 4.12-4.20. Comparing these results with that in Figs. 4.3 to 4.11 for  $\delta=2.0 \text{ mm}$  indicates that the effects of the refrigerant vapor quality, mass flux and saturated temperature and the imposed heat flux on the R-134a evaporation heat transfer coefficient exhibit similar trends for both  $\delta=1.0$  and  $2.0 \text{ mm}$ . A close inspection of these data, however,

reveals that some differences do exist. Specifically, at the smaller  $\delta$  of 1.0 mm the increase of the R-134a evaporation heat transfer coefficient with the vapor quality is slightly larger. For example, at  $q=5 \text{ kW/m}^2$ ,  $G=500 \text{ kg/m}^2\text{s}$  and  $T_{\text{sat}}=15^\circ\text{C}$ , the R-134a evaporation heat transfer coefficients at  $x_m=0.06$  and  $0.95$  are respectively  $2,201$  and  $3,571 \text{ W/m}^2\text{C}$  (Fig. 4.14(a)). Hence an increase of  $62.2\%$  in  $h_r$  occurs for  $x_m$  raised from  $0.06$  to  $0.95$  for this case. Besides, we compare the data at the same  $T_{\text{sat}}$ ,  $G$  and  $q$  in Fig. 4.14 and Fig 4.5 respectively for  $\delta=1.0$  and  $2.0$  mm. Note that the R-134a evaporation heat transfer is significantly better for  $\delta=1.0$  mm for the same  $G$  of  $500 \text{ kg/m}^2\text{s}$ . For clear comparison we compare the data for  $\delta=1.0$  and  $2.0$  mm in Figs. 4.21-4.23. Quantitatively, Fig. 4.21(c) shows that the quality-averaged  $h_r$  for  $\delta=1.0$  and  $2.0$  mm at  $G=500 \text{ kg/m}^2\text{s}$ ,  $T_{\text{sat}}=15^\circ\text{C}$  and  $q=5 \text{ kW/m}^2$  are  $2,875$  and  $2,345 \text{ W/m}^2\text{C}$ , respectively. An increase of  $22.6\%$  in  $h_r$  occurs for the duct gap reduced from  $2.0$  mm to  $1.0$  mm. This increase in  $h_r$  at reducing  $\delta$  can be attributed to the fact that at a smaller gap the average liquid film thickness is thinner (Table 4.1). Hence the thermal resistance of the liquid film is reduced and heat transfer across the film is improved.

Next, contrasting the results in Figs. 4.12-4.14 for  $\delta=1.0$  mm with that in Figs. 4.3-4.5 for  $\delta=2.0$  mm suggests that the refrigerant mass flux shows milder effects on  $h_r$  in the narrower duct for  $q=5$  &  $10 \text{ kW/m}^2$ , as evident from the data shown in Fig. 4.24. According to the data in Fig. 4.13(c) for  $T_{\text{sat}}=10^\circ\text{C}$  and  $q=15 \text{ kW/m}^2$  the quality-averaged evaporation heat transfer coefficients for  $G=600$  and  $700 \text{ kg/m}^2\text{s}$  are  $3,801 \text{ W/m}^2\text{C}$  and  $4,139 \text{ W/m}^2\text{C}$ , respectively. Thus,  $\bar{h}_r$  is only increased by  $8.8\%$  in the narrower duct with  $\delta=1.0$  mm for the R-134a mass flux raised from  $600$  to  $700 \text{ kg/m}^2\text{s}$ .

Then, a comparison of the data in Figs. 4.15-4.17 for  $\delta=1.0$  mm with that in Figs.

4.6-4.8 for  $\delta=2.0$  mm manifests that at low and intermediate imposed heat fluxes for  $q=5$  &  $10 \text{ kW/m}^2$  the effects of the refrigerant saturated temperature on the R-134a evaporation heat transfer coefficient are slightly less pronounced in the narrower duct. This can be more clearly seen in Fig. 4.25. Quantitatively, the quality-averaged evaporation heat transfer coefficients  $\bar{h}_r$  at  $G=700 \text{ kg/m}^2\text{s}$  and  $q=15 \text{ kW/m}^2$  are calculated from the data in Fig. 4.17(c) for  $\delta=1.0$  mm. The results show that at  $T_{\text{sat}}=5, 10$  and  $15^\circ\text{C}$ ,  $\bar{h}_r$  are about 3,826, 4,138 and  $4,472 \text{ W/m}^2\text{C}$ , respectively. Thus for  $T_{\text{sat}}$  raised from  $5^\circ\text{C}$  to  $15^\circ\text{C}$ ,  $\bar{h}_r$  is increased by 16.9%.

Finally, the data shown in Figs. 4.18-4.20 for  $\delta=1.0$  mm, when contrasted with that in Figs. 4.9-4.11 for  $\delta=2.0$  mm, indicate that in the narrower duct the effects of the imposed heat flux on the R-134a evaporation heat transfer coefficient are stronger at low vapor quality but the opposite is the case at high vapor quality, as clearly seen in Fig. 4.26. According to the data in Fig. 4.18(b) for  $T_{\text{sat}}=10^\circ\text{C}$  and  $G=500 \text{ kg/m}^2\text{s}$ , the quality-averaged evaporation heat transfer coefficients for  $q=5, 10$  and  $15 \text{ kW/m}^2$  are 2,761, 3,161 and  $3,743 \text{ W/m}^2\text{C}$ , individually. Thus for  $q$  raised from 5 to  $15 \text{ kW/m}^2$   $\bar{h}_r$  is increased by 35.6%.

#### 4.4 Characteristics of R-134a Evaporating Flow in Narrow Annular Duct

In addition to the heat transfer data presented above, the photos of the R-134a evaporating flow taken from the duct side over the entire duct and over a small region around the middle axial location are shown in Figs. 4.27-4.50 for various experimental parameters. The flow photos shown in Figs. 4.27-4.35 for  $\delta=2.0$  mm indicate that at the low vapor quality of 0.05 bubble nucleation on the heating surface is not clearly seen at the low imposed heat flux of  $5 \text{ kW/m}^2$ . But at the much higher  $q$  of  $15 \text{ kW/m}^2$  the bubble nucleation density is rather high. This apparently results from the fact that the heating surface is

entirely covered by the liquid R-134a even at the high vapor quality for  $x_m=0.95$ . Merging of small bubbles into large bubbles takes place frequently. Some bubbles are relatively large. Actually, they can be regarded as bubble slugs. Besides, bubbles dispersed in a large liquid slug appear in the duct. Moreover, due to the gravity effects the top and bottom parts of the duct are respectively dominated by the vapor and liquid flows. At the intermediate vapor quality of 0.54 some bubble nucleation on the heating surface can also be observed at a high  $q$ . Beyond the inlet region the flow in the duct is dominated by the vapor flow over thin liquid film around the inner pipe and it is an annular two-phase flow. Irregular moving waves appear at the vapor liquid-interface. We also observe a small liquid slug. In the entrance region of the duct bubbles interdisperse with liquid and both move irregularly. Coalescence of bubbles as they move downstream resulting in the annular flow. It is of interest to note that at the very high vapor quality of 0.94 bubble nucleation can still be seen at  $q=15 \text{ kW/m}^2$  although the liquid film covering the heating surface is very thin. Again at this high quality the duct is dominated by the annular two-phase flow except in the entrance region. At the vapor-liquid interface irregular wave still prevail. But no liquid slug exists.

Next, the effects of the experimental parameters on the global evaporating flow pattern are examined. Comparing the results in Figs. 4.27 and 4.28 indicates that at the higher imposed heat flux a big liquid slug forms at  $x_m=0.05$  and at  $x_m \geq 0.54$  the annular flow prevails in a large portion of the duct. For a lowering of the refrigerant saturated temperature from  $15^\circ\text{C}$  to  $5^\circ\text{C}$  at  $x_m=0.05$  the liquid slug becomes larger due to less bubble nucleation at the lower  $T_{\text{sat}}$ , as evident from the photos in Figs. 4.28 and 4.29. Note that a number bubbles disperse in the liquid slug. We also note that at  $x_m=0.94$  for  $T_{\text{sat}}=5^\circ\text{C}$  the annular flow almost exists in the entire duct (Fig. 4.29(c)). As the refrigerant mass flux is raised from  $300 \text{ kg/m}^2\text{s}$  to  $400 \text{ kg/m}^2\text{s}$  less bubbles nucleate on the heating surface (Figs.

4.28 and 4.31). This results in the disappearance of the liquid slug at low  $x_m$  and a smaller region of annular flow in the duct for  $G=400 \text{ kg/m}^2\text{s}$  at  $T_{\text{sat}}=15^\circ\text{C}$ . Note that at the lower  $T_{\text{sat}}$  of  $5^\circ\text{C}$  for  $G=400 \text{ kg/m}^2\text{s}$  a liquid slug exists (Fig. 4.32 (a)).

Then, we summarize the effects of the experimental parameters on the local evaporating flow characteristics in Figs. 4.36-4.38 by showing the flow photos taken from the chosen small region at the middle axial location for various refrigerant mass fluxes at  $\delta=2.0 \text{ mm}$ . Some evaporating flow characteristics revealed above can be clearly seen here. These results suggest that at the high vapor quality of 0.95 the waves at the interface is rather pronounced and highly irregular. Moreover, at the higher mass flux of  $500 \text{ kg/m}^2\text{s}$  the interfacial waves are already highly irregular even at the intermediate quality of 0.52 (Fig. 4.38).

Finally, the photos of the evaporating flow in the narrower duct ( $\delta=1.0 \text{ mm}$ ) are presented in Figs. 4.39-4.47. The effects of the vapor quality, imposed heat flux and refrigerant mass flux and saturated temperature on the evaporating flow characteristics for  $\delta=1.0 \text{ mm}$  are qualitatively similar to that for  $\delta=2.0 \text{ mm}$  given in Figs. 4.27-4.35. The duct gap, however, exhibits some important influences. Contrasting the flow photos for  $\delta=1.0 \text{ mm}$  in Fig. 4.39 with that in Fig. 4.33 for  $\delta=2.0 \text{ mm}$  at the same  $G(=500 \text{ kg/m}^2\text{s})$ ,  $T_{\text{sat}}(=15^\circ\text{C})$  and  $q(=5 \text{ kW/m}^2)$  reveals that in the narrower duct the bubble coalescence is more frequent and we have more big bubbles in the duct at low  $x_m$ . Besides, at high  $x_m$  annular two-phase flow regions interrupted by liquid slugs prevail for  $\delta=1.0 \text{ mm}$ . This trend is also valid for the higher  $q$  (Figs. 4.34 and 4.40) and lower  $T_{\text{sat}}$  (Figs. 4.35 and 4.41). The effects of the experimental parameters on the local evaporating flow characteristics for  $\delta=1.0 \text{ mm}$  are summarized in Figs. 4.48-4.50.

## 4.5 Evaporation Heat Transfer and Flow Characteristics in Wider Annular Duct with $\delta=5.0$ mm

Having examined the evaporation of R-134a in the narrow annular duct with the duct gap of 1.0 and 2.0 mm, we move further to explore the characteristics of the R-134a evaporation heat transfer in the same duct but with a wider gap of 5.0 mm. The heat transfer data measured in the middle axial location for  $\delta=5.0$  mm are presented in Figs. 4.51-4.59 to illustrate the effects of the vapor quality, refrigerant mass flux and saturated temperature on the evaporation heat transfer coefficient. These results, when contrasted with that for  $\delta=2.0$  mm given in Figs. 4.3-4.11, indicate that except at the low refrigerant mass flux of 100 kg/m<sup>2</sup>s the evaporation heat transfer for  $\delta=5.0$  mm shows a similar trend to that for  $\delta=2.0$  mm. Specifically, the evaporation heat transfer coefficient increases with the local vapor quality, refrigerant mass flux and saturated temperature, and imposed heat flux. But for  $G=100$  kg/m<sup>2</sup>s and  $\delta=5.0$  mm the evaporation heat transfer coefficient increases with the vapor quality up to  $x_m$  around 0.5. Beyond this  $x_m$  the evaporation heat transfer coefficient first declines significantly with the increases in the vapor quality. Then it gradually levels off for a further increase in  $x_m$ . This decay of  $h_r$  with an increase in  $x_m$  is more pronounced at a lower refrigerant temperature and a higher imposed heat flux (Figs. 4.54 and 4.57). This decline in  $h_r$  at increasing  $x_m$  is the direct consequence of the partial dryout of the liquid film on the heating surface in the middle axial location, which only occurs for the cases with low refrigerant mass flux and at high vapor quality, as observed in the visualization of the evaporating flow. A close inspection of the data presented in Figs. 4.54 and 4.57 reveals that at  $G=100$  kg/m<sup>2</sup>s and at low  $x_m$  before the liquid film dryout the evaporation heat transfer coefficient increases slightly with  $x_m$  at the low  $q$  of 5 kw/m<sup>2</sup> but decreases slightly with  $x_m$  at the high  $q$  of 15 kw/m<sup>2</sup>. Besides, beyond the liquid film dryout the significant decline in  $h_r$  appears at a slightly lower  $x_m$  for a lower refrigerant saturated temperature and higher

imposed heat flux. Quantitatively, the evaporation heat transfer coefficients for  $G=100$  kg/m<sup>2</sup>s,  $q=5$  kW/m<sup>2</sup> and  $T_{\text{sat}}=15^{\circ}\text{C}$  based on the data in Fig 4.57(c) at  $x_m=0.05$ , 0.69 and 0.95 are about 768, 795 and 654 W/m<sup>2</sup>°C, respectively. Thus for  $x_m$  raised from 0.05 to 0.95,  $h_r$  is decreased by 14.9%. The quality-averaged evaporation heat transfer coefficient  $\bar{h}_r$  is 757 W/m<sup>2</sup>°C.

To illustrate the effects of the duct gap, the measured heat transfer coefficients for  $\delta=2.0$  and 5.0 mm are compared in Figs. 4.60-4.62 for the same  $G$ ,  $T_{\text{sat}}$  and  $q$ . Note that at the same  $G$  of 300 kg/m<sup>2</sup>s the evaporation heat transfer coefficient for R-134a in the duct with the wider gap of 5.0 mm is substantially lower than that in the narrow duct with  $\delta=2.0$  mm. Quantitatively, the quality-averaged  $h_r$  for  $\delta=5.0$  and 2.0 mm at  $G=300$  kg/m<sup>2</sup>s,  $T_{\text{sat}}=15^{\circ}\text{C}$  and  $q=5$  kW/m<sup>2</sup> are respectively 1,317 and 2,649 (Fig. 4.60(c)). A reduction of 50.3% in  $h_r$  occurs for the duct gap reduced from 5.0 mm to 2.0 mm. This decrease in  $h_r$  at bigger  $\delta$  can be attributed to the fact that at a larger duct gap the liquid film is much thicker (Table 4.1). Hence the thermal resistance of the liquid film is higher and heat transfer across the film is reduced.

Finally, the photos of the evaporating flow in the horizontal annular duct with the wide gap of 5.0 mm are shown in Figs. 4.63-4.71 for various  $G$ ,  $T_{\text{sat}}$  and  $q$  at selected local vapor qualities in the middle axial location. The results indicate that the effects of the gravity on the two-phase flow in the wider duct are rather significant. Specifically, in the upper part of the duct the vapor flow prevails and the liquid flow dominates in the lower part of the duct. Thus we have a stratified flow in the duct. Besides, at the low refrigerant mass flux of 100 kg/m<sup>2</sup>s and at higher vapor quality the liquid film on the heating surface dries out at certain downstream locations (Figs. 4.63-4.65). These liquid film dryout locations move upstream at higher vapor quality, lower refrigerant saturated temperature and higher imposed heat



flux. Note that at the higher  $G$  of 200 and 300 kg/m<sup>2</sup>s the dryout of the liquid film on the heating surface only occurs at the downstream locations near the duct exit (Figs. 4.66-4.71). We also note that in the wide duct at low vapor quality the liquid flow contains a large number of discrete disperse bubbles (Figs. 4.63(a)-4.71(a)). But at a high vapor quality the liquid and vapor phases mix irregularly in the large portion of the duct and the annular two-phase flow only prevails in a small portion of the duct, as evident from comparing the photos in Figs. 4.69-4.71 for  $\delta=5.0$  mm with that in Figs. 4.27-4.29 for  $\delta=2.0$  mm. The effects of the experimental parameters on the local evaporating flow characteristics for  $\delta=5.0$  mm are summarized in Figs. 4.72-4.74. Comparing the photos in Fig.4.74 for  $\delta=5.0$  mm with that in Fig. 4.36 for  $\delta=2.0$  mm at the same  $G$ ,  $q$ ,  $T_{\text{sat}}$  and  $x_m$  reveals that the bubble nucleation on the heating surface is significantly less in the wider duct, which is more prominent at higher  $q$ , lower  $x_m$  and higher  $T_{\text{sat}}$ .

#### 4.6 Correlation Equation for Evaporation Heat Transfer Coefficients

For practical application the present data for the R-134a evaporation in the narrow annular ducts need to be correlated empirically. The data presented above indicate that  $h_r$  varies linearly with the vapor quality except for cases with the liquid film dryout at the middle axial location and the correlation is thus expressed as

$$\text{Nu}_r = \frac{h_r \cdot D_h}{k_f} = m_1 x_m + m_2 \quad (4.7)$$

Where  $m_1$  and  $m_2$  can be correlated as

$$m_1 = f(\text{Bo}, \text{Re}) = a_1 + b_1 \text{Bo}^{c_1} \text{Re}^{d_1} \quad (4.8)$$

$$m_2 = f(\text{Bo}, \text{Re}) = a_2 \text{Bo}^{b_2} \text{Re}^{c_2} \quad (4.9)$$



For the ducts with  $\delta=1.0$  and  $2.0$  mm, the values for the coefficients in the  $m_1$  and  $m_2$  are  $a_1=30$ ,  $b_1=0.187$ ,  $c_1=2.9$ ,  $d_1=3.09$ ,  $a_2=24.7$ ,  $b_2=0.68$  and  $c_2=0.855$ . For the wider duct with  $\delta=5.0$  mm, the values for the coefficients in the  $m_1$  and  $m_2$  are the same as that for the narrower duct except  $c_1=3.2$  and  $c_2=0.796$ . The Boiling number and Reynolds number for the flow are defined respectively as

$$Bo = \frac{q}{G \cdot i_{fg}} \quad (4.10)$$

$$Re = \frac{G \cdot D_h}{\mu_l} \quad (4.11)$$

Comparison of the above correlation with the present experimental data shown in Figs. 4.75 and 4.76 indicate that more than 96% and 98% of the present data for  $h_r$  fall within  $\pm 25\%$  of Eq. (4.7), and the mean absolute error (MAE) between the present data for  $h_r$  and the proposed correlation for both the narrower and wider ducts are 10.3% and 8.9%.

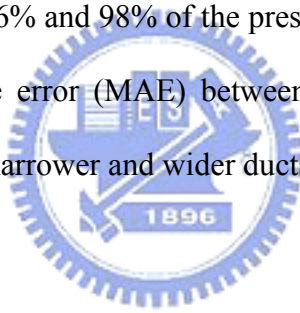


**Table 4.1 Relation between the mean vapor quality, void fraction and liquid film thickness estimated from the separated two-phase flow model.**

T <sub>sat</sub> =5°C (P <sub>sat</sub> =349.8kPa)					T <sub>sat</sub> =15°C (P <sub>sat</sub> =488.6kPa)				
x <sub>m</sub>	α <sub>m</sub>	δ=1 mm	δ=2 mm	δ=5 mm	x <sub>m</sub>	α <sub>m</sub>	δ=1 mm	δ=2 mm	δ=5 mm
		t <sub>lf</sub> (μm)					t <sub>lf</sub> (μm)		
0.05	0.69	333	708	2,359	0.05	0.66	359	762	2,539
0.10	0.77	242	513	1,711	0.10	0.75	262	555	1,851
0.15	0.81	196	416	1,388	0.15	0.80	213	452	1,506
0.20	0.84	167	354	1,179	0.20	0.83	181	385	1,282
0.25	0.86	145	308	1,026	0.25	0.85	158	336	1,119
0.30	0.88	128	272	906	0.30	0.87	140	297	990
0.35	0.89	114	242	808	0.35	0.88	125	265	884
0.40	0.90	102	217	722	0.40	0.89	112	238	793
0.45	0.91	92	194	648	0.45	0.90	101	214	713
0.50	0.92	82	174	581	0.50	0.91	91	192	640
0.55	0.93	73	156	519	0.55	0.92	81	172	574
0.60	0.94	65	138	460	0.60	0.93	72	153	511
0.65	0.95	57	122	405	0.65	0.94	64	135	451
0.70	0.95	50	106	352	0.70	0.95	56	118	393
0.75	0.96	42	90	300	0.75	0.96	48	101	336
0.80	0.97	35	74	247	0.80	0.96	39	84	279
0.85	0.97	27	58	193	0.85	0.97	31	66	220
0.90	0.98	19	41	137	0.90	0.98	22	47	157
0.95	0.99	11	23	76	0.95	0.99	12	26	88

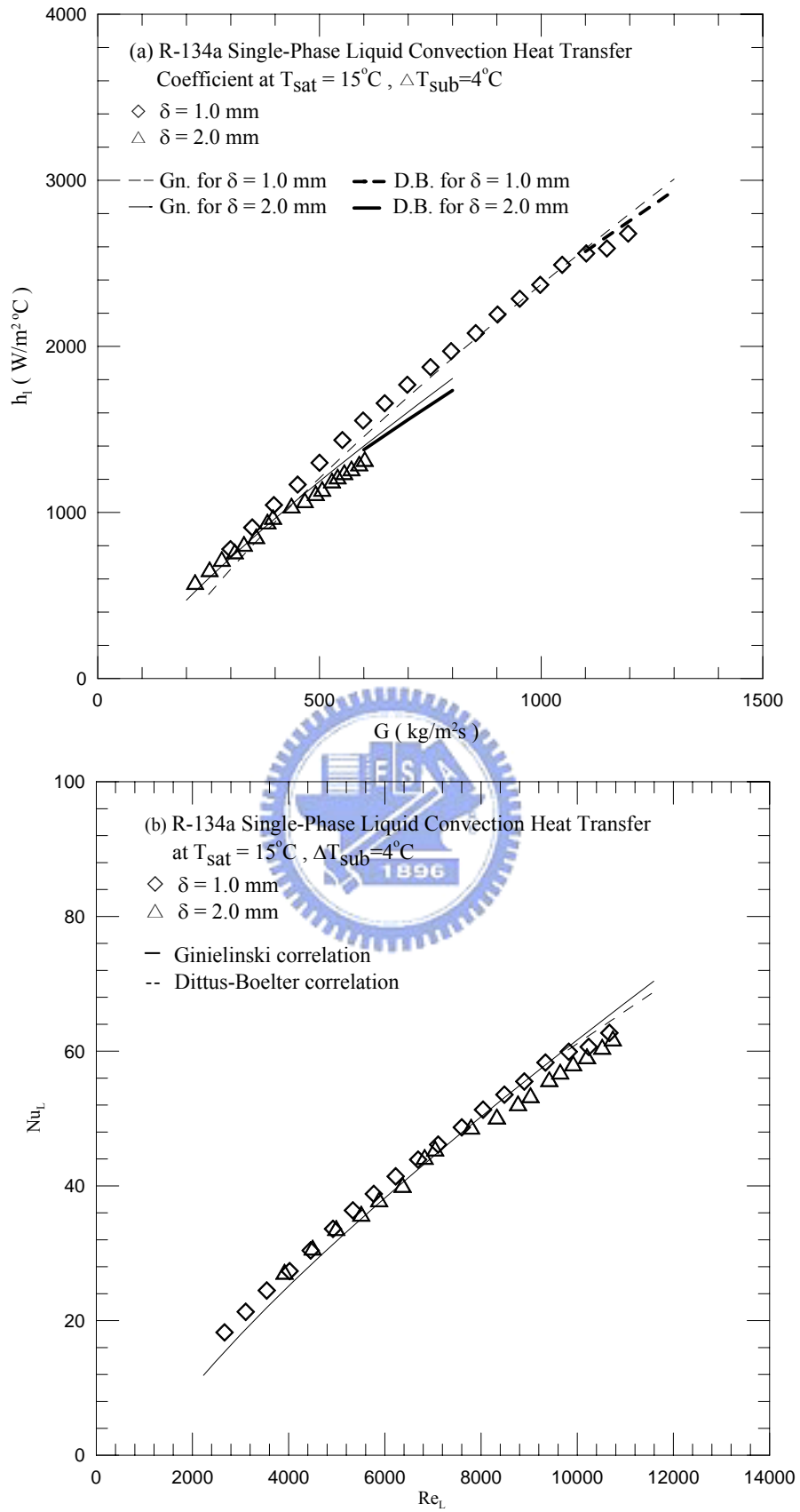


Fig. 4.1 Comparison of the present single-phase liquid convection heat transfer data  $h_l$ (a) and  $Nu_l$ (b) with the correlations of Gnielinski and Dittus-Boelter.

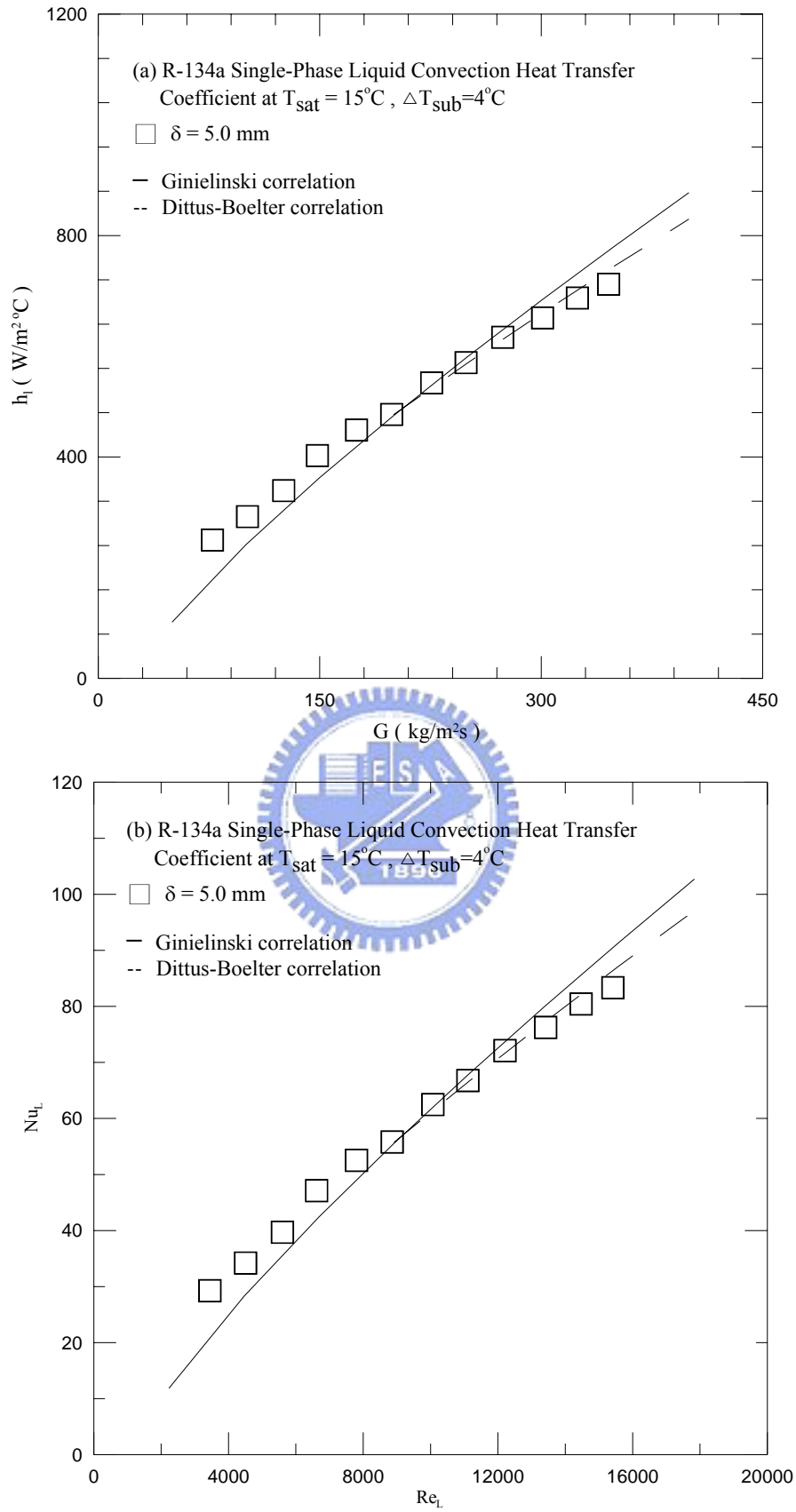


Fig. 4.2 Comparison of the present single-phase liquid convection heat transfer data  $h_l$ (a) and  $Nu_l$ (b) with the correlations of Gnielinski and Dittus-Boelter.

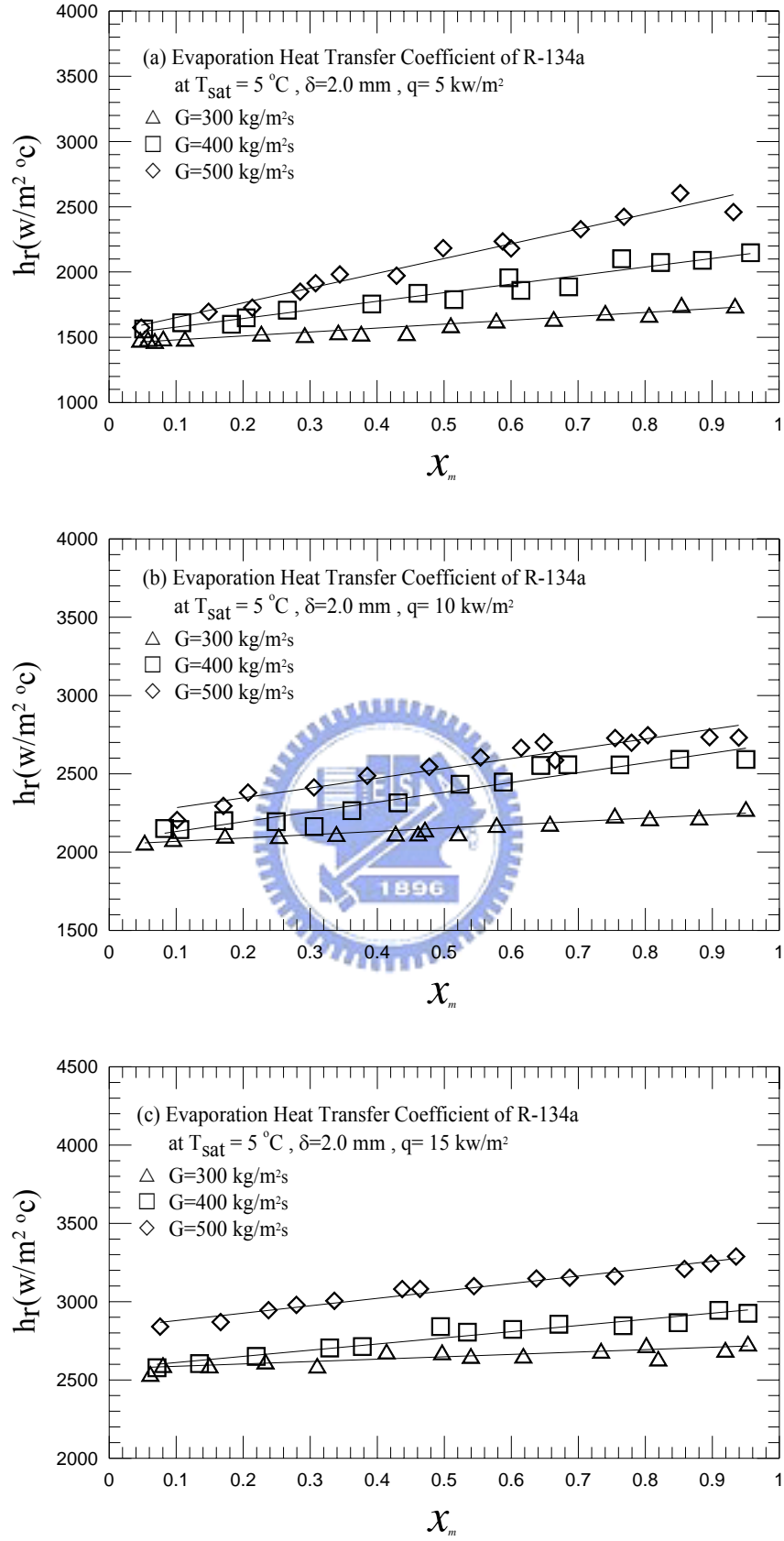


Fig. 4.3 Variations of R-134a evaporation heat transfer coefficient with vapor quality in  $\delta = 2.0 \text{ mm}$  narrow duct at  $T_{\text{sat}} = 5^\circ\text{C}$  for various  $G$  for (a)  $q = 5 \text{ kW/m}^2$ , (b)  $q = 10 \text{ kW/m}^2$  and (c)  $q = 15 \text{ kW/m}^2$ .

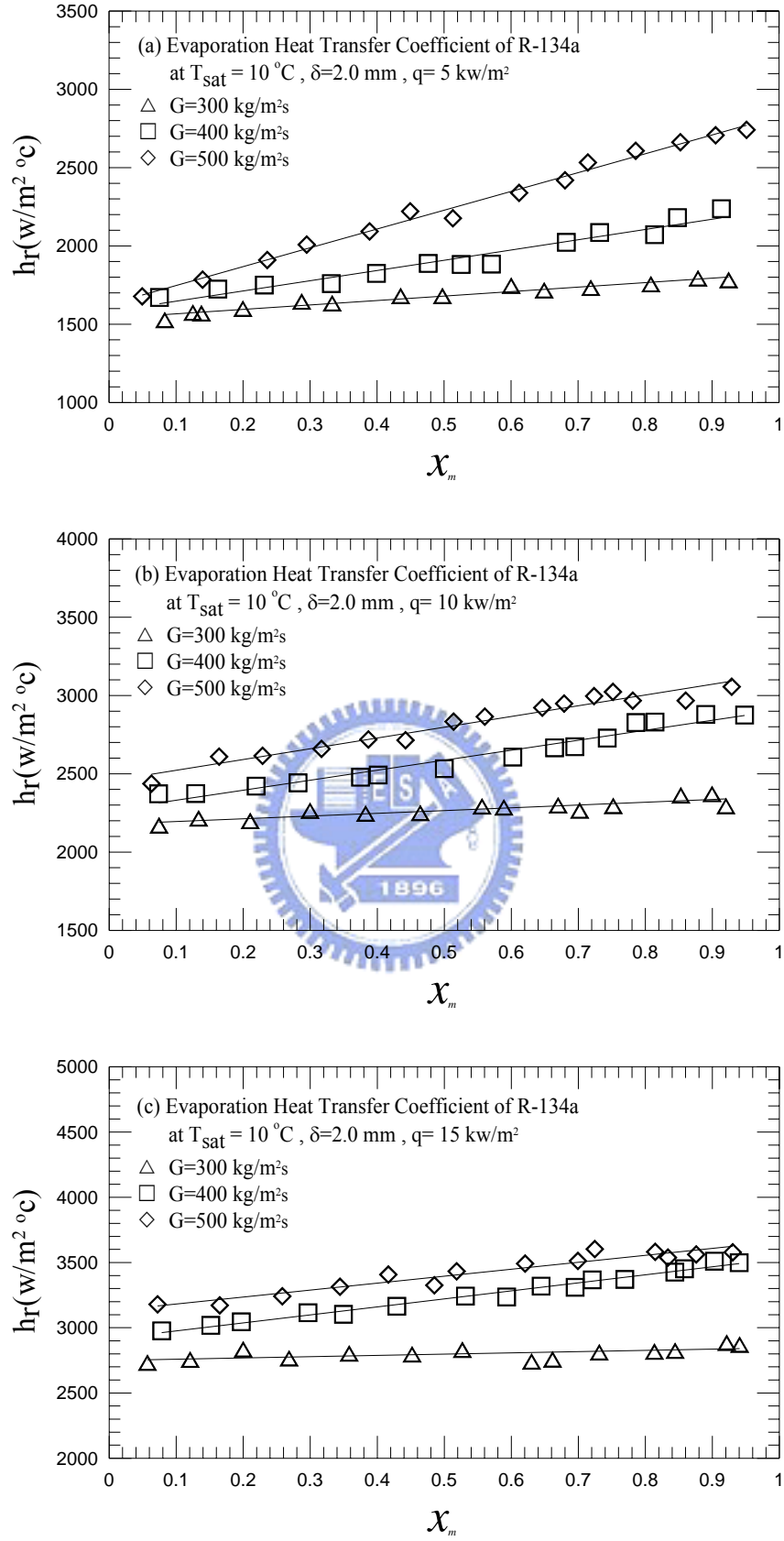


Fig. 4.4 Variations of R-134a evaporation heat transfer coefficient with vapor quality in  $\delta = 2.0\text{ mm}$  narrow duct at  $T_{\text{sat}} = 10^\circ\text{C}$  for various  $G$  for (a)  $q = 5\text{ kW/m}^2$ , (b)  $q = 10\text{ kW/m}^2$  and (c)  $q = 15\text{ kW/m}^2$ .

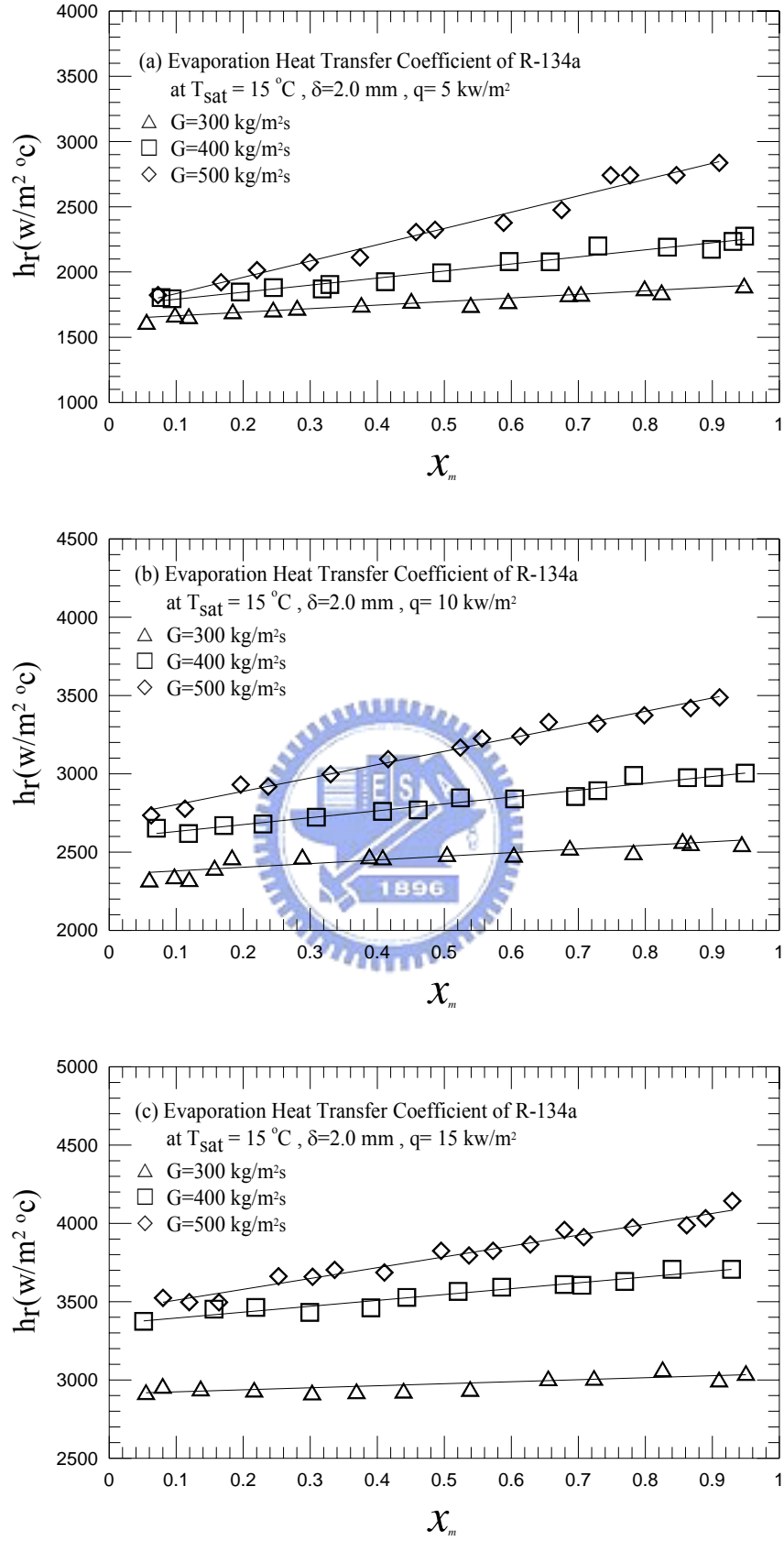


Fig. 4.5 Variations of R-134a evaporation heat transfer coefficient with vapor quality in  $\delta = 2.0 \text{ mm}$  narrow duct at  $T_{\text{sat}} = 15^\circ\text{C}$  for various  $G$  for (a)  $q = 5 \text{ kW/m}^2$ , (b)  $q = 10 \text{ kW/m}^2$  and (c)  $q = 15 \text{ kW/m}^2$ .

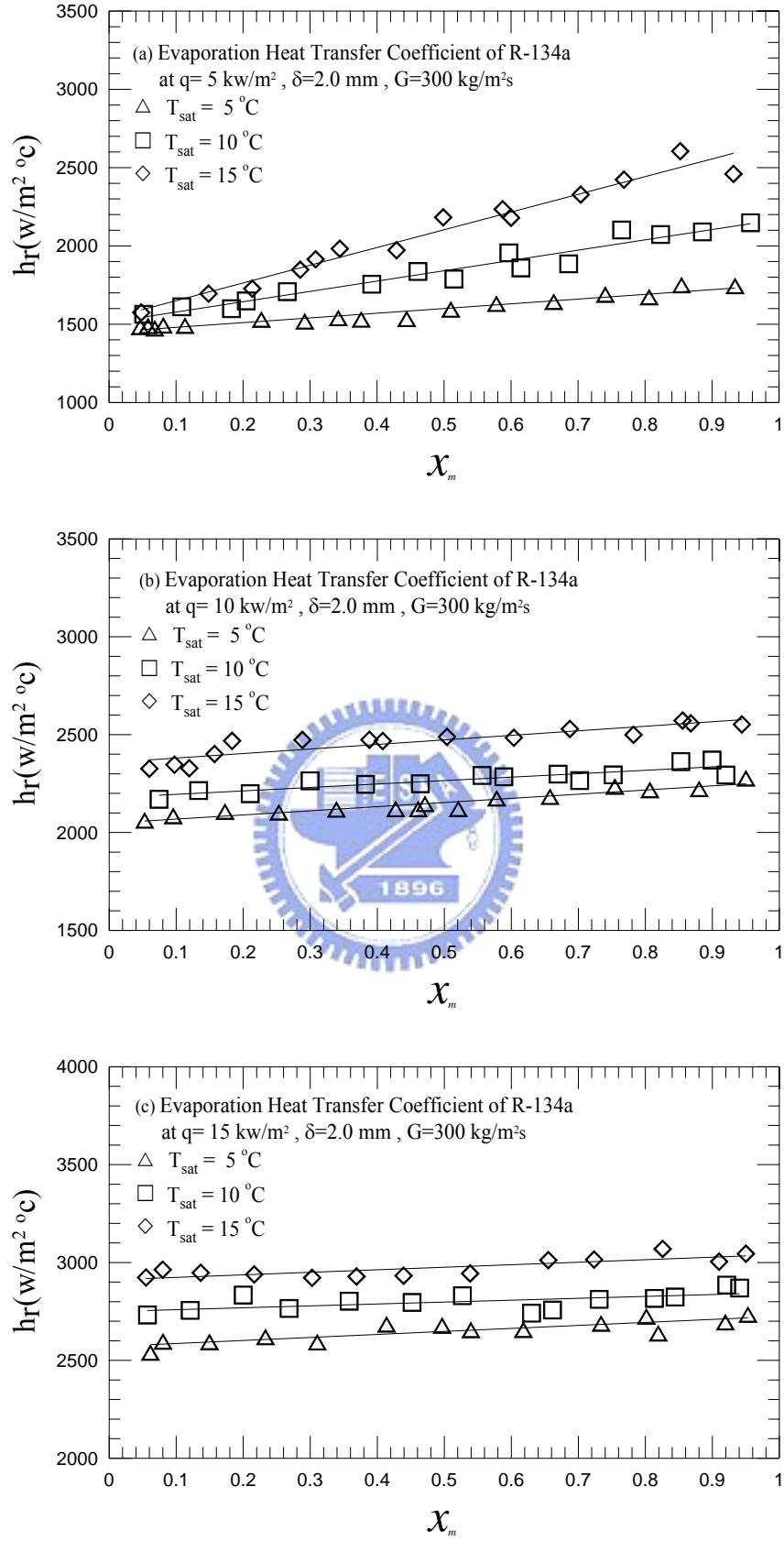


Fig. 4.6 Variations of R-134a evaporation heat transfer coefficient with vapor quality in  $\delta = 2.0 \text{ mm}$  narrow duct at  $G = 300 \text{ kg/m}^2\text{s}$  for various  $T_{\text{sat}}$  for (a)  $q = 5 \text{ kW/m}^2$ , (b)  $q = 10 \text{ kW/m}^2$  and (c)  $q = 15 \text{ kW/m}^2$ .



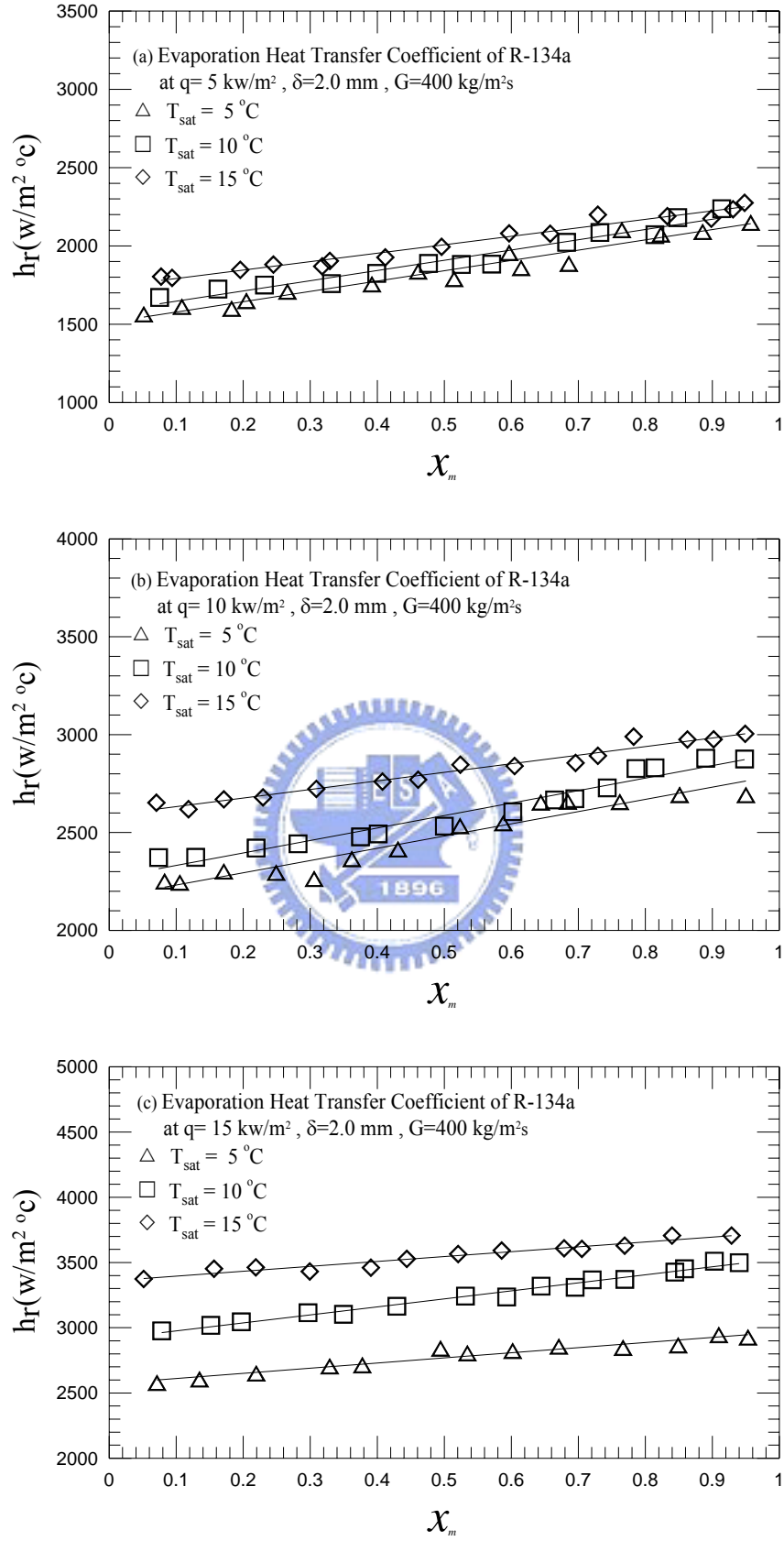


Fig. 4.7 Variations of R-134a evaporation heat transfer coefficient with vapor quality in  $\delta = 2.0 \text{ mm}$  narrow duct at  $G = 400 \text{ kg/m}^2\text{s}$  for various  $T_{\text{sat}}$  for (a)  $q = 5 \text{ kW/m}^2$ , (b)  $q = 10 \text{ kW/m}^2$  and (c)  $q = 15 \text{ kW/m}^2$ .

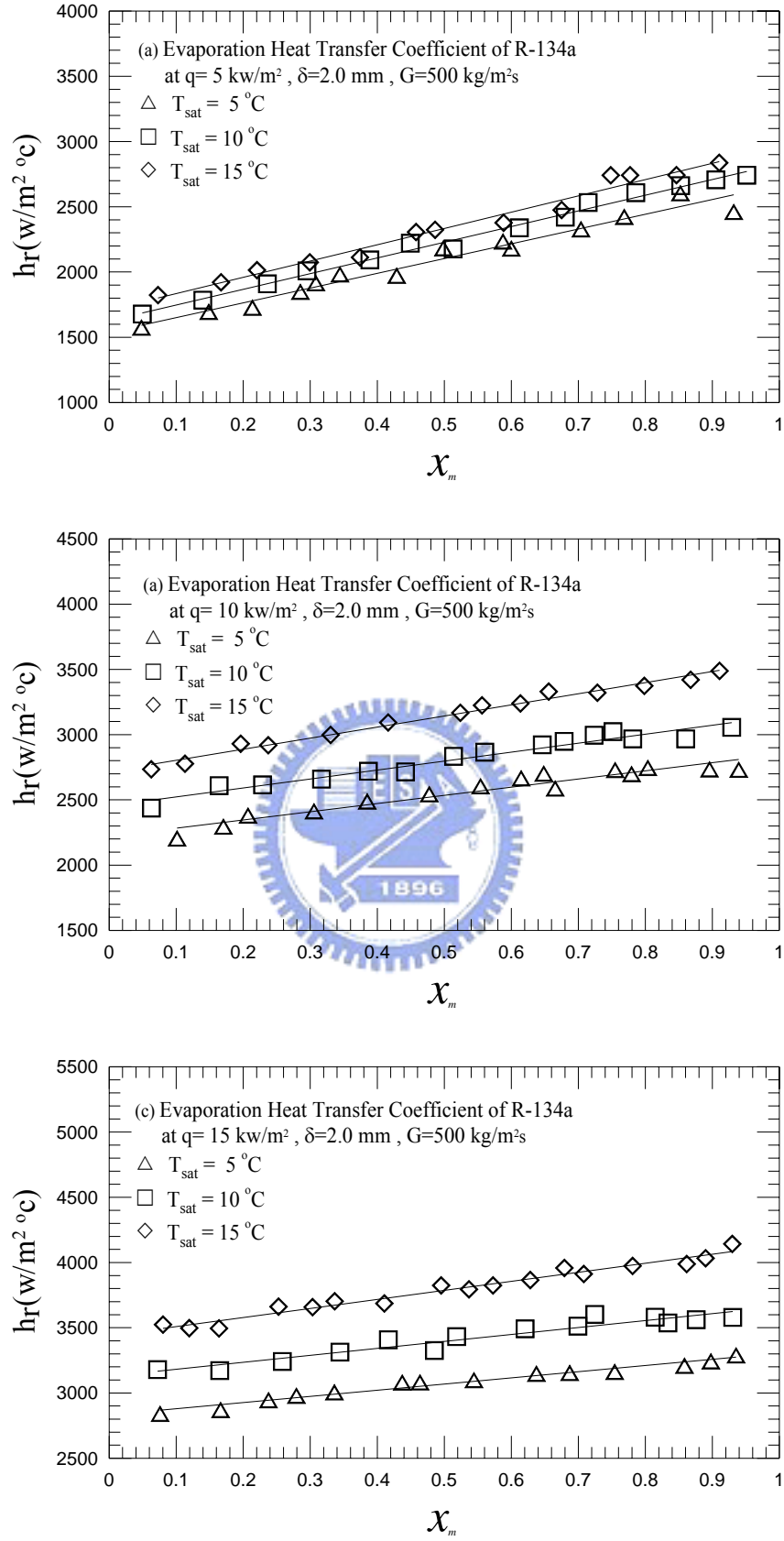


Fig. 4.8 Variations of R-134a evaporation heat transfer coefficient with vapor quality in  $\delta = 2.0 \text{ mm}$  narrow duct at  $G = 500 \text{ kg/m}^2\text{s}$  for various  $T_{\text{sat}}$  for (a)  $q = 5 \text{ kW/m}^2$ , (b)  $q = 10 \text{ kW/m}^2$  and (c)  $q = 15 \text{ kW/m}^2$ .

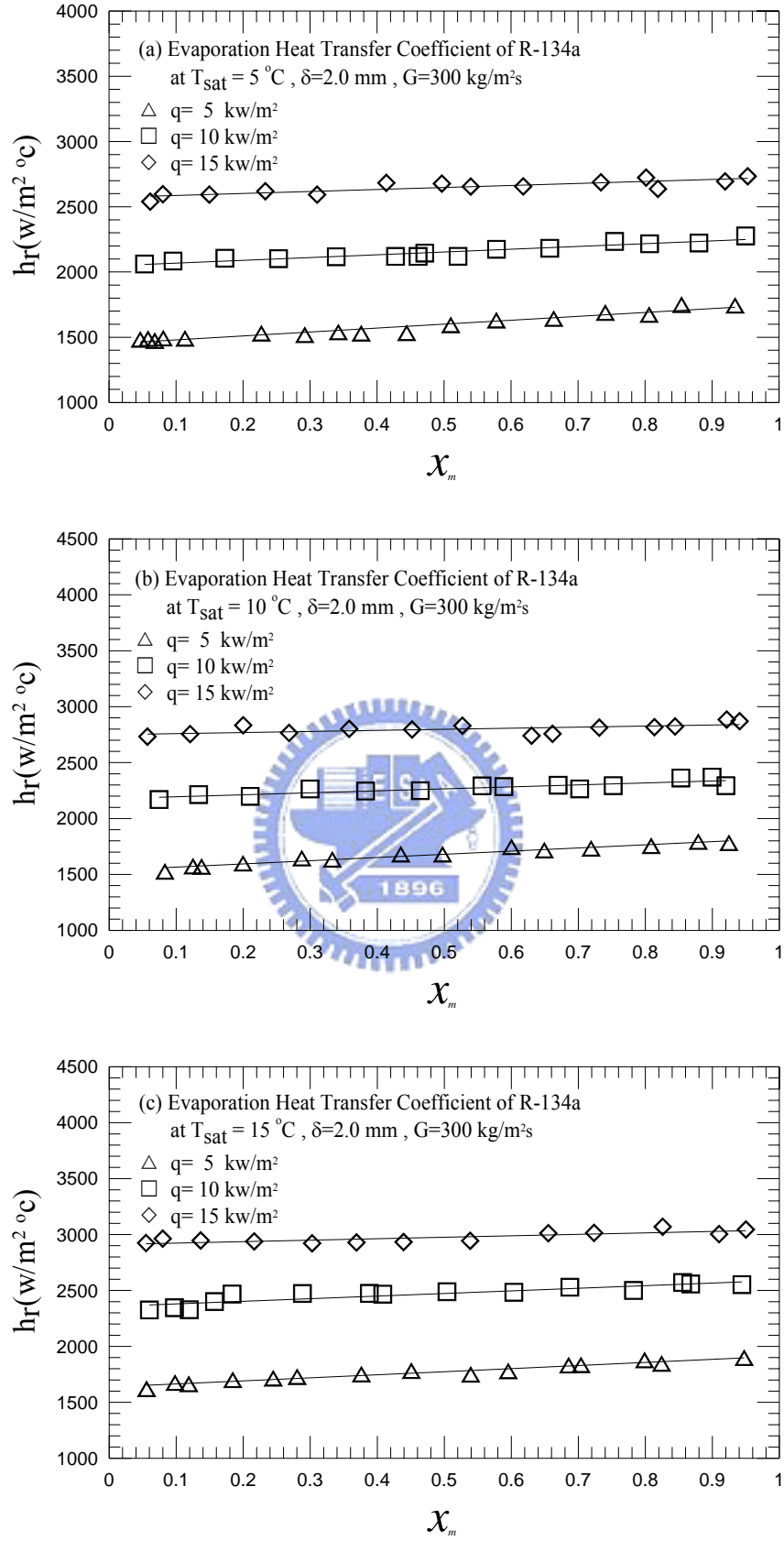


Fig. 4.9 Variations of R-134a evaporation heat transfer coefficient with vapor quality in  $\delta = 2.0\text{ mm}$  narrow duct at  $G = 300\text{ kg/m}^2\text{s}$  for various  $q$  for (a)  $T_{\text{sat}} = 5^\circ\text{C}$ , (b)  $T_{\text{sat}} = 10^\circ\text{C}$  and (c)  $T_{\text{sat}} = 15^\circ\text{C}$ .

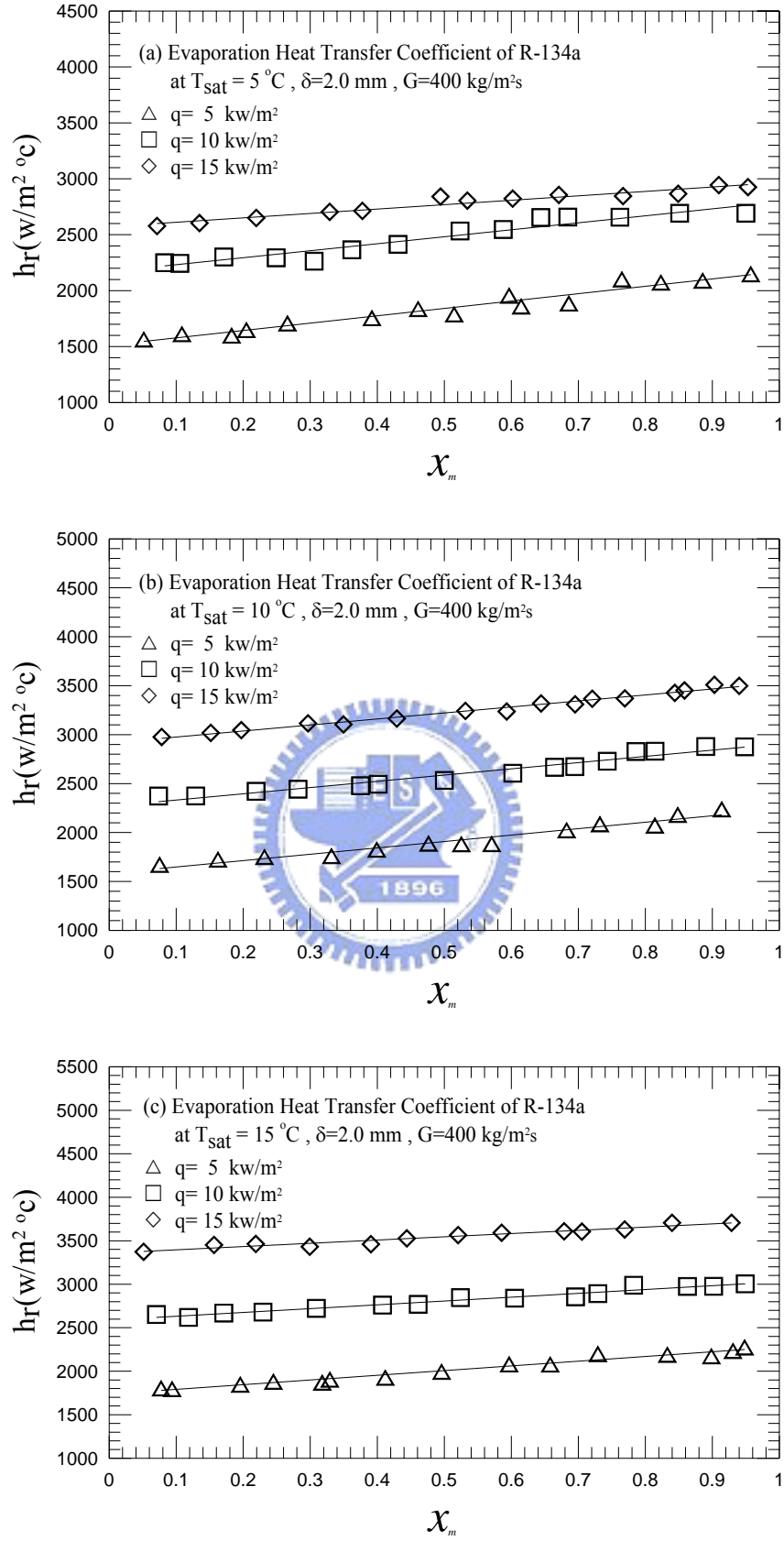


Fig. 4.10 Variations of R-134a evaporation heat transfer coefficient with vapor quality in  $\delta = 2.0\text{ mm}$  narrow duct at  $G = 400\text{ kg/m}^2\text{s}$  for various  $q$  for (a)  $T_{\text{sat}} = 5^\circ\text{C}$ , (b)  $T_{\text{sat}} = 10^\circ\text{C}$  and (c)  $T_{\text{sat}} = 15^\circ\text{C}$ .

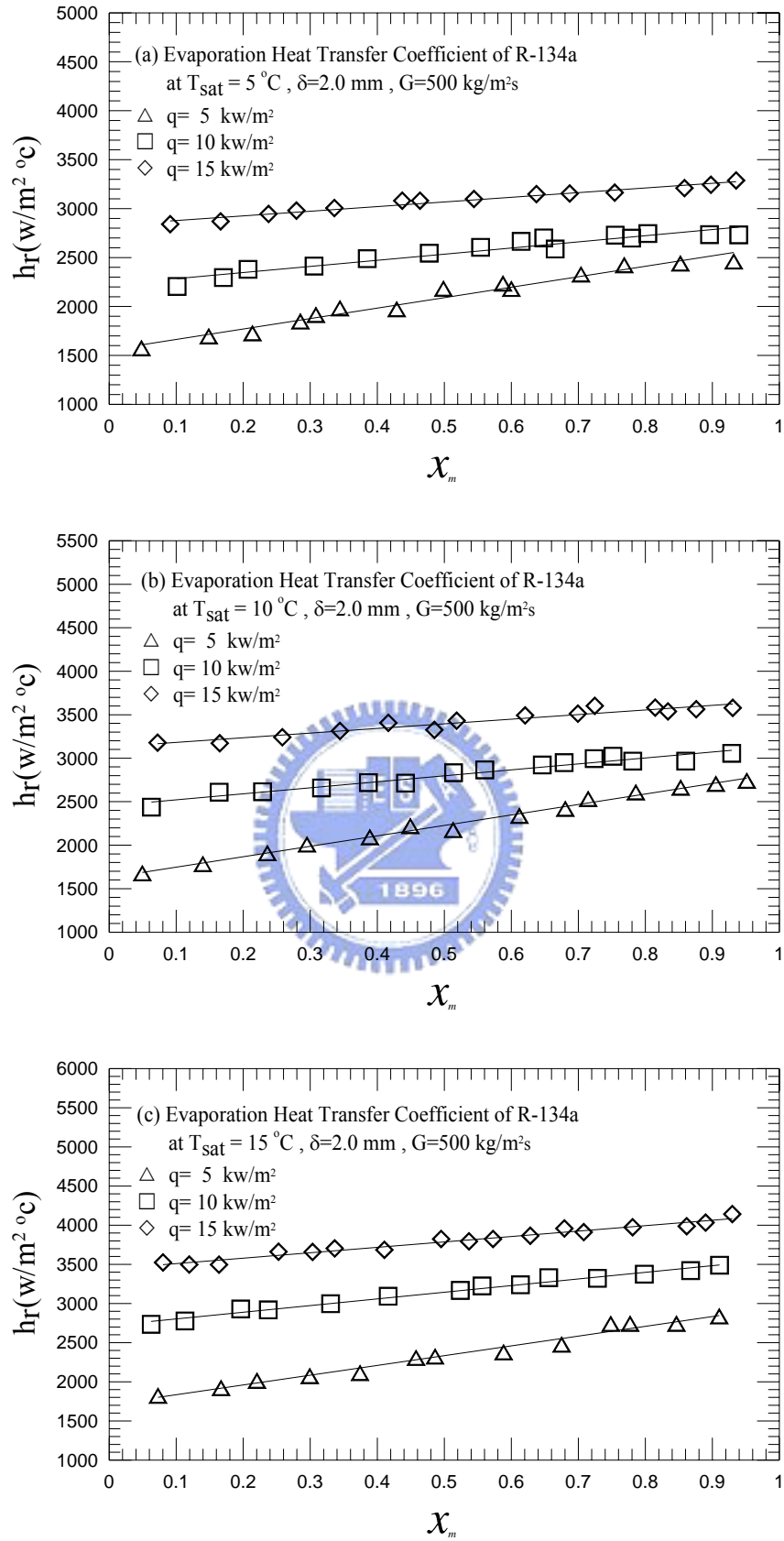


Fig. 4.11 Variations of R-134a evaporation heat transfer coefficient with vapor quality in  $\delta = 2.0\text{ mm}$  narrow duct at  $G = 500\text{ kg/m}^2\text{s}$  for various  $q$  for (a)  $T_{\text{sat}} = 5^\circ\text{C}$ , (b)  $T_{\text{sat}} = 10^\circ\text{C}$  and (c)  $T_{\text{sat}} = 15^\circ\text{C}$ .

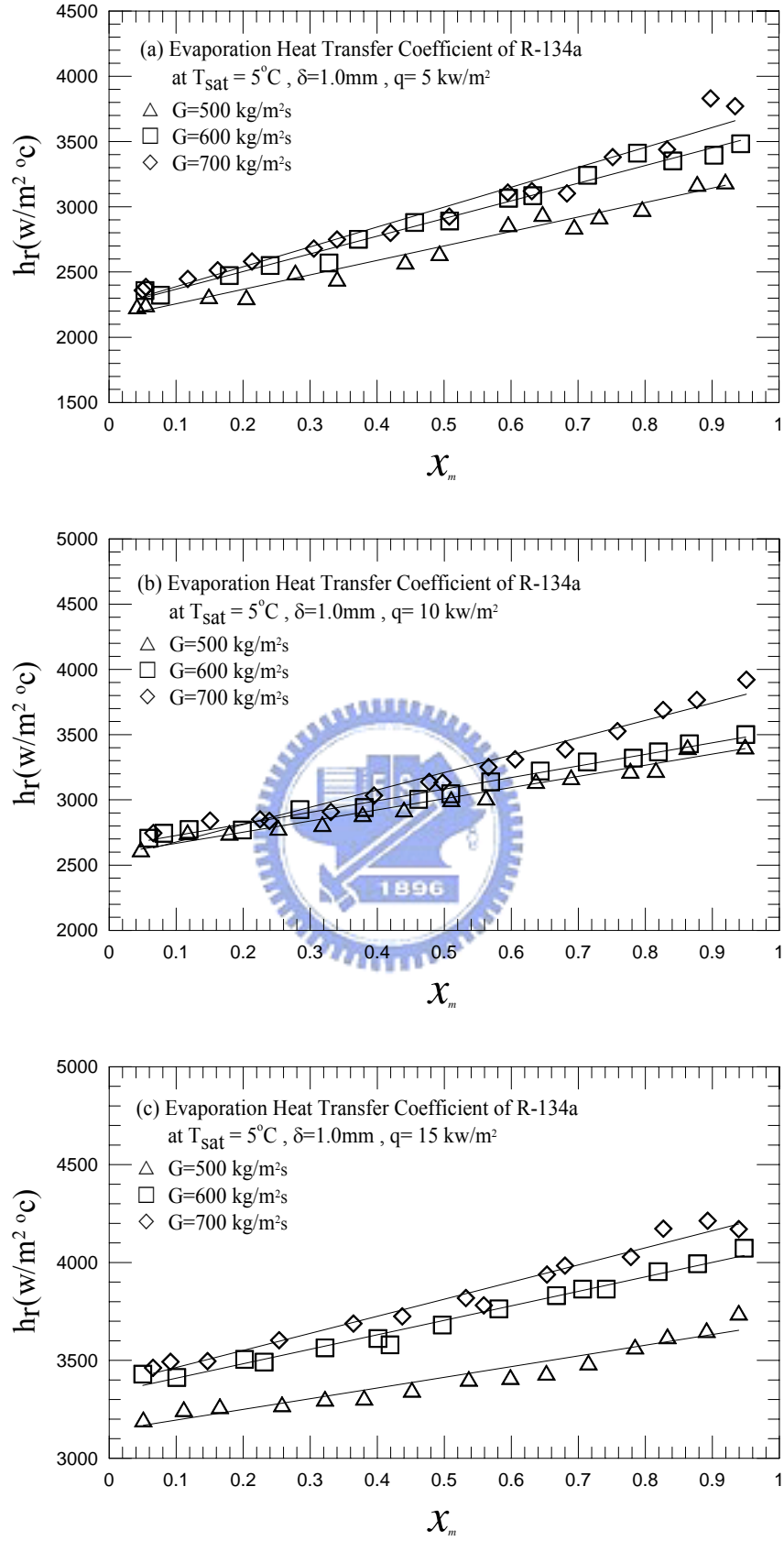


Fig. 4.12 Variations of R-134a evaporation heat transfer coefficient with vapor quality in  $\delta = 1.0\text{ mm}$  narrow duct at  $T_{\text{sat}} = 5^\circ\text{C}$  for various  $G$  for (a)  $q = 5\text{ kW/m}^2$ , (b)  $q = 10\text{ kW/m}^2$  and (c)  $q = 15\text{ kW/m}^2$ .

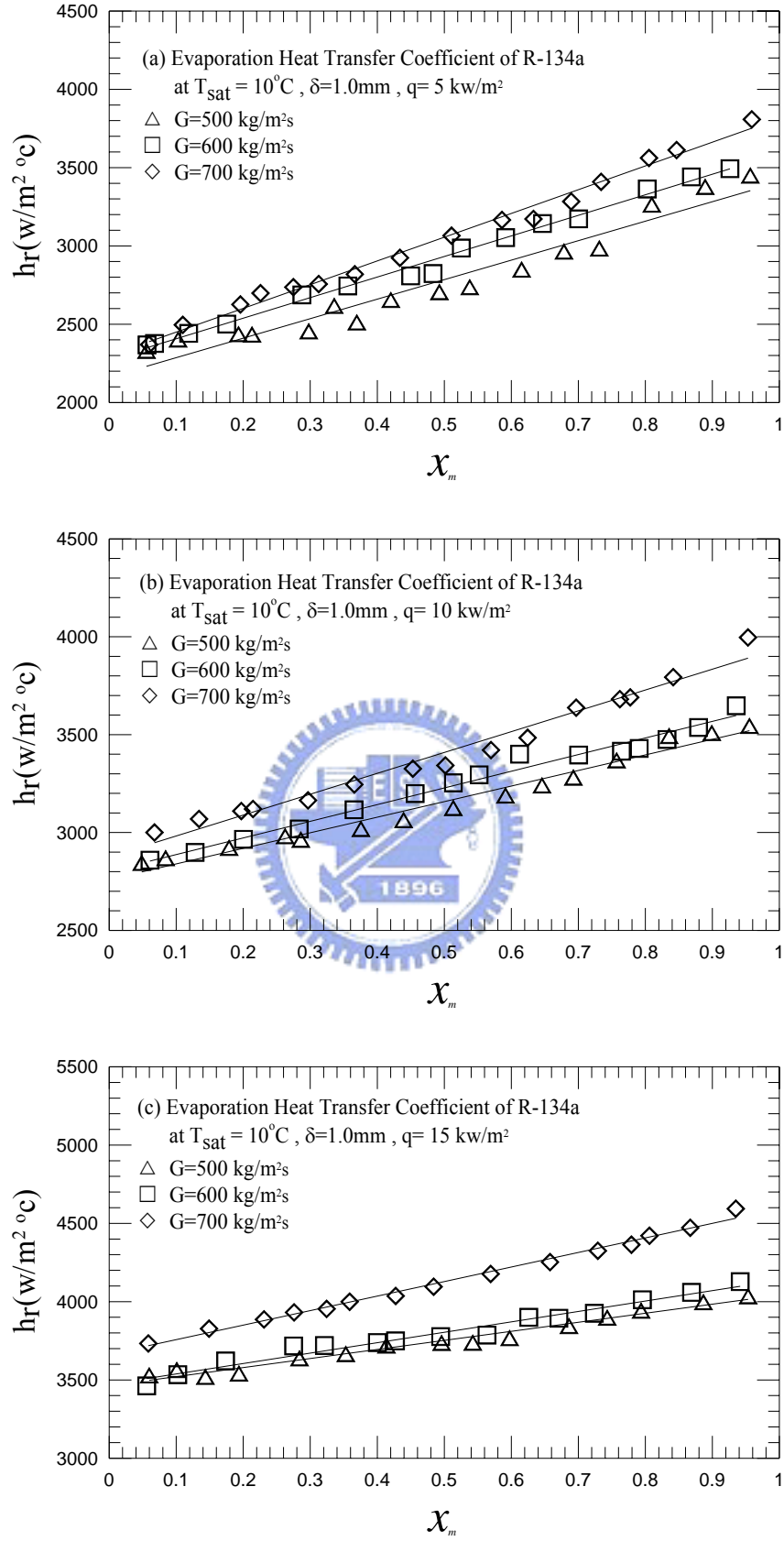


Fig. 4.13 Variations of R-134a evaporation heat transfer coefficient with vapor quality in  $\delta = 1.0\text{ mm}$  narrow duct at  $T_{\text{sat}} = 10^\circ\text{C}$  for various  $G$  for (a)  $q = 5\text{ kW/m}^2$ , (b)  $q = 10\text{ kW/m}^2$  and (c)  $q = 15\text{ kW/m}^2$ .

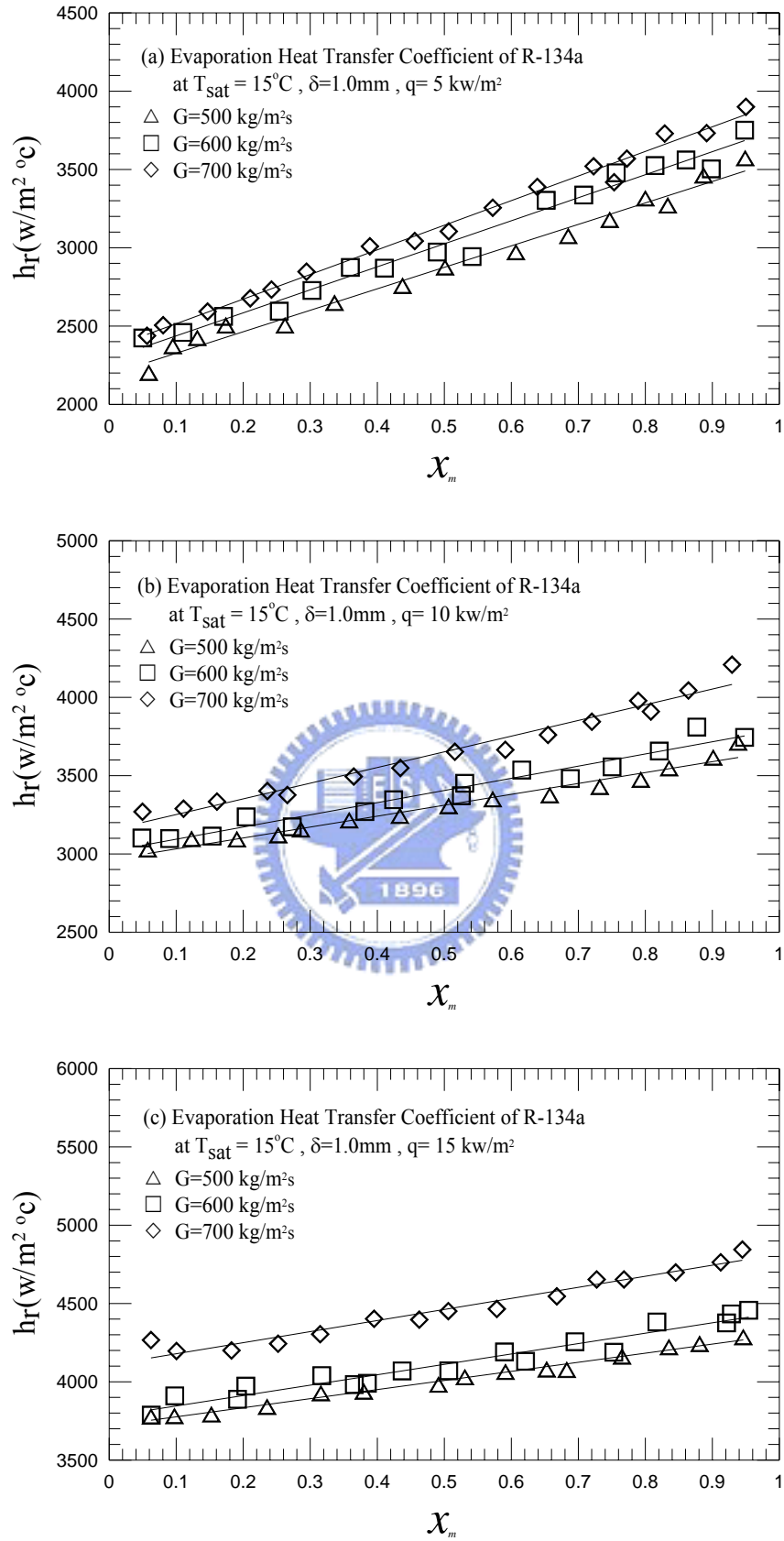


Fig. 4.14 Variations of R-134a evaporation heat transfer coefficient with vapor quality in  $\delta = 1.0 \text{ mm}$  narrow duct at  $T_{\text{sat}} = 15^\circ\text{C}$  for various  $G$  for (a)  $q = 5 \text{ kW/m}^2$ , (b)  $q = 10 \text{ kW/m}^2$  and (c)  $q = 15 \text{ kW/m}^2$ .



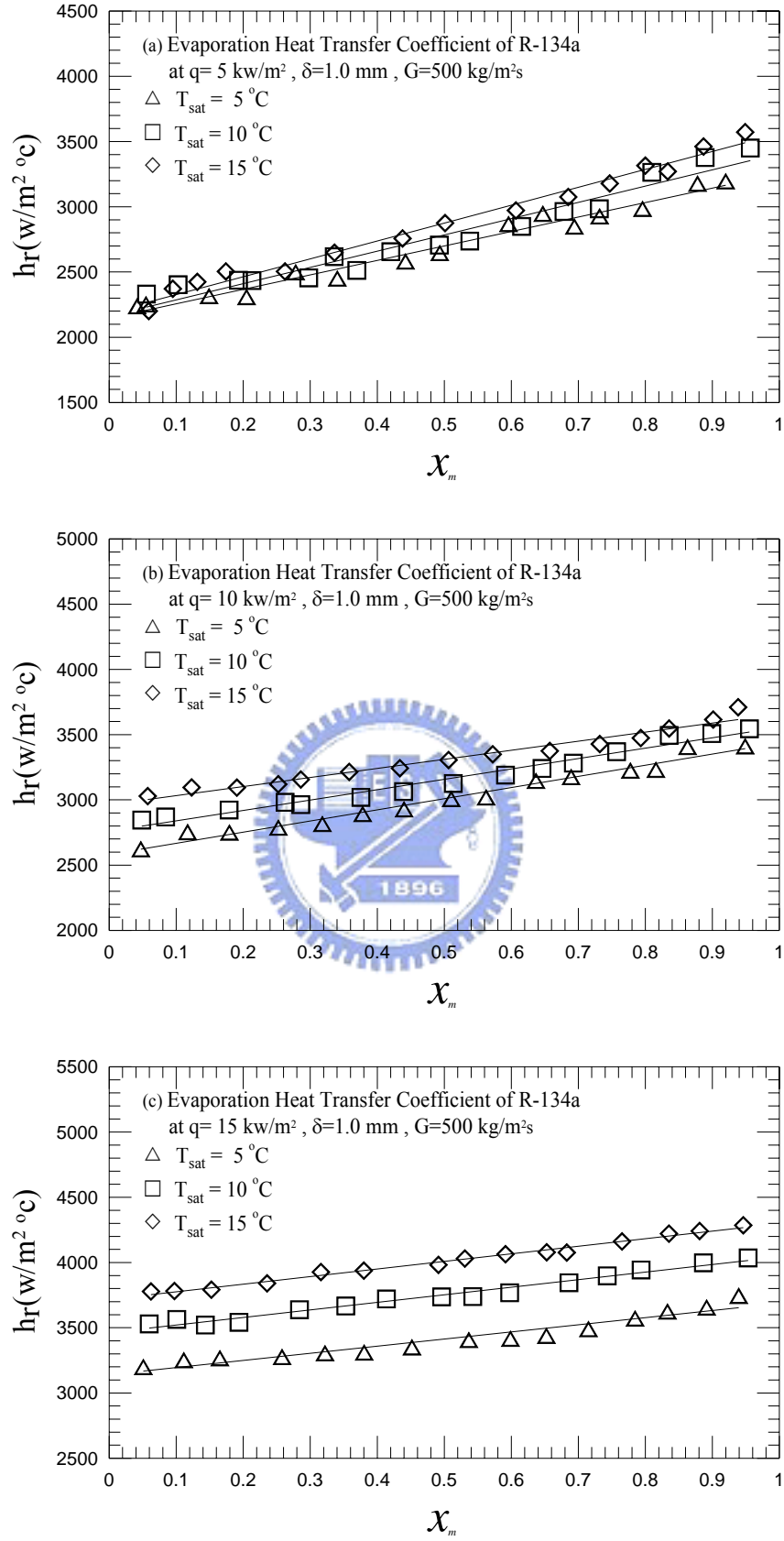


Fig. 4.15 Variations of R-134a evaporation heat transfer coefficient with vapor quality in  $\delta = 1.0 \text{ mm}$  narrow duct at  $G = 500 \text{ kg/m}^2\text{s}$  for various  $T_{\text{sat}}$  for (a)  $q = 5 \text{ kW/m}^2$ , (b)  $q = 10 \text{ kW/m}^2$  and (c)  $q = 15 \text{ kW/m}^2$ .

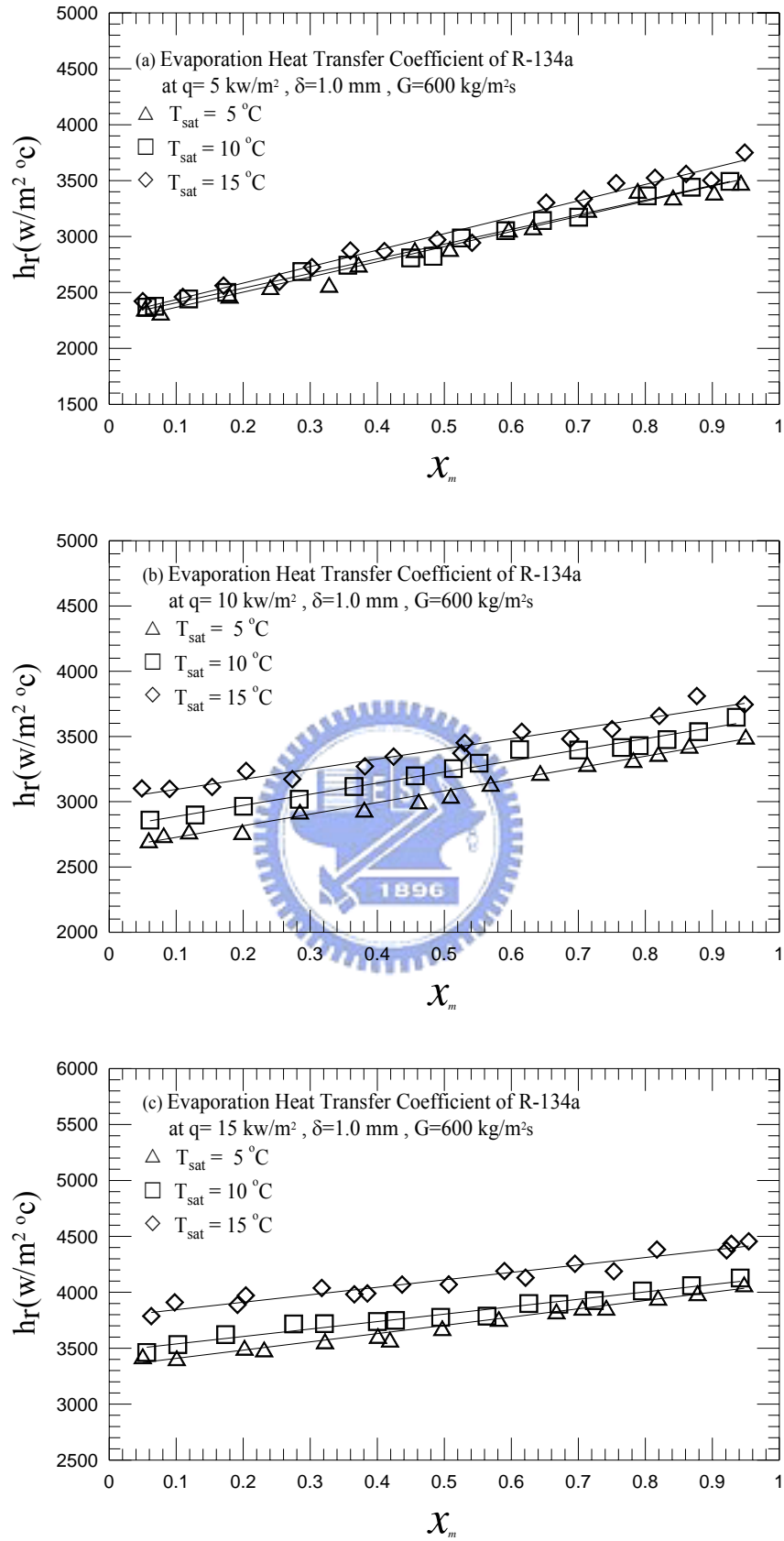


Fig. 4.16 Variations of R-134a evaporation heat transfer coefficient with vapor quality in  $\delta = 1.0 \text{ mm}$  narrow duct at  $G = 600 \text{ kg/m}^2\text{s}$  for various  $T_{\text{sat}}$  for (a)  $q = 5 \text{ kW/m}^2$ , (b)  $q = 10 \text{ kW/m}^2$  and (c)  $q = 15 \text{ kW/m}^2$ .

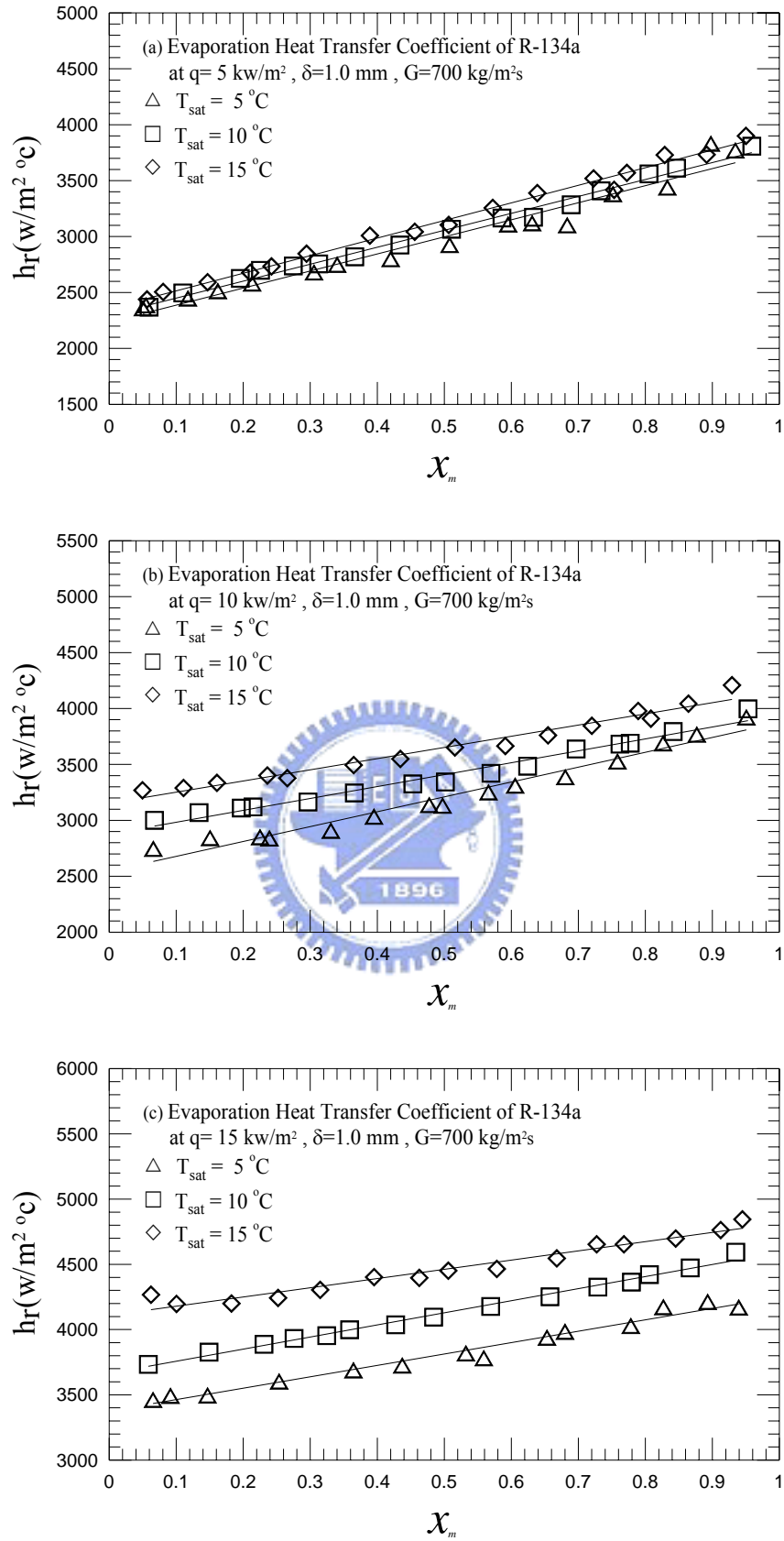


Fig. 4.17 Variations of R-134a evaporation heat transfer coefficient with vapor quality in  $\delta = 1.0 \text{ mm}$  narrow duct at  $G = 700 \text{ kg/m}^2\text{s}$  for various  $T_{\text{sat}}$  for (a)  $q = 5 \text{ kW/m}^2$ , (b)  $q = 10 \text{ kW/m}^2$  and (c)  $q = 15 \text{ kW/m}^2$ .

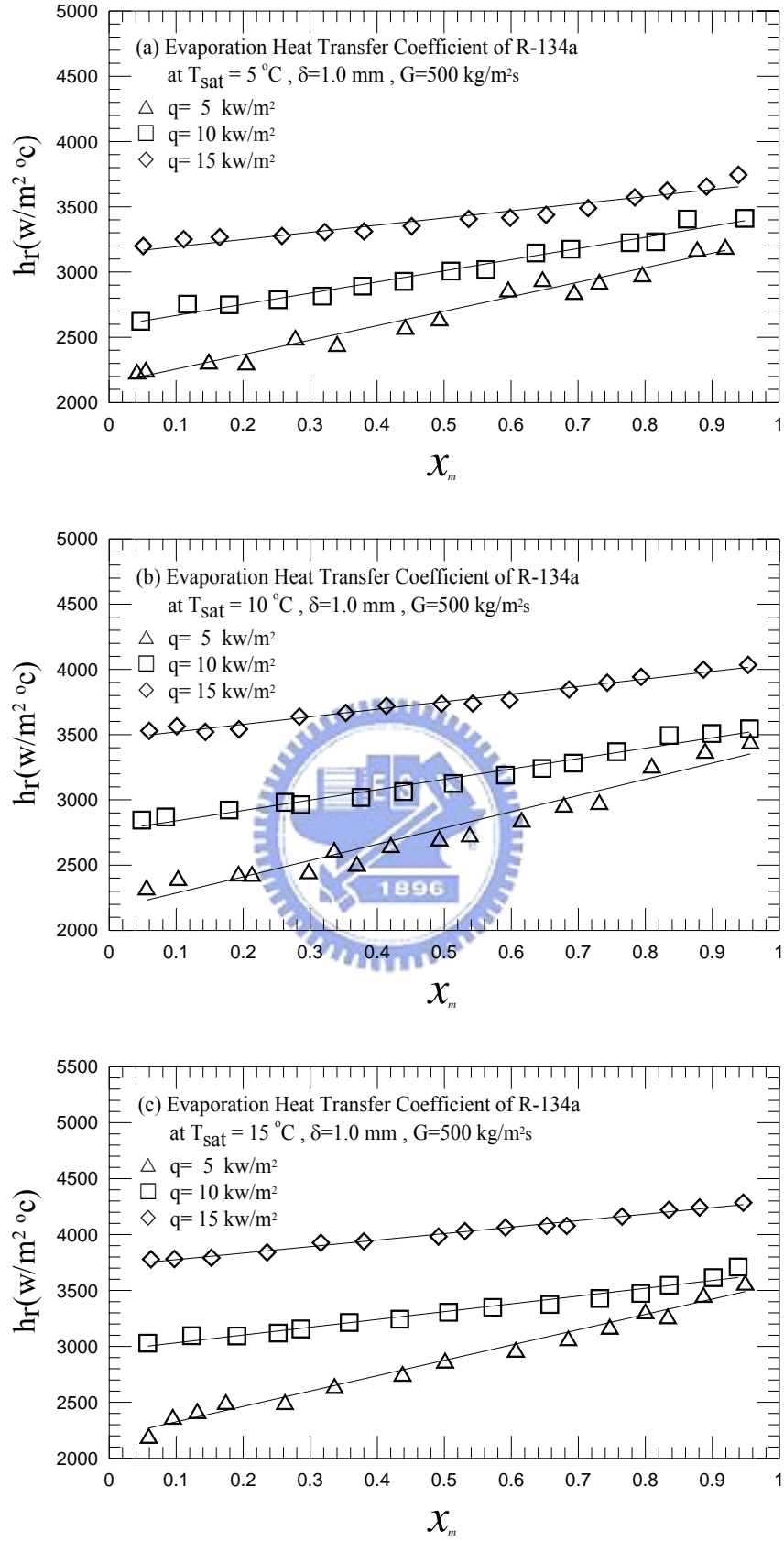


Fig. 4.18 Variations of R-134a evaporation heat transfer coefficient with vapor quality in  $\delta = 1.0\text{ mm}$  narrow duct at  $G = 500\text{ kg/m}^2\text{s}$  for various  $q$  for (a)  $T_{\text{sat}} = 5^\circ\text{C}$ , (b)  $T_{\text{sat}} = 10^\circ\text{C}$  and (c)  $T_{\text{sat}} = 15^\circ\text{C}$ .

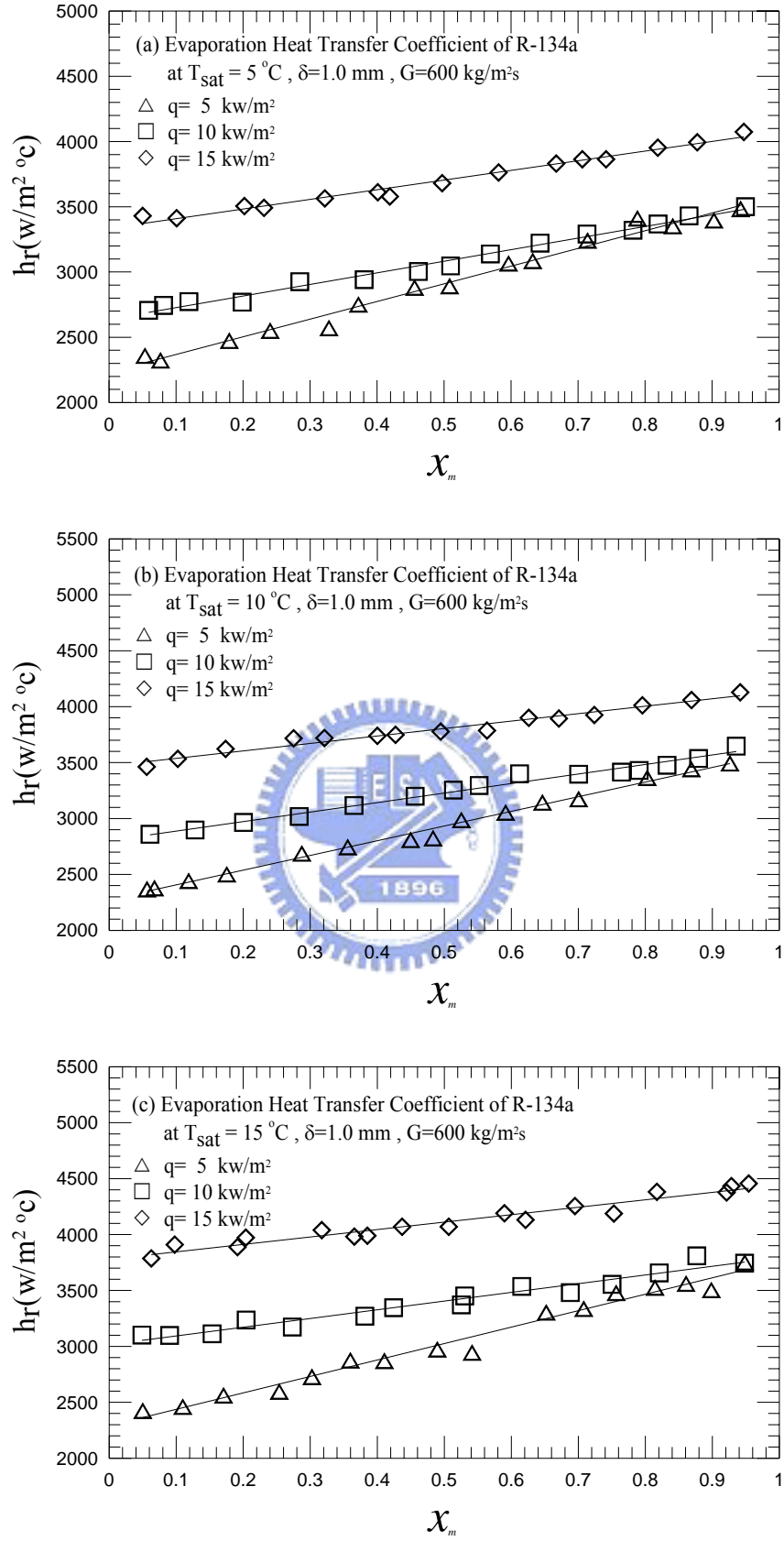


Fig. 4.19 Variations of R-134a evaporation heat transfer coefficient with vapor quality in  $\delta = 1.0\text{ mm}$  narrow duct at  $G = 600\text{ kg/m}^2\text{s}$  for various  $q$  for (a)  $T_{\text{sat}} = 5^\circ\text{C}$ , (b)  $T_{\text{sat}} = 10^\circ\text{C}$  and (c)  $T_{\text{sat}} = 15^\circ\text{C}$ .

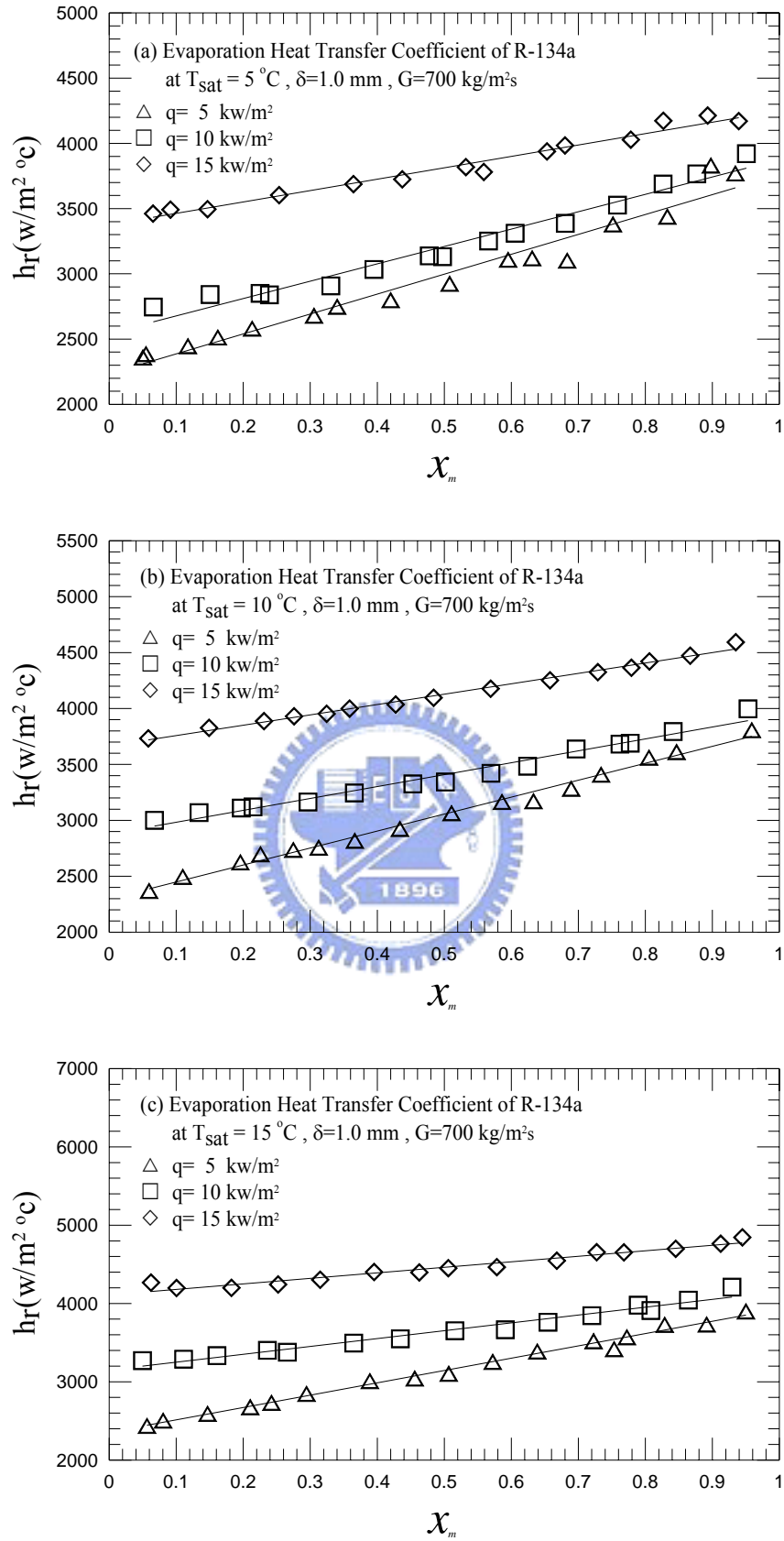


Fig. 4.20 Variations of R-134a evaporation heat transfer coefficient with vapor quality in  $\delta = 1.0\text{ mm}$  narrow duct at  $G = 700\text{ kg/m}^2\text{s}$  for various  $q$  for (a)  $T_{\text{sat}} = 5^\circ\text{C}$ , (b)  $T_{\text{sat}} = 10^\circ\text{C}$  and (c)  $T_{\text{sat}} = 15^\circ\text{C}$ .

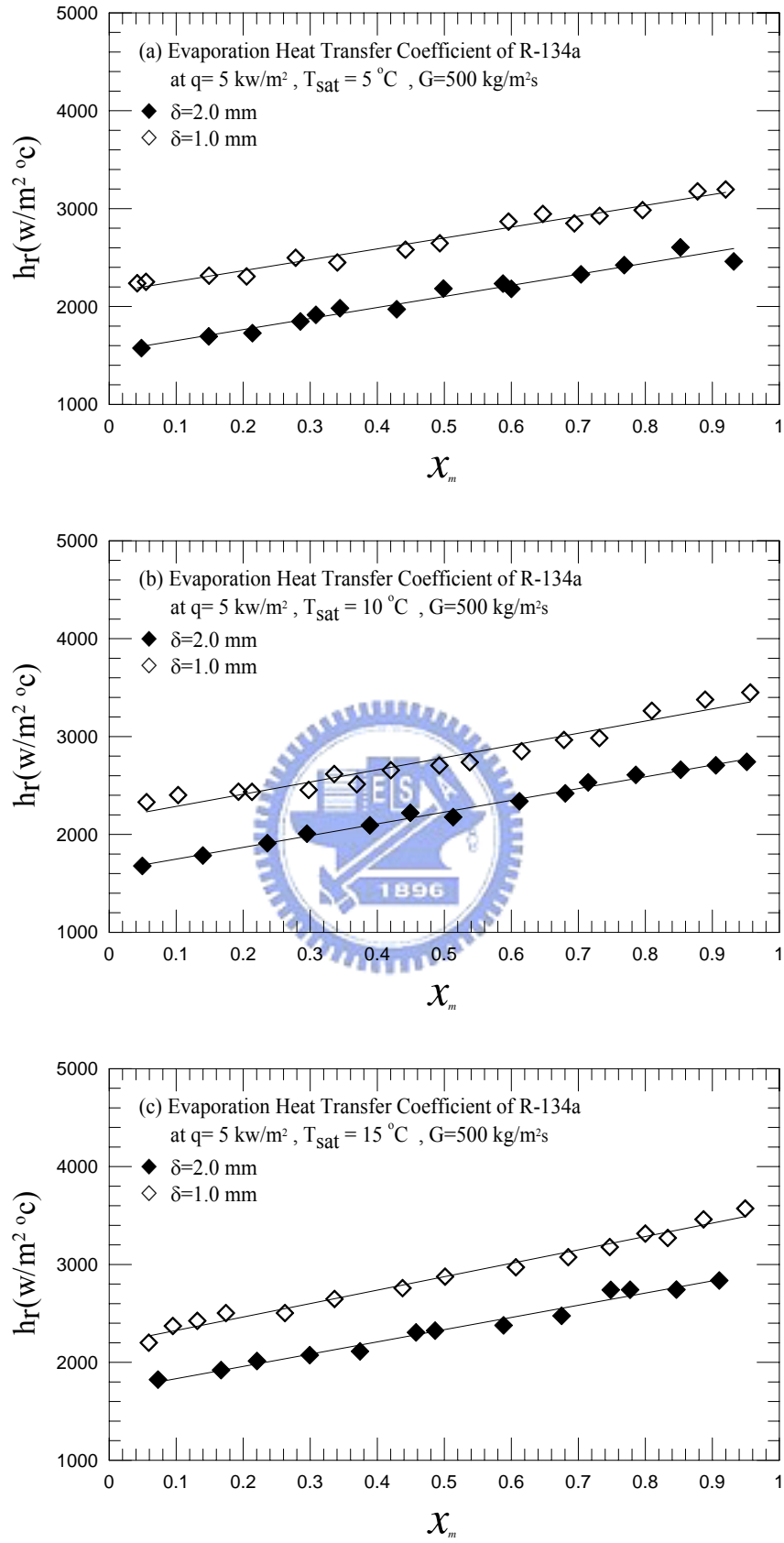


Fig. 4.21 Variations of R-134a evaporation heat transfer coefficient with vapor quality at  $q = 5 \text{ kW/m}^2$  and  $G = 500 \text{ kg/m}^2\text{s}$  for various  $\delta$  for (a)  $T_{\text{sat}} = 5^\circ\text{C}$ , (b)  $T_{\text{sat}} = 10^\circ\text{C}$  and (c)  $T_{\text{sat}} = 15^\circ\text{C}$ .

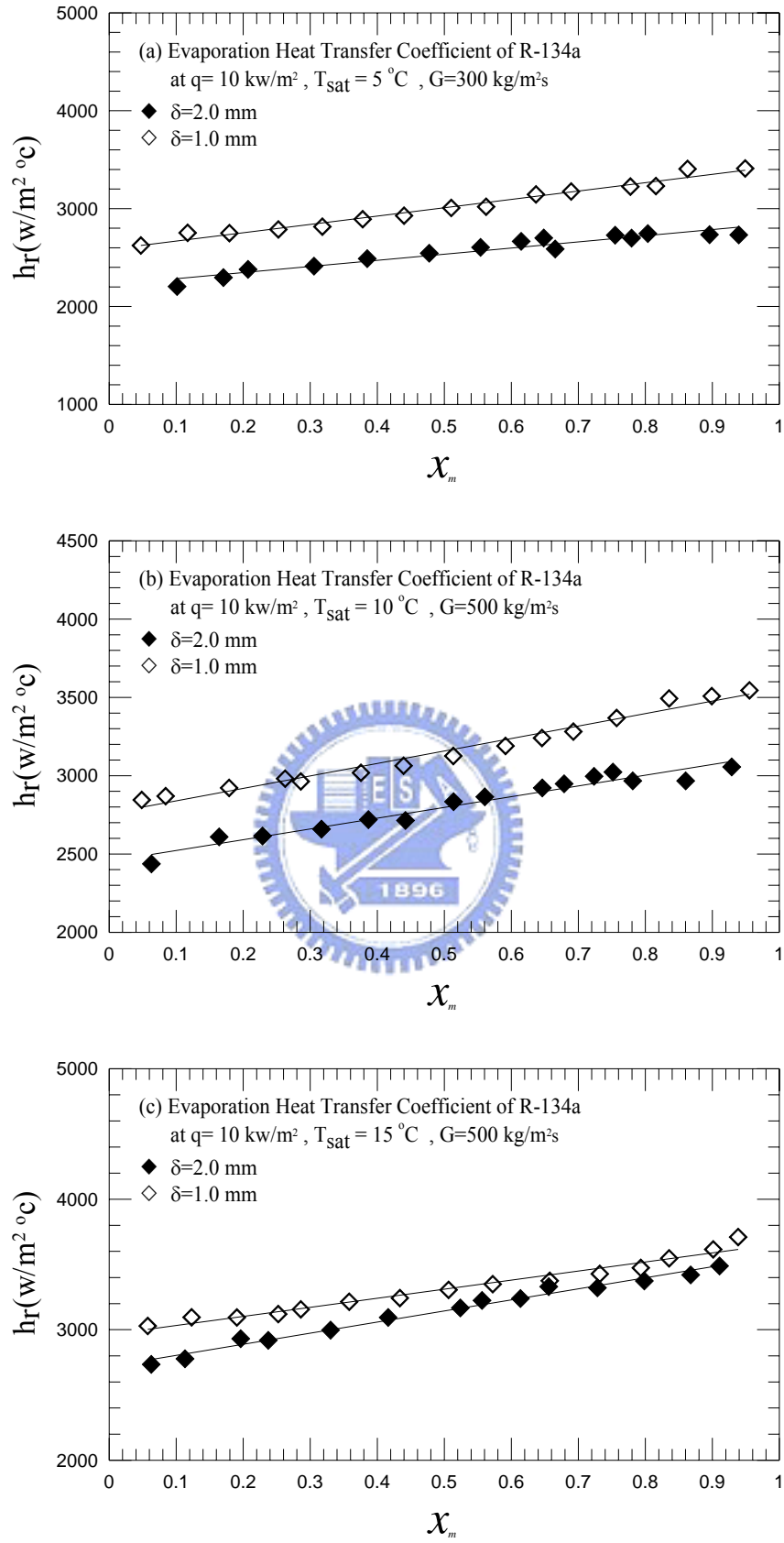


Fig. 4.22 Variations of R-134a evaporation heat transfer coefficient with vapor quality at  $q = 10 \text{ kW/m}^2$  and  $G = 500 \text{ kg/m}^2\text{s}$  for various  $\delta$  for (a)  $T_{\text{sat}} = 5^\circ\text{C}$ , (b)  $T_{\text{sat}} = 10^\circ\text{C}$  and (c)  $T_{\text{sat}} = 15^\circ\text{C}$ .



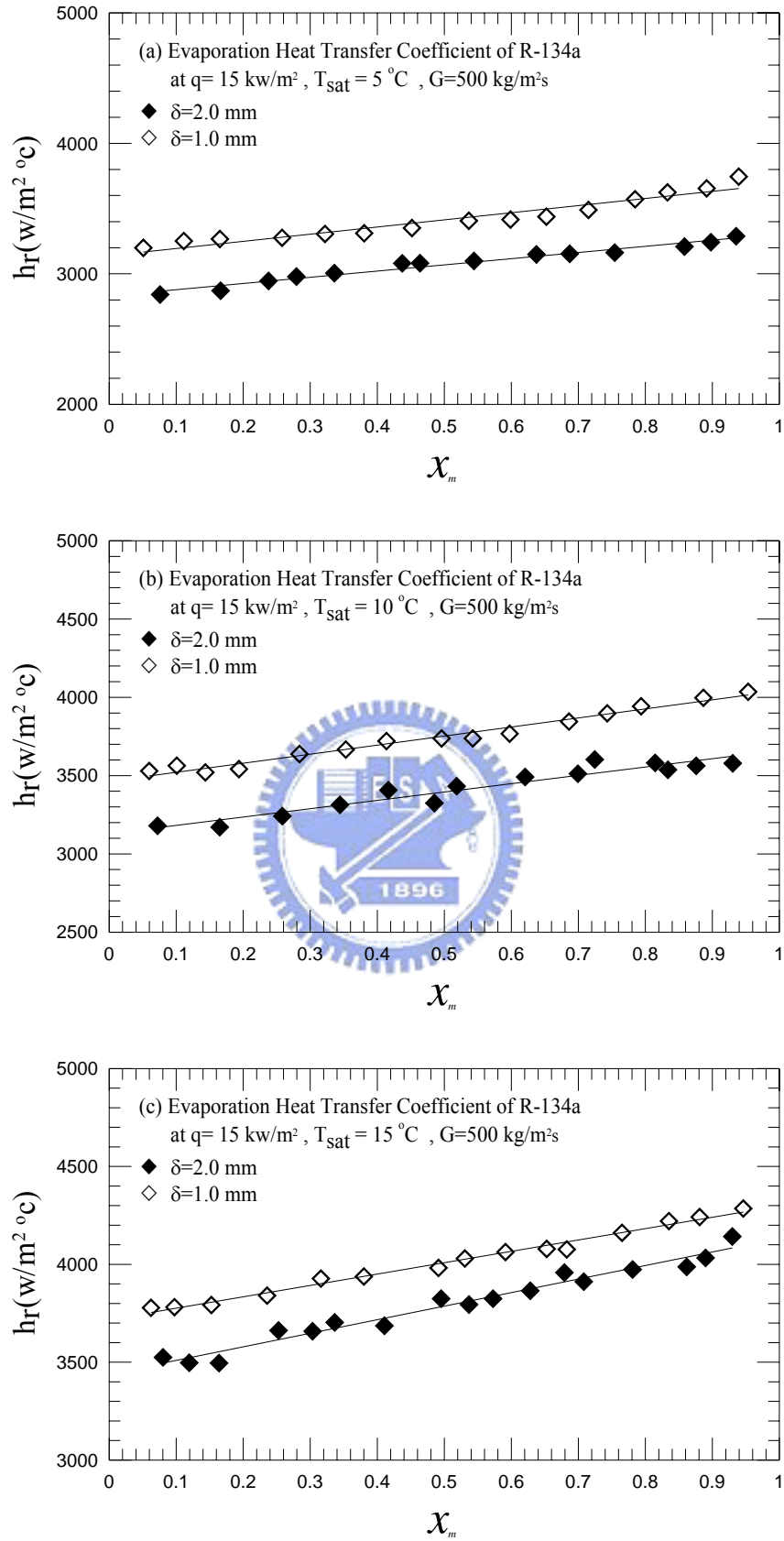


Fig. 4.23 Variations of R-134a evaporation heat transfer coefficient with vapor quality at  $q = 15 \text{ kW/m}^2$  and  $G = 500 \text{ kg/m}^2\text{s}$  for various  $\delta$  for (a)  $T_{\text{sat}} = 5^\circ\text{C}$ , (b)  $T_{\text{sat}} = 10^\circ\text{C}$  and (c)  $T_{\text{sat}} = 15^\circ\text{C}$ .

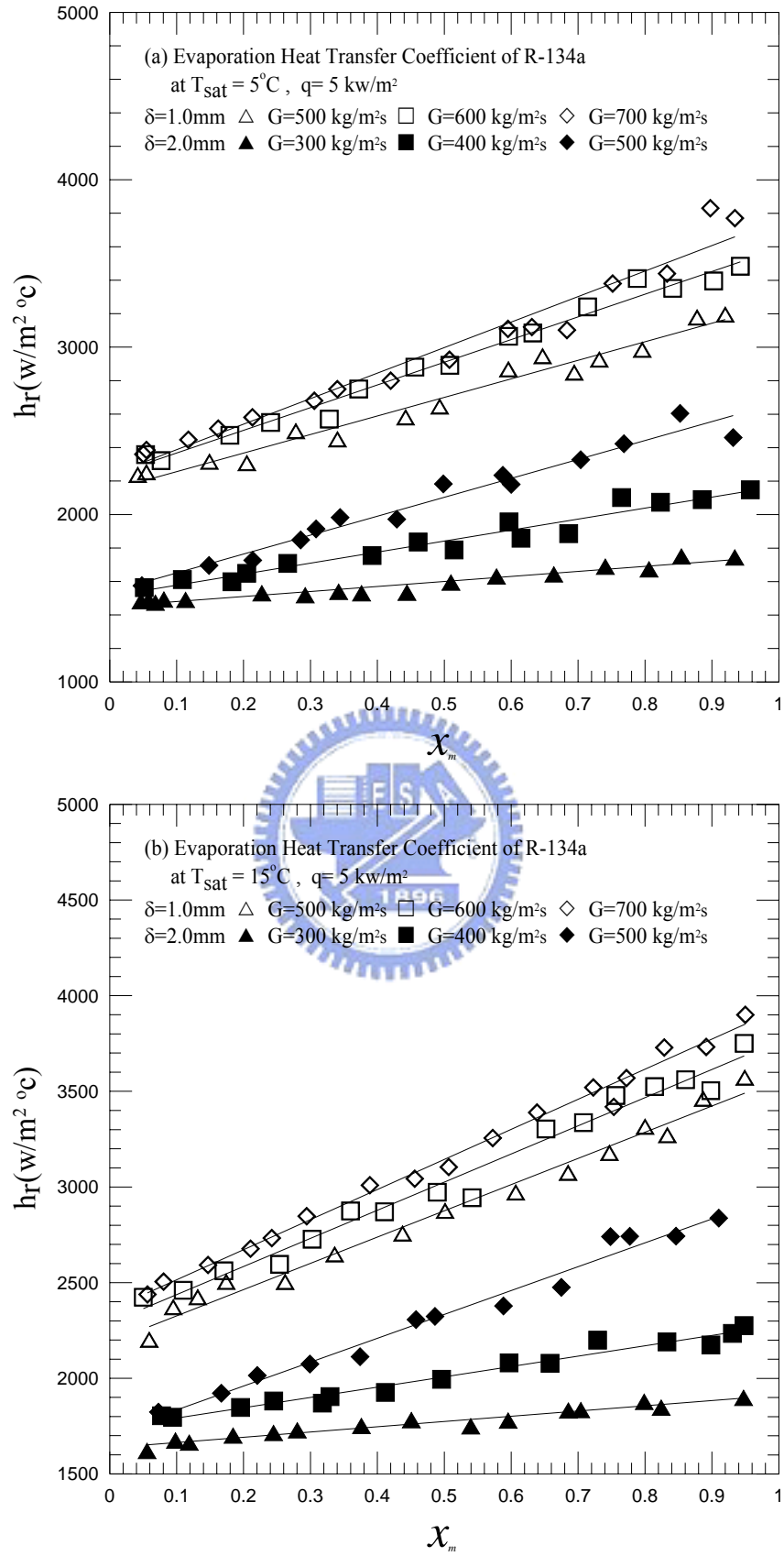


Fig. 4.24 Variations of R-134a evaporation heat transfer coefficient with vapor quality at  $q = 5 \text{ kW/m}^2$ ,  $\delta = 1.0 \text{ mm}$  and  $\delta = 2.0 \text{ mm}$  for various  $G$  for (a)  $T_{\text{sat}} = 5^\circ\text{C}$  and (b)  $T_{\text{sat}} = 15^\circ\text{C}$ .

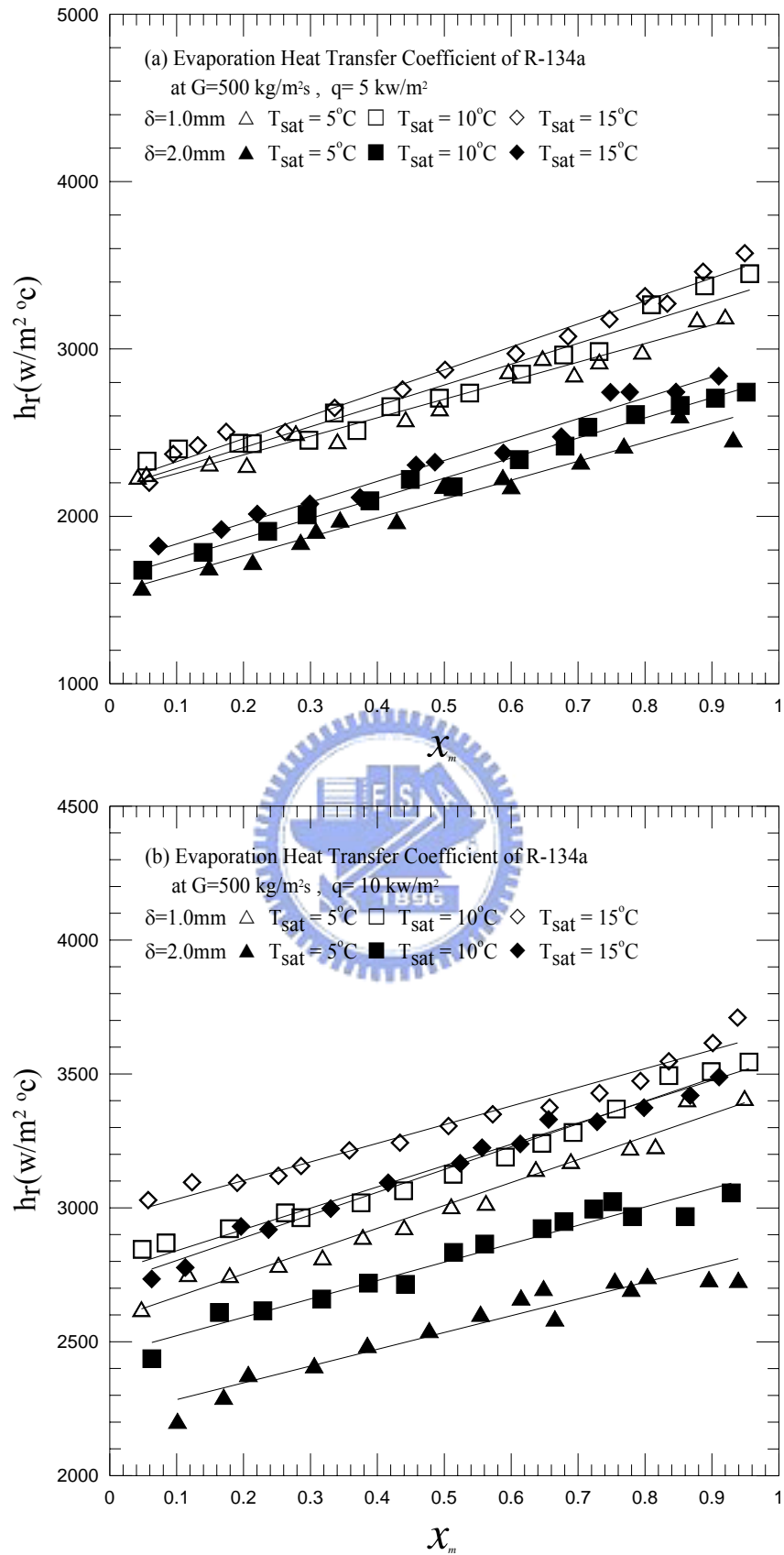


Fig. 4.25 Variations of R-134a evaporation heat transfer coefficient with vapor quality at  $G=500 \text{ kg/m}^2\text{s}$ ,  $\delta=1.0 \text{ mm}$  and  $\delta=2.0 \text{ mm}$  for various  $T_{\text{sat}}$  for (a)  $q=5 \text{ kW/m}^2$  and (b)  $q=10 \text{ kW/m}^2$ .

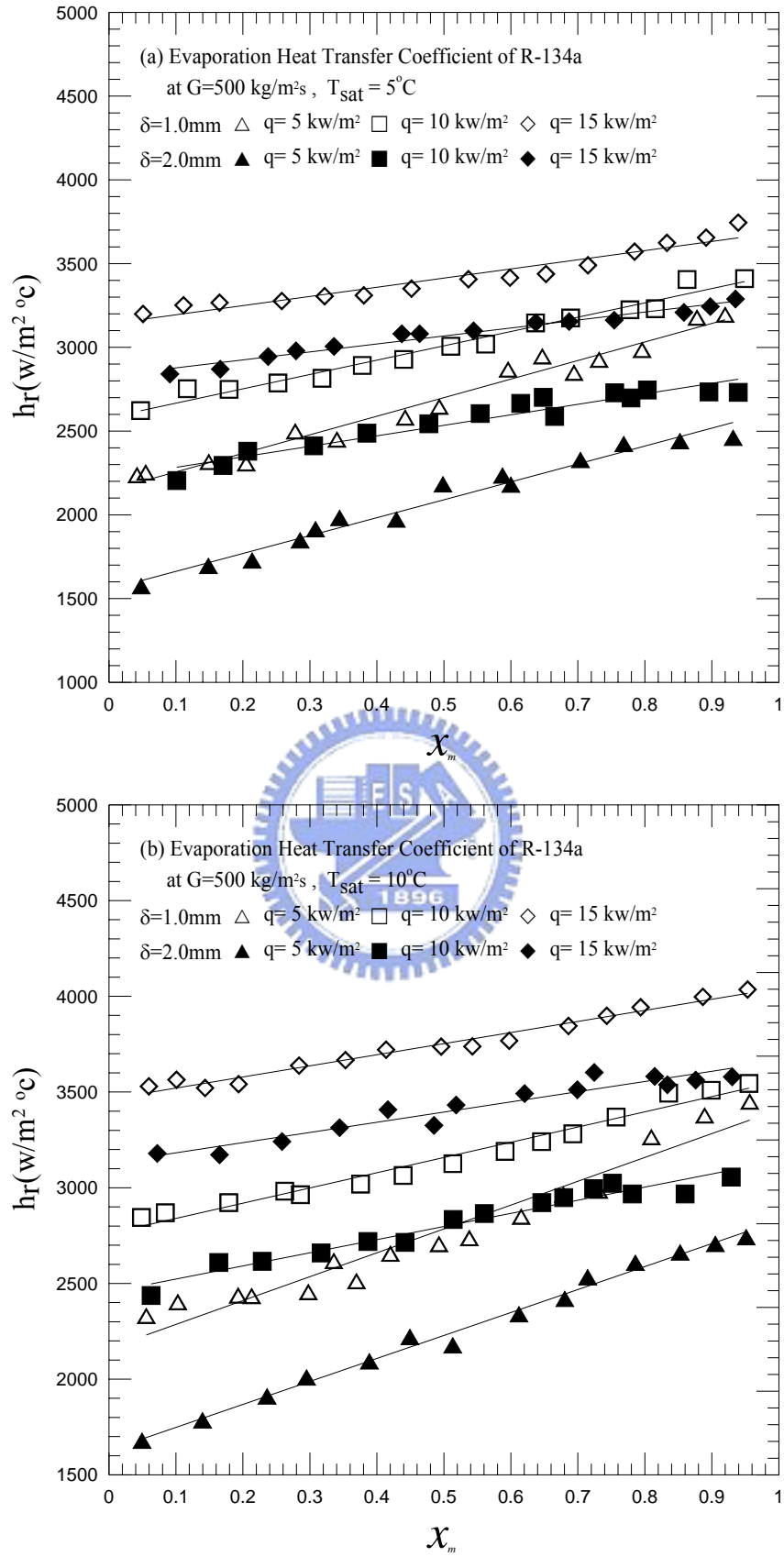


Fig. 4.26 Variations of R-134a evaporation heat transfer coefficient with vapor quality at  $G=500 \text{ kg/m}^2\text{s}$ ,  $\delta = 1.0 \text{ mm}$  and  $\delta = 2.0 \text{ mm}$  for various  $q$  for (a)  $T_{\text{sat}}=5^\circ\text{C}$ , (b)  $T_{\text{sat}}=10^\circ\text{C}$  and (c)  $T_{\text{sat}}=15^\circ\text{C}$ .

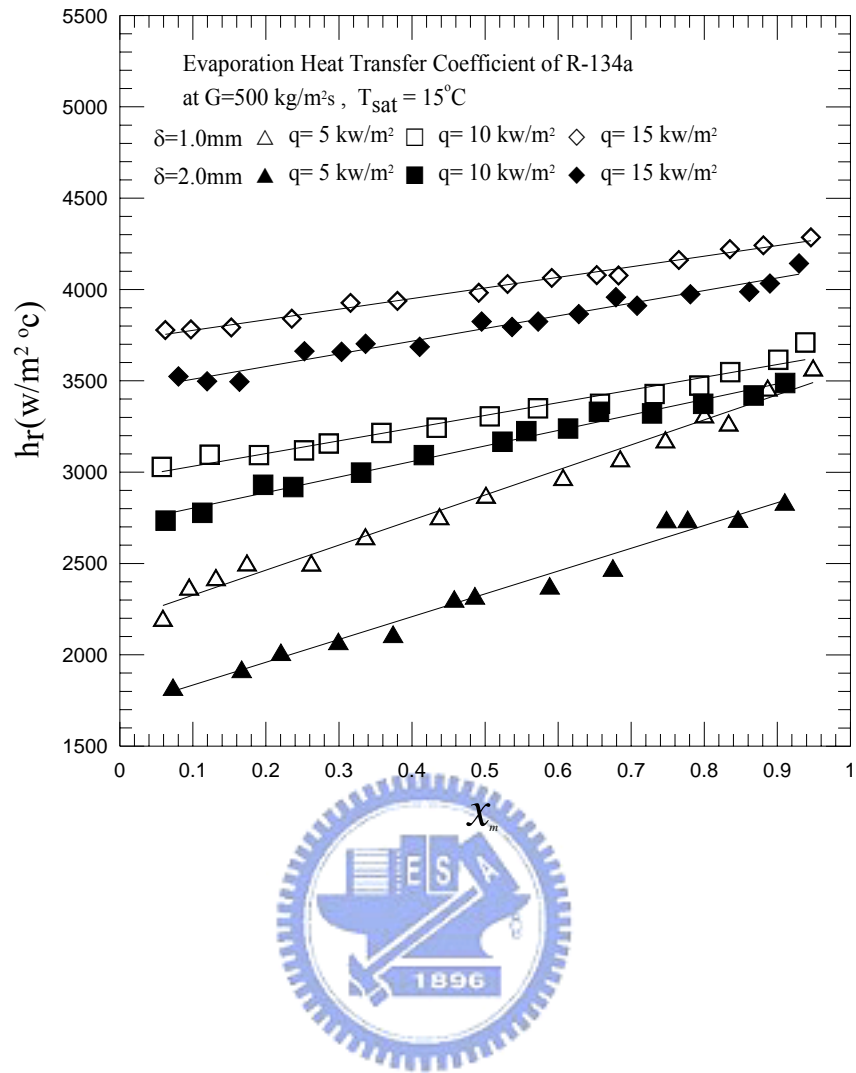


Fig. 4.26 Continued.

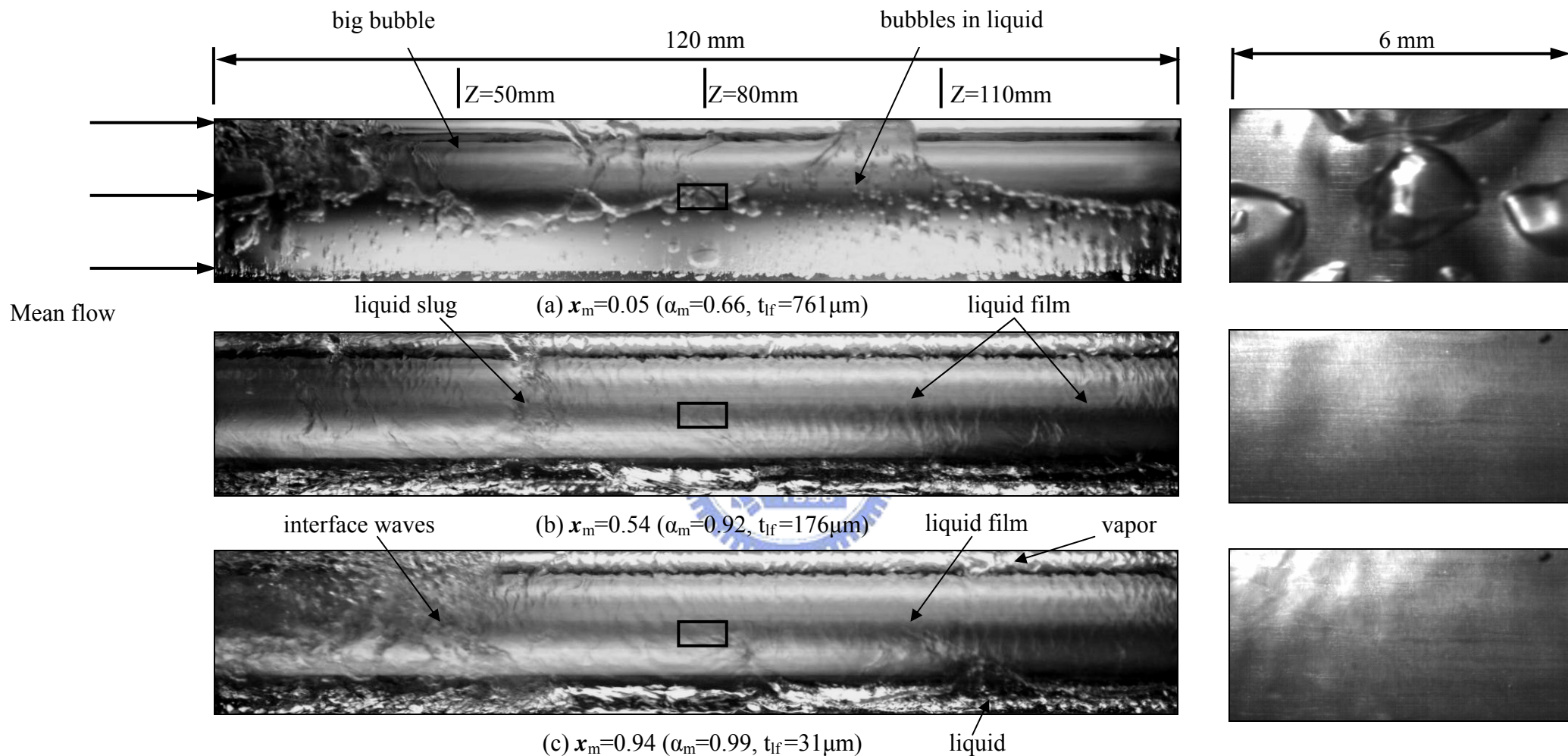


Fig.4.27 Photos of flow in the evaporation of R-134a in the entire duct and a small region around middle axial location at  $G=300 \text{ kg/m}^2\text{s}$ ,  $T_{\text{sat}} = 15^\circ\text{C}$ ,  $\delta = 2.0 \text{ mm}$ ,  $q = 5 \text{ kW/m}^2$  for (a)  $x_m = 0.05$ , (b)  $x_m = 0.54$  and (c)  $x_m = 0.94$ .

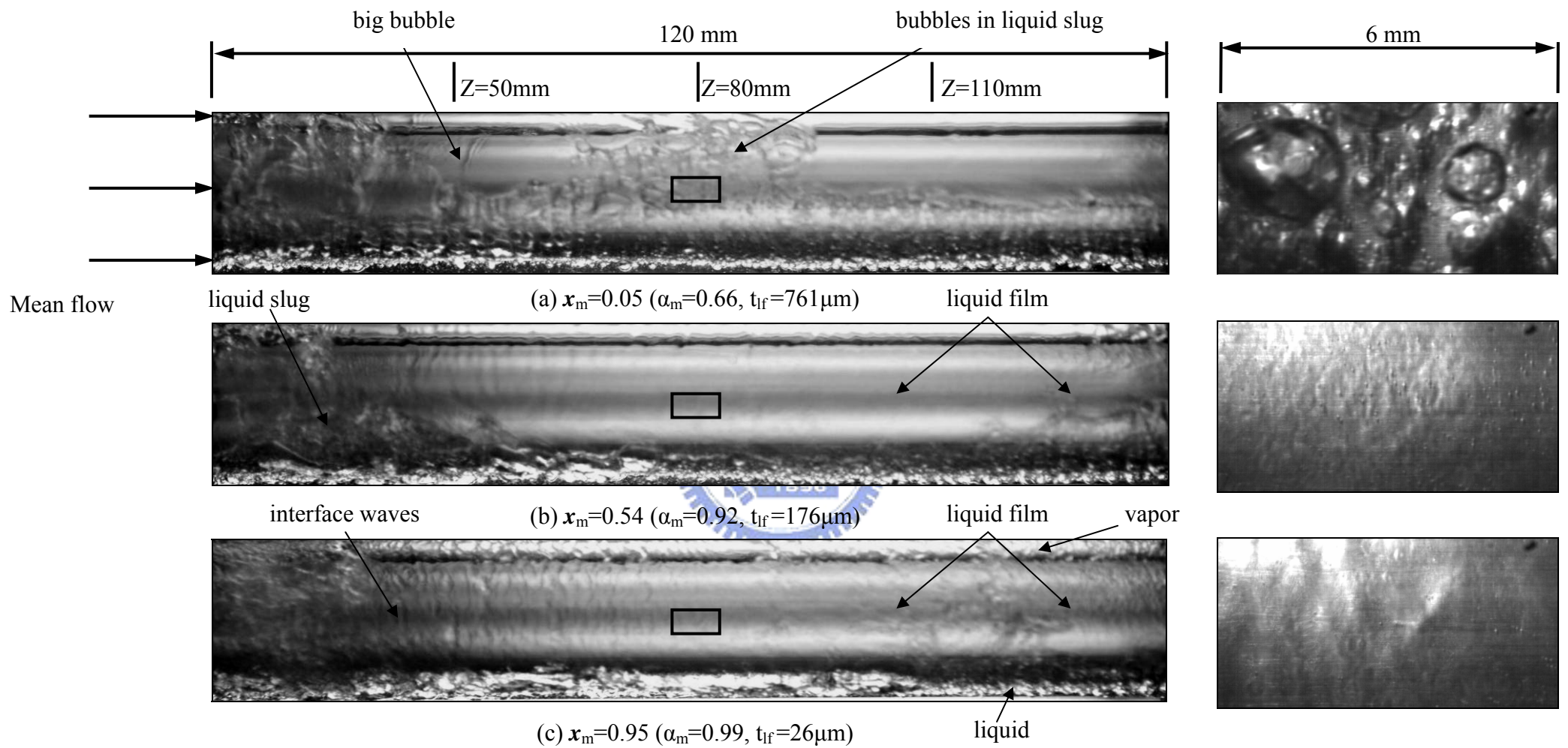


Fig.4.28 Photos of flow in the evaporation of R-134a in the entire duct and a small region around middle axial location at  $G=300\text{ kg/m}^2\text{s}$ ,  $T_{\text{sat}} = 15^\circ\text{C}$ ,  $\delta = 2.0\text{ mm}$ ,  $q = 15\text{ kW/m}^2$  for (a)  $x_m = 0.05$ , (b)  $x_m = 0.54$  and (c)  $x_m = 0.95$ .



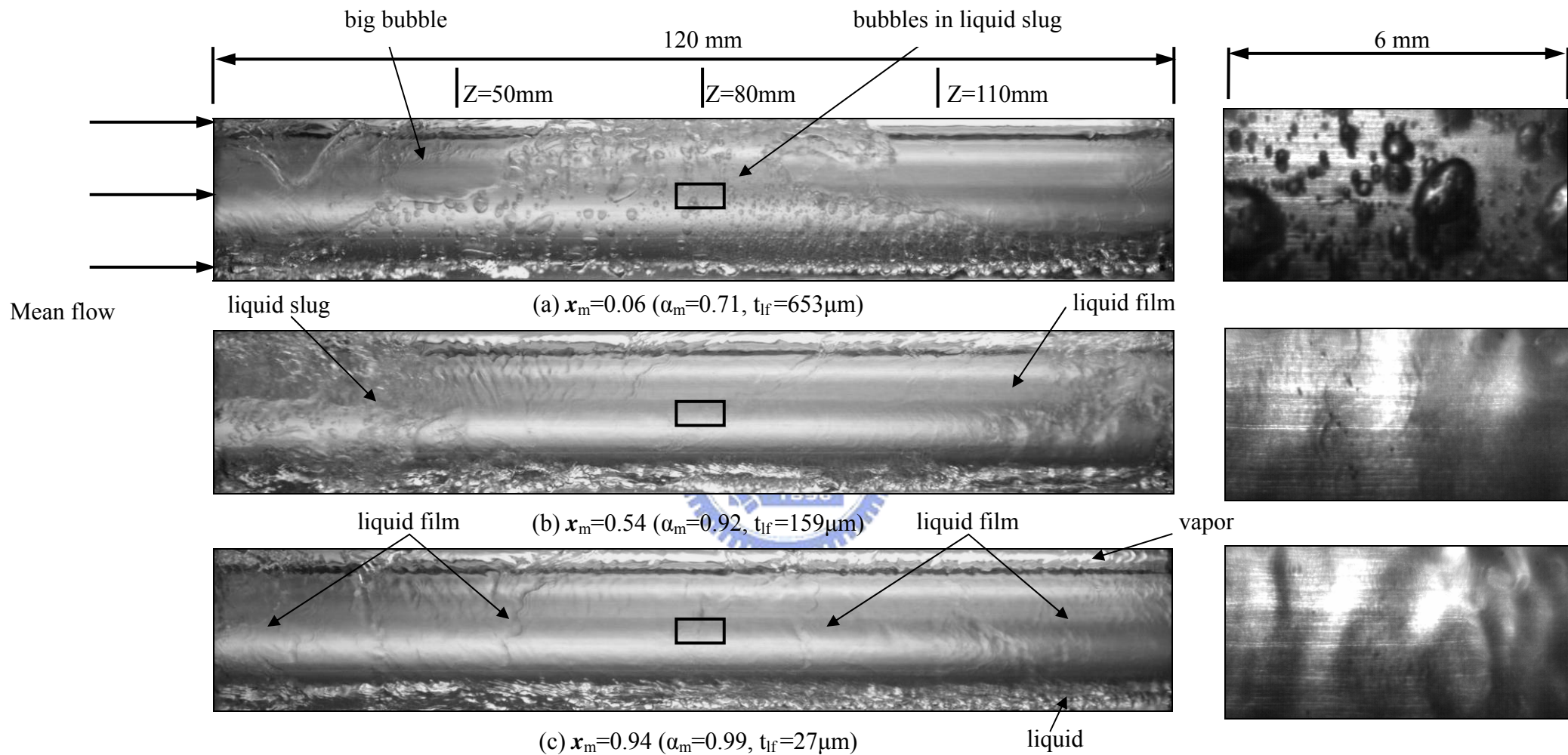


Fig.4.29 Photos of flow in the evaporation of R-134a in the entire duct and a small region around middle axial location at  $G=300 \text{ kg/m}^2\text{s}$ ,  $T_{\text{sat}} = 5^\circ\text{C}$ ,  $\delta = 2.0 \text{ mm}$ ,  $q = 15 \text{ kW/m}^2$  for (a)  $x_m = 0.06$ , (b)  $x_m = 0.50$  and (c)  $x_m = 0.94$ .



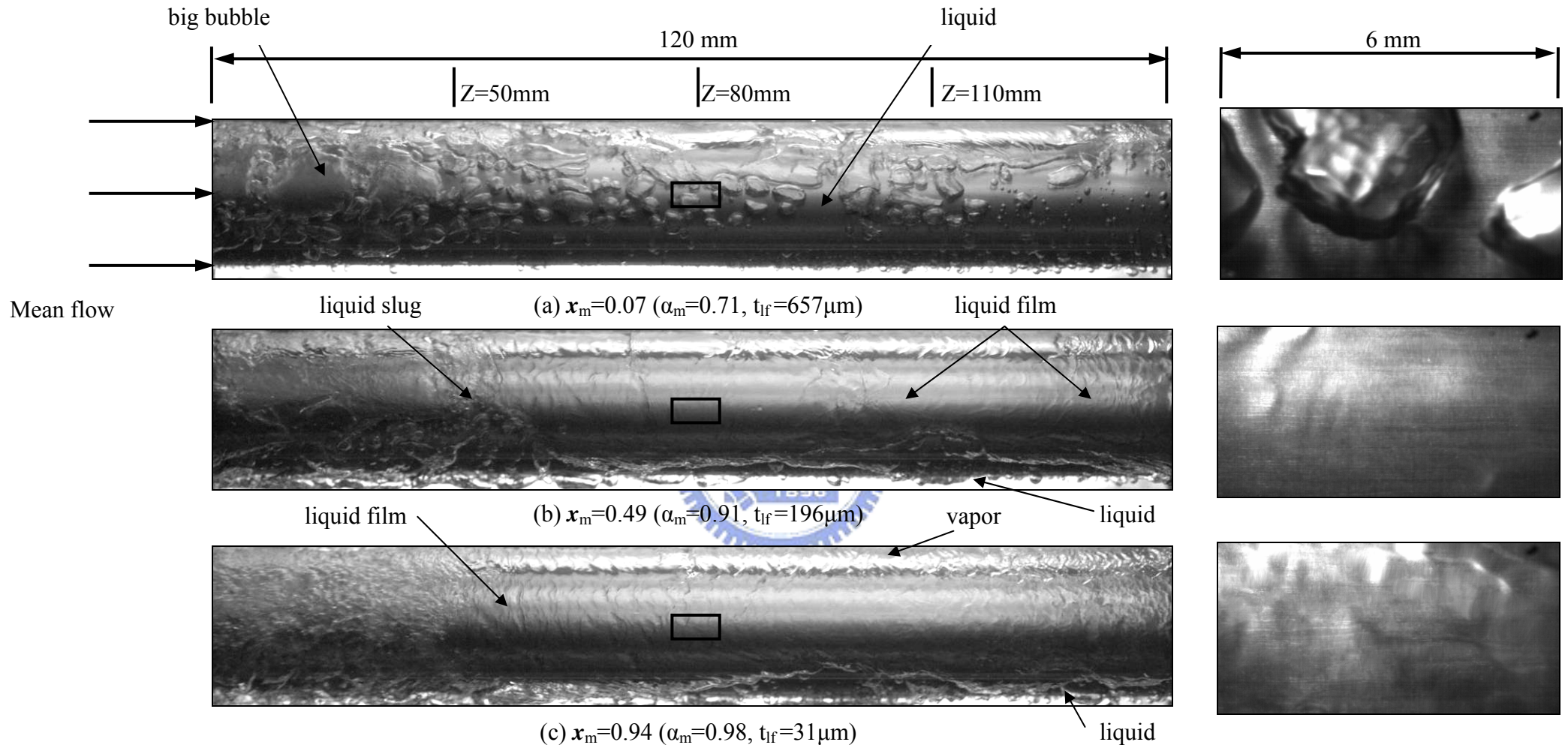


Fig.4.30 Photos of flow in the evaporation of R-134a in the entire duct and a small region around middle axial location at  $G=400 \text{ kg/m}^2\text{s}$ ,  $T_{\text{sat}} = 15^\circ\text{C}$ ,  $\delta = 2.0 \text{ mm}$ ,  $q = 5 \text{ kW/m}^2$  for (a)  $x_m = 0.07$ , (b)  $x_m = 0.49$  and (c)  $x_m = 0.94$ .

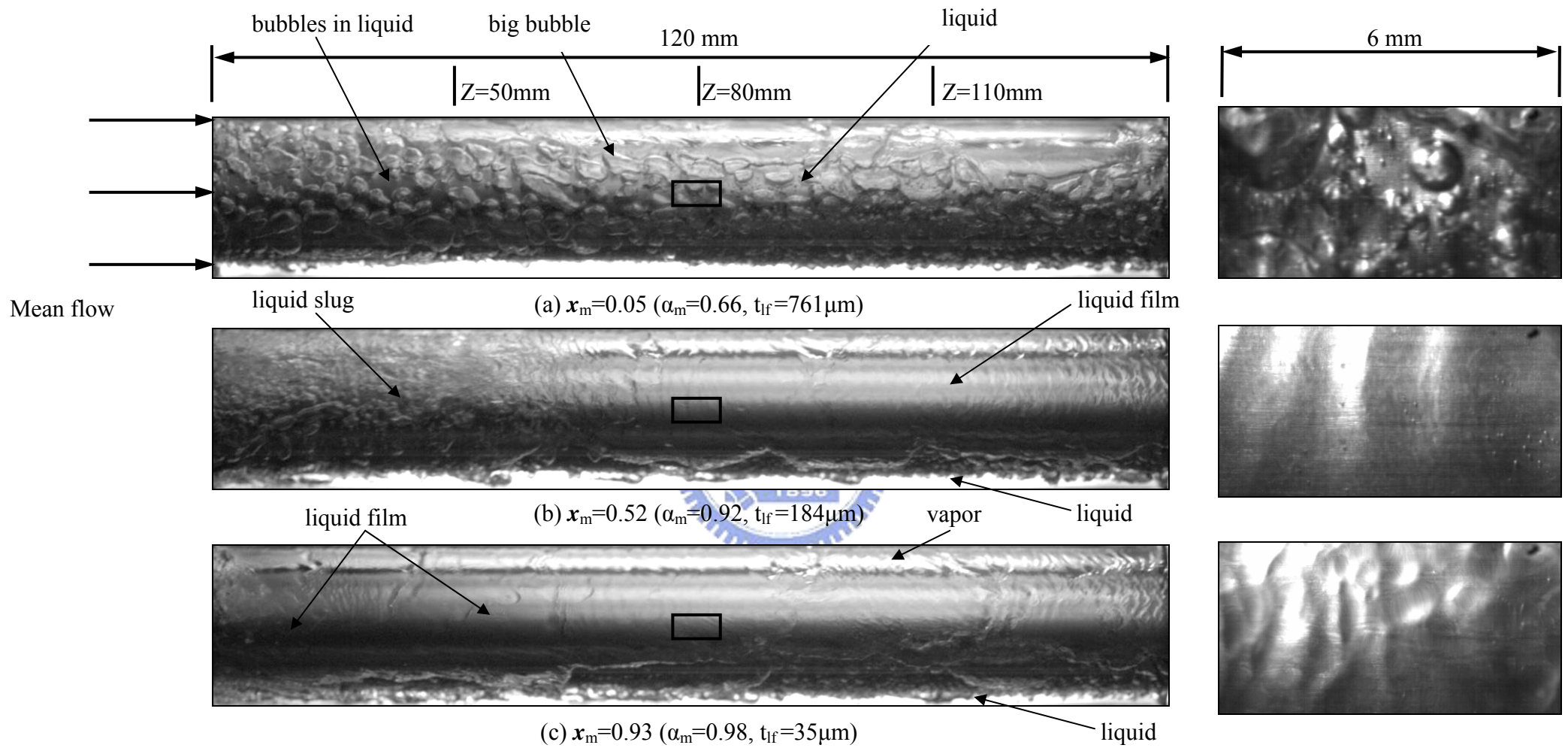


Fig.4.31 Photos of flow in the evaporation of R-134a in the entire duct and a small region around middle axial location at  $G=400 \text{ kg/m}^2\text{s}$ ,  $T_{\text{sat}} = 15^\circ\text{C}$ ,  $\delta = 2.0 \text{ mm}$ ,  $q = 15 \text{ kW/m}^2$  for (a)  $x_m = 0.05$ , (b)  $x_m = 0.52$  and (c)  $x_m = 0.93$ .

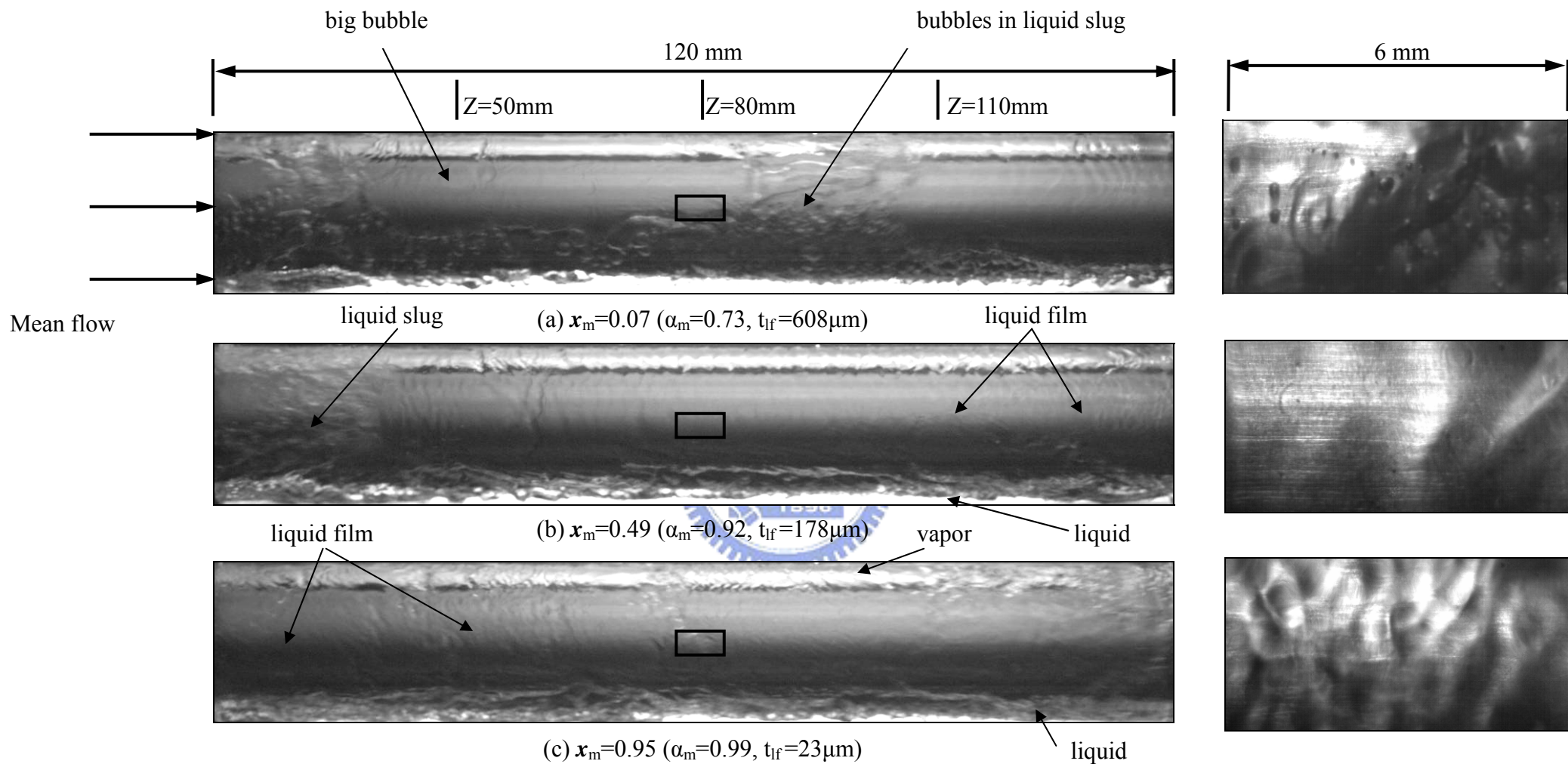


Fig.4.32 Photos of flow in the evaporation of R-134a in the entire duct and a small region around middle axial location at  $G=400 \text{ kg/m}^2\text{s}$ ,  $T_{\text{sat}} = 5^\circ\text{C}$ ,  $\delta = 2.0 \text{ mm}$ ,  $q = 15 \text{ kW/m}^2$  for (a)  $x_m = 0.07$ , (b)  $x_m = 0.49$  and (c)  $x_m = 0.95$ .



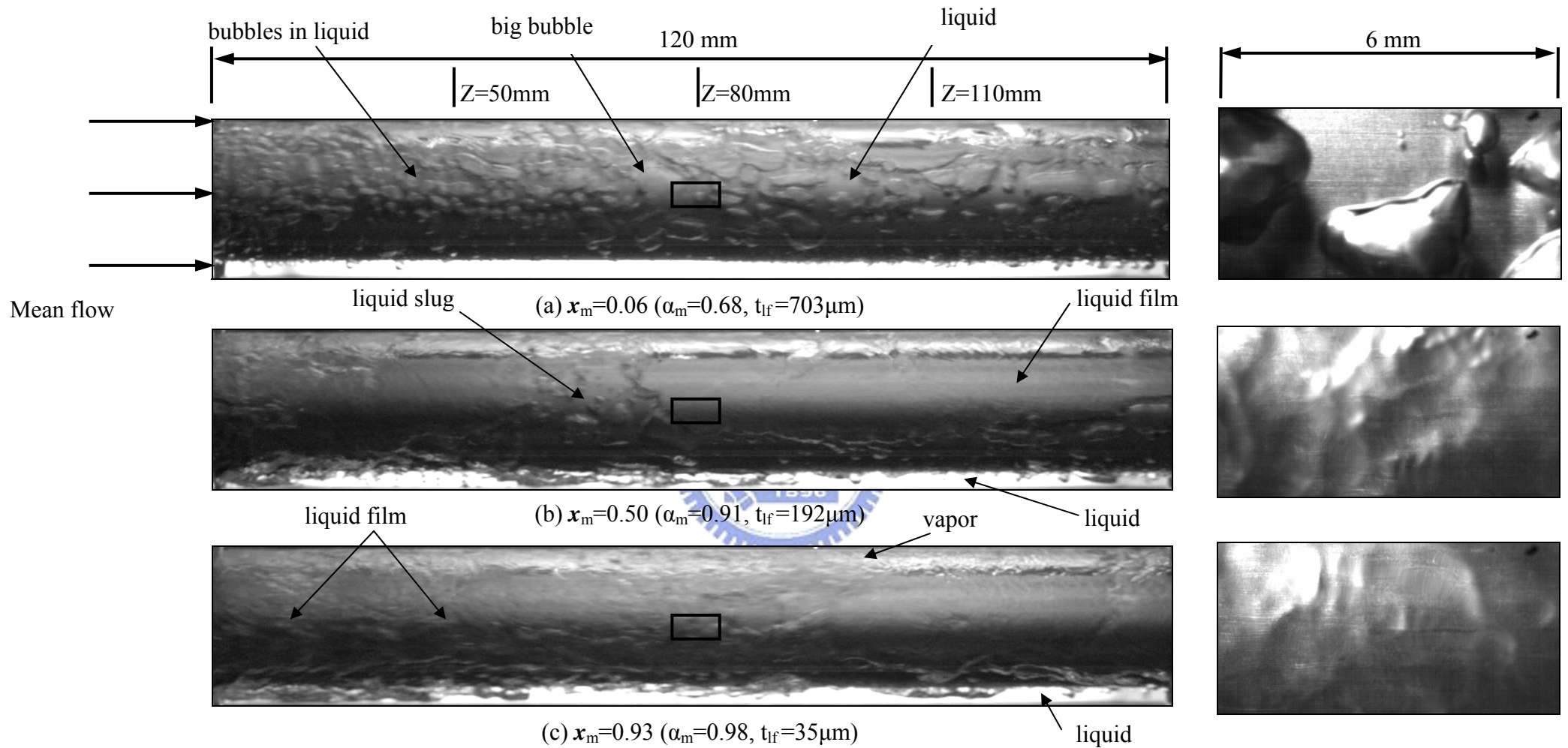


Fig.4.33 Photos of flow in the evaporation of R-134a in the entire duct and a small region around middle axial location at  $G=500 \text{ kg/m}^2\text{s}$ ,  $T_{\text{sat}} = 15^\circ\text{C}$ ,  $\delta = 2.0 \text{ mm}$ ,  $q = 5 \text{ kW/m}^2$  for (a)  $x_m = 0.06$ , (b)  $x_m = 0.50$  and (c)  $x_m = 0.93$ .

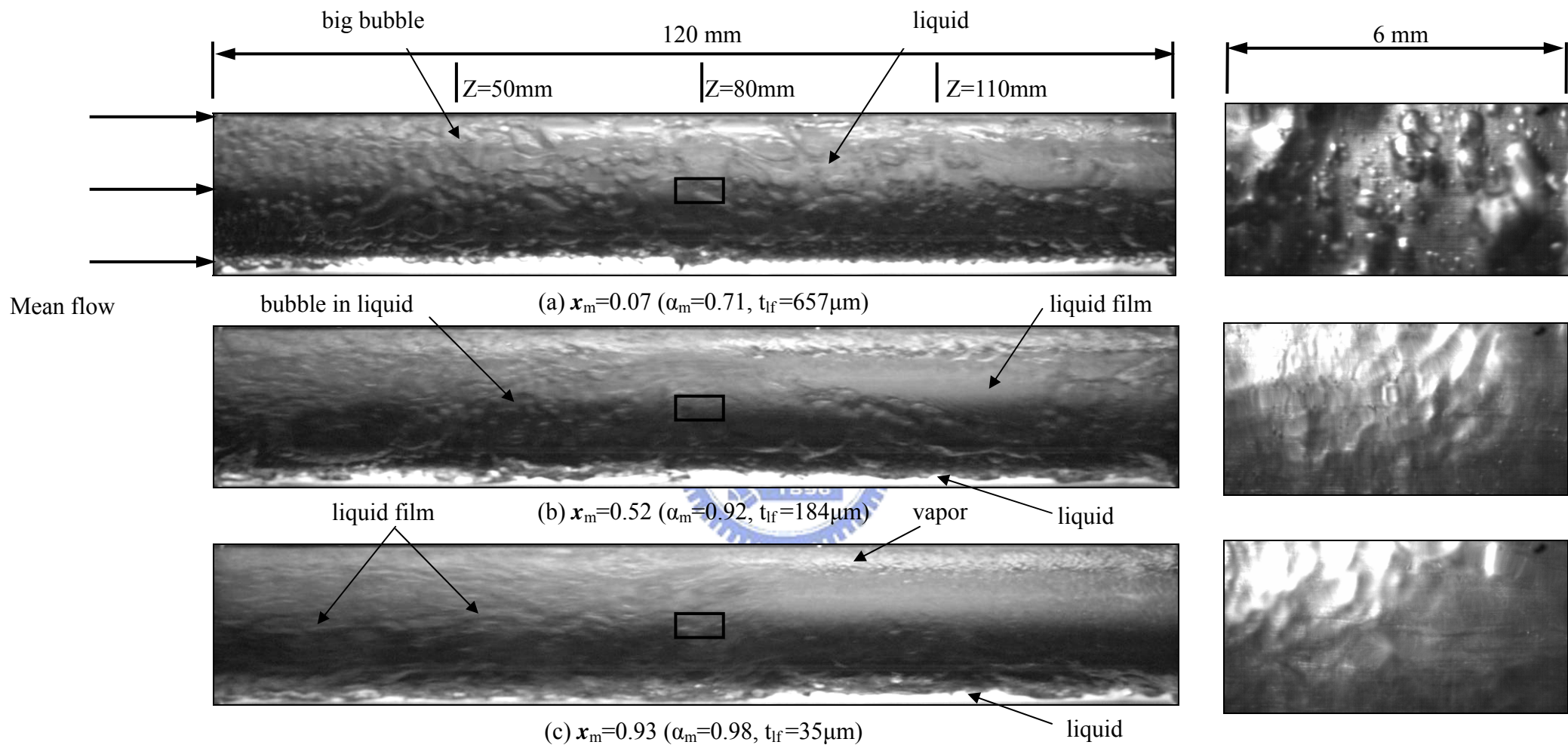


Fig.4.34 Photos of flow in the evaporation of R-134a in the entire duct and a small region around middle axial location at  $G=500 \text{ kg/m}^2\text{s}$ ,  $T_{\text{sat}} = 15^\circ\text{C}$ ,  $\delta = 2.0 \text{ mm}$ ,  $q = 15 \text{ kW/m}^2$  for (a)  $x_m = 0.07$ , (b)  $x_m = 0.52$  and (c)  $x_m = 0.93$ .

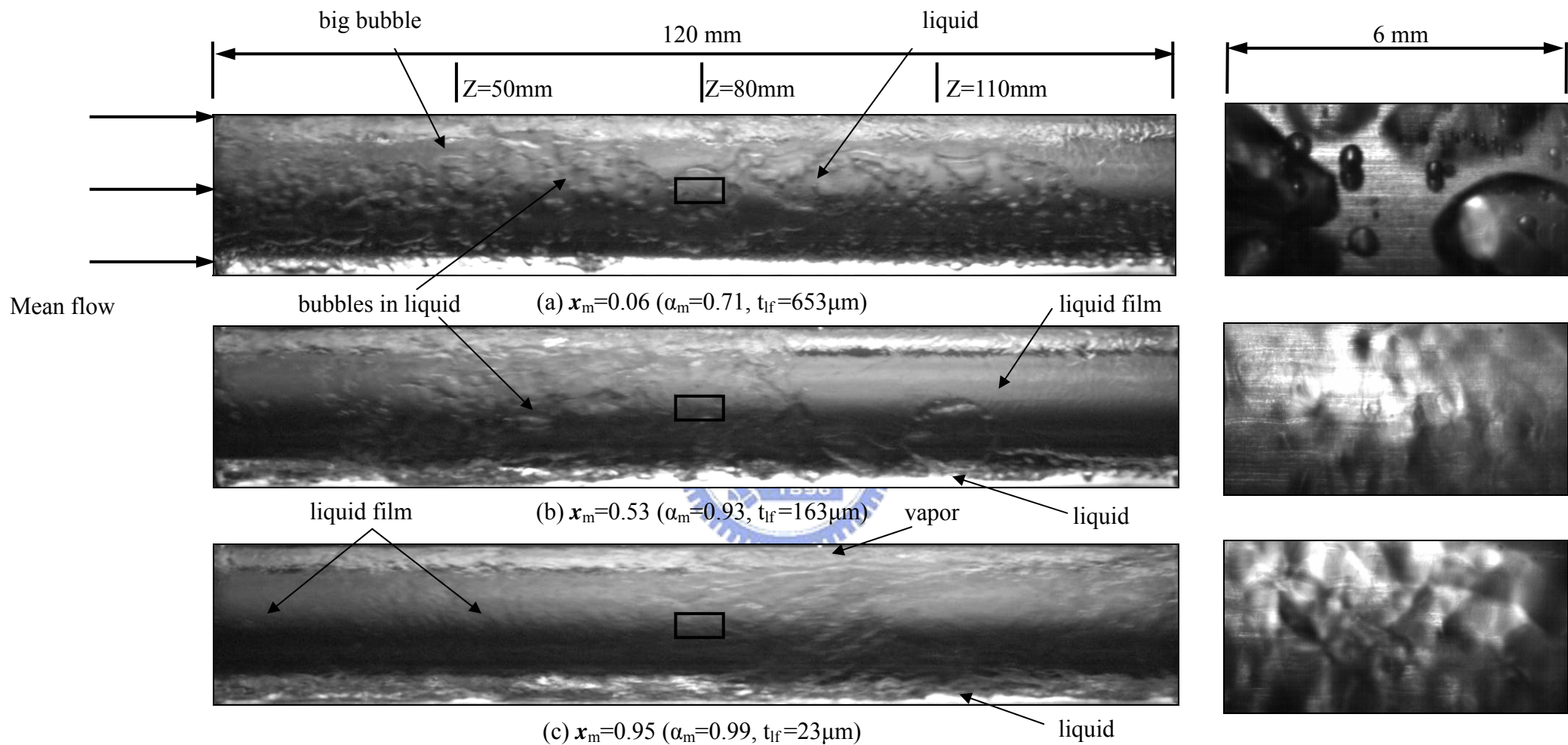


Fig.4.35 Photos of flow in the evaporation of R-134a in the entire duct and a small region around middle axial location at  $G=500 \text{ kg/m}^2\text{s}$ ,  $T_{\text{sat}} = 5^\circ\text{C}$ ,  $\delta = 2.0 \text{ mm}$ ,  $q = 15 \text{ kW/m}^2$  for (a)  $x_m = 0.06$ , (b)  $x_m = 0.53$  and (c)  $x_m = 0.95$ .



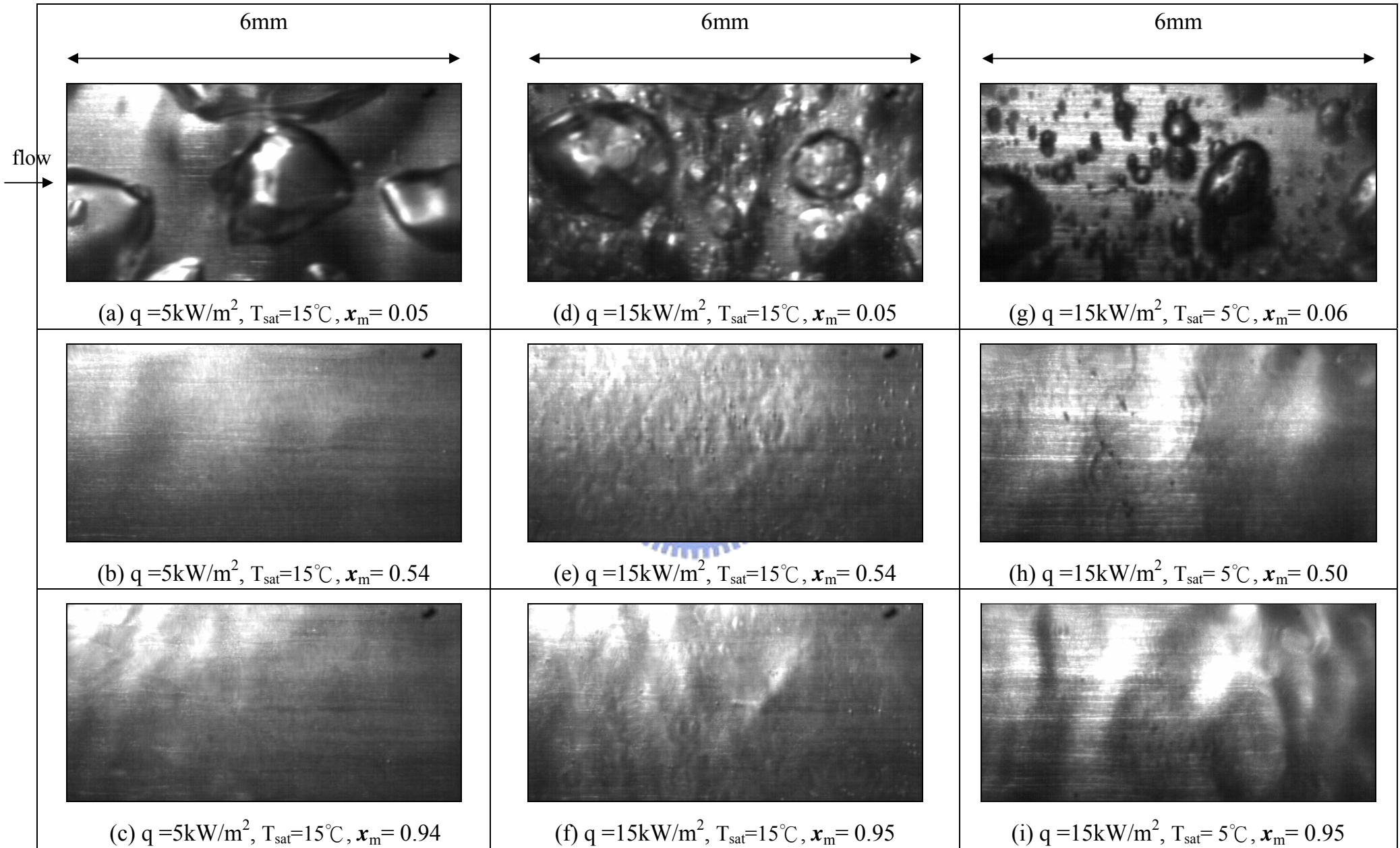


Fig. 4.36 Photos of flow in the evaporation of R-134a in a small region around middle axial location at  $\delta = 2.0 \text{ mm}$  and  $G = 300 \text{ kg/m}^2\text{s}$  for various imposed heat fluxes, saturated temperatures and vapor quality.

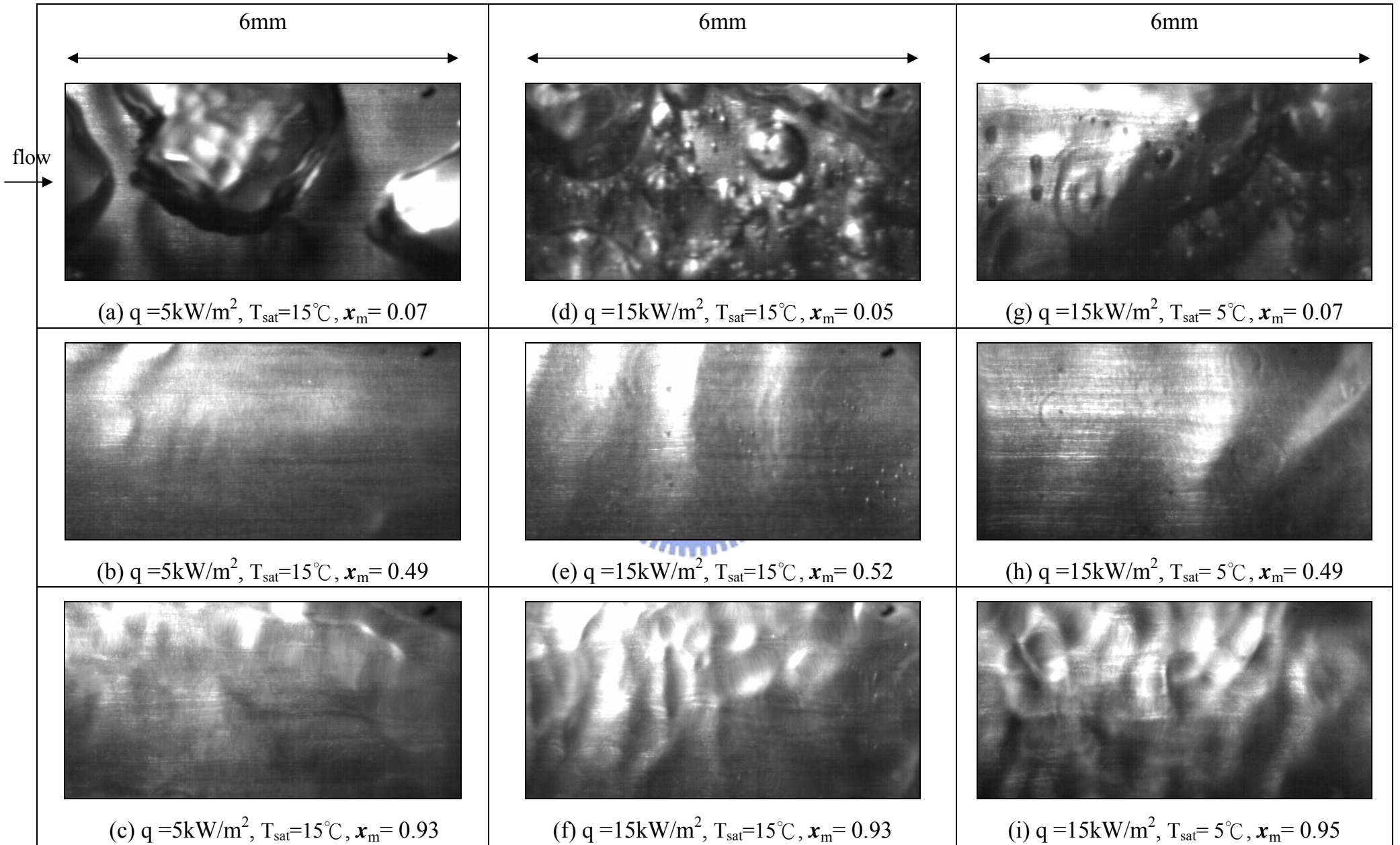


Fig. 4.37 Photos of flow in the evaporation of R-134a in a small region around middle axial location at  $\delta = 2.0$  mm and  $G = 400$  kg/m<sup>2</sup>s for various imposed heat fluxes, saturated temperatures and vapor quality.



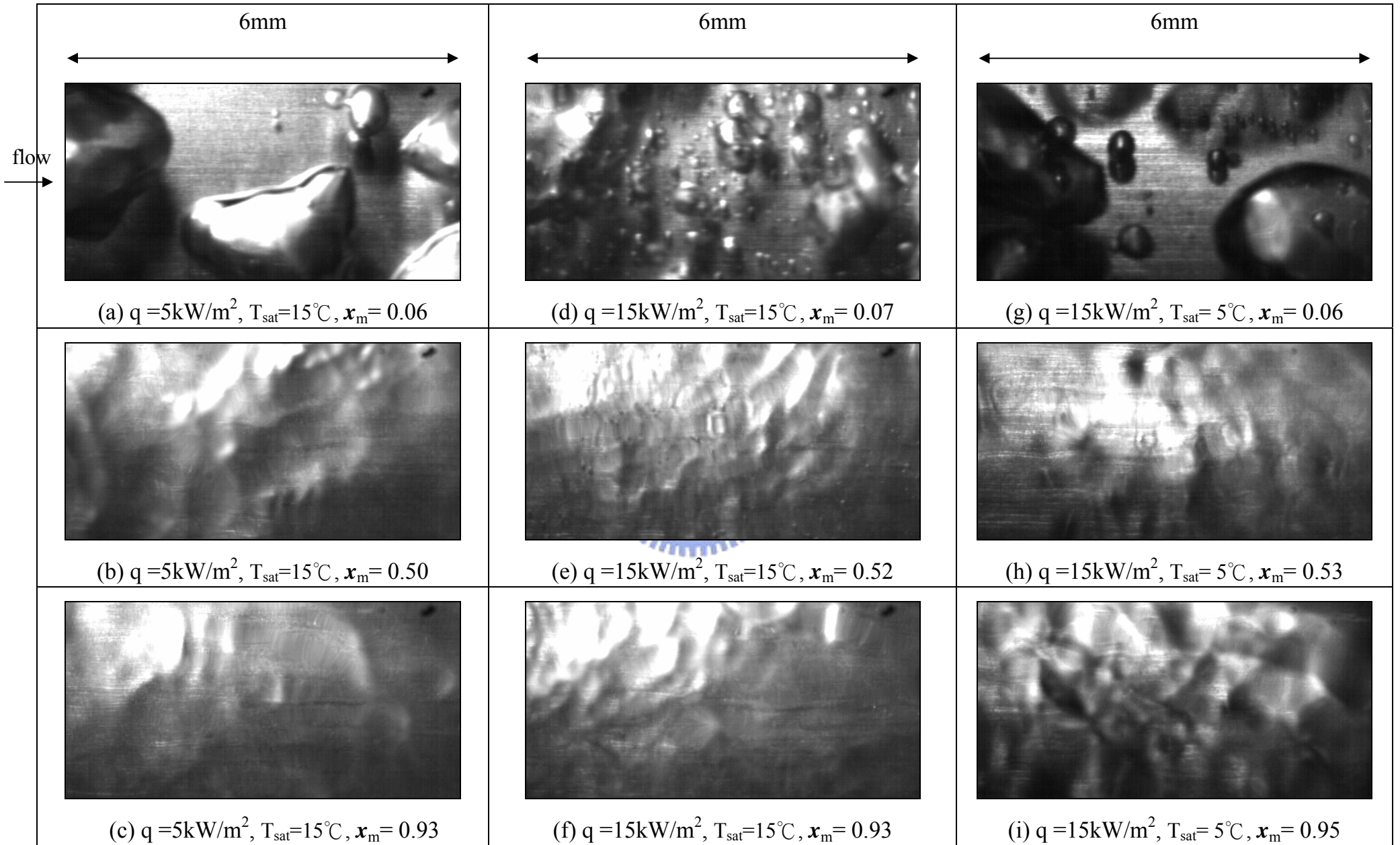


Fig. 4.38 Photos of flow in the evaporation of R-134a in a small region around middle axial location at  $\delta = 2.0 \text{ mm}$  and  $G = 500 \text{ kg/m}^2\text{s}$  for various imposed heat fluxes, saturated temperatures and vapor quality.

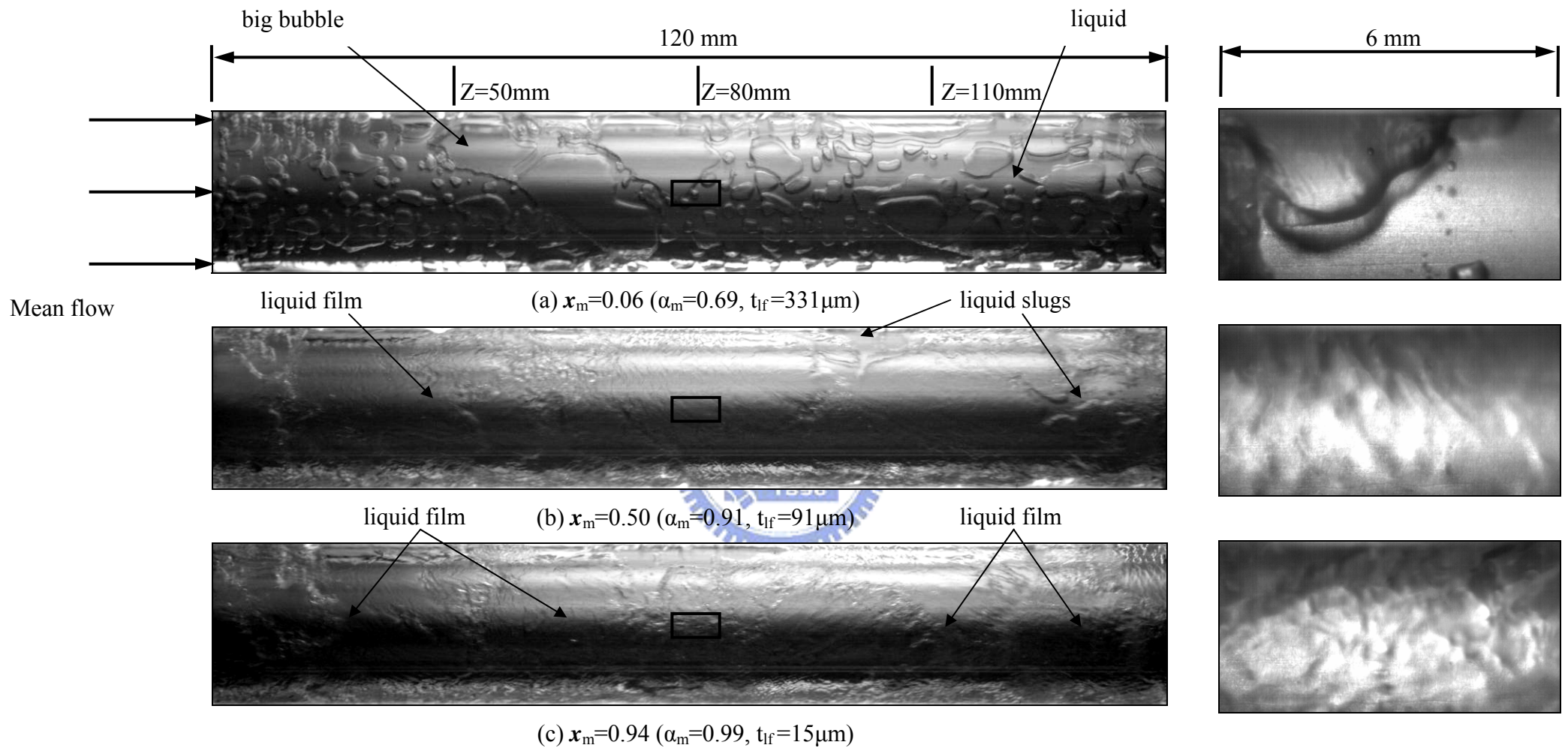


Fig.4.39 Photos of flow in the evaporation of R-134a in the entire duct and a small region around middle axial location at  $G=500 \text{ kg/m}^2\text{s}$ ,  $T_{\text{sat}} = 15^\circ\text{C}$ ,  $\delta = 1.0 \text{ mm}$ ,  $q = 5 \text{ kW/m}^2$  for (a)  $x_m = 0.06$ , (b)  $x_m = 0.50$  and (c)  $x_m = 0.94$ .

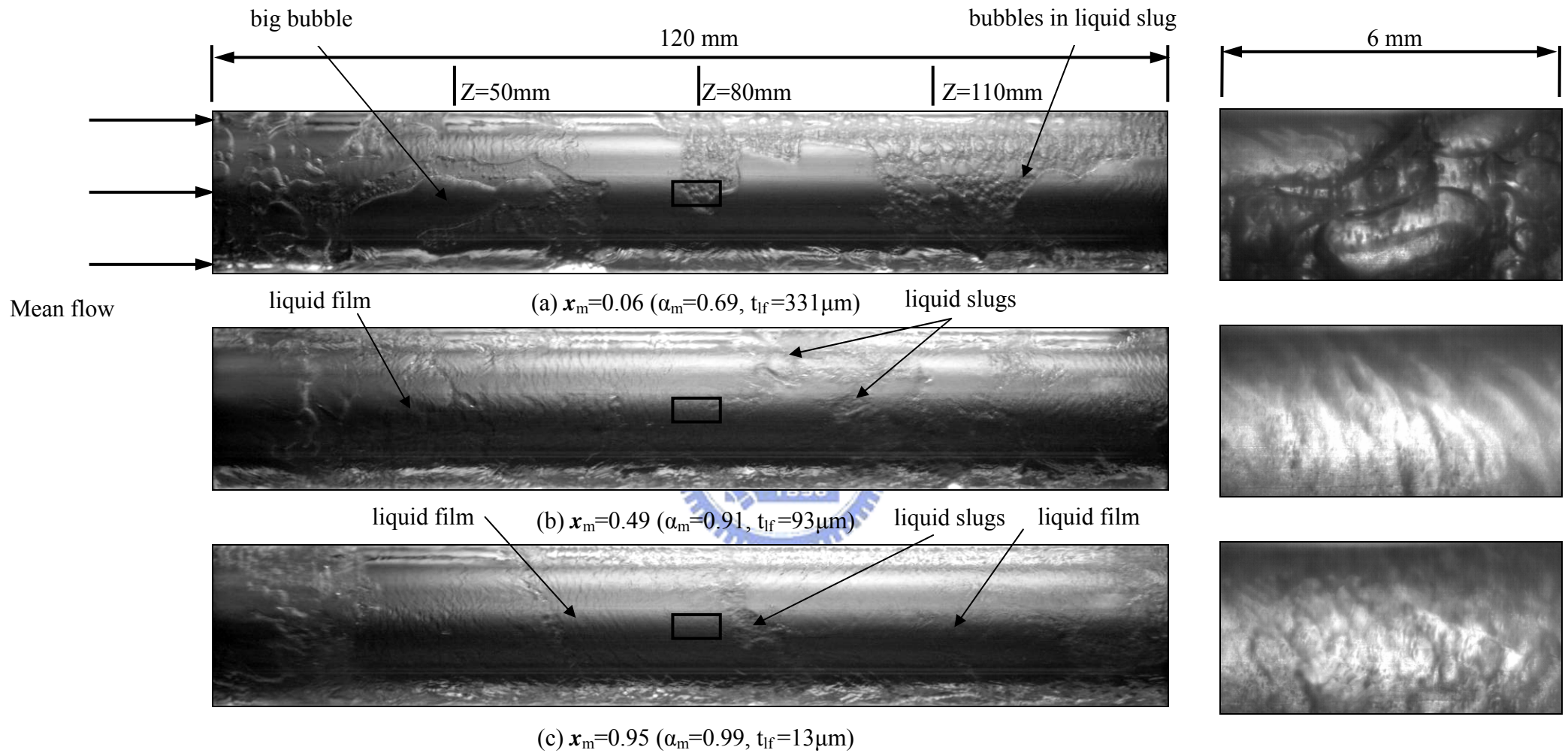


Fig.4.40 Photos of flow in the evaporation of R-134a in the entire duct and a small region around middle axial location at  $G=500 \text{ kg/m}^2\text{s}$ ,  $T_{\text{sat}} = 15^\circ\text{C}$ ,  $\delta = 1.0 \text{ mm}$ ,  $q = 15 \text{ kW/m}^2$  for (a)  $x_m = 0.06$ , (b)  $x_m = 0.49$  and (c)  $x_m = 0.95$ .



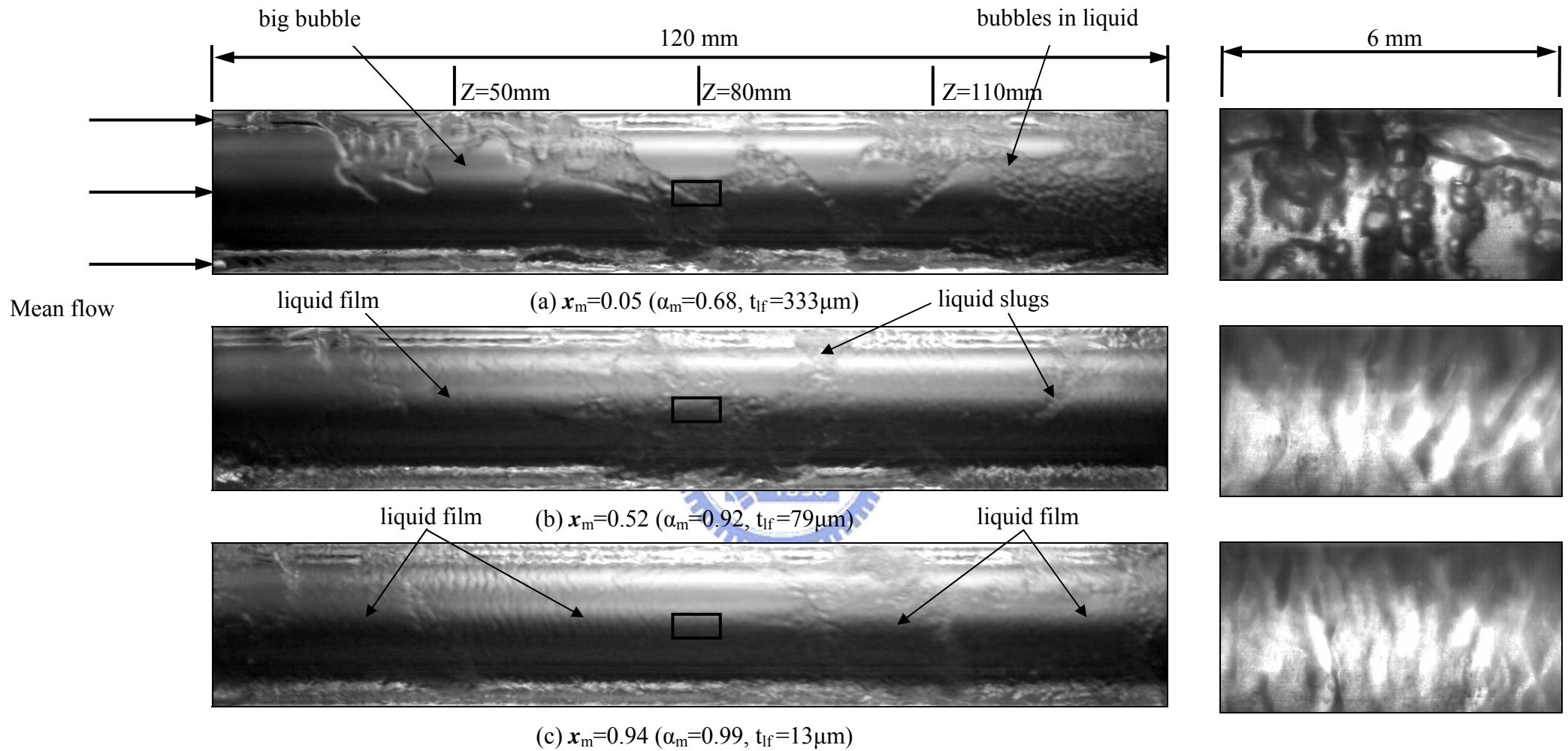


Fig.4.41 Photos of flow in the evaporation of R-134a in the entire duct and a small region around middle axial location at  $G=500 \text{ kg/m}^2\text{s}$ ,  $T_{\text{sat}} = 5^\circ\text{C}$ ,  $\delta = 1.0 \text{ mm}$ ,  $q = 15 \text{ kW/m}^2$  for (a)  $x_m = 0.05$ , (b)  $x_m = 0.52$  and (c)  $x_m = 0.94$ .

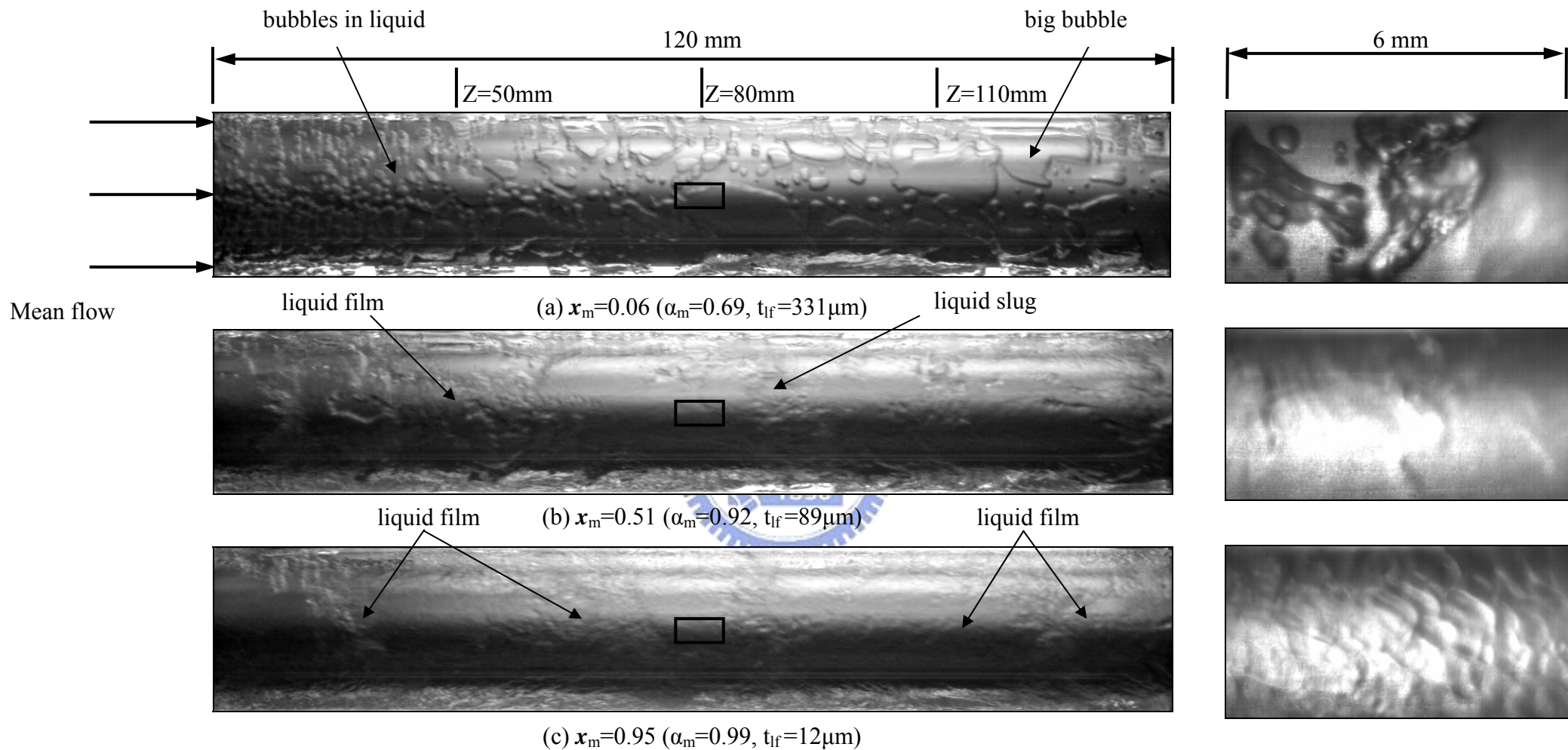


Fig.4.42 Photos of flow in the evaporation of R-134a in the entire duct and a small region around middle axial location at  $G = 600 \text{ kg/m}^2\text{s}$ ,  $T_{\text{sat}} = 15^\circ\text{C}$ ,  $\delta = 1.0 \text{ mm}$ ,  $q = 5 \text{ kW/m}^2$  for (a)  $x_m = 0.06$ , (b)  $x_m = 0.51$  and (c)  $x_m = 0.95$ .

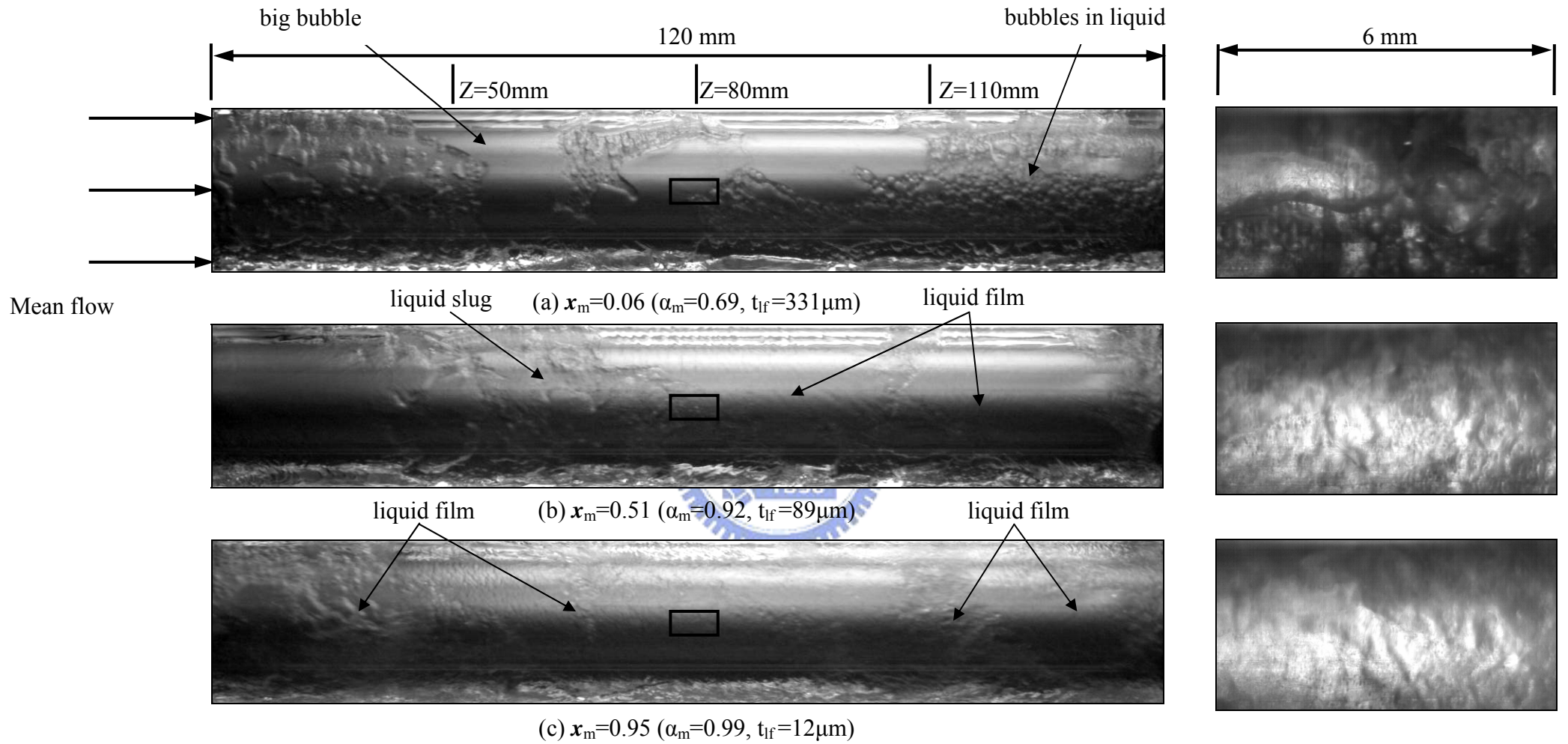


Fig.4.43 Photos of flow in the evaporation of R-134a in the entire duct and a small region around middle axial location at  $G=600\text{ kg/m}^2\text{s}$ ,  $T_{\text{sat}} = 15^\circ\text{C}$ ,  $\delta = 1.0\text{ mm}$ ,  $q = 15\text{ kW/m}^2$  for (a)  $x_m = 0.06$ , (b)  $x_m = 0.51$  and (c)  $x_m = 0.95$ .



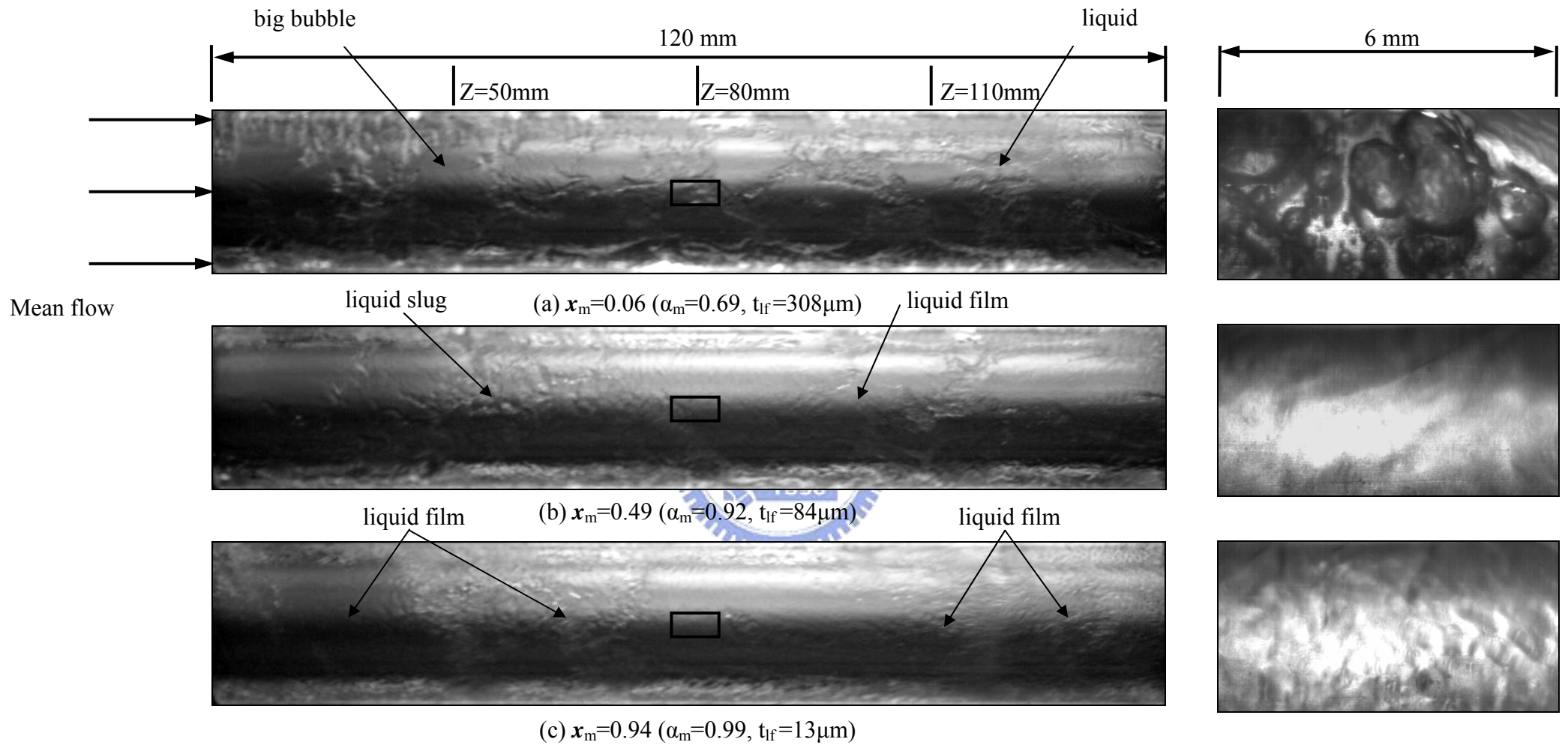


Fig.4.44 Photos of flow in the evaporation of R-134a in the entire duct and a small region around middle axial location at  $G=600 \text{ kg/m}^2\text{s}$ ,  $T_{\text{sat}} = 5^\circ\text{C}$ ,  $\delta = 1.0 \text{ mm}$ ,  $q = 15 \text{ kW/m}^2$  for (a)  $x_m = 0.06$ , (b)  $x_m = 0.49$  and (c)  $x_m = 0.94$ .

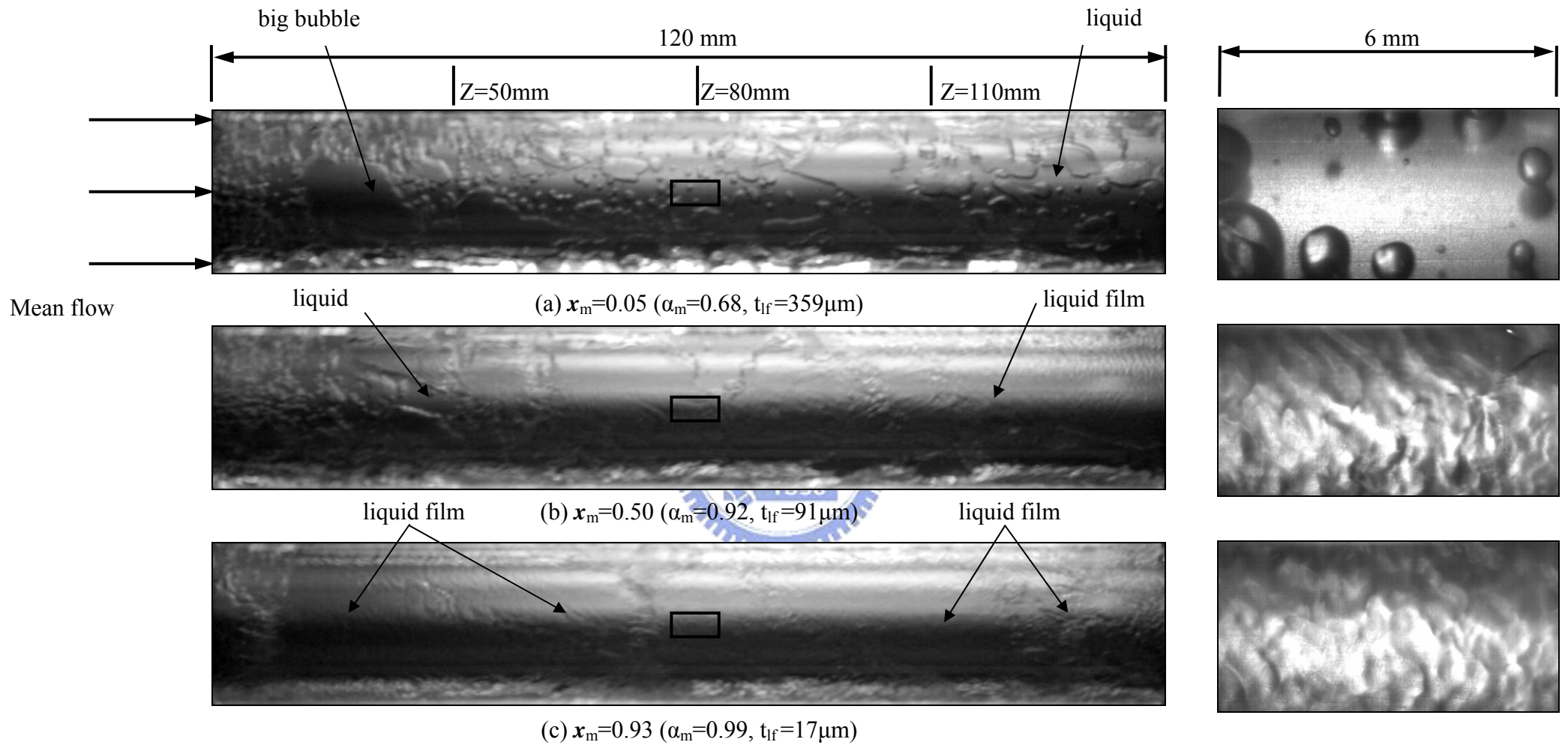


Fig.4.45 Photos of flow in the evaporation of R-134a in the entire duct and a small region around middle axial location at  $G=700 \text{ kg/m}^2\text{s}$ ,  $T_{\text{sat}} = 15^\circ\text{C}$ ,  $\delta = 1.0 \text{ mm}$ ,  $q = 5 \text{ kW/m}^2$  for (a)  $x_m = 0.05$ , (b)  $x_m = 0.50$  and (c)  $x_m = 0.93$ .



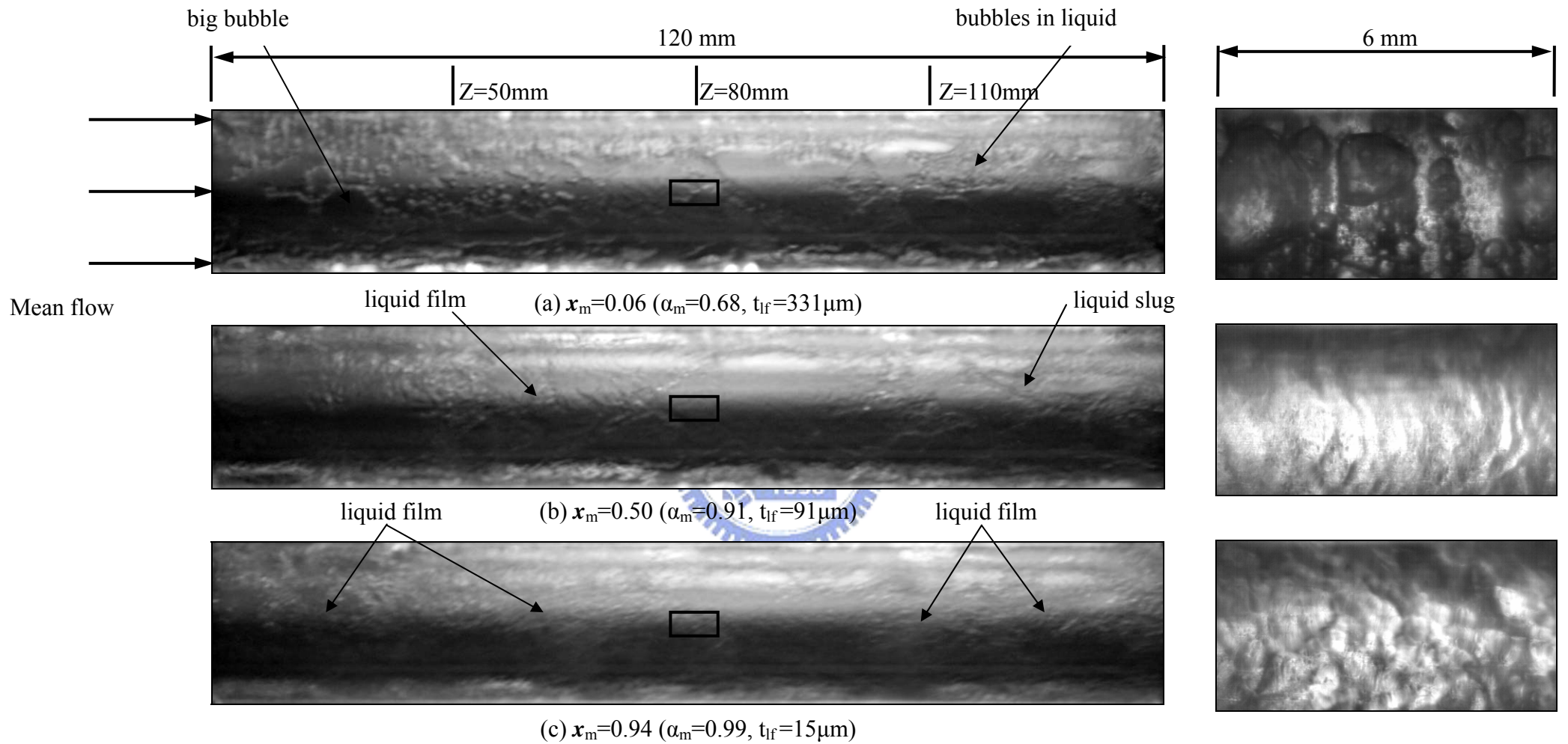


Fig.4.46 Photos of flow in the evaporation of R-134a in the entire duct and a small region around middle axial location at  $G=700\text{ kg/m}^2\text{s}$ ,  $T_{\text{sat}} = 15^\circ\text{C}$ ,  $\delta = 1.0\text{ mm}$ ,  $q = 15\text{ kW/m}^2$  for (a)  $x_m = 0.06$ , (b)  $x_m = 0.50$  and (c)  $x_m = 0.94$ .

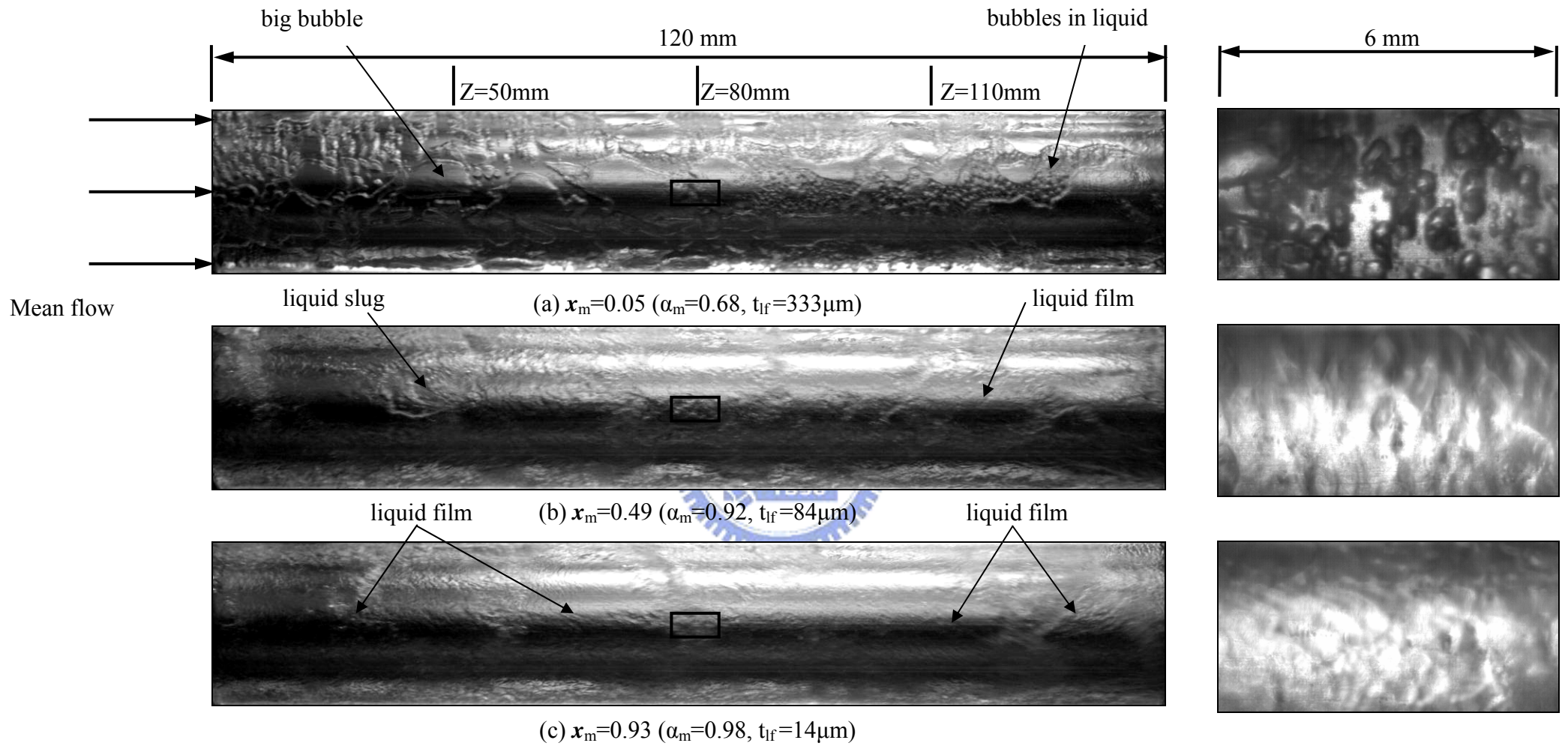


Fig.4.47 Photos of flow in the evaporation of R-134a in the entire duct and a small region around middle axial location at  $G=700 \text{ kg/m}^2\text{s}$ ,  $T_{\text{sat}} = 5^\circ\text{C}$ ,  $\delta = 1.0 \text{ mm}$ ,  $q = 15 \text{ kW/m}^2$  for (a)  $x_m = 0.05$ , (b)  $x_m = 0.49$  and (c)  $x_m = 0.93$ .

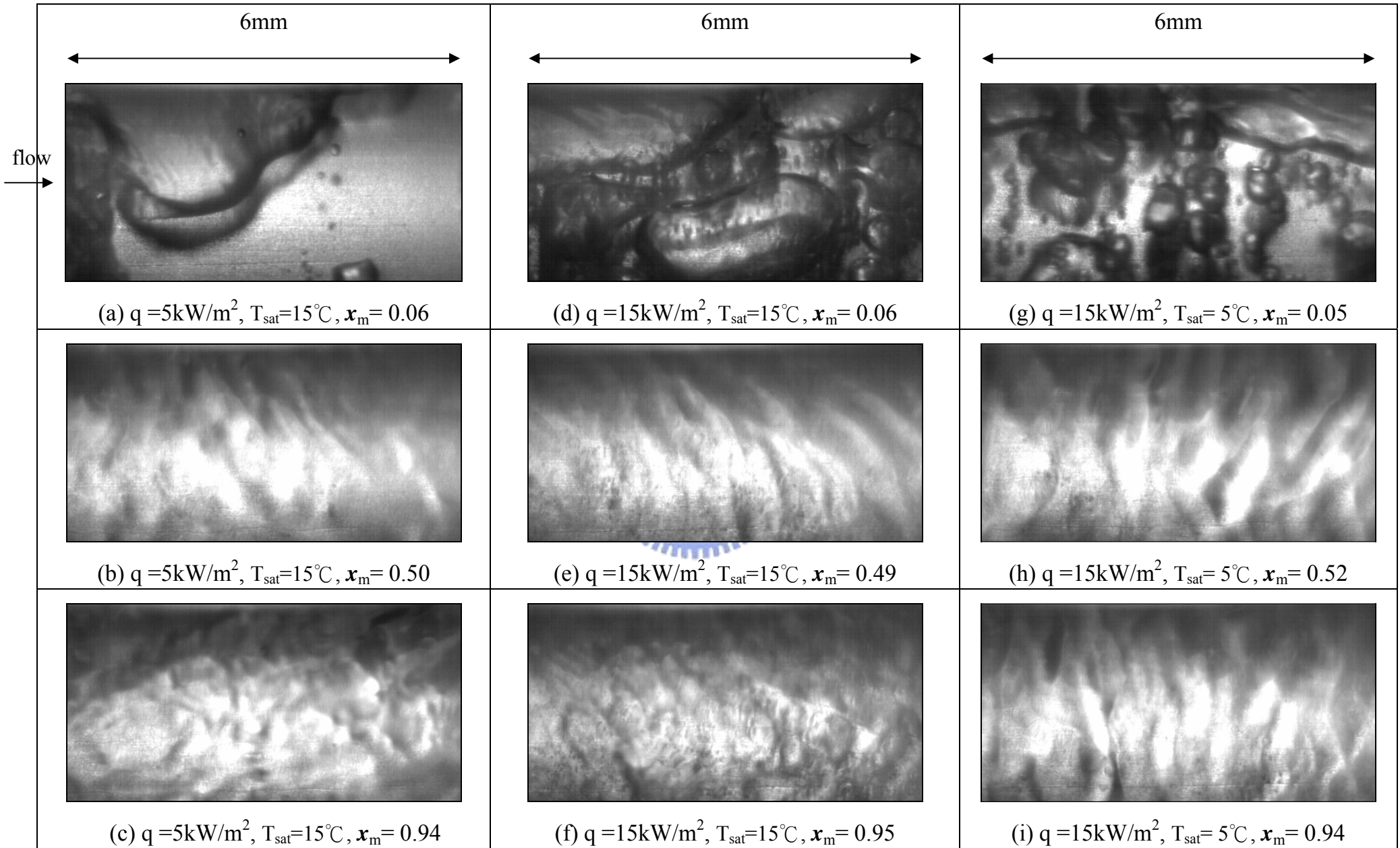


Fig. 4.48 Photos of flow in the evaporation of R-134a in a small region around middle axial location at  $\delta = 1.0$  mm and  $G = 500$  kg/m<sup>2</sup>s for various imposed heat fluxes, saturated temperatures and vapor quality.



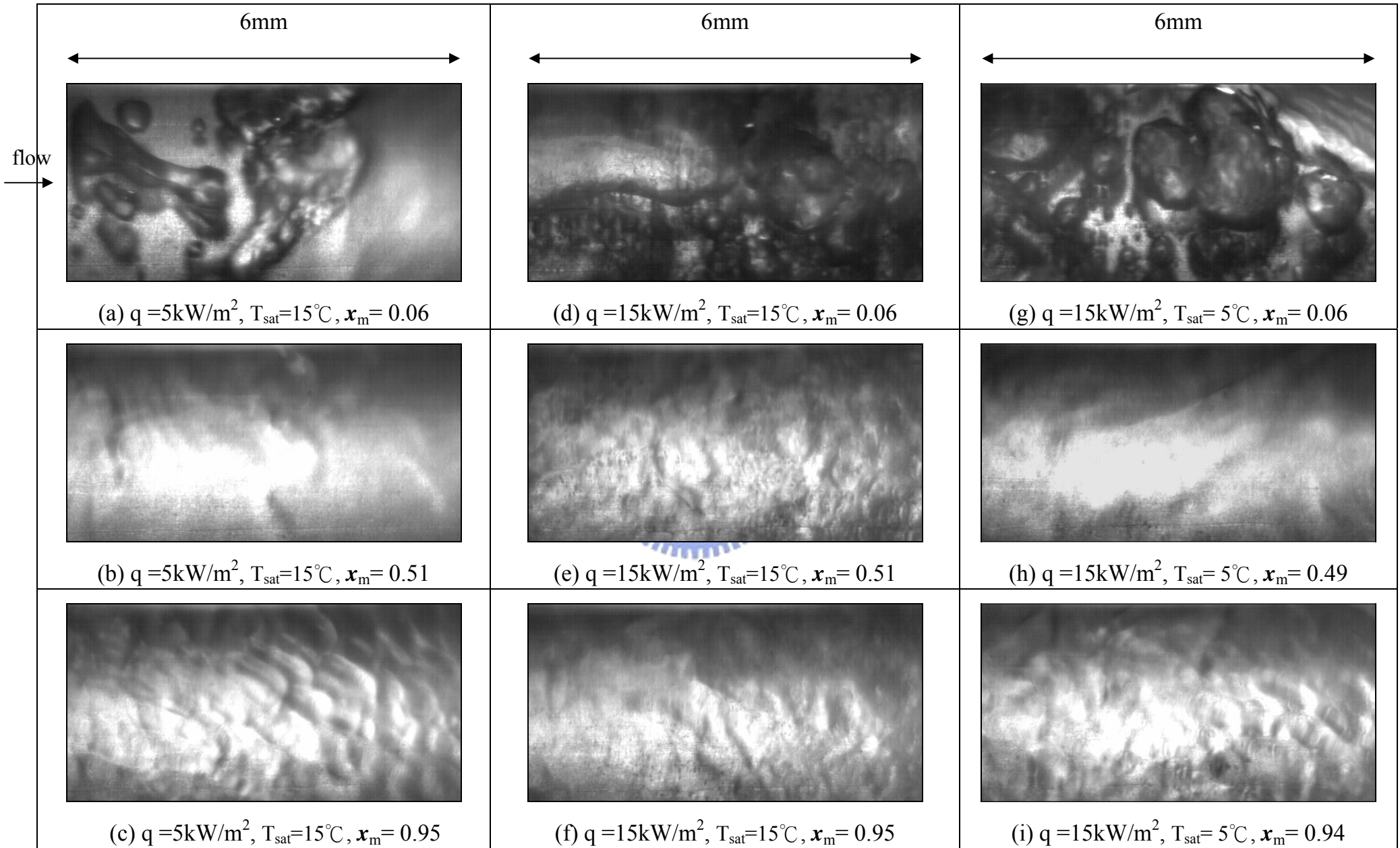


Fig. 4.49 Photos of flow in the evaporation of R-134a in a small region around middle axial location at  $\delta = 1.0$  mm and  $G = 600$  kg/m<sup>2</sup>s for various imposed heat fluxes, saturated temperatures and vapor quality.

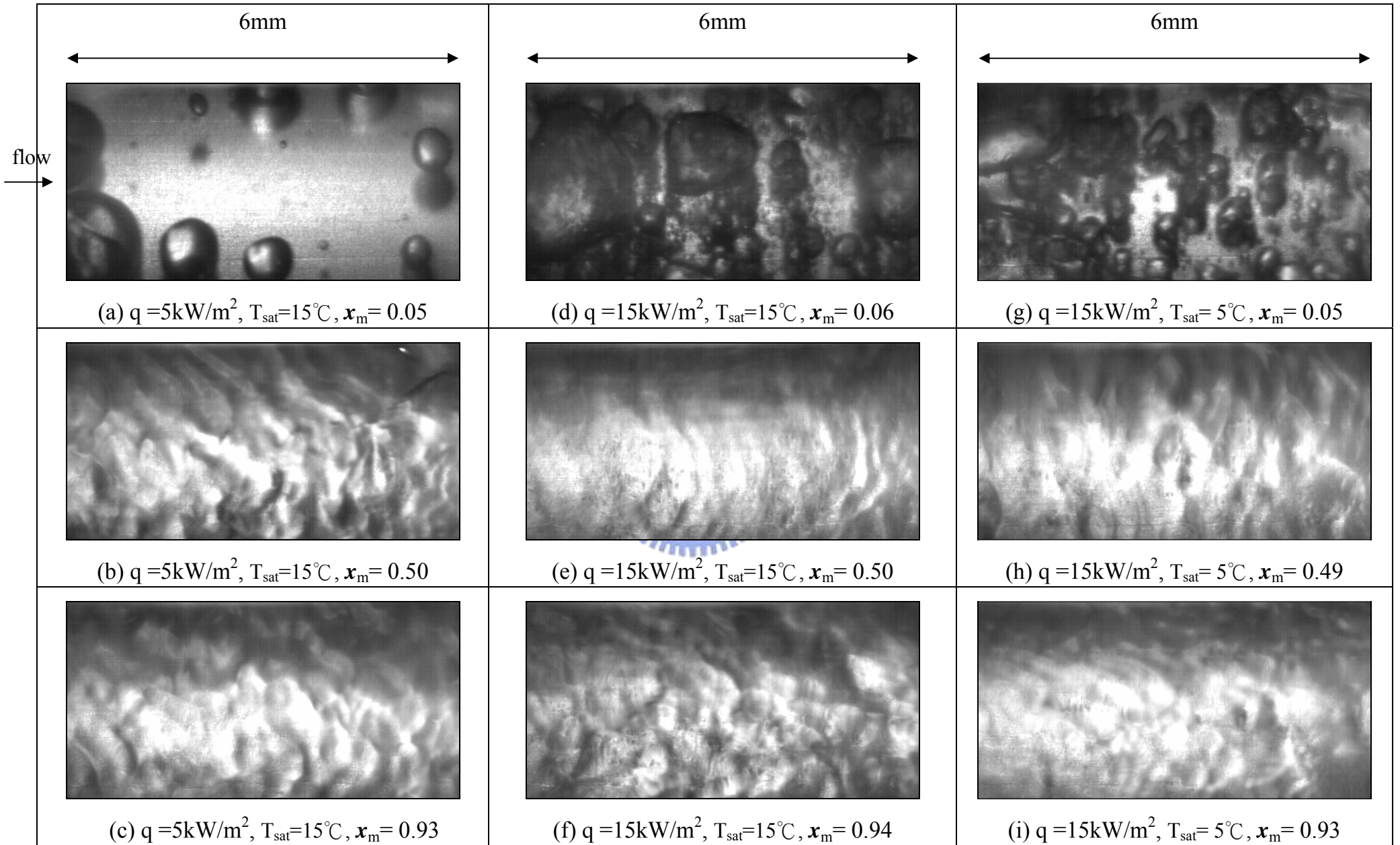


Fig. 4.50 Photos of flow in the evaporation of R-134a in a small region around middle axial location at  $\delta = 1.0$  mm and  $G = 700$  kg/m<sup>2</sup>s for various imposed heat fluxes, saturated temperatures and vapor quality.

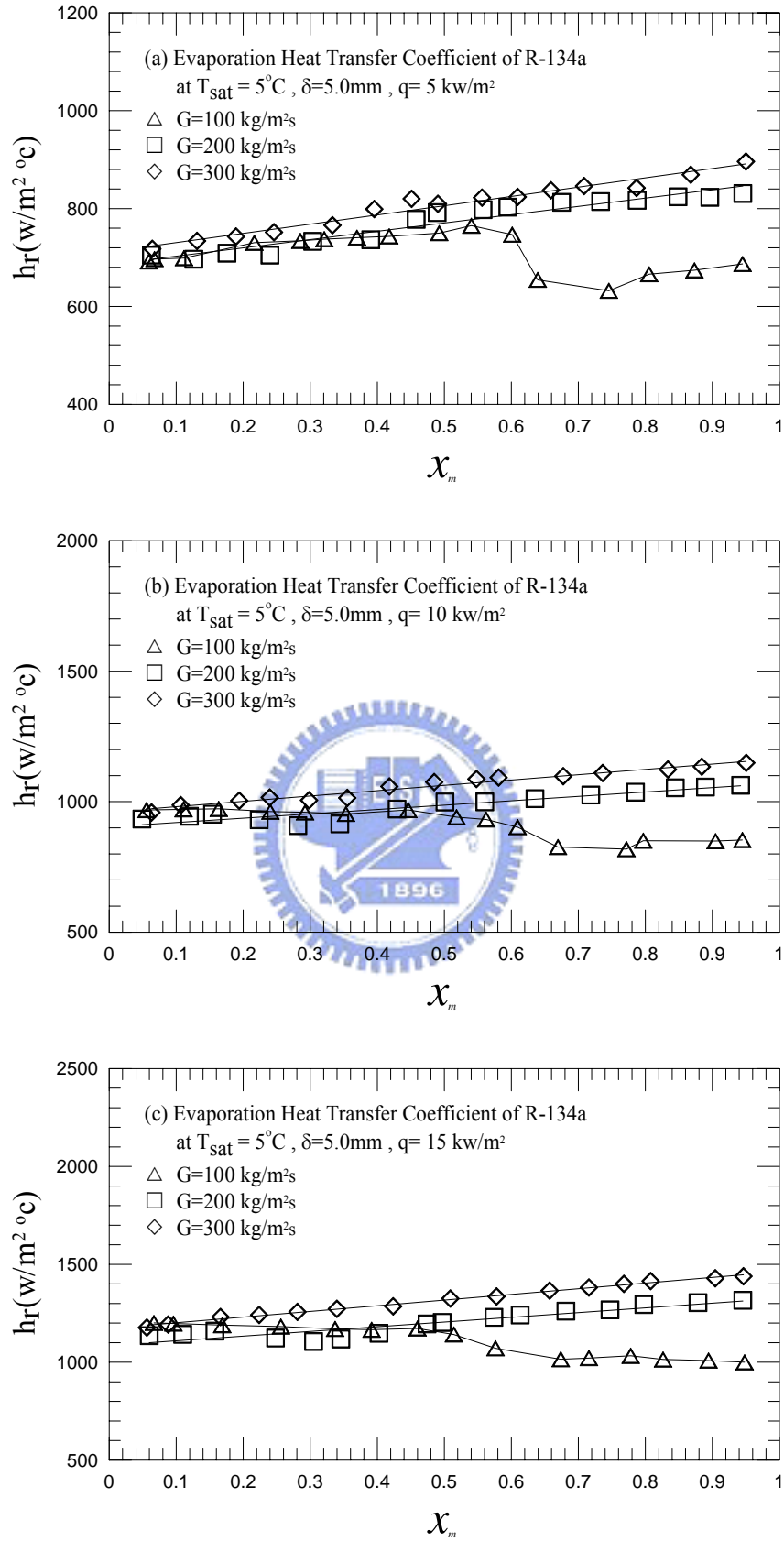


Fig. 4.51 Variations of R-134a evaporation heat transfer coefficient with vapor quality in  $\delta = 5.0 \text{ mm}$  narrow duct at  $T_{\text{sat}} = 5^\circ\text{C}$  for various  $G$  for (a)  $q = 5 \text{ kW/m}^2$ , (b)  $q = 10 \text{ kW/m}^2$  and (c)  $q = 15 \text{ kW/m}^2$ .

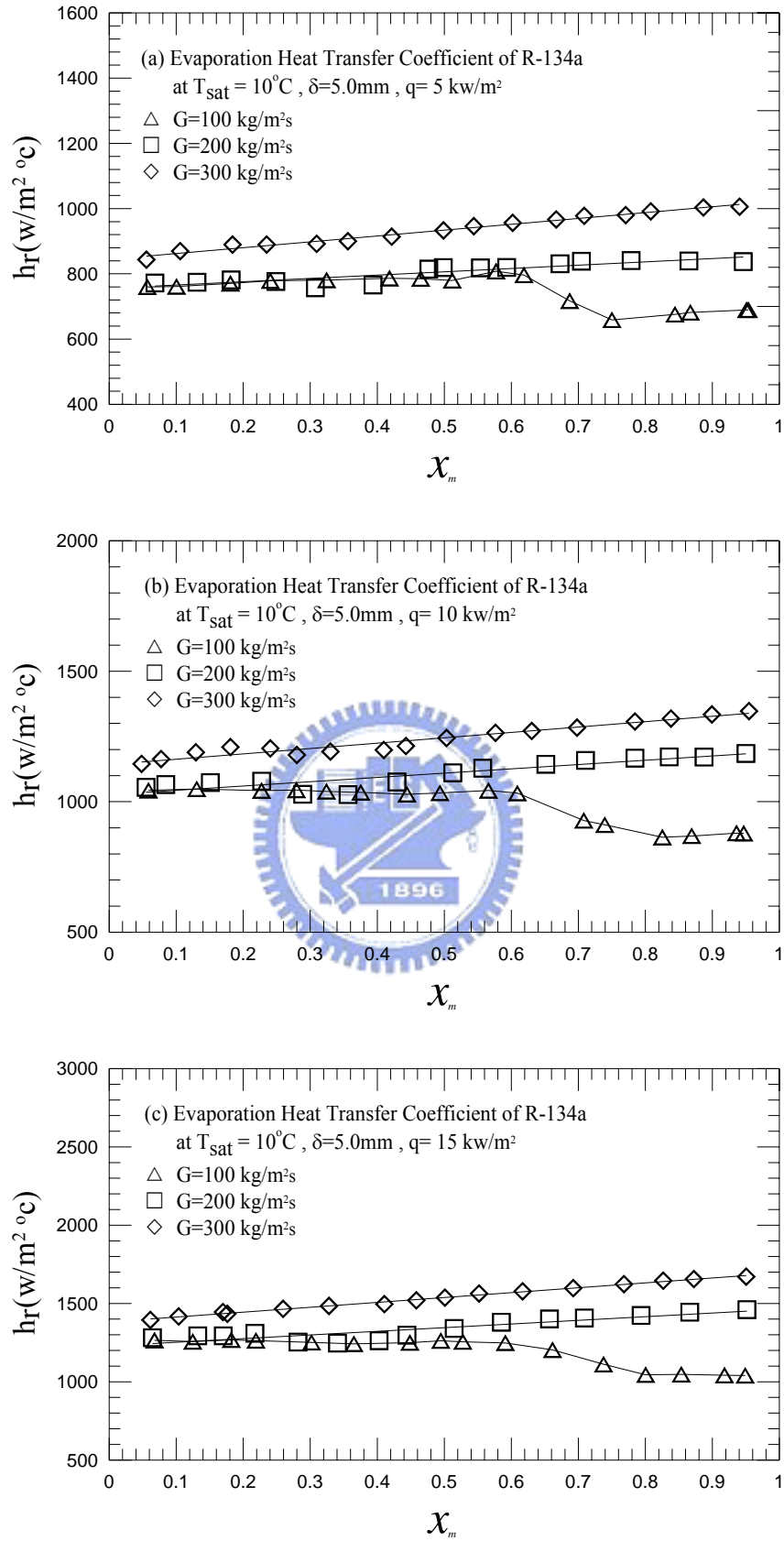


Fig. 4.52 Variations of R-134a evaporation heat transfer coefficient with vapor quality in  $\delta = 5.0 \text{ mm}$  narrow duct at  $T_{\text{sat}} = 10^\circ\text{C}$  for various  $G$  for (a)  $q = 5 \text{ kW/m}^2$ , (b)  $q = 10 \text{ kW/m}^2$  and (c)  $q = 15 \text{ kW/m}^2$ .

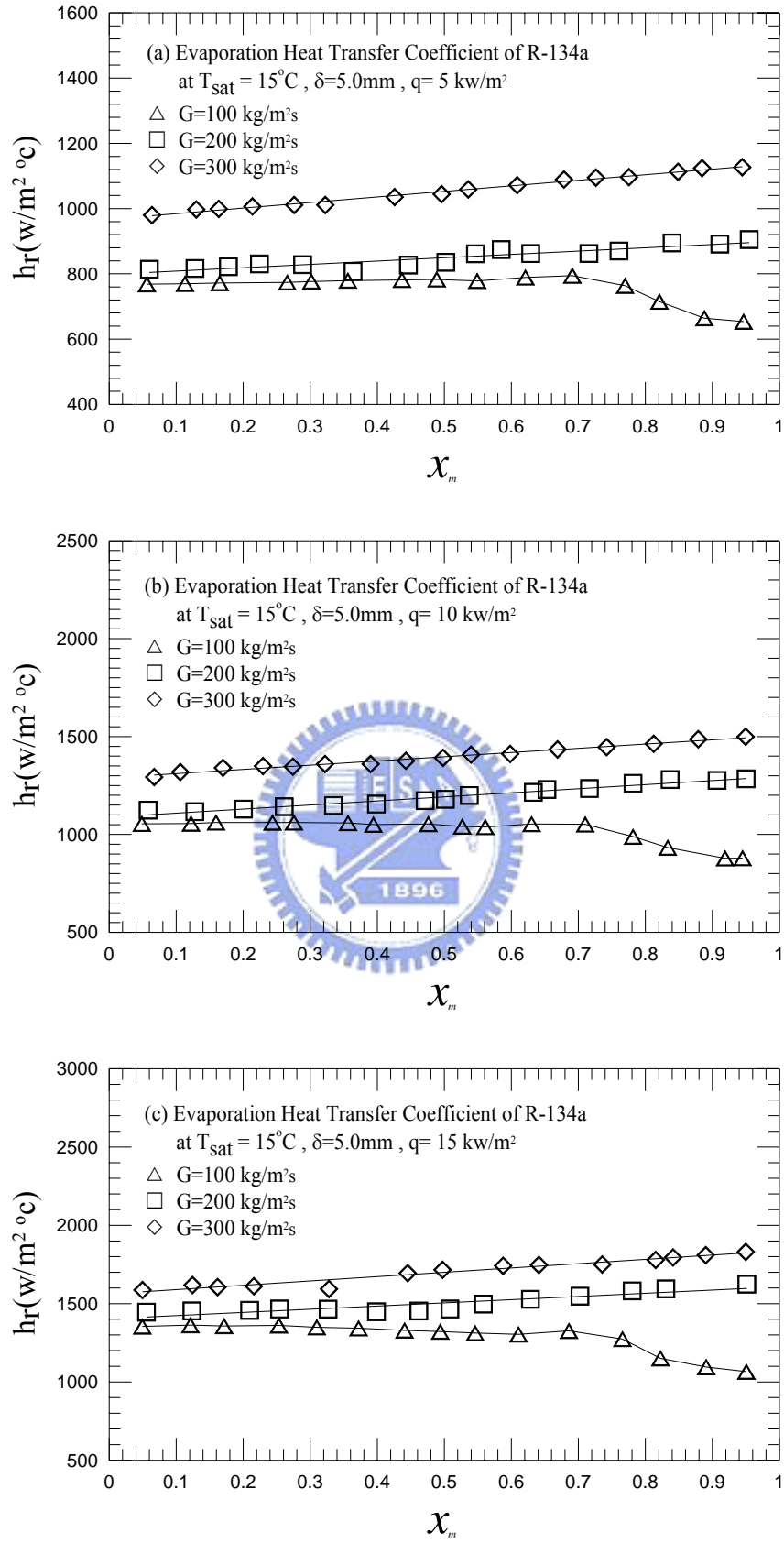


Fig. 4.53 Variations of R-134a evaporation heat transfer coefficient with vapor quality in  $\delta = 5.0 \text{ mm}$  narrow duct at  $T_{\text{sat}} = 15^\circ\text{C}$  for various  $G$  for (a)  $q = 5 \text{ kW/m}^2$ , (b)  $q = 10 \text{ kW/m}^2$  and (c)  $q = 15 \text{ kW/m}^2$ .



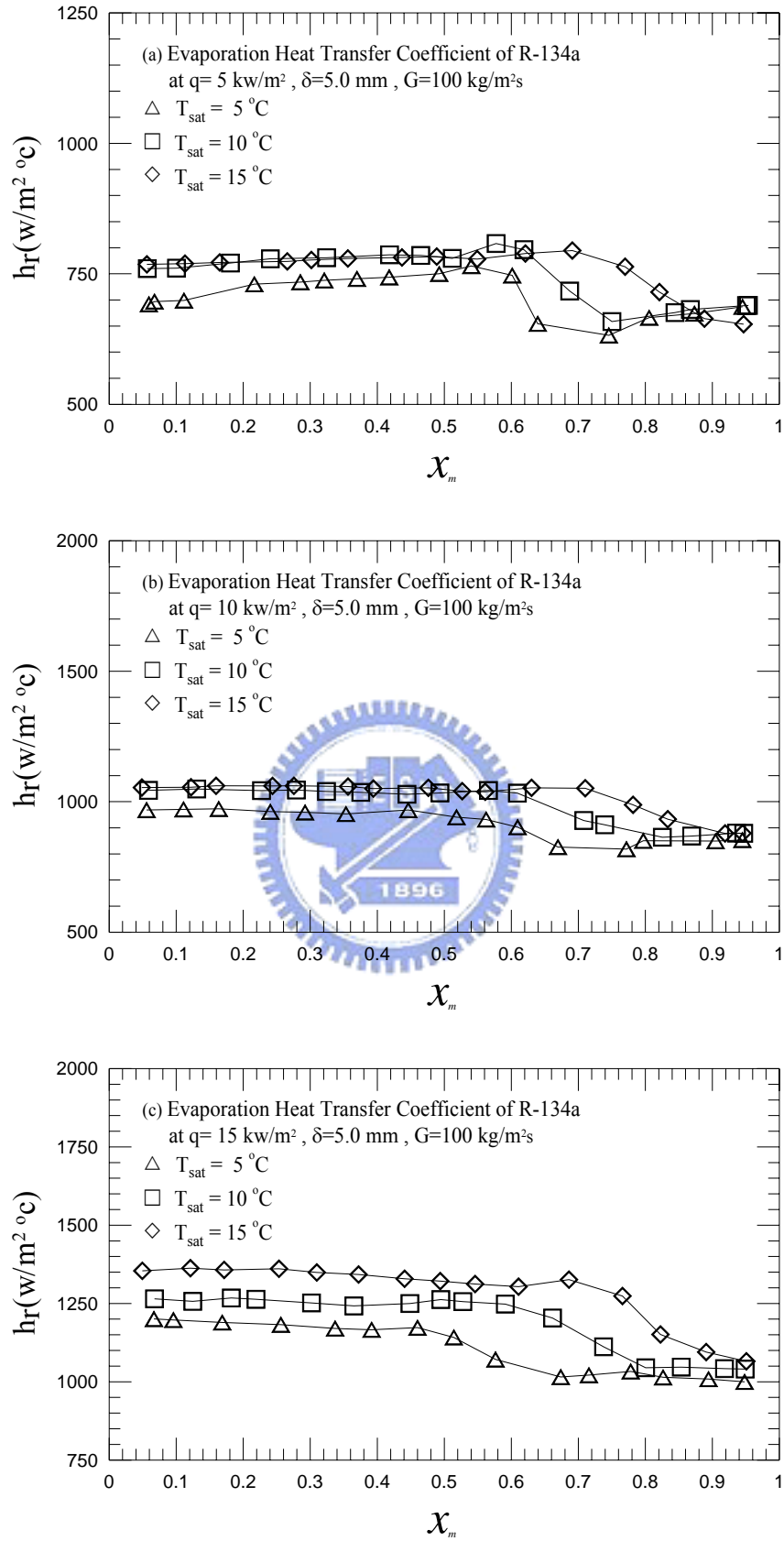


Fig. 4.54 Variations of R-134a evaporation heat transfer coefficient with vapor quality in  $\delta = 5.0 \text{ mm}$  narrow duct at  $G=100 \text{ kg/m}^2\text{s}$  for various  $T_{\text{sat}}$  for (a)  $q = 5 \text{ kW/m}^2$ , (b)  $q = 10 \text{ kW/m}^2$  and (c)  $q = 15 \text{ kW/m}^2$ .

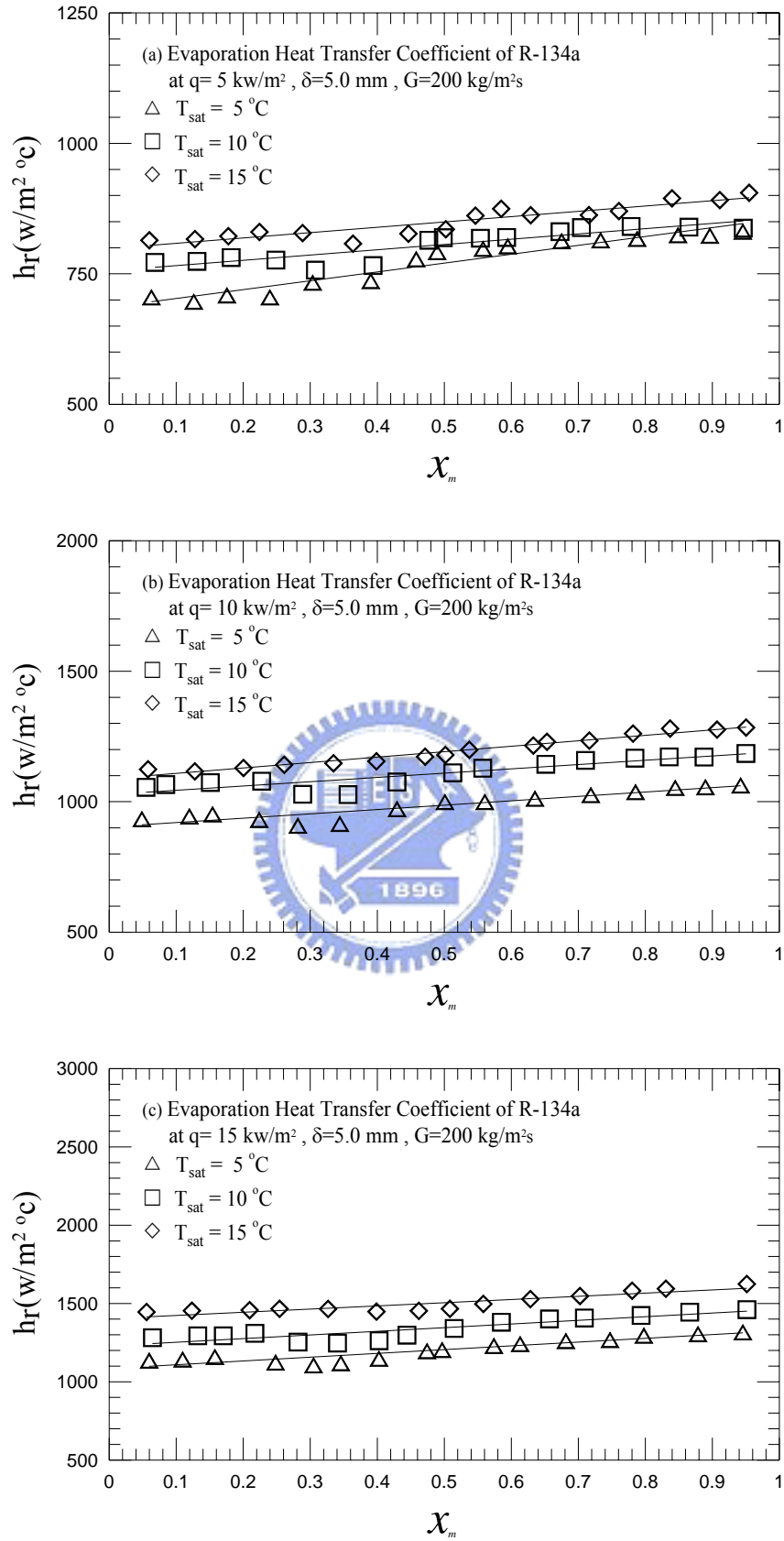


Fig. 4.55 Variations of R-134a evaporation heat transfer coefficient with vapor quality in  $\delta = 5.0 \text{ mm}$  narrow duct at  $G = 200 \text{ kg/m}^2\text{s}$  for various  $T_{\text{sat}}$  for (a)  $q = 5 \text{ kW/m}^2$ , (b)  $q = 10 \text{ kW/m}^2$  and (c)  $q = 15 \text{ kW/m}^2$ .

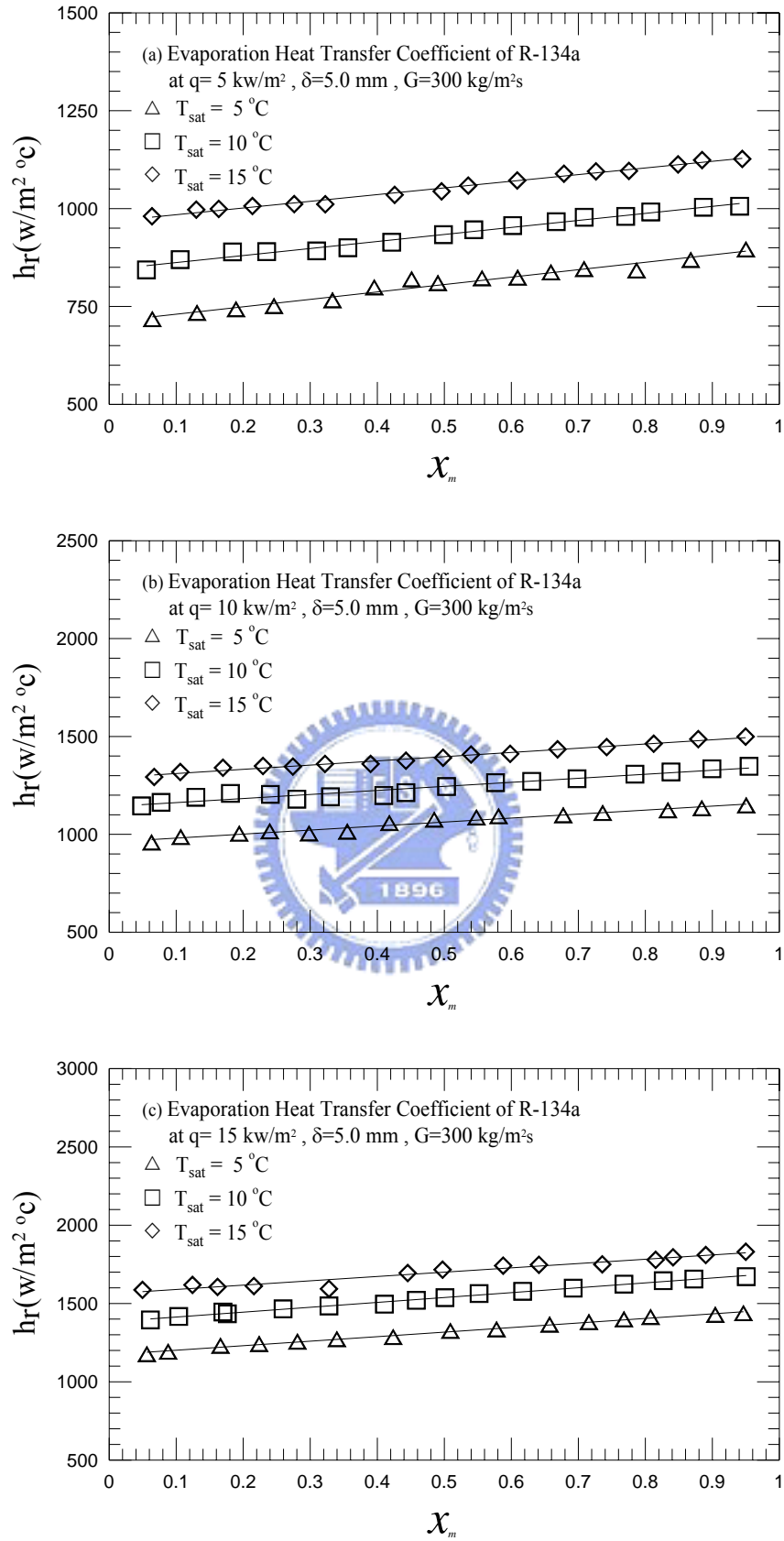


Fig. 4.56 Variations of R-134a evaporation heat transfer coefficient with vapor quality in  $\delta = 5.0 \text{ mm}$  narrow duct at  $G = 300 \text{ kg/m}^2\text{s}$  for various  $T_{\text{sat}}$  for (a)  $q = 5 \text{ kW/m}^2$ , (b)  $q = 10 \text{ kW/m}^2$  and (c)  $q = 15 \text{ kW/m}^2$ .

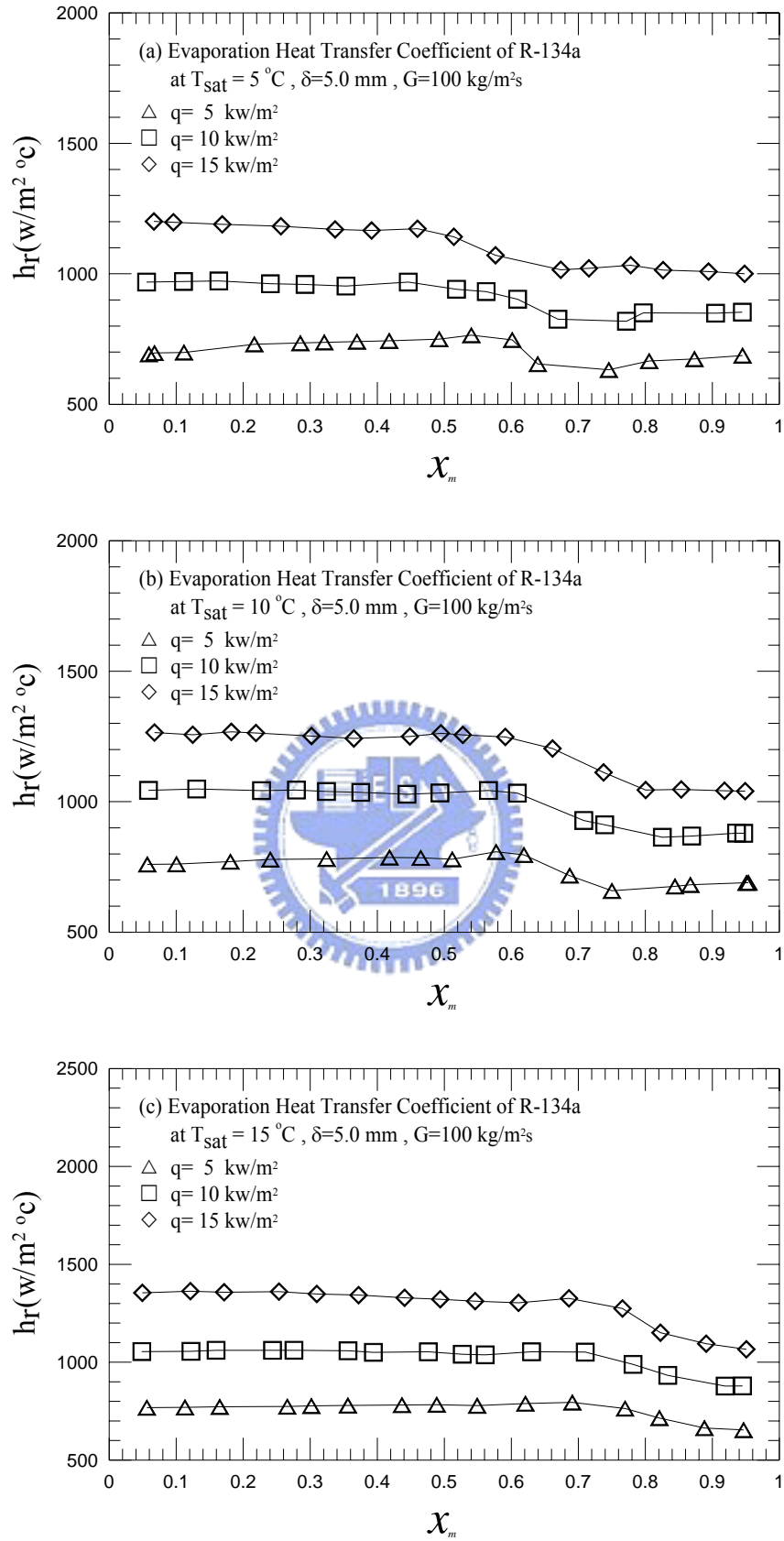


Fig. 4.57 Variations of R-134a evaporation heat transfer coefficient with vapor quality in  $\delta = 5.0\text{ mm}$  narrow duct at  $G = 100\text{ kg/m}^2\text{s}$  for various  $q$  for (a)  $T_{\text{sat}} = 5^\circ\text{C}$ , (b)  $T_{\text{sat}} = 10^\circ\text{C}$  and (c)  $T_{\text{sat}} = 15^\circ\text{C}$ .

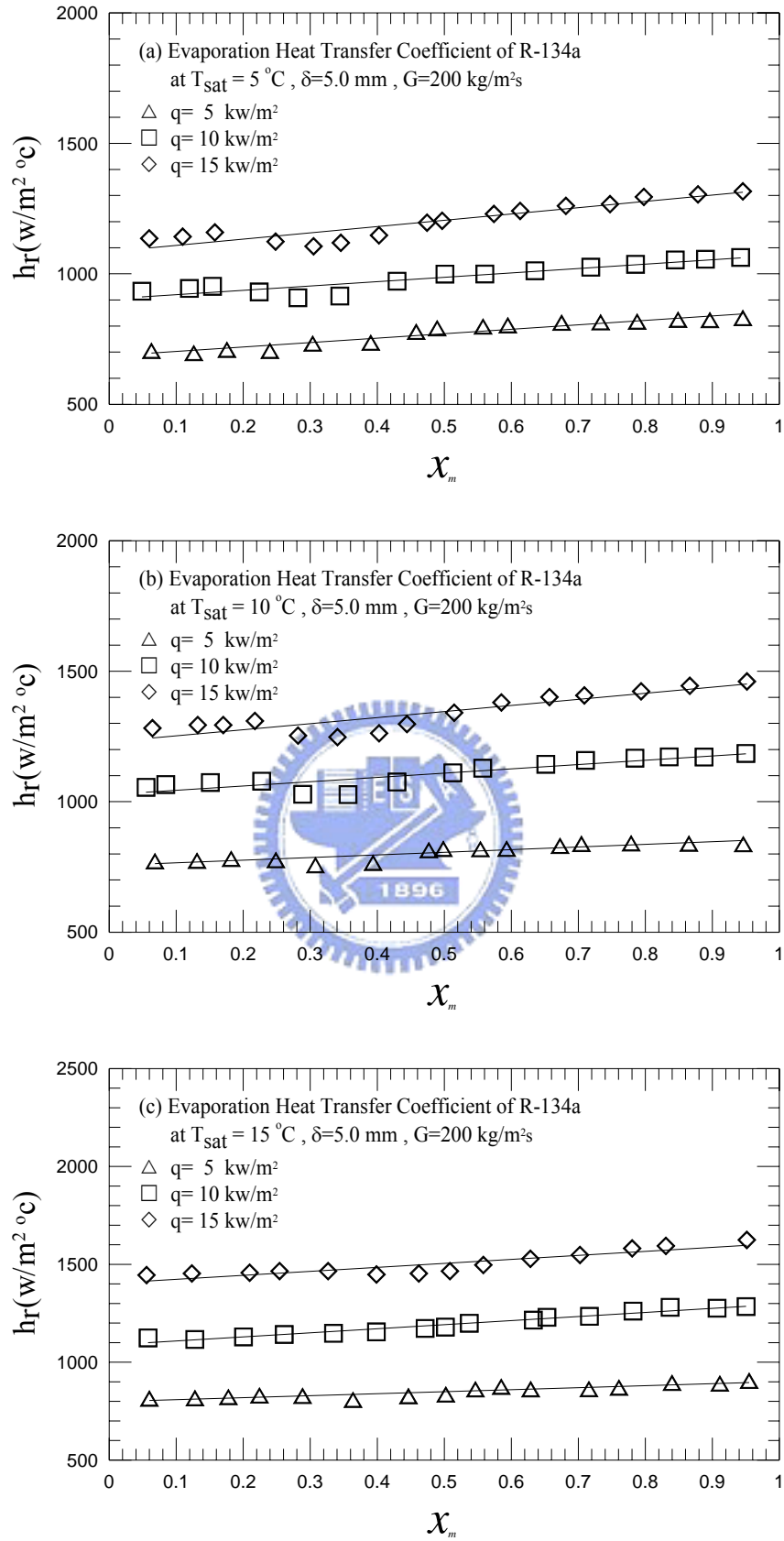


Fig. 4.58 Variations of R-134a evaporation heat transfer coefficient with vapor quality in  $\delta = 5.0\text{ mm}$  narrow duct at  $G = 200\text{ kg/m}^2\text{s}$  for various  $q$  for (a)  $T_{\text{sat}} = 5^\circ\text{C}$ , (b)  $T_{\text{sat}} = 10^\circ\text{C}$  and (c)  $T_{\text{sat}} = 15^\circ\text{C}$ .

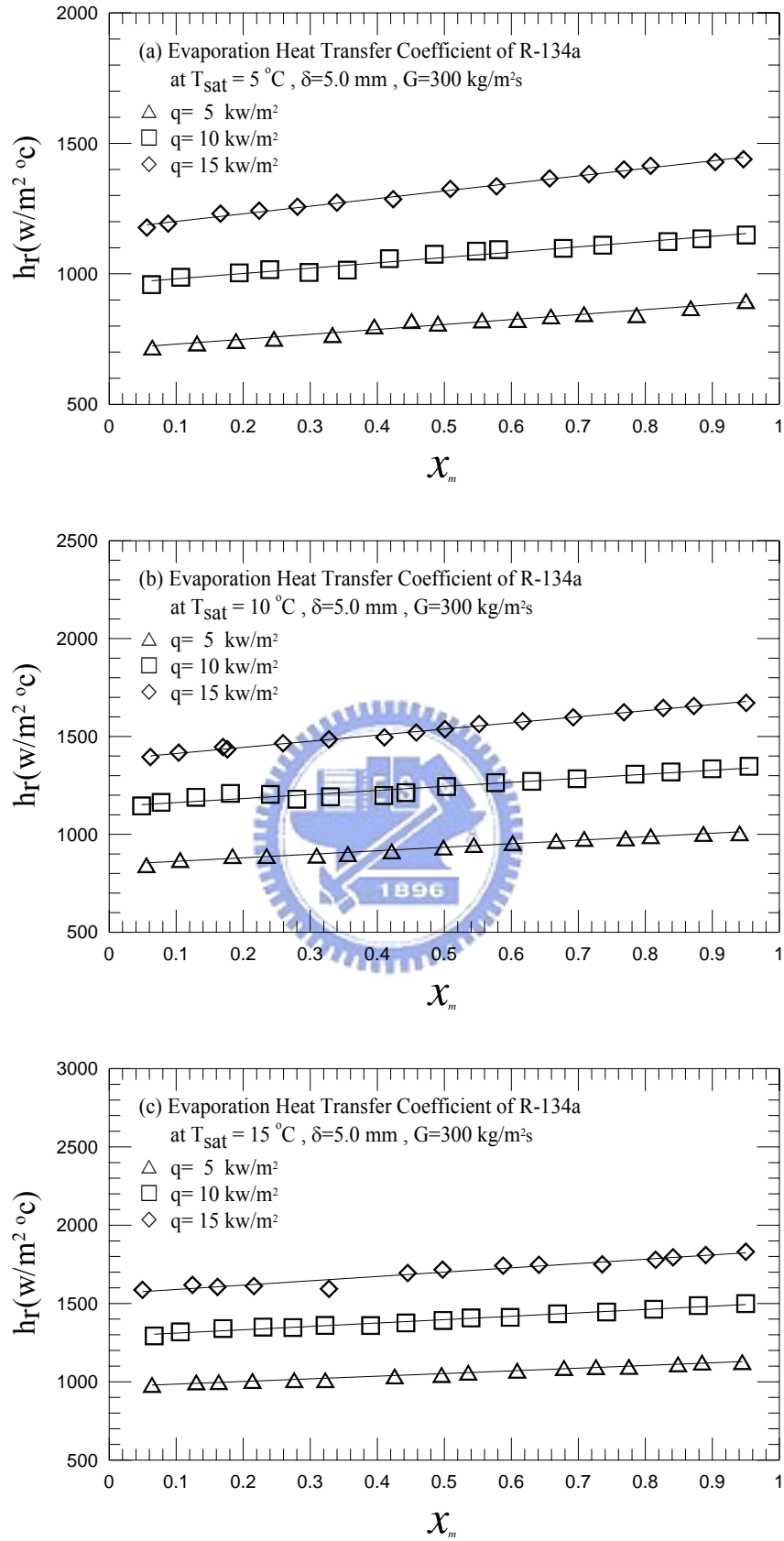


Fig. 4.59 Variations of R-134a evaporation heat transfer coefficient with vapor quality in  $\delta = 5.0\text{ mm}$  narrow duct at  $G = 300\text{ kg/m}^2\text{s}$  for various  $q$  for (a)  $T_{\text{sat}} = 5^\circ\text{C}$ , (b)  $T_{\text{sat}} = 10^\circ\text{C}$  and (c)  $T_{\text{sat}} = 15^\circ\text{C}$ .

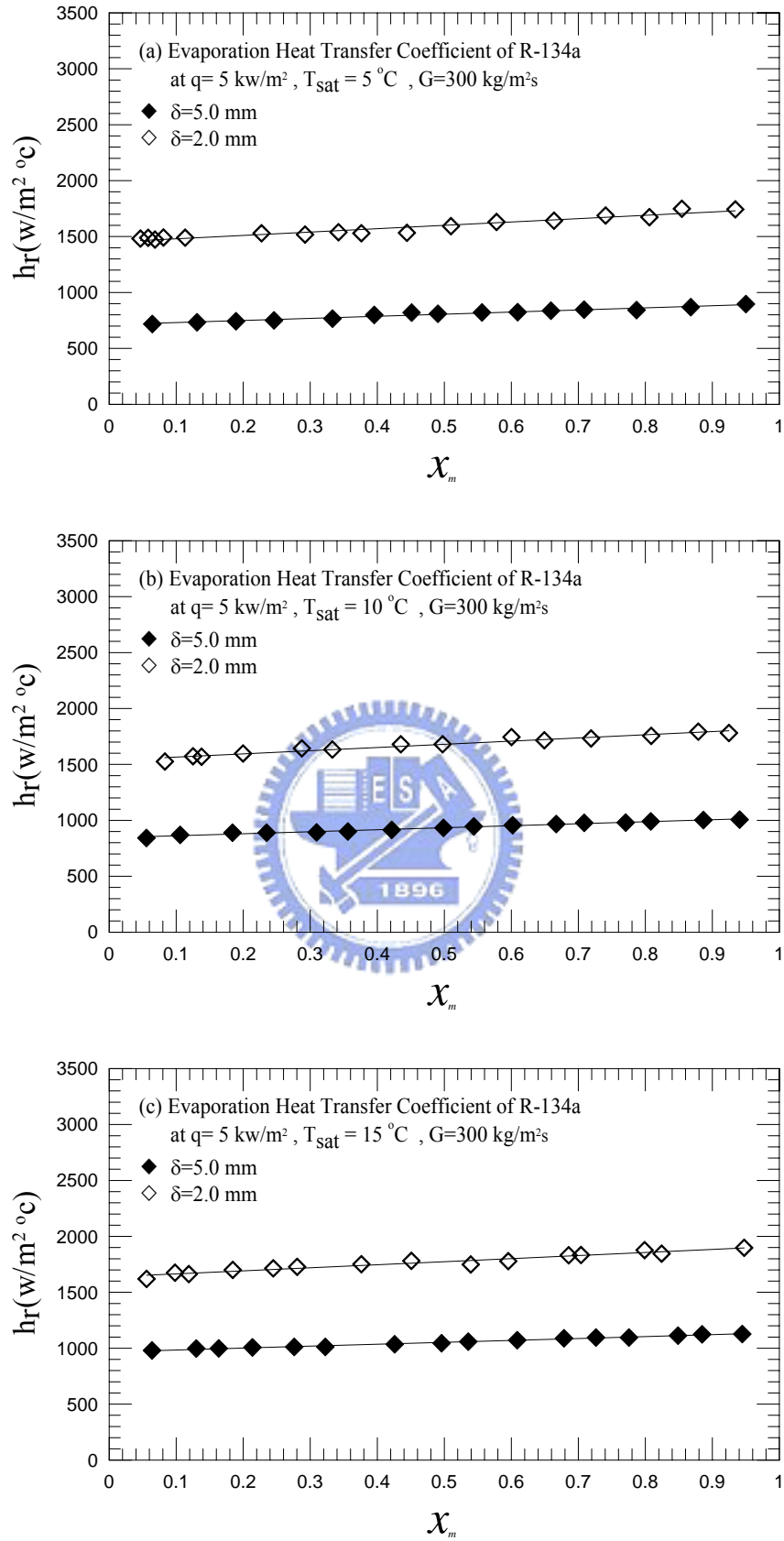


Fig. 4.60 Variations of R-134a evaporation heat transfer coefficient with vapor quality at  $q = 5 \text{ kW/m}^2$  and  $G = 300 \text{ kg/m}^2\text{s}$  for various  $\delta$  for (a)  $T_{\text{sat}} = 5^\circ\text{C}$ , (b)  $T_{\text{sat}} = 10^\circ\text{C}$  and (c)  $T_{\text{sat}} = 15^\circ\text{C}$ .

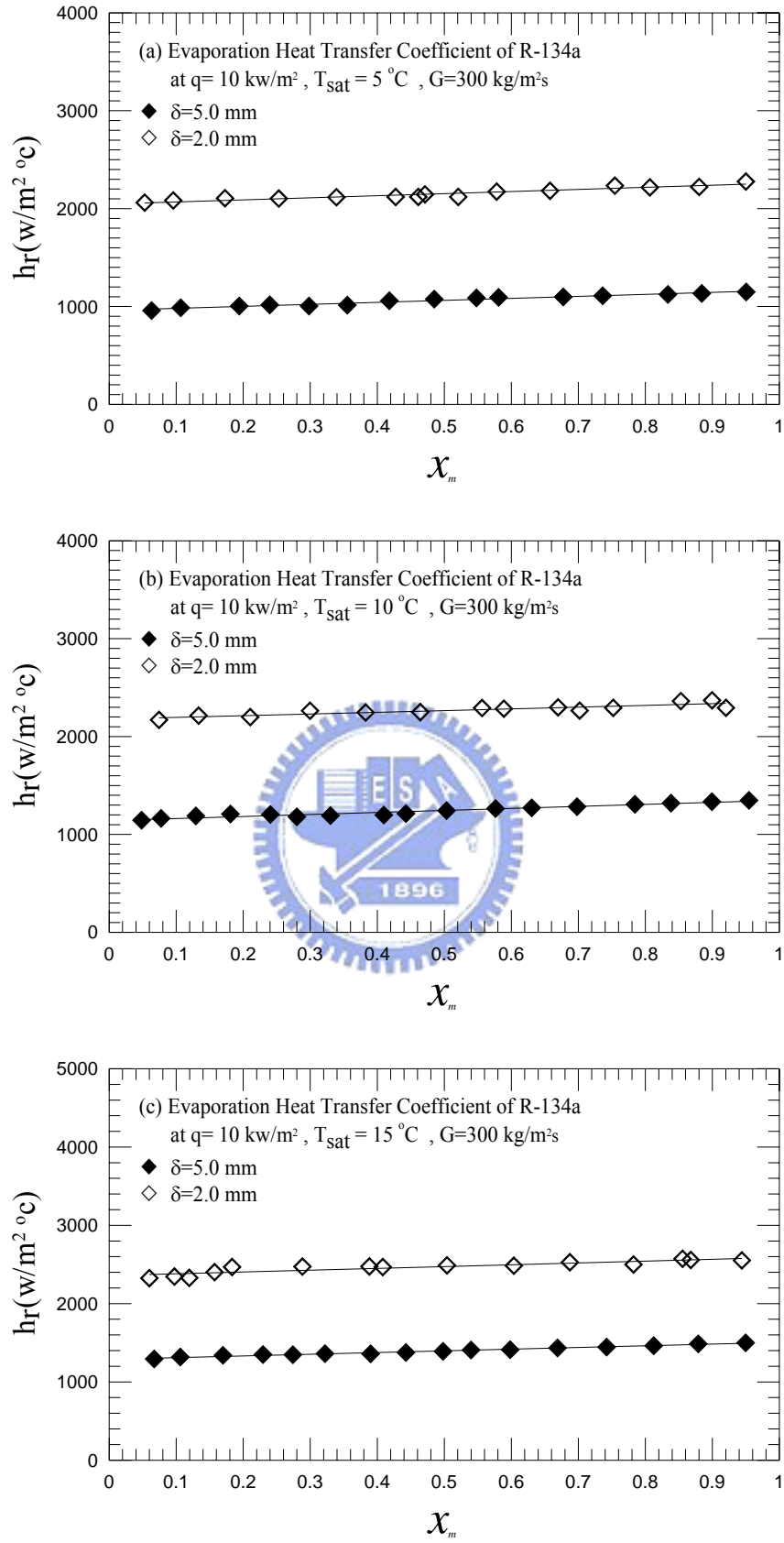


Fig. 4.61 Variations of R-134a evaporation heat transfer coefficient with vapor quality at  $q = 10 \text{ kW/m}^2$  and  $G = 300 \text{ kg/m}^2\text{s}$  for various  $\delta$  for (a)  $T_{\text{sat}} = 5^\circ\text{C}$ , (b)  $T_{\text{sat}} = 10^\circ\text{C}$  and (c)  $T_{\text{sat}} = 15^\circ\text{C}$ .



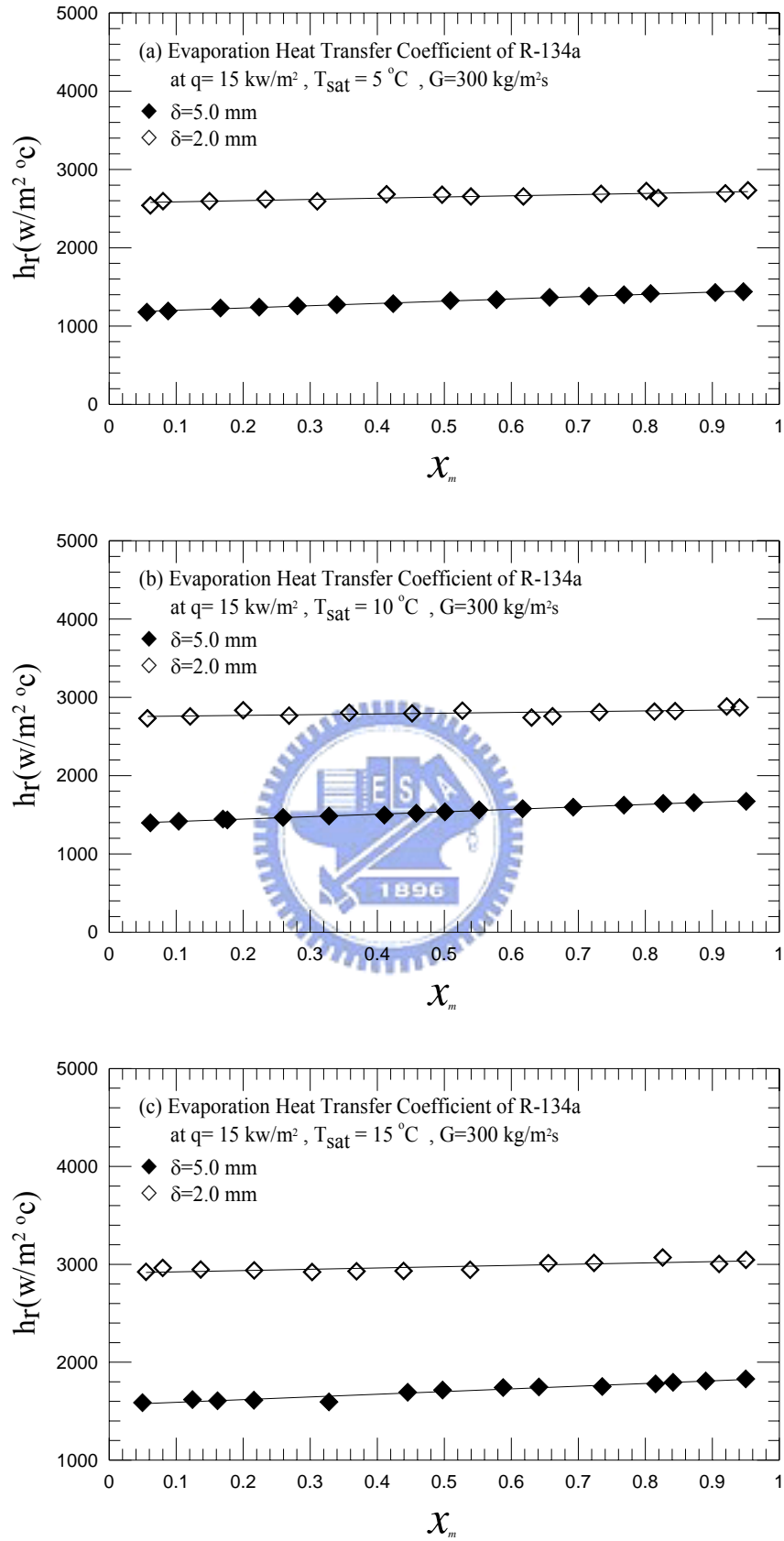


Fig. 4.62 Variations of R-134a evaporation heat transfer coefficient with vapor quality at  $q = 15 \text{ kW/m}^2$  and  $G = 300 \text{ kg/m}^2\text{s}$  for various  $\delta$  for (a)  $T_{\text{sat}} = 5^\circ\text{C}$ , (b)  $T_{\text{sat}} = 10^\circ\text{C}$  and (c)  $T_{\text{sat}} = 15^\circ\text{C}$ .

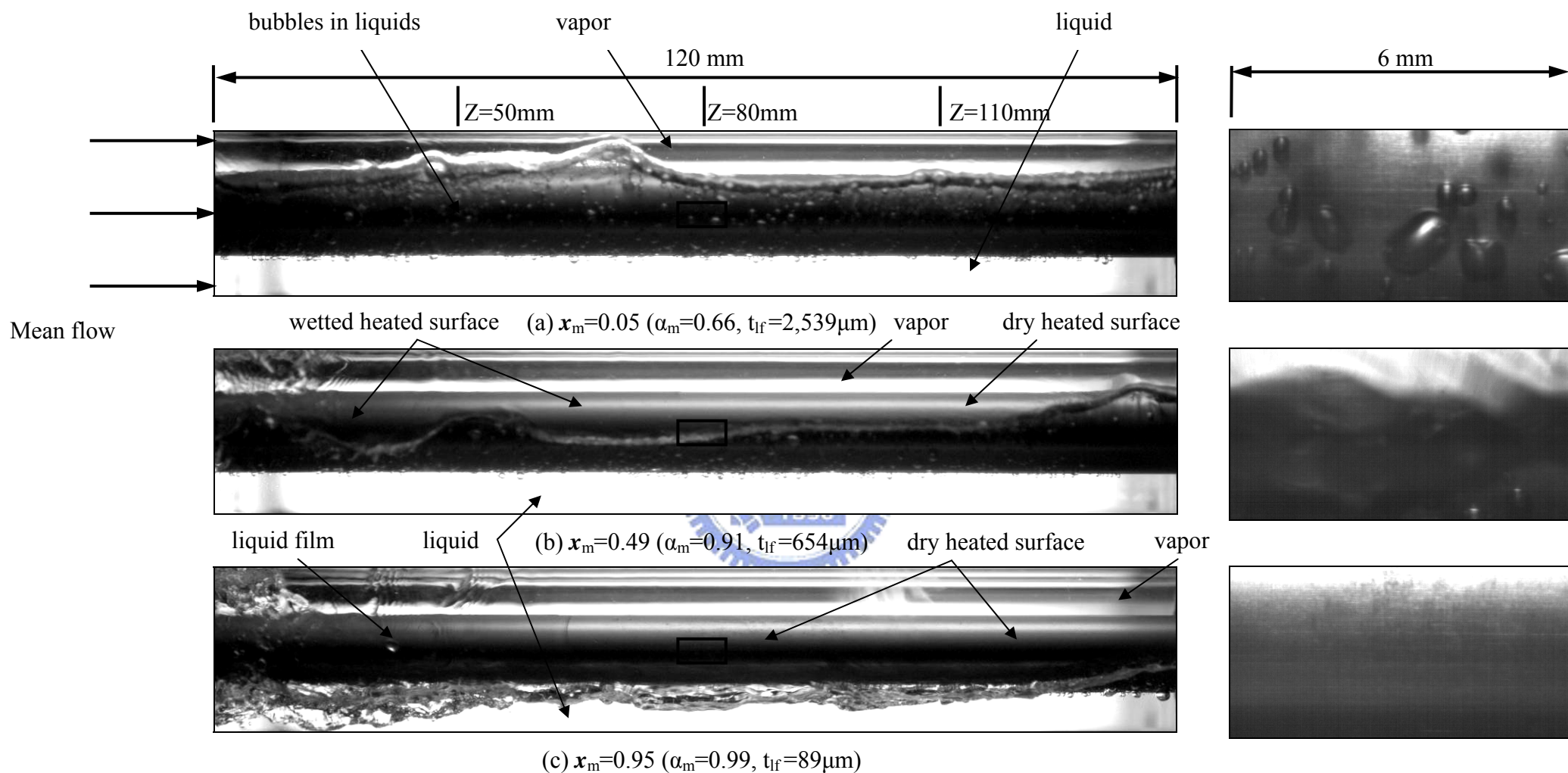


Fig.4.63 Photos of flow in the evaporation of R-134a in the entire duct and a small region around middle axial location at  $G=100 \text{ kg/m}^2\text{s}$ ,  $T_{\text{sat}} = 15^\circ\text{C}$ ,  $\delta = 5.0 \text{ mm}$ ,  $q = 5 \text{ kW/m}^2$  for (a)  $x_m = 0.05$ , (b)  $x_m = 0.49$  and (c)  $x_m = 0.95$ .

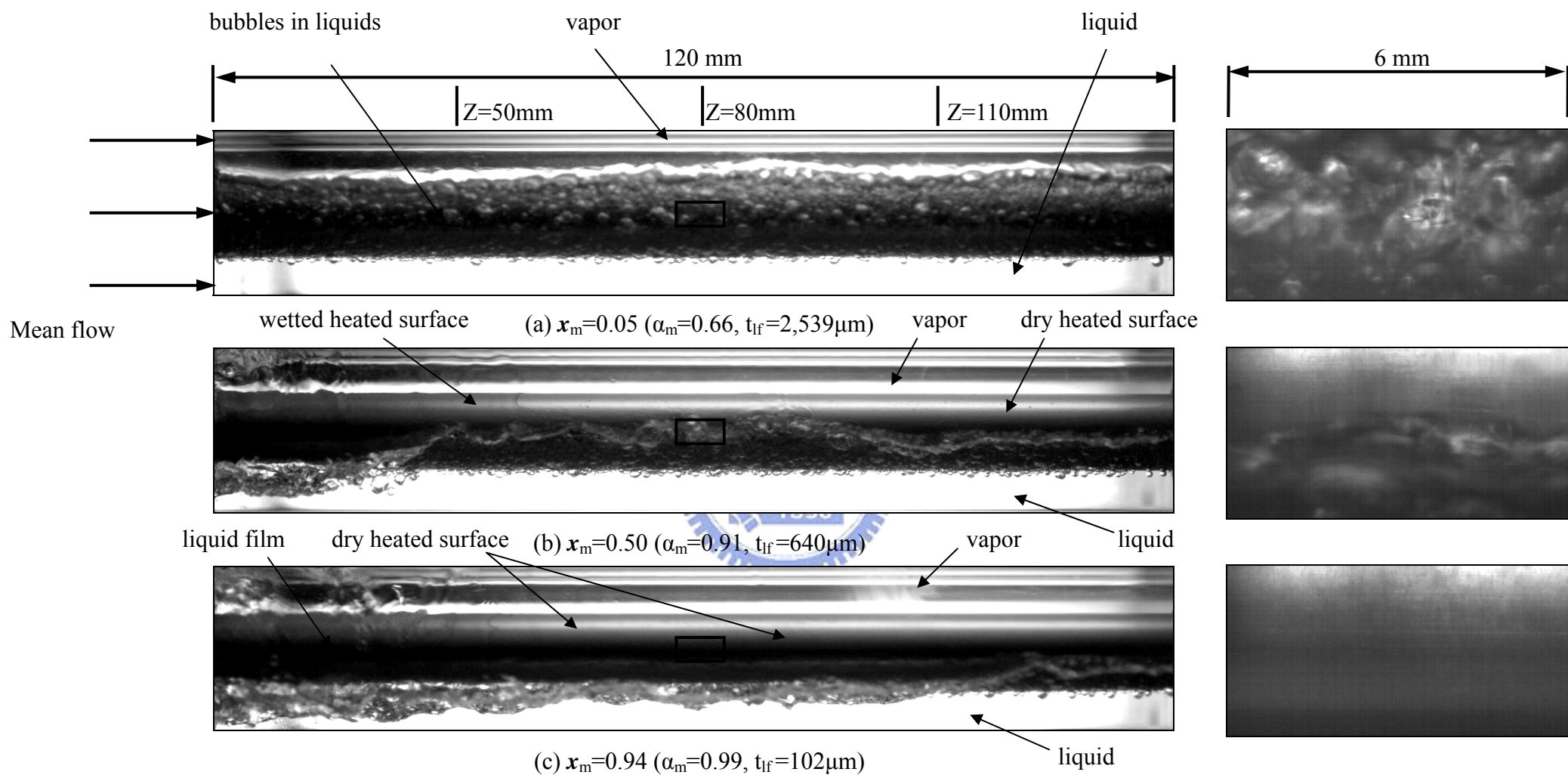


Fig.4.64 Photos of flow in the evaporation of R-134a in the entire duct and a small region around middle axial location at  $G=100 \text{ kg/m}^2\text{s}$ ,  $T_{\text{sat}} = 15^\circ\text{C}$ ,  $\delta = 5.0 \text{ mm}$ ,  $q = 15 \text{ kW/m}^2$  for (a)  $x_m = 0.05$ , (b)  $x_m = 0.50$  and (c)  $x_m = 0.94$ .

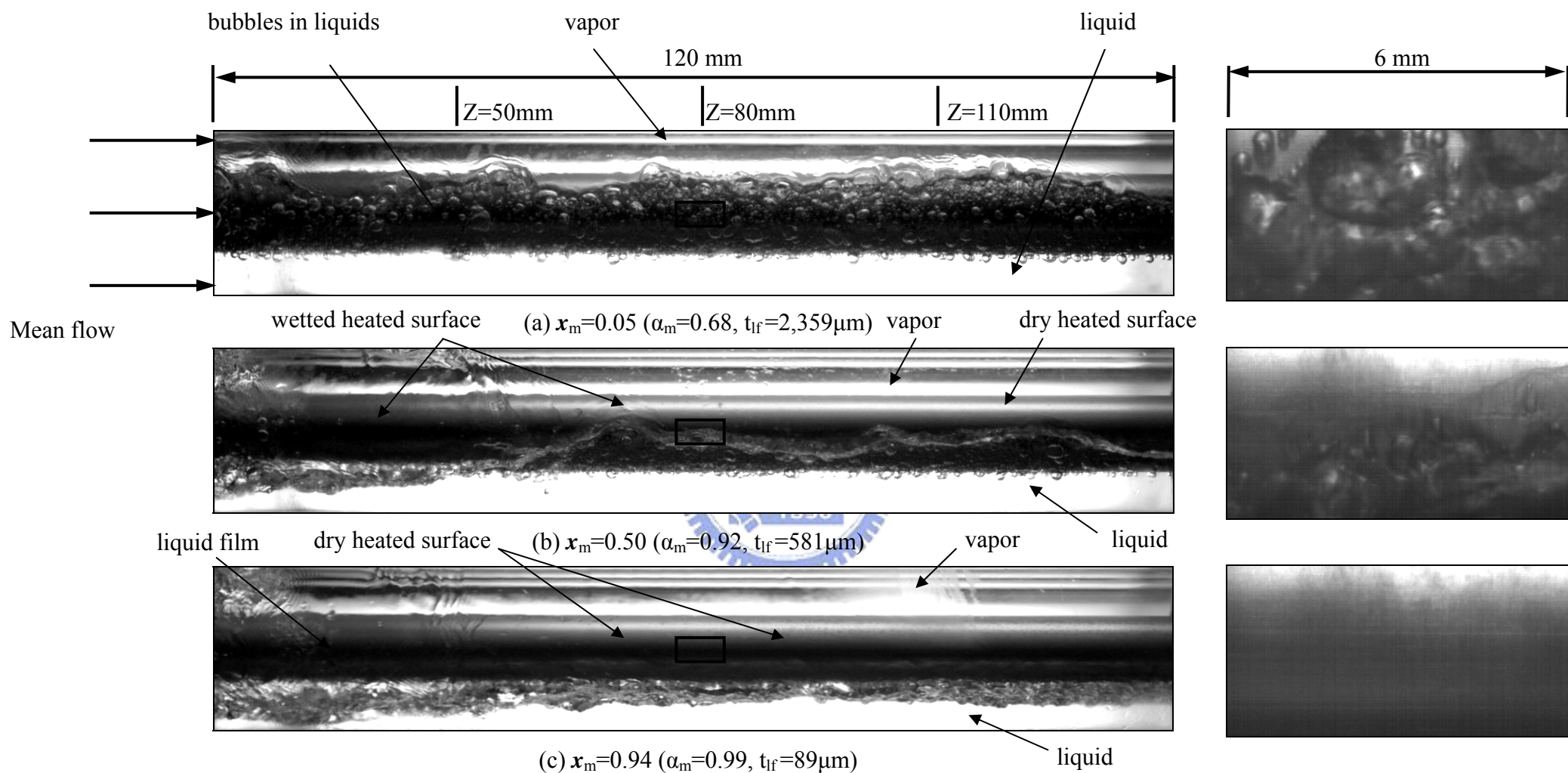


Fig.4.65 Photos of flow in the evaporation of R-134a in the entire duct and a small region around middle axial location at  $G=100 \text{ kg/m}^2\text{s}$ ,  $T_{\text{sat}} = 5^\circ\text{C}$ ,  $\delta = 5.0 \text{ mm}$ ,  $q = 15 \text{ kW/m}^2$  for (a)  $x_m = 0.05$ , (b)  $x_m = 0.50$  and (c)  $x_m = 0.94$ .



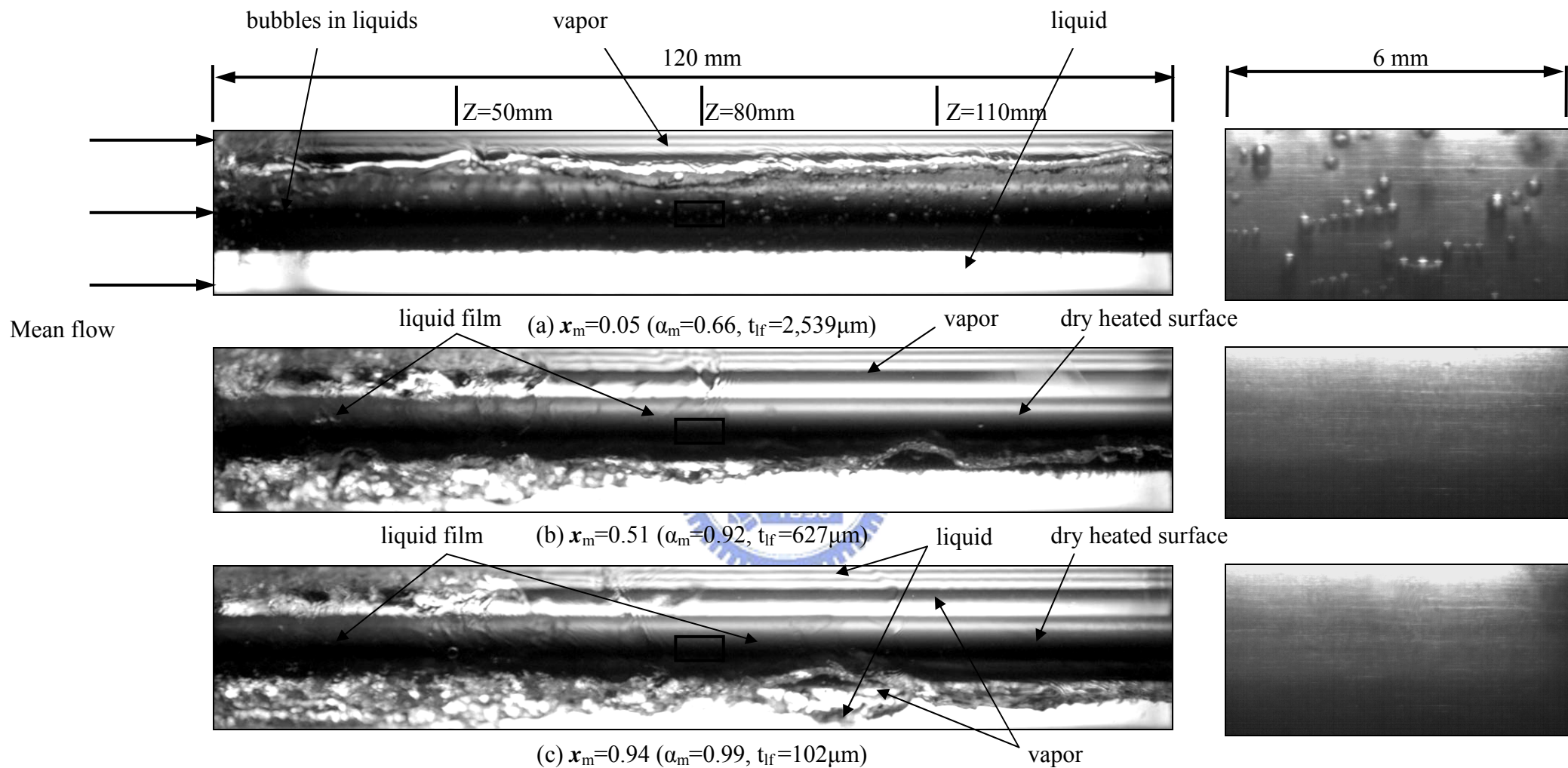


Fig.4.66 Photos of flow in the evaporation of R-134a in the entire duct and a small region around middle axial location at  $G=200 \text{ kg/m}^2\text{s}$ ,  $T_{\text{sat}} = 15^\circ\text{C}$ ,  $\delta = 5.0 \text{ mm}$ ,  $q = 5 \text{ kW/m}^2$  for (a)  $x_m = 0.05$ , (b)  $x_m = 0.51$  and (c)  $x_m = 0.94$ .

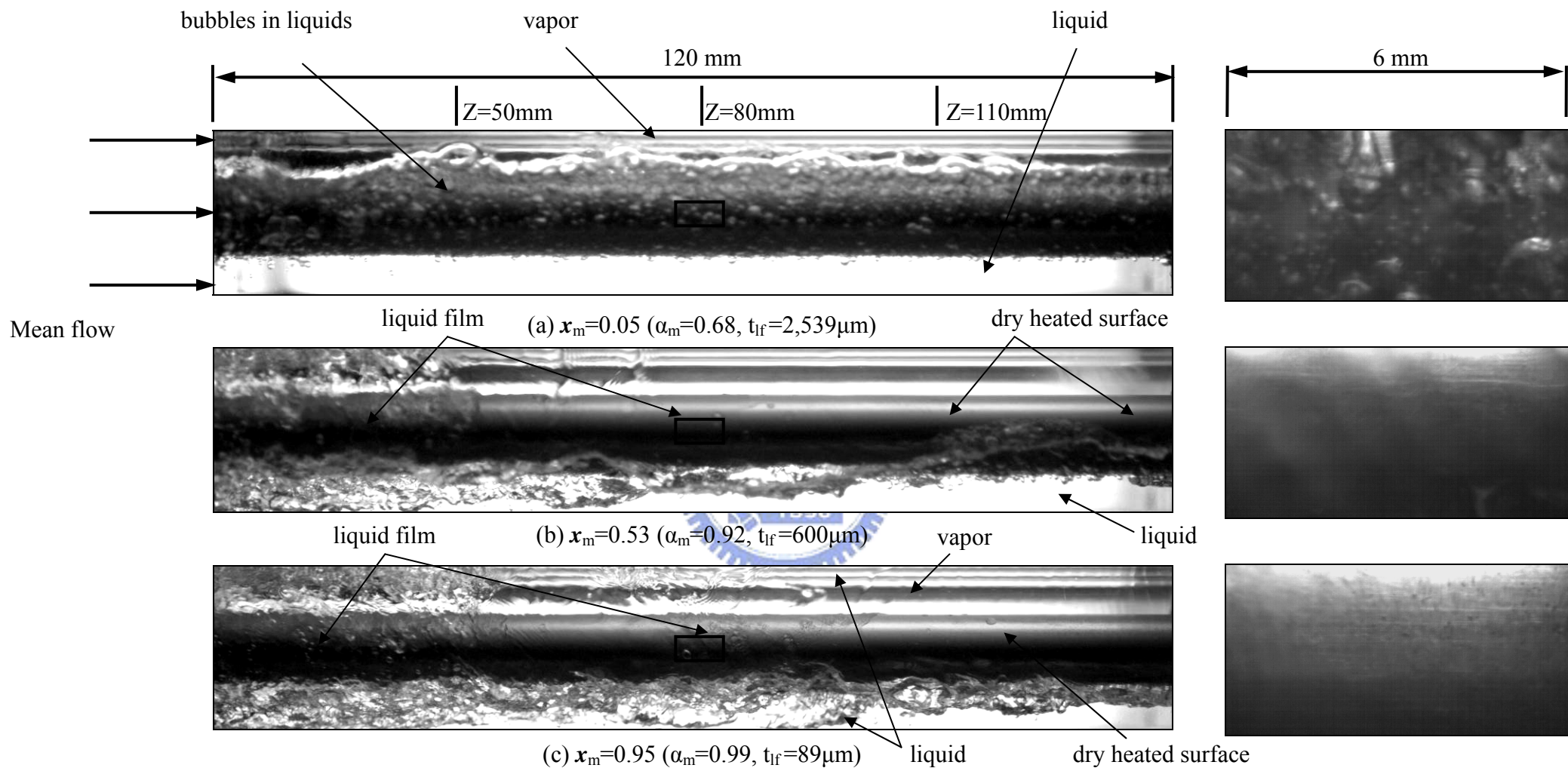


Fig.4.67 Photos of flow in the evaporation of R-134a in the entire duct and a small region around middle axial location at  $G=200 \text{ kg/m}^2\text{s}$ ,  $T_{\text{sat}} = 15^\circ\text{C}$ ,  $\delta = 5.0 \text{ mm}$ ,  $q = 15 \text{ kW/m}^2$  for (a)  $x_m = 0.05$ , (b)  $x_m = 0.53$  and (c)  $x_m = 0.95$ .

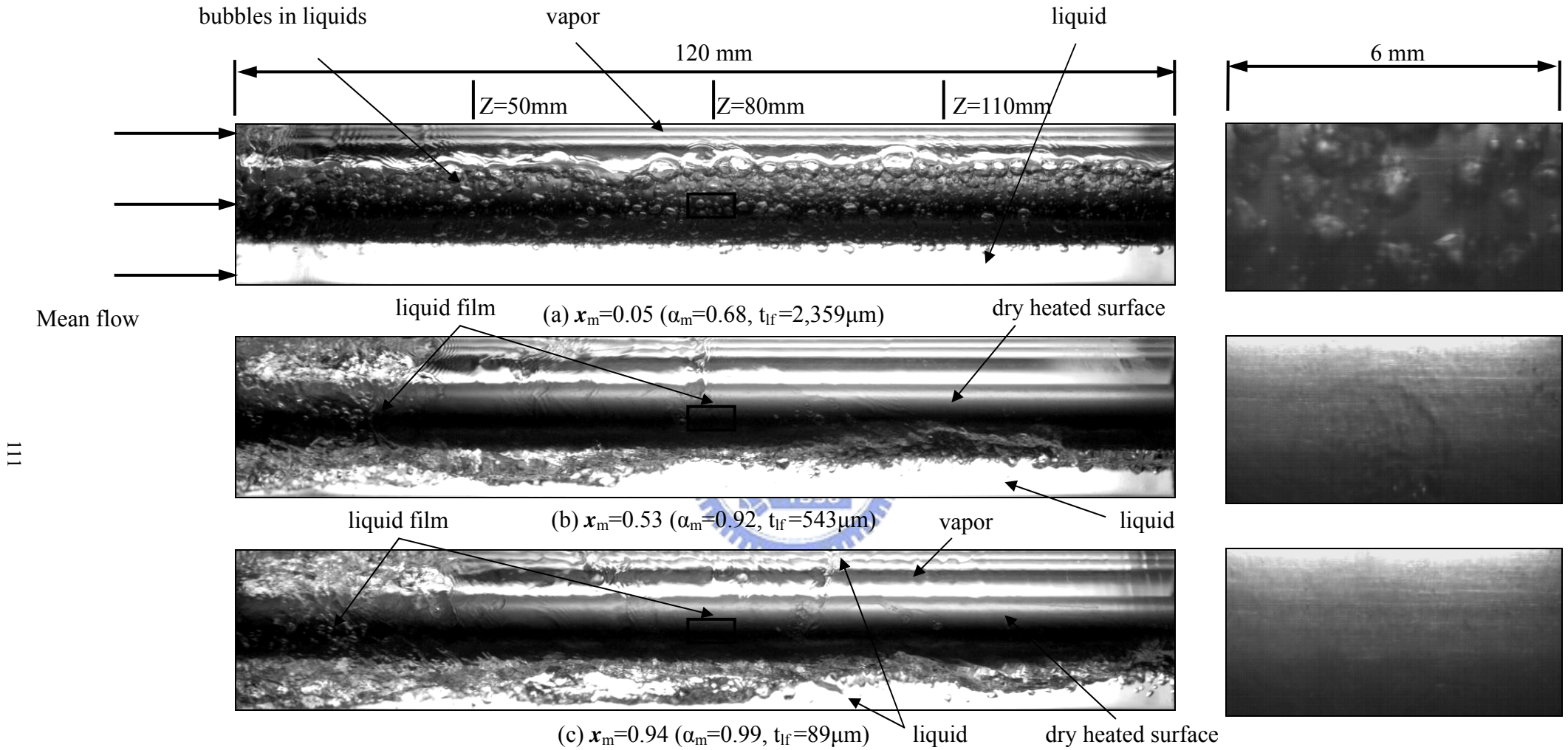


Fig.4.68 Photos of flow in the evaporation of R-134a in the entire duct and a small region around middle axial location at  $G=200 \text{ kg/m}^2\text{s}$ ,  $T_{\text{sat}} = 5^\circ\text{C}$ ,  $\delta = 5.0 \text{ mm}$ ,  $q = 15 \text{ kW/m}^2$  for (a)  $x_m = 0.05$ , (b)  $x_m = 0.53$  and (c)  $x_m = 0.94$ .



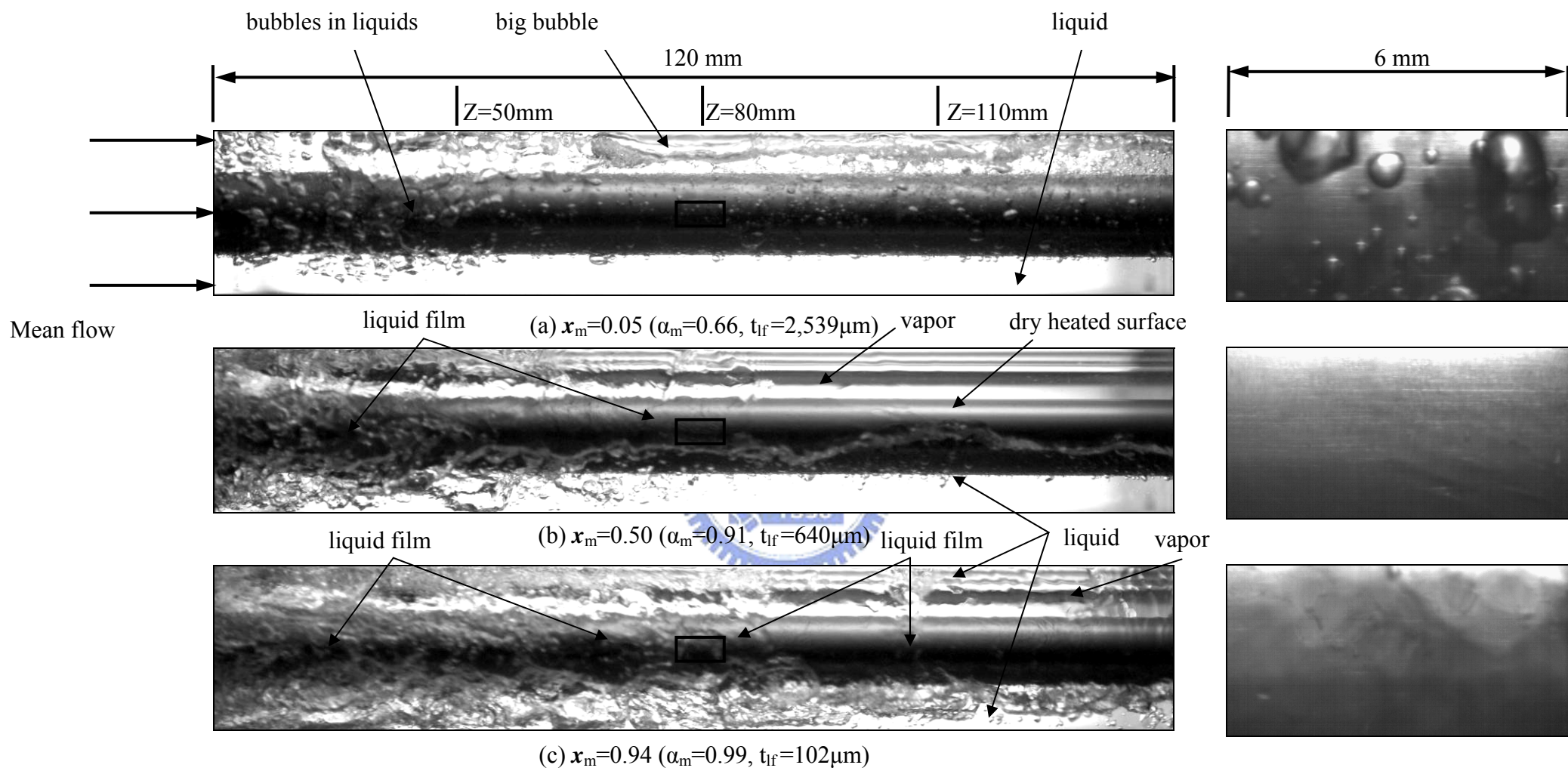


Fig.4.69 Photos of flow in the evaporation of R-134a in the entire duct and a small region around middle axial location at  $G=300 \text{ kg/m}^2\text{s}$ ,  $T_{\text{sat}} = 15^\circ\text{C}$ ,  $\delta = 5.0 \text{ mm}$ ,  $q = 5 \text{ kW/m}^2$  for (a)  $x_m = 0.05$ , (b)  $x_m = 0.50$  and (c)  $x_m = 0.94$ .

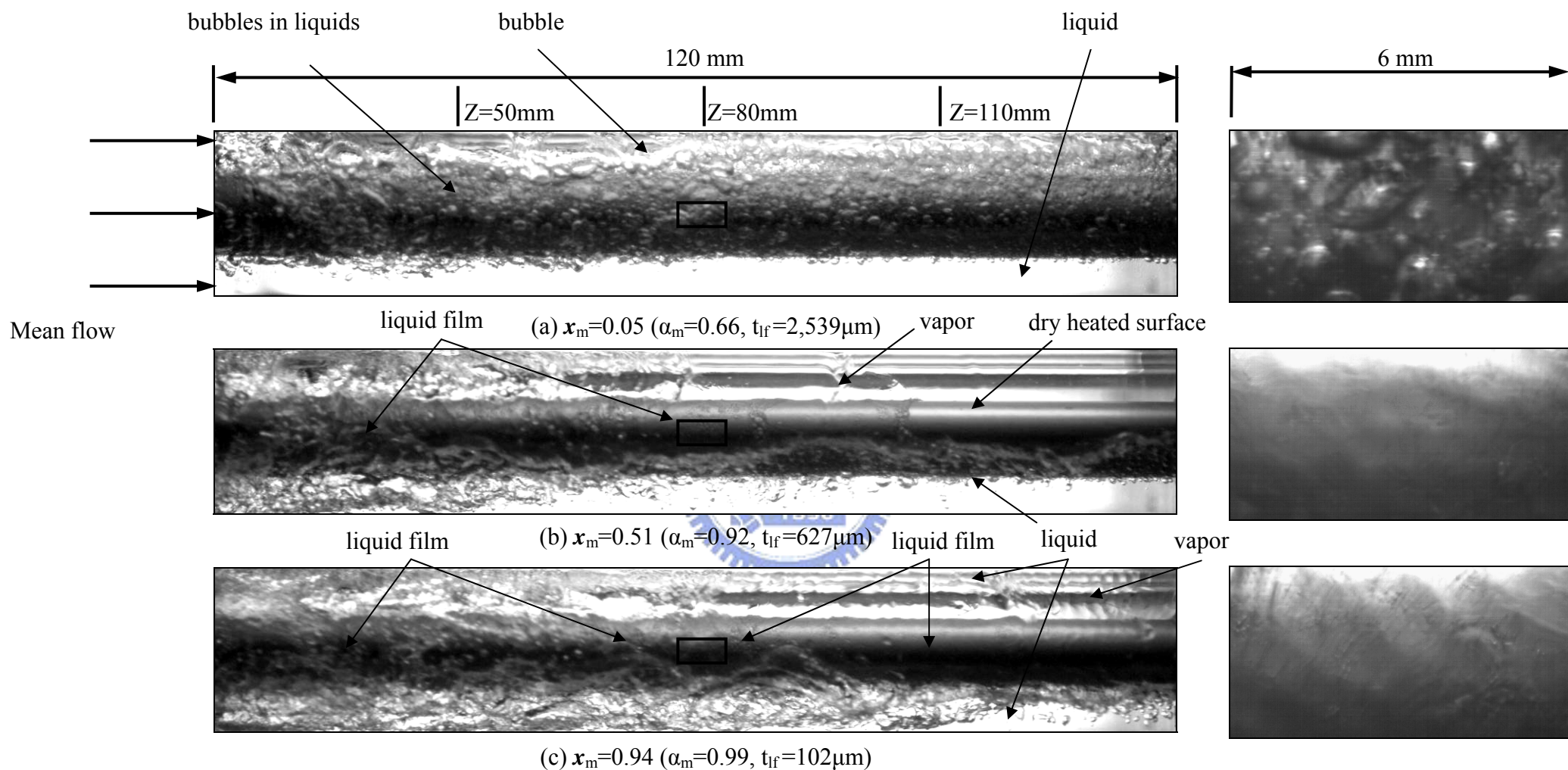


Fig.4.70 Photos of flow in the evaporation of R-134a in the entire duct and a small region around middle axial location at  $G=300\text{ kg/m}^2\text{s}$ ,  $T_{\text{sat}} = 15^\circ\text{C}$ ,  $\delta = 1.0\text{ mm}$ ,  $q = 15\text{ kW/m}^2$  for (a)  $x_m = 0.05$ , (b)  $x_m = 0.51$  and (c)  $x_m = 0.94$ .

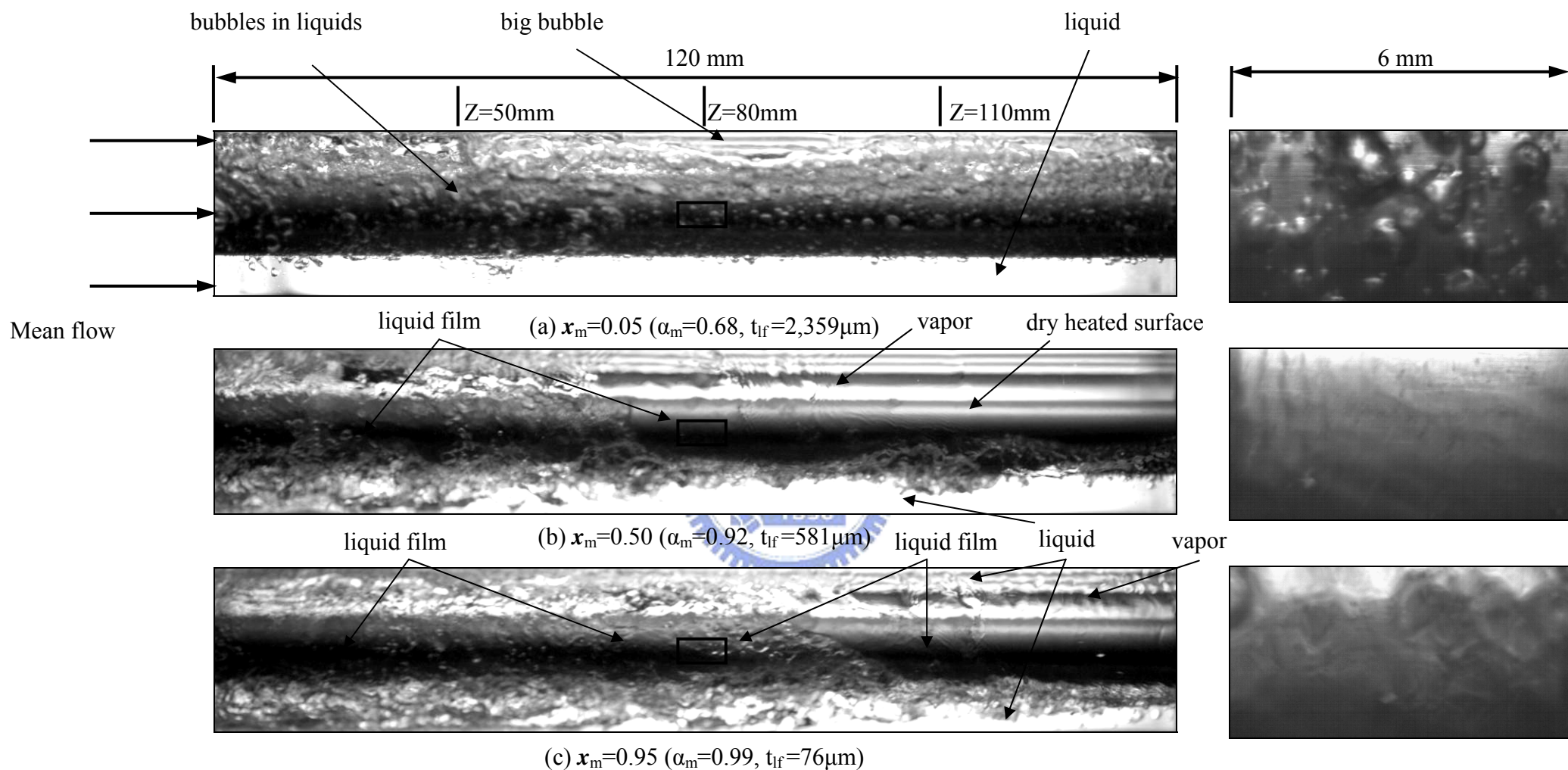


Fig.4.71 Photos of flow in the evaporation of R-134a in the entire duct and a small region around middle axial location at  $G=300 \text{ kg/m}^2\text{s}$ ,  $T_{\text{sat}} = 5^\circ\text{C}$ ,  $\delta = 5.0 \text{ mm}$ ,  $q = 15 \text{ kW/m}^2$  for (a)  $x_m = 0.05$ , (b)  $x_m = 0.50$  and (c)  $x_m = 0.95$ .



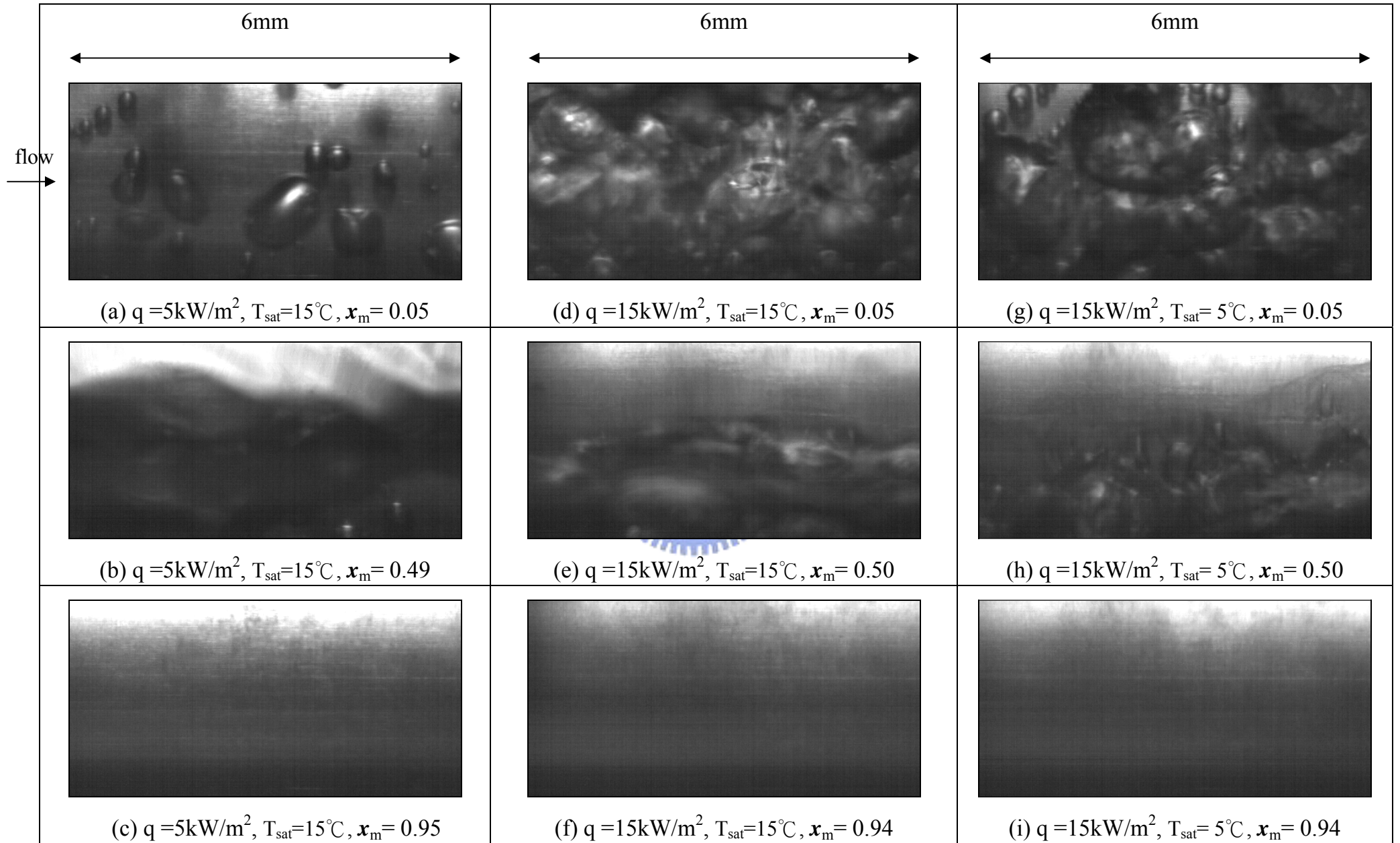


Fig. 4.72 Photos of flow in the evaporation of R-134a in a small region around middle axial location at  $\delta = 5.0$  mm and  $G = 100$  kg/m<sup>2</sup>s for various imposed heat fluxes, saturated temperatures and vapor quality.

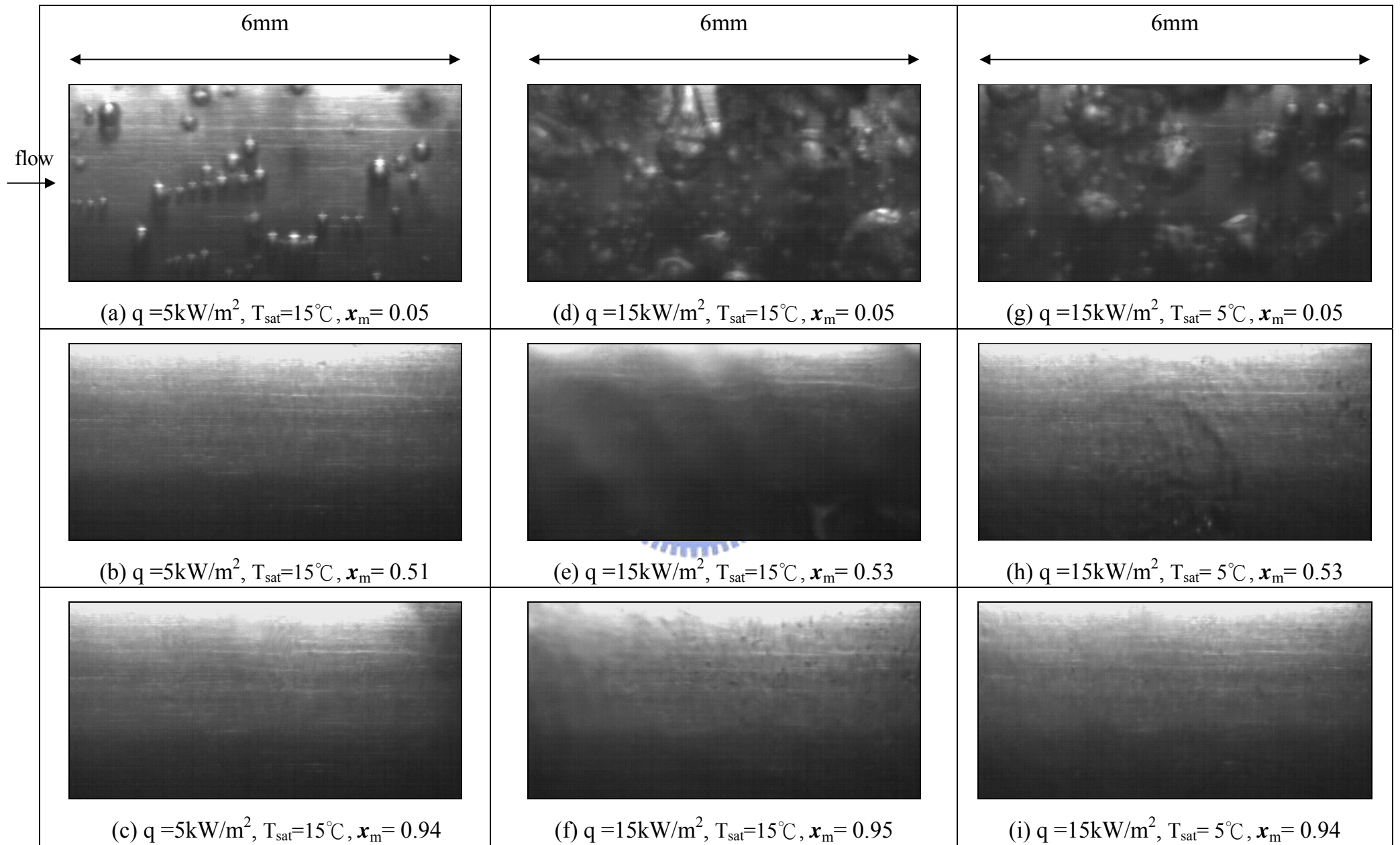


Fig. 4.73 Photos of flow in the evaporation of R-134a in a small region around middle axial location at  $\delta = 5.0$  mm and  $G = 200$  kg/m<sup>2</sup>s for various imposed heat fluxes, saturated temperatures and vapor quality.

Fig. 4.74 Photos of flow in the evaporation of R-134a in a small region around middle axial location at  $\delta = 5.0$  mm and  $G=300$  kg/m<sup>2</sup>s for various imposed heat fluxes, saturated temperatures and vapor quality.

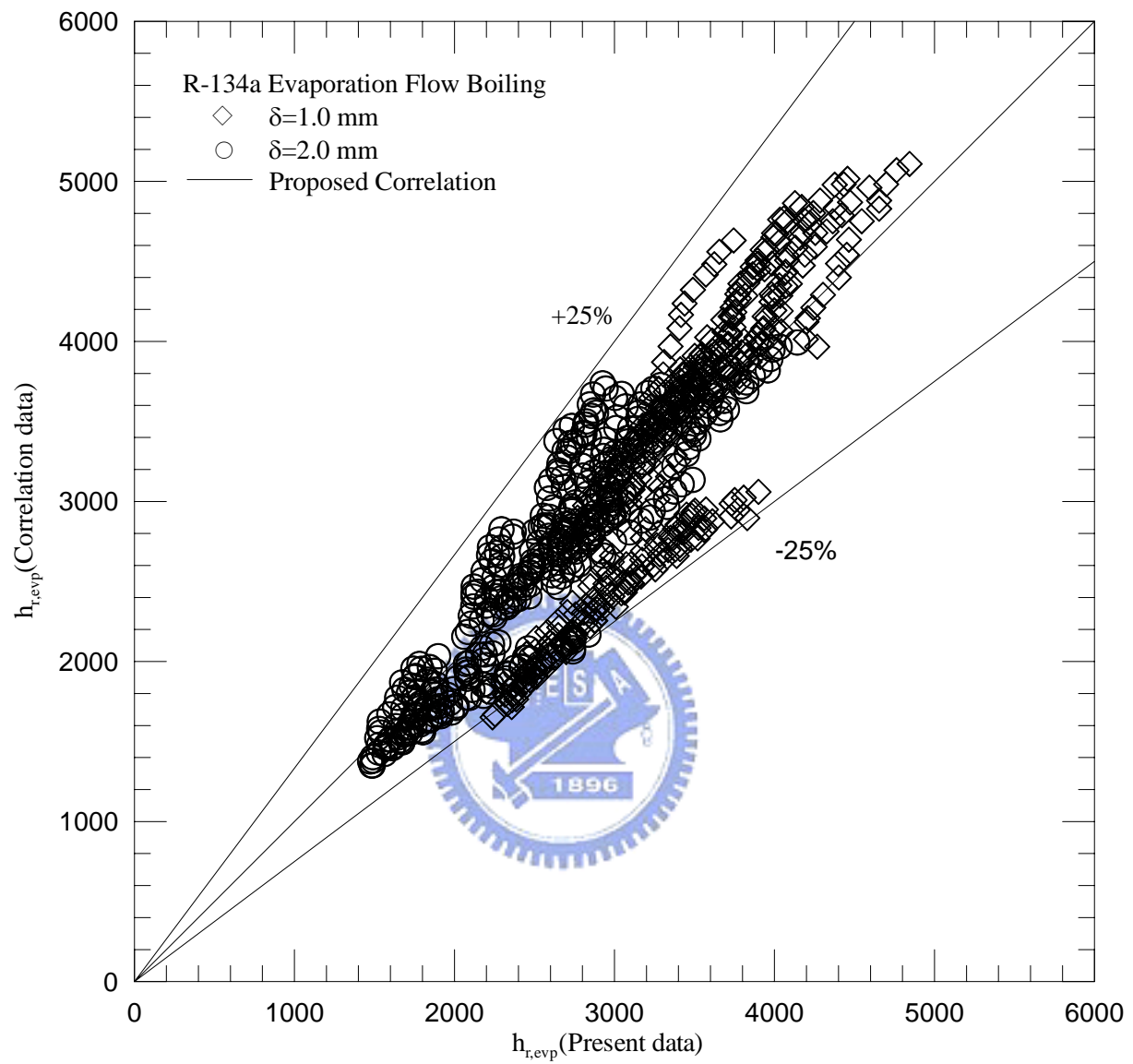


Fig. 4.75 Comparison of the measured data for heat transfer coefficient for the evaporation of R-134a in gap of 1.0 mm and 2.0 mm narrow ducts with the proposed correlation.



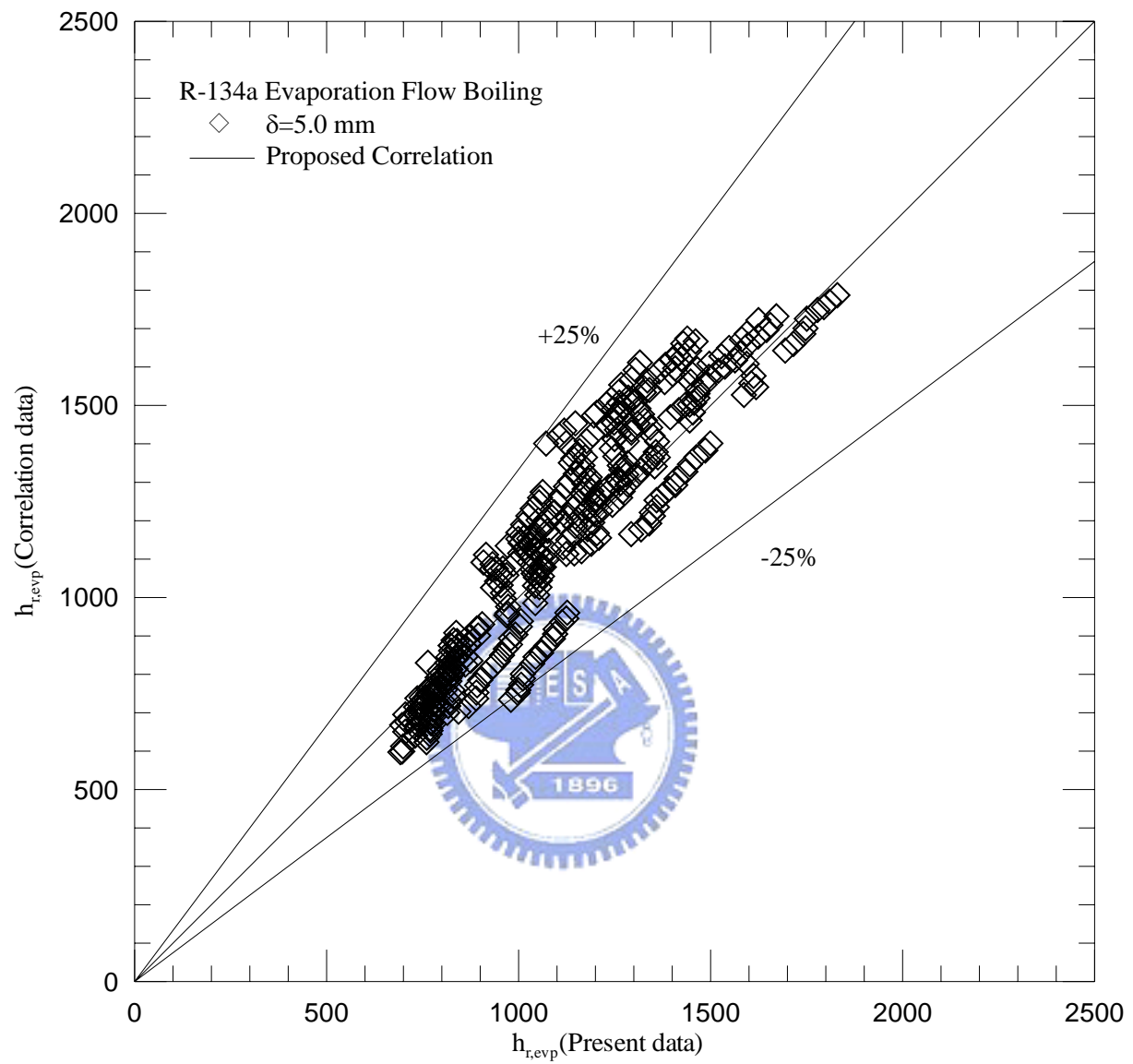


Fig. 4.76 Comparison of the measured data for heat transfer coefficient for the evaporation of R-134a in gap of 5.0 mm wider duct with the proposed correlation.



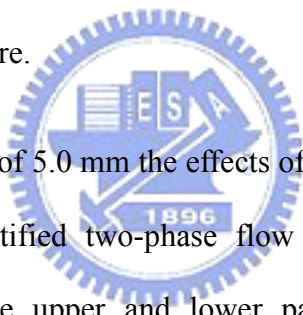
## CHAPTER 5

### CONCLUDING REMARKS

In this study, we have experimentally measured the heat transfer coefficients and visualized the two-phase flow patterns for the R-134a evaporation in the horizontal narrow annular ducts with  $\delta=1.0, 2.0$  and  $5.0$  mm. The effects of the refrigerant saturated temperature, mass flux, imposed heat flux, vapor quality and gap size of R-134a on the evaporation heat transfer coefficients at the middle axial location of the duct have been examined in detail. A summary of the major findings from the present results is given in the following.

- (1) The R-134a evaporation heat transfer coefficient in the small ducts ( $\delta=1.0 \cdot 2.0$  mm) increases almost linearly with the vapor quality and the increase is more significant at a higher refrigerant mass flux. Besides, increases in the refrigerant mass flux and saturated temperature and imposed heat flux can substantially improve the evaporation heat transfer. The effects of  $G$  and  $T_{\text{sat}}$  on  $h_r$  are less pronounced for  $\delta=1.0$  mm.
- (2) The effects of the refrigerant vapor quality, saturated temperature, imposed heat flux and mass flux in the wider annular duct with  $\delta=5.0$  mm on the R-134a evaporation heat transfer coefficient exhibit similar trends to that in the narrow duct for  $\delta=1.0$  and  $2.0$  mm. But partial dryout of the liquid film on the heating surface at high  $x_m$  and low mass flux occurs, leading to a reduction in  $h_r$  at increasing  $x_m$ .
- (3) Reducing the gap size of the duct causes a significant increase in the R-134a evaporation heat transfer coefficient.
- (4) In flow visualization for the small ducts with  $\delta=1.0$  and  $2.0$  mm the bubble nucleation on

the heating surface is found to be important at low vapor quality. Besides, at low vapor quality merging of small bubbles to form big bubbles and merging of big bubbles into bubble slugs take place, which is more pronounced at the smaller duct gap for  $\delta=1.0$  mm. Moreover, bubbles dispersed in a large liquid slug appear in the duct. At the intermediate vapor quality some bubble nucleation on the heating surface also exists and the flow in the duct is dominated by the vapor flow over thin liquid film around the inner pipe, an annular two-phase flow. Irregular waves appear at the vapor-liquid interface. At the very high vapor quality bubble nucleation can still be seen at high imposed heat flux although the liquid film covering the heating surface is relatively thin. At this high quality the duct is also dominated by the annular two-phase flow. The annular two-phase flow prevails in a larger portion of the duct at higher imposed flux, lower refrigerant mass flux, and higher refrigerant saturated temperature.

- 
- (5) In the duct with the wider gap of 5.0 mm the effects of the gravity on the evaporating flow are stronger, resulting a stratified two-phase flow with the vapor and liquid flows respectively dominated in the upper and lower parts of the duct. Besides, at low refrigerant mass flux and high vapor quality dryout of the liquid film on the heating surface occurs at some downstream locations. These dryout locations move upstream at higher vapor quality, higher imposed heat flux and lower refrigerant saturated temperature.
- (6) Empirical equation to correlate the present data for the heat transfer coefficient for the R-134a evaporation in the annular ducts are provided.

## REFERENCES

1. Alberto Cavallini, Working fluids for mechanical refrigeration- Invited paper presented at the 19<sup>th</sup> International Congress of Refrigeration, The Hague, Int. J. Refrig. 19 (1996) 485-496.
2. S. Devotta, A.V. Waghmare, N.N. Sawant, B.M. Domkundwar, Alternatives to HCFC-22 for air conditioners, Applied Thermal Engineering 21 (2001) 703-715.
3. S.G. Kandlikar, Fundamental issues related to flow boiling in minichannels and microchannels, Experimental Thermal and Fluid Science 26 (2002) 389-407.
4. S.G. Kandlikar, and W.J. Grande, Evolution of microchannel flow passages-thermohydraulic performance and fabrication technology, Heat Transfer Engineering 24 (1) (2003) 3-17.
5. P.A. Kew, K. Cornwell, Correlations for the prediction of boiling heat transfer in small-diameter channels, Applied Thermal Engineering 17 (1997) 705-715.
6. X. F. Peng, B. X. Wang, G. P. Peterson and H. B. Ma, Experimental investigation of heat transfer in flat plates with rectangular microchannels, Int. J. heat Mass Transfer 38 (1) (1995) 127-137
7. X. F. Peng and G. P. Peterson, Convective heat transfer and flow friction for water flow in microchannel structures, Int. J. Heat Mass Transfer 39 (12) (1996) 2599-2608.
8. B. Agostini, B. Watel, A. Bontemps and B. Thonon, Friction factor and heat transfer coefficient of R134a liquid flow in mini-channels, Applied Thermal Engineering 22 (16) (2002) 1821-1834.
9. V. Gnielinski, New equations for heat and mass transfer in turbulent pipe and channel flow, International Chemical Engineering 16 (2) (1976) 359-368.

10. F. W. Dittus, L. M. K. Boelter, Heat transfer in automobile radiator of the tube type, Publication in Engineering, University of California, Berkley, (2) (1930) 250.
11. G. M. Lazarek and S. H. Black, Evaporative heat transfer, pressure drop and critical heat flux in a small vertical tube with R-113, Int. J. Heat Mass Transfer 25 (1982) 945-960.
12. Chi-chuan Wang and Ching-shan Chiang, Two-phase heat transfer characteristics for R-22/R-407C in a 6.5-mm smooth tube, Int. J. Heat and Fluid Flow 18 (1997) 550-558.
13. J. P. Hartnett and W. J. Minkowycz, Two-phase evaporative heat transfer coefficients of refrigerant HFC-134a under forced flow conditions in a small horizontal tube, Int. Comm. Heat Mass Transfer 27 (2000) 35-48.
14. T. Y. Choi, Y. J. Kim, M. S. Kim, S. T. Ro, Evaporation heat transfer of R-32, R-134a, R-32/134a, and R-32/125/134a inside a horizontal smooth tube, International Journal of Heat and Mass Transfer 43 (2000) 3651-3660.
15. Ming- huei Yu, Tsun-kuo Lin, Chyuan-chyi Tseng, Heat transfer and flow pattern during two-phase flow boiling of R-134a in horizontal smooth and microfin tubes, International Journal of Refrigeration 25 (2002) 789-798.
16. Ho-Saeng Lee, Jung-In Yoon, Jae-Dol Kim, P. K. Bansal, Characteristics of condensing and evaporating heat transfer using hydrocarbon refrigerants, Applied Thermal Engineering 26 (2006) 1054-1062.
17. Somchai Wongwises and Maitree Polsongkram, Evaporation heat transfer and pressure drop of HFC-134a in a helically coiled concentric tube-in-tube heat exchanger, International Journal of Heat and Mass Transfer 49 (2006) 658-670.
18. C. Y. Park and P. S. Hrnjak, CO<sub>2</sub> and R410A flow boiling heat transfer, pressure drop, and flow pattern at low temperatures in a horizontal smooth tube, International Journal of



Refrigeration 30 (2007) 166-178.

19. M. A. Akhavan-Behabadi, Ravi Kumar, S. G. Mohseni, Condensation heat transfer of R-134a inside a microfin tube with different tube inclinations, *International Journal of Heat and Mass Transfer* 50 (2007) 4864-4871.
20. B. Watel, Review of saturated flow boiling in small passages of compact heat-exchangers, *International Journal of Thermal sciences* 42 (2) (2003) 107-140.
21. Yi- Yie Yan and Tsing-Fa Lin, Evaporation heat transfer and pressure drop of refrigerant R-134a in a small pipe, *International Journal of Heat and Mass Transfer* 41 (1998) 4183-4194.
22. Y. Y. Yan and T. F. Lin, Reply to Prof. R.L. Webb's and Dr. J.W. Paek's comments, *International Journal of Heat Transfer* 46 (6) (2003) 1111-1113.
23. Rin Yun, Yongchan Kim, Min Soo Kim, Convective boiling heat transfer characteristics of CO<sub>2</sub> in microchannels, *International Journal of Heat and Mass Transfer* 48 (2005) 235-242.
24. Y. M. Lie, F. Q. Su, R. L. Lai, T. F. Lin, Experimental study of evaporation heat transfer characteristics of refrigerants R-134a and R-407C in horizontal small tubes, *International Journal of Heat and Mass Transfer* 49 (2006) 207-218.
25. Rin Yun, Jae Hyeok Heo, Yongchan Kim, Evaporative heat transfer and pressure drop of R410A in microchannels, *International Journal of Refrigeration* 29 (2006) 92-100.
26. Kwang-Il Choi, A. S. Pamitran, Chun-Young Oh, Jong-Taek Oh, Boiling heat transfer of R-22, R-134a, and CO<sub>2</sub> in horizontal smooth minichannels, *International Journal of Refrigeration* (2007) 1-11.
27. ASHRAE Handbook of Fundamentals 1968

28. S.W. Churchill, H.H.S. Chu, Correlating equations for laminar and turbulent free convection from a horizontal cylinder, International Journal of Heat and Mass Transfer 18(1975)1049-1053.
29. S. J. Kline, F. A. McClintock, Describing uncertainties in single-sample experiments, Mech. Eng. 75 (1) (1953) 3-12.
30. Lockhart, R.W. and Martinelli, R.C., Proposed correlation of data for isothermal two-phase two-component flow in pipes, Chem. Eng. Prog. 45 (1949) 39-48.

